Copyright

by

Harpreet Singh

2014

The Dissertation Committee for Harpreet Singh Certifies that this is the approved version of the following dissertation:

Scale-up of Reactive Processes in Heterogeneous Media

Committee:

Sanjay Srinivasan, Supervisor

Larry W. Lake

David DiCarlo

Peter Eichhubl

Mojdeh Delshad

Scale-up of Reactive Processes in Heterogeneous Media

by

Harpreet Singh, B. Tech; M.S.E.

Dissertation

Presented to the Faculty of the Graduate School of

The University of Texas at Austin

in Partial Fulfillment

of the Requirements

for the Degree of

Doctor of Philosophy

The University of Texas at Austin
December 2014

Dedication

To my mother, Amarjeet Kaur.

Acknowledgements

I would like to express my sincere gratitude to my supervising professor, Dr. Sanjay Srinivasan, for his supervision and support throughout the duration of my graduate studies. If it was not for the confirmation of financial support from him while I was still in India, I would have probably not been able to come to UT. Under his supervision I have learnt to think independently and innovatively, which I think will be useful in my career ahead. I would like to appreciate and thank my committee members for steering me towards a clear and robust hypothesis for my dissertation.

I would like to extend my thanks to my colleagues at PGE, from both past and present: Aarti, Ankesh, Azor, Brandon, Cesar, Colin, Deji, Dhananjay (DJ), Hamid Lashgari, Hapiz, Henry, Hoonyoung, James, John, Juliana, Krupa, Kwangjin, Mayuri, Mohsen Rezaveisi, Morteza, Nader, Naveed, Nitish, Namdi, Sayantan, Selin, Travis and YoungKim.

I owe a big thank you and gratitude to all my friends who made this journey enjoyable and memorable. Even though there are many people with whom I became friends, hung out and spent time with, I would specifically like to mention and appreciate friendship of Puneet, Prashant Verma, Holida, JD, Abhishek Gupta, Fahad, Khalid, Samie, Zohar, Sarah Brundrett, Sarah Moreno and Deepti.

I would like to thank and acknowledge the resources and administrative help provided by the friendly staff of this department, especially Jin Lee, Barbara Messmore, Dr. Roger Terzian, Frankie Hart, Joanna Castillo and Mary Pettengill. I am also grateful

to the Center for Frontiers of Subsurface Energy Security (CFSES), the U.S. Department of Energy, for providing the financial support for this research project.

Finally, I would like to acknowledge my mother as she is the reason of where I am today. Her character and life reminds me of the quote: “Courage does not always roar. Sometimes courage is the quiet voice at the end of the day that says I’ll try again tomorrow.”

Scale-up of Reactive Processes in Heterogeneous Media

Harpreet Singh, Ph.D.

The University of Texas at Austin, 2014

Supervisor: Sanjay Srinivasan

Physical and chemical heterogeneities cause the porous media transport parameters to vary with scale, and between these two types of heterogeneities geological heterogeneity is considered to be the most important source of scale-dependence of transport parameters. Subsurface processes associated with chemical alterations result in changing reservoir properties with interlinked spatial and temporal scale, and there is uncertainty in the evolution of those properties and the chemical processes. This dissertation provides a framework and procedures to quantify the spatiotemporal scaling characteristics of reservoir attributes and transport processes in heterogeneous media accounting for chemical alterations in the reservoir.

Conventional flow scaling groups were used to assess their applicability in scaling of recovery and Mixing Zone Length (MZL) in presence of chemical reactivity and permeability heterogeneity through numerical simulations of CO_2 injection. It was found out that these scaling groups are not adequate enough to capture the scaling of recovery and transport parameters in the combined presence of chemical reactivity and physical heterogeneity. In this illustrative example, MZL was investigated as a function of spatial scale, temporal scale, multi-scale heterogeneity, and chemical reactivity; key conclusions

are that 1) the scaling characteristics of MZL distinctly differ for low permeability and high permeability media, 2) heterogeneous media with spatial arrangements of both high and low permeability regions exhibit scaling characteristics of both high and low permeability media, 3) reactions affect scaling characteristics of MZL in heterogeneous media, 4) a simple rescaling can combine various MZL curves by merging them into a single MZL curve irrespective of the correlation length of heterogeneity, and 5) estimates of MZL (and consequently predictions of oil recovery) will fluctuate corresponding to displacements in a permeable medium whose lateral length is smaller than the correlation length of geological formation.

We illustrate and extend the procedure of estimating *Representative Elementary Volume* (REV) to include temporal scale by coupling it with spatial scale. The current practice is to perform spatial averaging of attributes and account for residual variability by calibration and history matching. This results in poor predictions of future reservoir performance. The proposed semi-analytical technique to scale-up in both space and time provides guidance for selection of spatial and temporal discretizations that takes into account the uncertainties due to sub-processes.

Finally, a probabilistic particle tracking (PT) approach is proposed to scale-up flow and transport of diffusion-reaction (DR) processes while addressing multi-scale and multi-physics nature of DR mechanisms and also maintaining consistent reservoir heterogeneity at different levels of scales. This multi-scale modeling uses a hierarchical approach which is based on passing the macroscopic subsurface heterogeneity down to the finer scales and then returning more accurate reactive flow response. This PT method

can quantify the impact of reservoir heterogeneity and its uncertainties on statistical properties such as reaction surface area and MZL, at various scales.

Table of Contents

List of Tables xviii

List of Figures xix

Chapter 1: Introduction 1

1.1 Problem Description 1

1.1.1 Spatial Scaling of Reservoir Model Parameters 3

1.1.2 Spatial Scaling of Transport Processes 3

1.1.3 Temporal Scaling of Reservoir Parameters and Flow Processes 3

1.2 Significance of Spatial and Temporal Scaling Of Reactive Processes 4

1.3 Research Objectives 6

1.4 Dissertation Outline 8

Chapter 2: Literature Review 10

2.1 Overview 10

2.2 Conceptual Understanding Of Scale-up And Upscaling 10

2.2.1 Upscaling 10

2.2.2 Scale-up 11

2.3 Scale-up Methods 13

2.3.1 Scale-up of Reservoir Attributes 13

2.3.2 Scale-up of Flow and Transport....17

2.3.1.1 Dimensionless Groups....18

2.3.1.2 Averaging of Transport Equations....21

2.3.1.3 Particle Tracking Approach....25

2.4 Reactive Transport Processes In Porous Media....28

2.4.1 Diffusion....30

2.4.1.1 Non-Fickian Diffusion....30

2.4.2 Reaction....31

2.5 Spatiotemporal Statistics....32

2.5.1 Spatiotemporal Covariance....34

2.5.1.1 Product-Sum Model (De Iaco et al. 2001)....35

2.6 Lessons Learnt And Extension of Previous Literature....38

Chapter 3: An Investigation of Scaling of Advection-Dispersion-Reaction Processes in Heterogeneous Media....41

3.1 Overview....41

3.2 Objective....42

3.3 Introduction....44

3.4 Case Study 1: Investigation Of Mixing Zone Length And Its Scale-up in Both Space and Time....45

3.4.1 Description of Case Study 1 45

3.4.1.1 Geological Characteristics 48

3.4.1.2 Relative Permeability Curve 49

3.4.1.3 Fluid, Mineralogy and Reactions 50

3.4.1.4 Models for Reaction Kinetics and Porosity Evolution ...54

3.4.2 Mixing Zone Length and Dispersion Coefficient 56

3.4.3 Results and Discussions 58

3.4.3.1 Breakthrough Curves and Concentration Profiles of $CO_2$58

3.4.3.2 Spatiotemporal Evolution of MZL/Dispersion Coefficient62

3.5 Case Study 2: Effect Of Multi-Scale Heterogeneity On Scaling Of Mixing Zone Length 67

3.5.1 Description of Case Study 2 67

3.5.1.1 Numerical modeling of flow and transport 69

3.5.2 Scaling of MZL 70

3.5.2.1 Dimensionless Scaling Group 70

3.5.2.2 REV 74

3.5.3 Time-dependence of MZL 77

3.6 Summary and Conclusions 78

Chapter 4: A Statistical Analysis of Scaling of Advection-Dispersion-Reaction Processes in Heterogeneous Media....81

4.1 Overview....81

4.2 Objective....82

4.3 Review Of Statistical Concepts....83

4.3.1 Variance of the Mean: REV....83

4.3.2 Semivariogram....85

4.3.2.1 Principal Features of a Stable Semivariogram....85

4.3.2.2 Spatiotemporal Variogram/Covariance....86

4.3.3 Spatiotemporal Variogram Model: Product-Sum Model (De Iaco et al. 2001)....86

4.4 Illustration of Key Concepts Using Synthetic Case Studies....88

4.4.1 Space-Time Evolution of Processes Associated With CO_2 Migration....88

4.4.2 Description of Case Study....89

4.4.3 Empirical Variograms....91

4.4.3.1 Purely Spatial and Purely Temporal Variograms....91

4.4.3.2 Spatiotemporal Variograms With Discrete Time Lags...93

4.4.3.3 Spatiotemporal Variograms with Continuous Time Lags95

4.4.3 Modeled Spatiotemporal Variograms 96

4.4.4 Variance of Mean: REV 97

4.4.5 Conclusions 100

4.5 Scale-up Analysis of Diffusion-Reaction Processes 101

4.5.1 Theoretical Basis 101

4.5.2 Description of Case Study 102

4.5.3 Covariance of Diffusion-Reaction Equation 103

4.5.4 Variance of the Mean: REV 105

4.5.4.1 Scale-up Using Correlation Function of DR Equation .105

4.5.4.2 Scale-up Using Spatiotemporal Concentration Profile .107

4.5.5 Conclusions 113

Chapter 5: Application to Scale-up Analysis of Pore-Scale Spatiotemporal CO_2 Dissolution Data 114

5.1 Overview 114

5.2 Objective 115

5.3 Method 117

5.3.1 Representation of Pore Scale Porous Media 117

5.3.2 Simulated Concentration Data: Model Description/Mathematical Formulation 117

5.3.2.1 Mathematical Formulation for Conservative Process...118

5.3.2.2 Mathematical Formulation for Reactive Process.....119

5.3.2.3 Modified Moving Particle Semi-Implicit (MMPS) Formulation.....120

5.3.3 Scale-up Analysis.....122

5.4 Data.....124

5.4.1 Conservative Process (Advection-Diffusion).....124

5.4.2 Reactive Process.....126

5.5 Results and Discussion.....134

5.5.1 Conservative (Advection-Diffusion) Process.....134

5.5.1.1 Scale-up Using Variogram.....134

5.5.1.2 Scale-up Using Averaging.....136

5.5.2 Reactive (Advection-Diffusion-Reaction) Process.....142

5.5.2.1 Scale-up Using Variogram.....142

5.5.3 Reaction Rate Constant.....148

5.5.3.1 Derivation of Fine-Scale Reaction Rate Constant.....148

5.5.3.2 Scale-up of Reaction Rate Constant Using Averaging.150

5.6 Conclusions.....153

Chapter 6: A Particle Tracking Approach for Analyzing Scale-up of Reactive-Diffusive Process in Heterogeneous Media 156

6.1 Overview 156

6.2 Objective 157

6.3 Particle Tracking 159

6.3.1 General Description 159

6.3.2 Reactive Flow Proxy 160

6.3.2.1 Automated Procedure to Determine the Location of Reaction Front Boundary 161

6.4 Development Of Nested Heterogeneous Models 163

6.5 Consistent Covariance Modeling Across Scales 164

6.6 Results And Discussion 167

6.6.1 Covariance Modeling Across Scales 167

6.6.2 Flow Modeling Across Scales 174

6.6.3 Scale-up of Reaction Surface Area 177

6.6.4 Scale-up of Mixing Zone Length 181

6.7 Conclusions 185

Chapter 7: Conclusions and Recommendations for Future Work 187

7.1 Conclusions 187

7.2 Contributions....190

7.3 Implications of This Research 191

7.4 Recommendations For Future Work....192

Appendix A: Illustration for Computing Spatiotemporal Variogram....194

Appendix B: Code for Covariance Downscaling and Particle Tracking 196

B.1 Code For Covariance Downscaling....196

B.2 Code For Particle Tracking 199

Glossary 206

Symbols: 206

Greek Symbols:....208

Subscripts:....209

Acronyms:....210

Notes: 210

Bibliography 211

List of Tables

Table 3-1: PVT properties of CO_2 and C_1 (Nghiem et al. 2004) 52

Table 3-2: (a) Typical reactions of CO_2-brine mixture with rock minerals such as at the Crystal Geyser site in Utah, (b) Initial aqueous species concentration at 25 ^{o}C, (c) Reaction parameters for aqueous chemical equilibrium, (d) Reaction parameters for minerals 53

Table 6-1: Parameters of the covariance models at various spatial scales 173

List of Figures

Figure 1-1: A schematic illustration of percentage hydrocarbon recovery at disparate scales 2

Figure 1-2: Active and fossil CO_2 seeps along the Little Grand Wash Fault Zone in Utah (Urquhart 2011).....5

Figure 2-1: Conceptual illustration of upscaling 11

Figure 2-2: Conceptual understanding of scale-up 12

Figure 2-3: Concept of REV (Costanza-Robinson et al. 2011) 14

Figure 2-4: Variance of mean plot estimated for several correlation lengths and averaging schemes (Leung 2009) 16

Figure 2-5: Recovery of reservoir fluids using various recovery processes as a function of volume scale (adapted from Lake et al. 2005; Leung 2009) 17

Figure 3-1: Cross-sectional reservoir models corresponding to three different length scales 47

Figure 3-2: Schematic representation of a CO_2 plume on the field scale 48

Figure 3-3: Several realizations of spatial heterogeneity in permeability and its mean used for scenario 2 49

Figure 3-4: Typical Gas-liquid (CO_2-brine) relative permeability curve used in simulations 50

Figure 3-5: History of breakthrough CO_2 (global mole fraction) for 3 different permeability models of 150 md (top row), 1 md (middle row) and heterogeneous field (bottom row) at (a) Scale 1 (all subplots on left column), (b) Scale 3 (all subplots on right column) 60

Figure 3-6: History of breakthrough CO_2 (global mole fraction) when reactions are modeled for 3 different permeability models of 150 md (top row), 1 md (middle row) and heterogeneous field (bottom row) at (a) Scale 1 (all subplots on left column), (b) Scale 3 (all subplots on right column)61

Figure 3-7: Maps of global CO_2 mole fraction at similar pore volumes injected for three different spatial scales in a heterogeneous permeability model (a) Scale 1 without reactions, (b) Scale 1 with reactions, (c) Scale 2 without reactions, (d) Scale 2 with reactions, (e) Scale 3 without reactions, (f) Scale 3 with reactions 62

Figure 3-8: Spatiotemporal variation of normalized MZL (top row) and normalized dispersion coefficient (bottom row) for different permeability models of 150 md (1^{st} column), 1 md (2^{nd} column) and heterogeneous medium (3^{rd} column). Six different legends represent 3 spatial scale models, where each model is populated with or without reactions.....66

Figure 3-9: Five permeability models representative of the coarsest scale and sharing the same covariance model. 68

Figure 3-10: Schematic illustration of the models with different scales of heterogeneity extracted from the largest scale.....69

Figure 3-11: Sub-samples of permeability at different scales extracted from large scale realizations of dimension 200 X 100, and the mean of the subsamples 72

Figure 3-12: For three different spatial scales a) MZL in absolute value versus pore volumes injected, b) MZL normalized by lateral length versus pore volumes injected, c) MZL and pore volumes injected after rescaling to account for the correlation length of heterogeneity 74

Figure 3-13: Spatiotemporal variance of mean MZL a) in form of a surface plot, b) in form of a diagonal plot with three different oblique cuts along the MZL surface plot.....76

Figure 3-14: Spatial variance of mean MZL obtained by averaging over all times.77

Figure 3-15: Variance of mean MZL in time after taking mean along all spatial scales. 78

Figure 4-1: Concentration profiles in space and time corresponding to a simplified components-of-variation model for concentration.....90

Figure 4-2: Purely spatial and purely temporal variograms (normalized) by the variance of the lag-pairs.....92

Figure 4-3: Top row: Spatiotemporal variograms (normalized) for various time lags along N-W, E-W and NW-SE, and Bottom row: Spatiotemporal variograms averaged over all time lags along N-W, E-W and NW-SE94

Figure 4-4: Top row: Spatiotemporal variogram (normalized) 3-D surface plots, and Bottom row: Diagonal sections through surface plots in the N-W, E-W and NW-SE directions, where the x-axis on diagonal sections represent the product of spatial and temporal lags. 96

Figure 4-5: Top row: Spatiotemporal fitted variogram (normalized) 3-D surface plots, and Bottom row: Diagonal sections through surface plots in the N-W, E-W and NW-SE directions, where the x-axis on diagonal sections represent the product of spatial and temporal lags. Note the x-axis is the product of the spatial and temporal lags. 97

Figure 4-6: Variance of mean concentration computed using a) numerical values of concentration, and b) variogram, from Eqn. (4.2) 99

Figure 4-7: Variance of mean concentration computed a) by averaging the concentration values, and b) by evaluating the space-time integrals of the spatiotemporal covariance, c) along the diagonal cut through the surface in (a), d) along the diagonal cut through the surface in (b).....100

Figure 4-8: Spatial and temporal correlation function of concentration in presence of (a) diffusion and reaction, (b) no diffusion and no reaction, (c) reactions but no diffusion, and (d) diffusion but no reactions.....104

Figure 4-9: Spatiotemporal variance of mean concentration computed by integrating the spatiotemporal covariance over spatial and temporal lags.....106

Figure 4-10: Spatiotemporal variance along a diagonal through the 3-D surface plot of the variance of the mean computed using the spatiotemporal covariance. 107

Figure 4-11: Simulated numerical solution of $c(s;t)$. Each 1D slice through the above figure represents the concentration distribution at a particular snapshot in time. 110

Figure 4-12: Numerical solutions of concentration in presence of (a) no diffusion and no reaction, (b) reactions but no diffusion, and (c) diffusion but no reactions 111

Figure 4-13: Spatiotemporal variance of mean concentration computed by numerically solving the DR equation and averaging the concentration values. 111

Figure 4-14: Spatiotemporal variance, using $\mathrm{var}\{\bar{c}(s;t)\}$, along the diagonal of surf plot shown in Figure 4- 112

Figure 5-1: Schematic representation of the changes introduced in reservoir due to reactive flow because of CO_2 injection.....116

Figure 5-2: Reconstruction of the porous media using X-ray microtomography for (a) matrix (b) pore space 117

Figure 5-3: Scatter dataset of pressure (in MPa) in 3-D space 125

Figure 5-4: Gridded dataset of pressure (in MPa) in 3-D space 125

Figure 5-5: Scatter dataset of pore geometry alteration PGA (top), change in porosity CIP (middle) and concentration of CO2 - CO2CONC (bottom) in 3-D space.....127

Figure 5-6: Gridded dataset of PGA (top), CIP (middle) and CO2CONC (bottom) computed in 3-D space.....128

Figure 5-7: Gridded 3-D spatial data for pore geometry (legend = 0, 1 for matrix and fluid, respectively) alteration (denoted as PGA) at all times 130
Figure 5-8: Gridded 3-D spatial data for dissolution due to change in porosity (denoted by CIP) at all times 131
Figure 5-9: Gridded 3-D spatial data for volume-based dimensionless CO_2 concentration (denoted by CO2CONC) at all times. 132
Figure 5-10: Gridded spatiotemporal variation of pore geometry alteration (PGA), change in porosity (CIP) and CO2CONC corresponding to a reactive transport process is shown. 133
Figure 5-11: Empirical variograms for 3D spatial data for pressure 135
Figure 5-12: A projection through the 3-D variogram model computed using the spatiotemporal data for pressure 135
Figure 5-13: Variance of mean pressure computed by evaluating the spatiotemporal integral of the model covariance 136
Figure 5-14: Variance of the mean along the diagonal of the plot shown in Figure 5-13.....136
Figure 5-15: Upscaled pressure using linear averaging for grid sizes of a) 25 X 25 X 5, b) 50 X 50 X 10 137
Figure 5-16: Variance of mean pressure computed directly using the pressure values available at the pore scale. 138
Figure 5-17: Variance of mean pressure extracted along the diagonal of the surface plot shown in Figure 5-16 138

Figure 5-18: Upscaled pressure using nonlinear averaging for grid sizes of a) 25 X 25 X 5, b) 50 X 50 X 10.....140
Figure 5-19: Variance of mean pressure computed directly using the pressure values available at the pore scale. 141
Figure 5-20: Variance of mean pressure extracted along the diagonal of the surface plot shown in Figure 5-19. 141
Figure 5-21: Empirical variograms of PGA (top), CIP (middle) and CO2CONC (bottom) computed using spatiotemporal data for the reactive process along a few select directions. 143
Figure 5-22: Spatiotemporal variogram models for PGA (top), CIP (middle) and CO2CONC (bottom).....144
Figure 5-23: Spatiotemporal variance of mean PGA by performing space-time integration of the spatiotemporal variogram model over spatial and temporal lags. 145
Figure 5-24(a): Spatiotemporal variance of mean CIP by performing integration of the spatiotemporal variogram model over spatial and temporal lags.146
Figure 5-24(b): Spatiotemporal variance of mean CIP by directly using the CIP data available at the pore scale. 146
Figure 5-25: Spatiotemporal variance of mean CO2CONC by performing integration of the spatiotemporal variogram model over spatial and temporal lags. 147
Figure 5-26: Variance of mean reaction rate constant computed using averaged concentrations corresponding to different spatial scales. 151

Figure 5-27: Variance of mean reaction rate constant computed using averaging Method-1.....152
Figure 6-1: Schematic of the possible particle movements from grid A to grid B160
Figure 6-2: Schematic of the volume used for performing scaling calculations. 162
Figure 6-3: Graphical representation of a property at two scales 165
Figure 6-4: Different realizations, their mean, and variance of the coarse scale (5X5) permeability 168
Figure 6-5: Different realizations, their mean, and variance at a finer scale (10X10) permeability. These realizations reflect a covariance model consistent with the coarse scale model. 169
Figure 6-6: Different realizations, their mean, and variance of fine scale (15X15) permeability. These realizations reflect a covariance model consistent with the coarse scale model. 170
Figure 6-7: Different realizations, their mean, and variance of fine scale (35X35) permeability. These realizations reflect a covariance model consistent with the coarse scale model. 171
Figure 6-8: Different realizations, their mean, and variance of fine scale (50X50) permeability. These realizations reflect a covariance model consistent with the coarse scale model. 172
Figure 6-9: a) sill, b) minor correlation length, and c) major correlation length – all at various scales. 174

Figure 6-10: Particle density corresponding to four permeability realizations at the coarse scale (5X5) a) Realization 1, b) Realization 2, c) Realization 3 d) Realization 4 e) Mean particle density over 12 realizations and f) normalized variance of particle density over 12 realizations.....175

Figure 6-11: Particle density corresponding to four permeability realizations at the 10X10 scale a) Realization 1, b) Realization 2, c) Realization 3 d) Realization 4 e) Mean particle density over 12 realizations and f) normalized variance of particle density over 12 realizations.....175

Figure 6-12: Particle density corresponding to four permeability realizations at the 15X15 scale a) Realization 1, b) Realization 2, c) Realization 3 d) Realization 4 e) Mean particle density over 12 realizations and f) normalized variance of particle density over 12 realizations.....176

Figure 6-13: Particle density corresponding to four permeability realizations at the 35X35 scale a) Realization 1, b) Realization 2, c) Realization 3 d) Realization 4 e) Mean particle density over 12 realizations and f) normalized variance of particle density over 12 realizations.....176

Figure 6-14: Particle density corresponding to four permeability realizations at the 50X50 scale a) Realization 1, b) Realization 2, c) Realization 3 d) Realization 4 e) Mean particle density over 12 realizations and f) normalized variance of particle density over 12 realizations.....177

Figure 6-15: Total number of particles (normalized) along the boundary as a function of model size. 179

Figure 6-16: Variance of all particles from any single model (normalized) along the boundary as a function of model size. 179
Figure 6-17: Length of boundary (formed by non-zero particles) as a function of model size based on results of PT.....181
Figure 6-18: Schematic of the concentration boundaries for c = 0.84 (black line) and c = 0.16 (red line), plus the perpendicular distances between the points on these two boundaries used for performing MZL calculations. 183
Figure 6-19: MZL as a function of model size based on results of PT.....184
Figure 6-20: Variance of a) MZL, and b) mean MZL as a function of model size185
Figure A-1: Concentration profiles in space and time 194
Figure A-2: Illustration of spatiotemporal variogram calculation along various directions.....195

Chapter 1: Introduction

1.1 Problem Description

The flow of reactive fluids in porous media such as during thermal recovery processes, chemical EOR and CO_2 sequestration is inherently multi-physics and the processes occur over multiple temporal and length scales. For example, temporally, advection and diffusion are much slower processes (years) than chemical reactions (minutes or hours), and spatially, advection and diffusion take place over the entire reservoir while chemical reactions in porous media occur locally around the reaction front. Percentage recovery of hydrocarbon from core floods, pilot tests and field-scale recovery processes show a wide variation and discrepancy on spatial scales as illustrated schematically in Figure 1-1. We expect the recovery to decrease as we go from laboratory core flood experiment to a pilot or field scale process implementation for similar geological settings. Additionally, it is expected that the recovery from several core flood experiments (variance of recovery) to exhibit more variability than the recovery from similar number of pilot or field scale implementations; this statement is valid under the assumption that all the base conditions such as geological setting, operating conditions, initial condition, boundary conditions etc. are consistent at all scales. When the fluid flow occurs at the field scale the effects of strong contrasts in reservoir properties are somewhat averaged, thereby resulting in less variability from one representation of the reservoir to the next. This spatial scale-dependent discrepancy in hydrocarbon recovery is primarily due to variation in 1) scaling characteristics of reservoir parameters such as

permeability, porosity, relative permeability etc., and 2) behavior of flow variables (physical and chemical) such as reactive surface area, mixing zone length (MZL) etc.

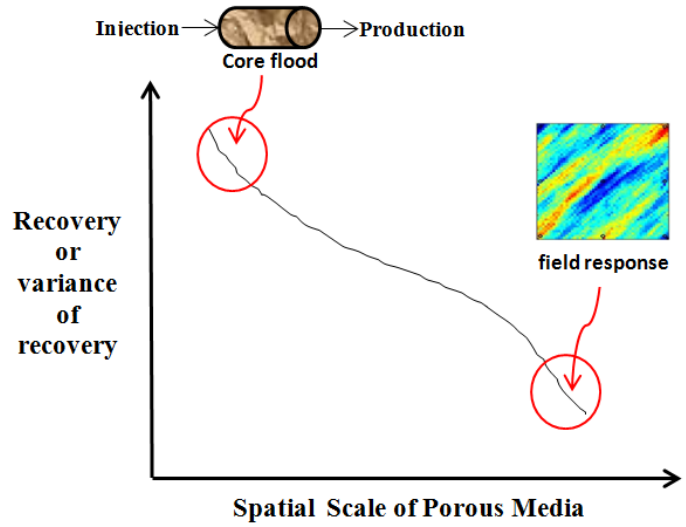

Figure 1-1: A schematic illustration of percentage hydrocarbon recovery at disparate scales

The discrepancy in recovery from laboratory to field scale is fundamentally because the transport processes (physical or chemical) exhibit a functional relationship with spatial scale. Predictions of recovery by application of a numerical model to simulate the recovery process at laboratory and field scales may show discrepancy because reservoir model parameters are not scaled appropriately before they are fed into a reservoir simulator. The dependence of model parameters and transport processes on spatial scale is explained further in two sub sections:

1.1.1 Spatial Scaling of Reservoir Model Parameters

Reservoir model parameters exhibit a dependence on scale because of two primary reasons, which are:

1. Different measurement/resolution scales for different types of data. For example, measurement scale of core/log data varies from few inches to few feet whereas for seismic, the measurement resolution is of the order of a few meters.
2. Heterogeneity at pore scale, referred to as sub-scale variability, introduces fluctuations and uncertainty in reservoir parameters.

1.1.2 Spatial Scaling of Transport Processes

As discussed above, the percentage recovery of hydrocarbon from core floods to field-scale reservoir decreases with increasing scale as illustrated schematically in Figure 1-1. Previous attempts to scale-up transport processes assumed the porous media to be homogeneous. However, it is well known that heterogeneity plays an important role in transport processes as it impacts non-Fickian diffusion and the MZL evolution of the fluid (Edery et al. 2011; Berkowitz et al. 2013).

1.1.3 Temporal Scaling of Reservoir Parameters and Flow Processes

Analysis of temporal scaling of subsurface flow processes is not a very well researched topic, and the limited literature that exists on this topic is specifically related to ground water flow. The concept of variation in groundwater flow dynamics due to topographical changes in the landscape as a function of time scale was first hypothesized

by Tóth (1962; 1963) in addition to other studies (Zijl 1999; Z. Li 2006). However, the relevance of temporal scaling on reservoir flow processes in oil and gas reservoirs is not due to topographical changes but due to the different dynamics of processes such as reactive flow that alter the reservoir pore structure with time. The alteration in reservoir pore structure with time could occur for processes such as in-situ combustion, thermal processes, CO2 sequestration, chemical EOR etc. For example, in CO_2 sequestration application, the reaction of CO_2 with rock minerals present in situ causes the effective properties of the medium to change with time and this in turn imparts a dependency of the reactive-transport process on the time scale (L. Li, Steefel, and Yang 2008; Battiato and Tartakovsky 2011) employed to study the process.

1.2 Significance of Spatial and Temporal Scaling Of Reactive Processes

Subsurface processes associated with chemical alterations change reservoir properties such as porosity, permeability etc. not just spatially but also temporally (Edery et al. 2011; Emmanuel and Berkowitz 2005; Urquhart 2011; Romushkevich et al. 2013). Hence, transport processes such as diffusion, reaction, thermal processes etc. that are functions of reservoir properties will also vary with time in addition to space. Therefore, accurate assessment of reservoir properties with their spatial and temporal variations is essential in order to correctly characterize the reservoir performance.

In the case of CO_2 injection into a brine-filled aquifer, the formation of a weak acid leads to rapid porosity and permeability changes in carbonate rocks and to a lesser extent in sandstones (Tutolo et al. 2014; Lamy-Chappuis et al. 2014; Luquot et al. 2014). A field scale example are the observations at the Grand Wash Fault in Utah where CO_2

seep sites migrate laterally with time due to calcification/clogging of porosity and permeability (Figure 1-2). However, there is no clear understanding yet to explain the physical mechanism behind this observation. Preliminary modeling work (Kim 2012) indicate that the migration of the seep spots may be related to the plugging of existing conduits due to mineral precipitation.

Figure 1-2: Active and fossil CO_2 seeps along the Little Grand Wash Fault Zone in Utah (Urquhart 2011)

Complex interdependencies between the spatial and temporal evolution of processes related to alterations in reservoir properties result in emergent patterns that are not just solely dependent on spatial scale or solely on temporal scale but rather on combination of spatial and temporal scales. Therefore, for processes which alter the pore space scale dependence as a function of space-time coupling is important and must be accounted for in scale-up.

1.3 RESEARCH OBJECTIVES

Physical and chemical heterogeneities cause the porous media transport parameters to vary with scale. As discussed earlier, geological/physical heterogeneity plays a major role in introducing the scale-dependence of transport parameters (Dai et al. 2004; Dai et al. 2005; Dai et al. 2007; Dai et al. 2009). Subsurface processes associated with chemical alterations such as chemical EOR, thermal recovery processes and CO_2 sequestration result in changing reservoir properties in both space and time and there is uncertainty in the evolution of those properties and the flow processes. Additionally, the evolution of these properties and processes in space and time and the uncertainties inherent in making predictions regarding them are often interlinked in space-time and non-separable. *Therefore, it is hypothesized that accurate assessment of the scaling characteristics of reactive-transport processes in reservoirs requires analysis of the spatiotemporal variability of the underlying rock properties of the reservoir.* The primary research objective is to provide a framework to quantify the spatiotemporal scaling characteristics of reservoir attributes and transport processes in heterogeneous media accounting for chemical alterations. This objective is split into following three parts:

1. Performance prediction of reactive processes such as those associated with injection of chemicals that react with rock and fluids require accurate models for the processes. Frequently, these processes are studied at laboratory scale and modeling them at the field scale entails scaling-up of laboratory observations taking into account the spatial variability of parameters. In the context, the following are two project research objectives:

a. Analyze spatiotemporal scale-up of MZL/dispersion coefficient in the combined presence of chemical reactivity and heterogeneity.
b. Assess applicability of conventional flow scaling groups in presence of chemical reactivity and permeability heterogeneity.
c. Evaluate the impact of multi-scale permeability heterogeneity on the spatiotemporal characteristics of MZL; propose a simple rescaling which can combine various MZL curves by merging them into a single MZL curve irrespective of the correlation length of heterogeneity.

2. Scale-up of flow and transport related reservoir attributes such as pressure, concentration etc. The current practice is to perform spatial averaging of attributes and account for residual variability by calibration and history matching, however, this result in poor predictions of future reservoir performance. A semi-analytical model considering both the spatial and temporal characteristics of the reservoir attribute is used to derive the *Representative Elementary Volume* (REV) of attribute in combined space and time.

3. It is well known that chemical reactions in porous media occur locally around the reaction front which is spatially on a very smaller scale compared to the field-scale. The reactions originate at nanoscale, however, and their evolution is manifested in the form of a complex emergent phenomenon at field-scale (Deyoreo and Depaolo 2009). The research objective is to scale-up the

behavior of reactive-diffusive processes in the geologic media from continuum to field-scale and specifically to:

a. Accurately scale-up properties accounting for the multi-scale and multi-physics nature of transport processes in heterogeneous medium.
b. Incorporating consistent reservoir heterogeneity at all scales of the model for the porous medium.

1.4 DISSERTATION OUTLINE

Chapter 2 presents a review of the relevant literature pertaining to scale-up of reservoir attributes and processes. Chapter 3 investigates the effect of permeability, reactivity and reservoir heterogeneity on Mixing Zone Length (MZL) as a function of spatial and temporal scales using full-physics numerical simulations. We use conventional flow scaling groups to assess their applicability in scaling of recovery and MZL in presence of chemical reactivity and permeability heterogeneity. Chapter 3 also investigates the effect of varying scales of geologic heterogeneity on the spatiotemporal evolution of MZL and provides a dimensionless number for scaling MZL in heterogeneous reservoirs. Chapter 4 utilizes some concepts from Chapter 2 to demonstrate a statistical approach to scale-up advection-dispersion-reaction (ADR) processes in heterogeneous media in space and time whose spatiotemporal evolution can be described using a space-time equation. This is illustrated using two case studies; the first case study uses a simple stochastic function to describe the evolution of concentration with time inside a reservoir and the second case study uses the stochastic partial differential equation (PDE) that describes the spatiotemporal evolution of CO_2 concentration associated with a diffusive-reactive

process in geological formations. Chapter 5 applies a statistical scale-up approach using high-resolution pore-scale data for conservative flow as well as for reactive flow measured under laboratory conditions. The available pore-scale reactive attribute data is used to obtain reaction rate constant from first order rate law principles. The reaction rate constant is then scaled-up to a spatiotemporal REV scale using a statistical approach. Chapter 6 utilizes concept of particle tracking to scale-up diffusive-reactive processes with scale-appropriate heterogeneity structure inferred by downscaling covariance from coarse scale to any scale of interest. The distribution of particles at the end of travel time for all models is used to derive statistical properties such as reaction surface area and mixing zone length (MZL) to characterize the scaling of reactive-diffusive processes. Chapter 7 summarizes key findings of the research, the contributions, implications and some ideas for future research.

Chapter 2: Literature Review

2.1 Overview

This chapter presents relevant literature on scale-up of reservoir attributes and flow and transport parameters in porous media. It begins with a brief discussion of keys concepts in scale-up analysis and upscaling including an attempt to differentiate between these two concepts. Next, we review literature on scale-up of reservoir attributes. This is followed by a review of some common approaches to scale-up fluid flow in a porous media – 1) Dimensionless groups, 2) Averaging of transport equations from fine scale to macroscopic scale, and 3) PT approach.

2.2 Conceptual Understanding Of Scale-up And Upscaling

2.2.1 Upscaling

Upscaling is the process of substituting the heterogeneous property variation within a region described by fine grid cells with the corresponding effective value assigned to a coarse-grid (Durlofsky 2003) as shown in Figure 2-1. Upscaling is generally categorized by the type of parameter to be upscaled, which could be either single or multi-phase flow parameters (Durlofsky 2003). For single-phase flow, upscaling is used to compute the effective absolute permeability whereas in multi-phase flow, upscaling is used to produce the effective relative permeability, capillary pressure value etc. There is a lot of literature on upscaling techniques (Christie, 2001; Qi and Hesketh 2005; Durlofsky, 2003; Hassanizadeh and Das, 2005) and the challenges associated with obtaining upscaled parameters corresponding to different flow and boundary conditions.

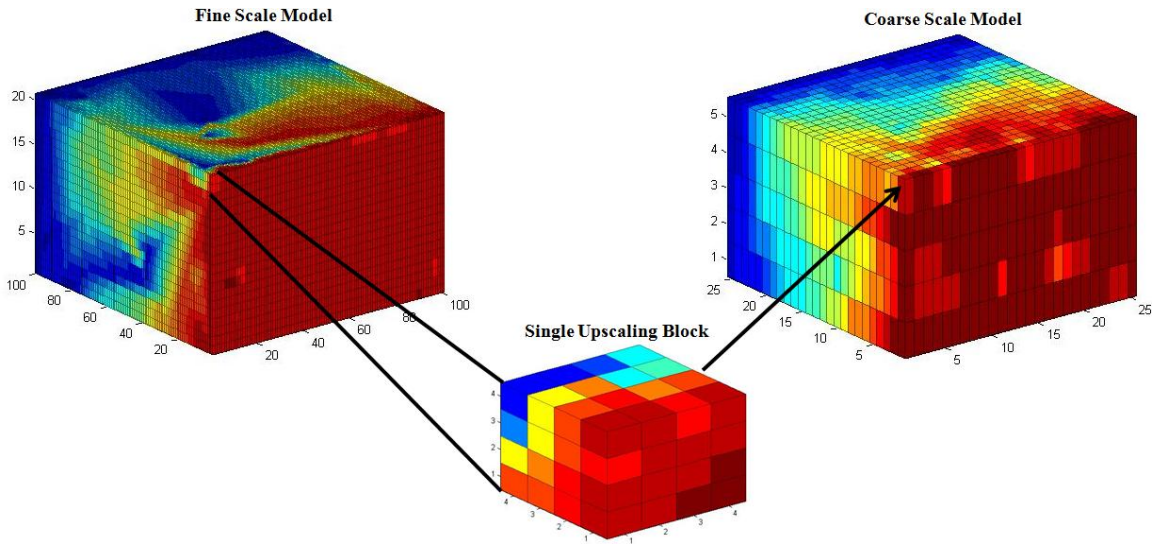

Figure 2-1: Conceptual illustration of upscaling

2.2.2 Scale-up

Scale-up is a computational process to represent phenomena observable at one scale to that at another scale. There are primarily two reasons why the behavior of phenomenon can be different at different scales – 1) different scales of measurement for different types of data, and 2) variation in behavior of the flow processes (physical and chemical) at different scales.

The primary difference between upscaling and scale-up is that upscaling forces the flow response such as pressure or flow rate to be equal at fine and coarse scales, whereas this assumption is not required in scale-up. In fact it is the objective of scale-up to describe the flow and transport at a coarse scale given the flow and transport at a fine scale. A typical example of scale-up would be to predict the response of a particular recovery process at field scale using the known response of a core flood in the laboratory

(Figure 2-2). However, scaling-up the lab scale response to field scale is challenging because of the multi-scale nature of porous media heterogeneity that in turn influences the scale-dependence of transport parameters (Dai et al. 2004; Dai, Ritzi, and Dominic 2005; Dai et al. 2007; Dai et al. 2009).

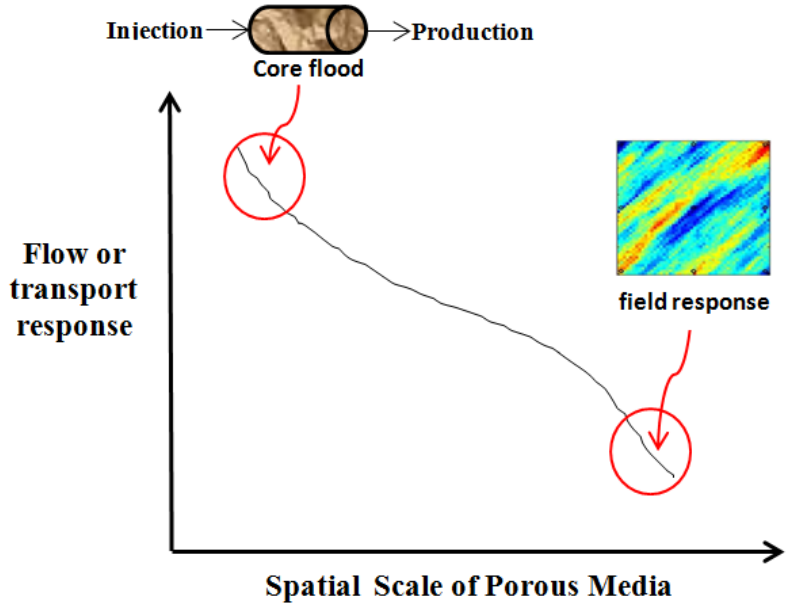

Figure 2-2: Conceptual understanding of scale-up

This dissertation primarily addresses the issue of scale-up, especially corresponding to multi-physics transport of species within the porous medium. However, some of the numerical examples for scale-up will use upscaling to ensure correspondence between reservoir parameters at different scales and subsequently illustrate the scale-up of other transport variables.

2.3 SCALE-UP METHODS

Scale-up methods can be further divided into two main categories – 1) Scale-up of reservoir attributes, and 2) Scale-up of flow and transport. In the subsequent section we will review the literature on scale-up of reservoir attributes and follow that up with a review of scale-up of flow and transport.

2.3.1 Scale-up of Reservoir Attributes

There are two primary reasons to perform scale-up of reservoir attributes:

1) Different measurement/resolution scales for different types of data. For example, measurement scale of log/core data varies from few inches to few feet whereas for seismic it is few meters.
2) Different scales of geological static models and flow simulation models. Scale of geological static models is quite fine compared to flow simulation models.

Broadly, the objective of scale-up of static reservoir attributes is to find the spatial variability of the attribute at target scale given the variability at a different scale. The spatial variability of a variable at a particular scale affects the manner in which the mean of that variable at a coarser scale varies spatially. In other words, the spatial variability exhibited by a variable at a particular scale affects the variance of the mean of that variable at a coarser scale. This concept underlies the notion of the *Representative Elementary Volume* (REV). REV is the volume at which the averaging of the reservoir attribute becomes stable (Bear 1972). The REV is therefore a measure of the behavior of the mean of a variable at different scales. The concept of REV is shown schematically in Figure 2-3 (Costanza-Robinson et al. 2011), where region I represents small pore scale

and scale III represents large macro scale. For homogeneous porous media, REV for a reservoir attribute is achieved at the boundary of region I and II, which means the measured value of attribute at this scale or larger will be constant and scale independent. However, for a heterogeneous media, the transition to the REV scale will be more uncertain and will generally lie at a scale between the region I and III.

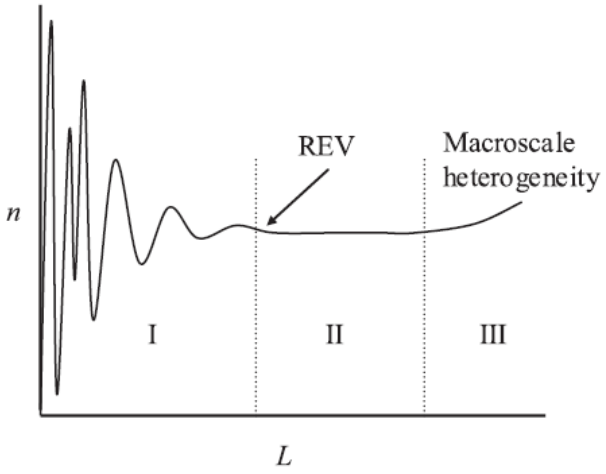

Figure 2-3: Concept of REV (Costanza-Robinson et al. 2011)

As shown in Figure 2-3 REV can be achieved at pore scale for some attributes in a homogeneous medium while for heterogeneous cases REV could be larger than the inter-well distance, specifically where heterogeneity exhibits long correlation lengths (Leung 2009).

The REV of an attribute can be determined from a log-log plot of the variance of attribute's *linear average* vs. length scale (Lake and Srinivasan 2004). This plot depicts a diagnostic signature of negative unit slope at scales larger than REV. The slope value signifies independence between the block means at that scale. The variances of the linear

average of an attribute *f* over a length scale *L* for a 1-D and 3-D volume are given by the following respective equations:

$$Var(\bar{f}) = \frac{2\sigma^2}{L^2}\left(\int_{\xi=0}^{\xi=L}\int_{\eta=0}^{\eta=\xi}\rho_{corr}(\eta)d\eta d\xi\right) \tag{2.1}$$

$$Var(\bar{f}) = \frac{2\sigma^2}{V^2}\left(\int_{V}\int_{\eta_i}\rho_{corr}(\eta)d\eta d\xi\right) \tag{2.2}$$

where,

σ^2 = variance of f

ρ_{corr} = spatial autocorrelation function

η_i = all possible spatial lags within L or $V\left(=L\times B\times H\right)$

Using the formulation described in Eqn. (2.1) or (2.2), one can estimate the variance of attribute's mean either by performing numerical integration of the correlation function such as variogram or covariance at various spatial scales, or for some cases of an analytical covariance model, by performing the integration analytically.

The general procedure to estimate REV from variance of the mean plot using the RHS of the above formulation is to model the variogram for point support data and then numerically compute the variance of mean by numerically integrating $\rho_{corr}(\eta)$ for all possible lag distances over the volume/length of investigation.

Alternatively if the reservoir attribute values at the fine scale are available, then the mean for different block sizes and the variance of mean can be computed. This would yield a variance of the mean plot similar to the one discussed before. This averaging process can be generalized to an arbitrary power average to indicate a non-linear relationship between the averaging at different scales as given by Eqn. (2.3):

$$\bar{f} = \left[\frac{1}{V_b}\int_{V_b}\left(f\right)^{\omega}dV\right]^{1/\omega} = \left[\frac{1}{V_b}\sum_{Z}\sum_{Y}\sum_{X}\left\{f\left(X,Y,Z\right)\right\}^{\omega}\right]^{1/\omega} \tag{2.3}$$

where,

$f(X,Y,Z)$ = Fine scale attribute

$\overline{f}$ = Mean of attribute

V_b = Coarse block bulk volume

ω = Averaging exponent

Leung (2009) reported some general results that compare variance of mean for different correlation lengths and different types of averaging scheme. As the autocorrelation length of the heterogeneous medium increases, the REV increases which means it takes a larger averaging volume for the fluctuations in the value of a chosen attribute to subside. Also, as ω decreases the REV increases.

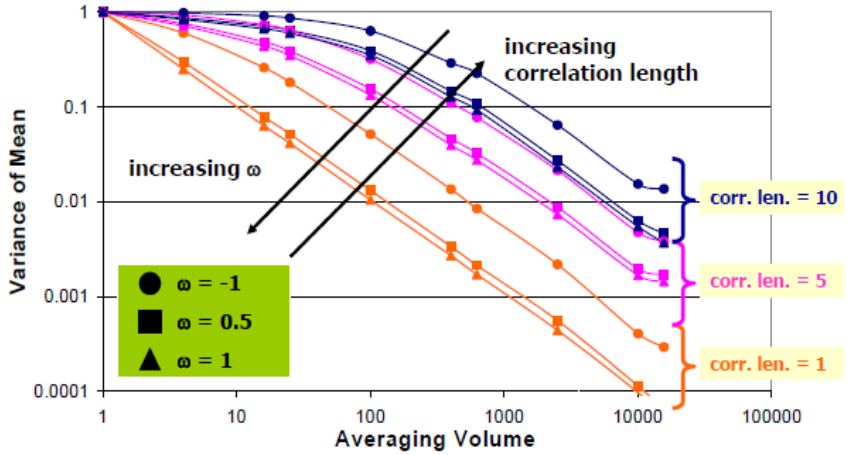

Figure 2-4: Variance of mean plot estimated for several correlation lengths and averaging schemes (Leung 2009)

In general, most reservoir attributes may not follow a linear averaging rule. For example, permeability at coarser scale is not generally related to that finer scale linearly Similarly, another important reservoir attribute that does not average linearly is fracture porosity as described in detail by Leung (2009).

2.3.2 Scale-up of Flow and Transport

Lake et al. (2005) showed how ultimate recoveries vary with spatial scale by employing data collected from various EOR and remediation processes including polymer and surfactant flooding, thermal and in-situ chemical oxidation. The data, as seen in Figure 2-5, shows that recovery factor (RF) decreases with increasing scale.

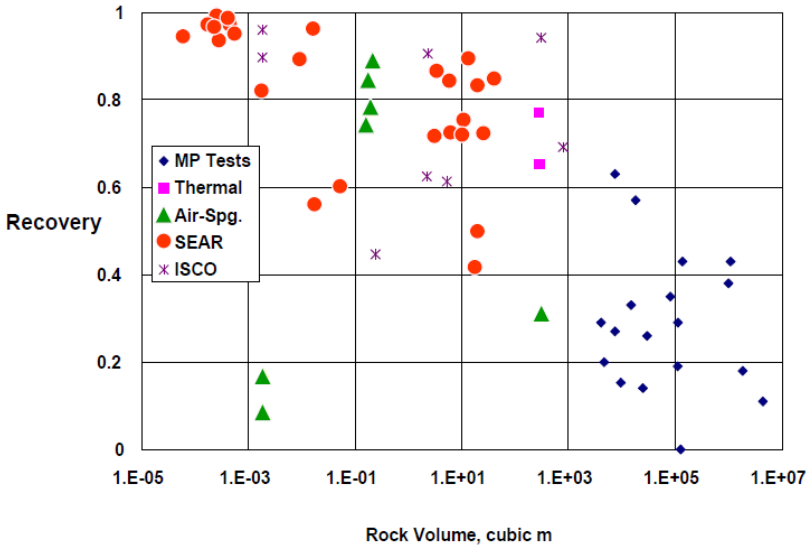

Figure 2-5: Recovery of reservoir fluids using various recovery processes as a function of volume scale (adapted from Lake et al. 2005; Leung 2009)

It is evident from Figure 2-5 that accurate methods for scaling-up flow and transport responses from laboratory to field scale are necessary prior to implementing a process in a pilot or at field scale. Three popular approaches to scale-up flow and transport currently used are - 1) Dimensionless groups, 2) Averaging of transport equations (ensemble averaging and volume averaging) from fine scale to macroscopic scale, and 3) Particle tracking approaches.

2.3.1.1 Dimensionless Groups

Dimensionless groups are used to estimate the relative importance of various types of transport processes. They are applied with the proven hypothesis that porous media at multiple scales will exhibit similar recovery response if the magnitudes of dimensionless groups defining the fundamental processes at multiple sizes are equal (D. Li and Lake 1996; Peters 1983; Shook et al. 1992; Wood et al. 2008; Gharbi et al. 1998). Li and Lake (1996) proposed two categories of dimensionless groups – *flow scaling groups* and *heterogeneity scaling groups*. For the first time they included a measure of reservoir heterogeneity within the dimensionless scaling method. The flow related variables (for example effective aspect ratio of permeability, dip angle, end-point mobility ratio etc.) were scaled using Shook's dimensionless groups (Shook et al. 1992). Their general method to scale-up immiscible displacement for two phase flow for anisotropic and heterogeneous porous media geometry is based on the assumption of statistical stationarity (i.e. a phenomenon whose mean and variance do not change with time and space). Porosity is treated as homogeneous just like the relative permeability functions. Flow scaling groups are composed of 5 dimensionless numbers that are (D. Li and Lake 1996):

Flow Scaling Group

Effective aspect ratio: $R_L = \frac{L}{H}\sqrt{\frac{\bar{k}_z}{\bar{k}_x}}$

Dip angle group: $N_\alpha = \frac{L}{H}\tan(\alpha_{\text{dip}})$

End-point mobility ratio: $M^o = \frac{\lambda^o_{r1}}{\lambda^o_{r2}} = \frac{k^o_{r1}\mu_2}{k^o_{r2}\mu_1}$

Buoyancy number: $N_g = \dfrac{\bar{k}_x \lambda_{r2}^o \Delta\rho g \cos(\alpha_{\text{dip}})}{u_T} \dfrac{H}{L}$

Capillary number: $N_{Pc} = \dfrac{\lambda_{r2}^o \sigma(\cos\theta)\sqrt{\bar{k}_x \phi}}{L u_T}$

$\lambda_{rj} = \lambda_{rj}^o s_{jD}^{n_j},\ j(s_{1D}) = (1 - s_{1D})^{n_{Pc}},\ \lambda_{rj}^o = \dfrac{k_{rj}^o}{\mu_j}$

where,

L = Global window length (or lateral length of reservoir)

H = Global window width (or width of reservoir)

μ_j = Viscosity of phase j

α_{dip} = Reservoir dip angle

θ = Contact angle

$\bar{k}_x$ = Average permeability in x-direction

$\Delta\rho$ = Density difference between two phases

u_i = Darcy or superficial velocity of phase i

σ = Oil/water interfacial tension

λ_{rj}^o = endpoint relative mobility of phase j

k_{rj}^o = endpoint relative permeability of phase j

$j(S_{1D})$ = Leverett j - function

S_{jD} = dimensionless (or normalized) saturation of phase j

$n_1,\ n_2,\ n_{Pc}$ = petrophysical relations

The key step in dimensionless group analysis is matching the above 5 dimensionless groups and the petrophysical relations n_1, n_2 and n_{Pc}, at different scales, for a flow problem with invariant geometry across scales to generate equivalent recovery results.

Heterogeneity scaling groups are statistical measures that are composed of spatial correlation of permeability at three scales – local, global, and zonal.

Heterogeneity Scaling Group

Heterogeneity scaling group is formulated in two steps. The first step is to generate spatially heterogeneous and anisotropic permeability field in dimensional form. The second step involves computing the actual permeability values corresponding to the dimensionless values generated in step 1.

Step 1: $k_x = k_x(x,z)$ and $k_z = k_z(x,z)$ are generated using a spatial simulation methods such as the matrix decomposition method (MDM or LUSIM - Yang 1990) which makes use of the semivariogram representation and the random field values to formulate the heterogeneity scaling group.

Step 2: Dimensionless anisotropic permeability is defined using the grid block permeability values within a window as:

$k_D = I + N_\sigma L_D(\lambda^*_{Dx}, \eta_{Dx}, \lambda^*_{Dz}, \eta_{Dz}, N_n, H)w$ for a normal distribution, and

$\ln(k_D) = I + N_\sigma L_{D\ln}(\lambda^*_{Dx}, \eta_{Dx}, \lambda^*_{Dz}, \eta_{Dz}, N_n, H)w$ for a lognormal distribution, and

where,

$N_\sigma = \frac{\sigma}{m}, N_n = \frac{C_o}{\sigma^2}$ for a normal distribution, and

$N_\sigma = \sigma_{\ln}, N_n = \frac{C_o}{\sigma^2_{\ln}}$ for a lognormal distribution

$V_{DP} = 1 - e^{-N_\sigma}$ for a lognormal distribution

σ = standard deviation of the window
m = mean of the window
I = unit matrix
L_D = lower triangular matrix of the Cholesky decomposition of the dimensionless co variance matrix
λ_{Di}^* = dimensionless effective correlation length in i direction (i = x or z)
$\lambda_{Dx}(=\lambda_x / L), \lambda_{Dz}(=\lambda_z / H)$ = dimensionless power-law upper cutoffs defined on a normally distributed field
η_{Dx}, η_{Dz} = sizes of a dimensionless pixel
C_o = variance at a lower cutoff
w = vector of N uncorrelated random variables from a standard normal distribution
N_n, N_σ = measures of local and global heterogeneities, respectively
V_{DP} = Dykstra-Parsons coefficient

Finally, the heterogeneity scaling numbers are N_σ, N_n, and λ_{Di}^* and H which define global, local, and zonal heterogeneities, respectively. These scaling groups are the measures of heterogeneity. They can have different values in different directions for anisotropic medium. For detailed derivation on how to obtain gridded permeability field using these heterogeneity scaling numbers, the reader can refer to Appendix A of Li and Lake (1996).

The limitation of the dimensionless groups is that it fails to incorporate the spatial variation in magnitude of reservoir parameters.

2.3.1.2 Averaging of Transport Equations

Flow and transport can also be scaled-up by averaging transport equation from fine scale to macroscopic scale, which provides the effective transport parameters at the coarse scale. The averaging of transport equations can be done using one of two

formalisms – 1) Ensemble Averaging (or Stochastic Perturbation), 2) Volume Averaging. These formalisms are employed to obtain effective transport parameters (or their variance) at multiple scales (Dongxiao and Winter 1999; Gelhar and Axness 1983; Cushman 1982; Howes and Whitaker 1985; Whitaker 1999). The effective transport parameters at various scales can then be used to predict flow and transport response as a function of scale. The difference between these two formalisms is the way the effective parameters are calculated. In stochastic perturbation methods, the initial and boundary conditions along with parameters are considered random variables with their corresponding probability distributions, and their ensemble or moment statistics are then used to obtain averaged transport parameters. On the other hand, volume averaging uses fine scale transport equations and spatial averaging is employed to produce scaled-up equations that can then be used to obtain effective transport parameters at the averaging scale.

2.3.1.2.1 Ensemble Averaging (or Stochastic Perturbation) Method

In the case of ensemble averaging method, uncertainties associated with boundary conditions, initial conditions, transport parameters, pressure, and flux are considered. As a result of these uncertainties, equations representing the transport phenomena would become stochastic differential equations (SDEs). In general, SDE cannot be solved exactly, but the first few moments of the variable of interest can be computed and it serves the purpose to depict the scaled-up transport phenomena at a coarser scale.

Initial work on ensemble averaging was based on many restrictive assumptions such as an unbounded domain, uniform mean flow, etc. and these assumptions greatly limited the applicability of the ensemble averaging method. Unbounded or infinite-acting reservoirs mean that the scaled up flow equations will only be applicable either for the early flow period or because of unlimited supply of oil or gas in the reservoir. Uniform mean flow implies that the scaled up equations do not take into account pumping or injection effects. Many of these earlier restrictions to this method have been modified (Dongxiao and Winter 1999), such as:

1. Inclusion of sink and source terms in the mass balance to modify earlier assumption of uniform mean flow.
2. Specification of complex boundary conditions and irregular geometries to modify earlier the assumption of infinite acting reservoirs with no boundary effects.
3. Incorporating second-order correction term for the mean head to modify earlier assumption of uniform mean flow in unbounded reservoir in a stationary medium.

Some of the major limitations of this approach which renders this method unsuitable for our research are:

1. It requires detailed knowledge of spatial structure of all parameters. Estimations to determine detailed knowledge of spatial structure of all parameters is not trivial; even if we have that knowledge about all parameters, they are usually inherited with significant uncertainty.
2. Assumption of Gaussian statistics.

3. Assumption that the spatial mean is same as the ensemble mean that holds only if scale of the problem is much larger than the correlation length.

2.3.1.2.2 Volume Averaging Method

Volume averaging technique is used to derive continuum equations for multiphase flow and multi-component transport. In volume averaging, equations that are valid within a particular region are spatially averaged to produce equations that are valid everywhere in the system (Whitaker 1999). In the case of volume averaging, the variable of interest is considered a spatial random field (Cushman 1982) and spatial averaging of the spatial random variable is performed. Thus, the transport equations that are applied on a fine scale are spatially averaged over a certain volume. Volume integrals are converted using the divergence theorem into surface integrals in order to derive the effective properties at various scales. A closure problem is also specified in order to satisfy boundary conditions. Specific applications pertaining to reactive transport processes have been studied using volume averaging methods by Quintard and Whitaker (1994) and Leung (2009). The limitation of volume averaging method is that they assume periodicity of the porous medium at some scale (Whitaker 1999) in order to derive closure consitions that are analytically tractable. Leung (2009) relaxed these assumptions by performing numerical integration of fine scale quantities corresponding to porous media exhibiting arbitrary heterogeneity. The closure equations were also solved numerically using an optimization procedure. The procedure by Leung (2009) however performs spatial averaging of dynamic variables such as concentrations and saturations at distinct time

intervals. The dynamic evolution of the process is therefore discretized into several quasi-steady states and therefore may not represent the true temporal evolution of the underlying processes.

In order to accurately characterize reactive processes there are two challenges that must be addressed: 1) accurate scale-up accounting for the multi-scale and multi-physics characteristics of advection-diffusion-reaction system in disordered medium, 2) incorporating consistent reservoir heterogeneity at all levels of scales. It has been difficult to address these two challenges using traditional volume-averaging or ensemble-averaging approaches based on partial differential equations (PDEs) with effective reaction and mass transfer parameters due to difficulty in treating heterogeneity at multiple scales (Palanichamy et al. 2009; Berkowitz et al. 2013).

2.3.1.3 Particle Tracking Approach

The two primary approaches for using particle tracking (PT) to simulate fluid flow and transport in porous media are 1) Random walker particle tracking (RWPT), and 2) Continuous time random walker (CTRW). The particle tracking approaches simulate the fluid flow and transport through random particles which are injected into the porous media and made to move using statistics and partial physics.

RWPT approach moves the random particles through a superposition of convective and dispersive terms, where the convective term comes from solving the advection-diffusion transport equation and the dispersive term is captured by Brownian motion which mimics the random nature of dispersion. The conceptual equation for

movement of a particle in a RWPT approach is given by the scheme (Gardiner 2009) described in Eqn. (2.4):

$$s(t+dt) = s(t) + \mathbf{a_1}(s,t).dt + \mathbf{a_2}(s,t).\gamma_m(t)\sqrt{dt} \tag{2.4}$$

where,

s = spatial distance along x, y or z direction

t = time

dt = time step (or temporal increment)

$\mathbf{a_1}$ = drift vector (related to advection)

$\mathbf{a_2}$ = displacement matrix (related to dispersion)

$\gamma_m(t)$ = mean-zero random effect representing time-specific variability common to all locations

The second approach to PT simulation is CTRW framework (introduced by Montroll and Weiss, 1965) in which the movement of particle from one grid block to the other is controlled by Monte-Carlo sampling of the transition probability distribution. This transition probability is typically an equation which is governed by the physics of flow and transport of the particular grid block. In Chapter 6 we will be using a PT formulation which is similar to the CTRW approach, therefore, following we review the mathematical formulation of CTRW in more detail.

In the CTRW approach, the governing equation for movement of particle in space and time is described by assigning random increments in space and time to the present location of particle (Edery et al. 2010). An injected particle jumps from one grid block to any one of the adjacent grid block based on the transition probability that reflects fluid properties and heterogeneities of the medium. Both the transition length and the transition time are treated as random variables in CTRW that are described by a joint space-time probability density function. The particle velocity at a particular step *i*, shown in Eqn.

(2.5), can be estimated simply by dividing the spatial increment with the temporal increment of the particle. The spatial and temporal increments (*ds* and *dt*, respectively) are described by the joint space-time probability density function (pdf) that reflects the fluid and matrix properties such as concentrations, pressures, pore structure heterogeneity etc. An example of joint space-time concentration pdf for advective-reactive transport with uncertain reaction rates (Tartakovsky et al. 2009) is shown in Eqn. (2.6)

$$\left.\begin{aligned} s^{i+1} &= s^i + ds^i, \qquad t^{i+1} = t^i + dt^i \\ v^i &= \frac{ds^i}{dt^i} \end{aligned}\right\} \tag{2.5}$$

$$\mathrm{p}(c;x,t) = \frac{1}{Da\left[\, a\left(c^a - 1\right)\right]}\, p_\kappa\left(\alpha;x,t\right) \tag{2.6}$$

where,

c = concentration

a = stoichiometric coefficient

Da = Damkohler number

α = reaction rate constant

$p_\kappa\left(\alpha;x,t\right)$ = pdf of reaction rate in combined space and time

CTRW is a popular PT approach which has been used to scale-up transport parameters and to quantify non-Fickian (anomalous) transport in a heterogeneous porous medium (Berkowitz et al. 2006; Dentz et al. 2004).

The advantages of PT methods are that 1) they can be applied to a grid free system if required, and 2) they are free of numerical dispersion. However, limitation of PT methods is that they cannot incorporate full physics of subsurface transport in their formulation. Incorporating the full physics of the processes in these methods is non-trivial and computationally very expensive. Solution to scale-up problems could be approached within the particle tracking framework by aggregating the particle statistics in

a random walk/PT method. PT approach has been used to scale-up fluid flow in fractured media, dispersion in porous media, regional flow channeling in fractured media etc., from small scale to macro scale (Nœtinger and Estebenet 2000; Bijeljic and Blunt 2006; Odén et al. 2008).

Each of the above approaches for scale-up of reservoir recovery processes has some limitations. For example, as discussed earlier, we cannot treat the effect of heterogeneity at multiple scales easily within any of these approaches. We investigate the use of hybrid approaches for performing scale-up in this work. For example, we employ the REV concept and a statistical approach to scale-up reservoir variables. In order to scale-up dynamic flow and transport variables, the concept of dimensionless numbers in conjunction with a PT approach is used.

2.4 Reactive Transport Processes In Porous Media

Reactive transport process in porous media typically occur over a range of scales, from very small nanometer scales such as at the reaction front of biochemical processes to hundreds of miles scale such as those result in pattern formation in geology (Grindrod 1991; Grzybowski 2009; Lake et al. 2002; Berkowitz et al. 2013; Szymczak and Ladd 2013). Fundamental understanding of reactive transport involves analysis of complex interactions between heat transfer, multi-phase fluid flow, fluid diffusion and chemical reactions between the various chemical species. In general, reactive transport processes in subsurface porous medium can be described by the following PDE:

$$\frac{\partial c(s;t)}{\partial t} + v\frac{\partial c(s;t)}{\partial s} - D\frac{\partial^2 c(s;t)}{\partial s^2} = r(c) \tag{2.7}$$

where,

s = spatial distance along x, y or z direction

t = time

$c(s;t)$ = concentration

v = Fluid flow velocity

D = Diffusion constant

$r(c)$ = reaction rate law term

Modeling and quantitative analysis of reactive transport processes in subsurface are associated with many uncertainties related to spatial and temporal variation in model parameters (Chen et al. 2013; Tartakovsky et al. 2009) and also the complex interaction between them. Some of the major sources of uncertainty are the spatial distribution of different minerals in porous medium, pore structure heterogeneity and uncertainty introduced by processes that occur at the molecular scale.

Our specific interest associated with reactive transport in porous media lies in the application of CO_2 storage in geological formations. Various subsurface trapping mechanisms for CO_2 sequestration process have been proposed in the literature and one of the most controversial and complex mechanisms is mineral trapping. Mineral trapping is a process by which CO_2 can be permanently stored in the subsurface systems, such as saline aquifer, when the CO_2 dissolved brine diffuses into rock minerals and reacts to precipitate in form of calcite. The calcite precipitates at a specific pH that is caused by the formation of carbonic acid when CO_2 dissolves in brine. Precipitation results in reduced rock permeability and trapping of the injected CO_2.

Because diffusion and reaction are important processes associated with mineral trapping of CO_2 sequestration in subsurface formations, we further elaborate on these two mechanisms.

2.4.1 Diffusion

Diffusion is different from advection because it is random in nature and does not necessarily depend on the path of fluid particle. Two primary characteristics of diffusion are that it is random in nature, and diffusion occurs from regions of high concentration to region of low concentration. Contribution of diffusion as a transport mechanism will be significant only at low velocities or low convective flux. Typically, diffusion in homogeneous media is well defined by Fick's law; however, porous media heterogeneity introduces complexity and consequently uncertainty and anomalous behavior.

Solute fluctuations at multiple scales in a heterogeneous media gives rise to anomalous (non-Fickian) diffusion (Berkowitz et al. 2013; Sagi et al. 2012; Aarão Reis and di Caprio 2014). This anomalous diffusion inside a heterogeneous porous media is due to restrictions on the movement of diffusing species.

2.4.1.1 Non-Fickian Diffusion

Porous media heterogeneity gives rise to anomalous diffusion behavior that is termed as non-Fickian diffusion (Berkowitz et al. 2013; Sagi et al. 2012; Aarão Reis and di Caprio 2014). Mathematically, in non-Fickian diffusion an additional second order derivative term in time is introduced that describes the dynamics of a Brownian particle (Das 1991). It is the addition of this stochastic Brownian motion that imparts an interesting scale-up characteristic to the diffusion process (Das 1991). A typical expression for the scaling of mean-square displacement of a diffusing species is:

$$\left\langle z^2 \right\rangle \sim t^{2b_1/b_2} \tag{2.8}$$

where,

z = direction perpendicular to the external surface

b_1 and b_2 = diffusion behavior parameters

For normal (Fickian) diffusion, $\langle z^2 \rangle$ is characterized by a spatially Gaussian distribution of the diffusing species and linearly increasing mean-square displacement (Aarão Reis and di Caprio 2014) which is given by $b_2 = 2$ and $b_1 = 1$. For all other values of b_1 and b_2, the process is termed anomalous or non-Fickian diffusion. The parameters b_1 and b_2 which define the behavior of diffusion depend on distribution of heterogeneity (Russian 2013).

The impact of heterogeneity on diffusion in porous media can be systematically described using a stochastic PDE, though the calculations are complicated (Russian 2013). Approximate solutions using particle tracking have also been attempted (Russian 2013).

2.4.2 Reaction

The permanent storage of CO_2 by mineral trapping takes significantly longer times in the order of hundreds to thousands of years (Gunter et al. 1997). For a simple bimolecular reaction such as $A + B \rightarrow C$, with reaction rate constant α, the reaction rate is given by the nonlinear law of mass action as follows:

$$r = \alpha c_A c_B \tag{2.9}$$

where,

r = reaction rate

α = reaction rate constant

c_i = concentration of species i

However, for a chemically and physically heterogeneous subsurface system, the reaction term can be highly empirical and a function of many parameters. For example, for typical CO_2 mineral trapping reactions, the reaction rate could be a function of reactive surface area, activation energy, temperature, pH etc. to name the few. Liu and Maroto-Valer (2011) have discussed the effect of a few parameters on reaction rate that could help shorten the time of initiation of mineral trapping mechanism. For example high pH, high reservoir temperature and high pressure favor the precipitation of mineral carbonates.

It is clear from the above discussions that the processes associated with the displacement of CO_2 in the subsurface reservoir exhibit tremendous variability in space across several scales. These processes are also dynamic in nature and occur over a range of temporal scales also. The temporal evolution of these processes are affected by uncertainties associated with reservoir and fluid parameters, boundary conditions and by our limited ability to describe all the sub-processes occurring over a range of time-scales. There is thus uncertainty in both space and time associated with these processes and that requires the development of specialized tools. These are described in the next section.

2.5 SPATIOTEMPORAL STATISTICS

Statistical tools for analyzing spatiotemporal processes are not yet as fully developed as those for purely spatial data or for purely temporal data/time series (Schabenberger and Gotway 2004). Generally, there is a natural tendency to model spatiotemporal process using one of the following three techniques:

1. Separate spatial analyses for each time snap shot;

2. Separate temporal analyses for each spatial location;
3. Spatiotemporal data analysis with random fields in R^{d+1} dimensions, where R^{d+1} indicates random fields in which d random fields defining spatial axes and 1 random field defining time axis.

The first two approaches are two-stage approaches that suffer from some serious shortcomings:

- Sparse data in time or space can pose problems. For example, if data are sparse in time then, even though spatial analysis can be performed, there will be considerable uncertainty in the temporal evolution of the process.
- A two-stage approach ignores the implicit relationship between the spatial variation in the process and its corresponding temporal evolution.

The third approach to model spatiotemporal process by considering time data as an extra spatial dimension to make it "3-D" data is not advisable (Schabenberger and Gotway 2004) because those two forms of data have different scales and units. As an example, consider the following illustration:

Suppose a phenomenon is described in two spatial dimensions. Let us consider the temporal component as the 3rd dimension. Then the coordinates of the 3D data would be $s_i = [x_i, y_i, t_i]'$. The space-time lag can then be represented as $\mathbf{s}_i - \mathbf{s}_j = [\mathbf{h}_{ij}, t_i - t_j]$. According to exponential correlation model, this 3D data can be modeled as shown:

$$\begin{aligned} \text{Corr}[\mathbf{Z}(s_i), \mathbf{Z}(s_j)] &= \exp\left\{-\theta\left[\left(x_i - x_j\right)^2 + \left(y_i - y_j\right)^2 + \left(t_i - t_j\right)^2\right]^{1/2}\right\} \\ &= \exp\left\{-\theta\left[\left\|\mathbf{h}_{ij}\right\|^2 + \left(t_i - t_j\right)^2\right]^{1/2}\right\} \end{aligned} \tag{2.10}$$

Because the spatial domain and time domain have different units and range, it can be difficult to practically interpret the resultant spatiotemporal covariance. Because of the differences in units, it may be difficult to define anisotropy parameters that are representative of the entire 3-D data. The correlation function in R^{d+1} can be written as:

$$\text{Corr}[\mathbf{Z}(s_i,t_i),\mathbf{Z}(s_j,t_j)] = \exp\left\{\theta_s \left\|\mathbf{h}_{ij}\right\|^2 + \theta_t k^2\right\} \quad (2.11)$$

where,

θ_s = spatial anisotropy parameter

θ_t = temporal anisotropy parameter

To overcome these above shortcomings, it is preferable to perform joint analyses of spatiotemporal data. Let $\left\{\mathbf{Z}(s,t): s \in D(t) \in R^d, t \in T\right\}$ be a strictly stationary space-time random field (typically Gaussian random function) in which space is represented by $s \in R^d$ and time by $t \in R^1$. The covariance function of this stationary space-time random field may be given as $C(\mathbf{h},\boldsymbol{\tau}) = \text{cov}\left\{\mathbf{Z}(s,t),\mathbf{Z}(s+h,t+\tau)\right\}$, where h and τ denote an arbitrary spatial lag and time lag, respectively.

2.5.1 Spatiotemporal Covariance

The variogram and covariance function are two of the most fundamental and necessary measures in geostatistical predictions and both measure the extent of statistical correlation as a function of spatial or temporal distance. Variogram and covariance function are two of the most important and key measures in spatiotemporal stochastic modeling. Some of the spatiotemporal covariance functions that have been proposed by various authors include those by Cressie and Huang (1999), Gneiting (2002), Ma (2003; 2005), De Cesare et al. (2001), Genton (2007), De Iaco et al. (2001)

The most commonly used and simplest form of the spatiotemporal covariance/variogram is the product-sum model of De Iaco et al. (2001) and it is described in detail in the following section.

2.5.1.1 Product-Sum Model (De Iaco et al. 2001)

The product-sum model is based on the Cressie-Huang theorem of covariance functions (Cressie and Huang 1999). For a second-order stationary spatiotemporal random field, where space is represented by $s \in R^d$ and time by $t \in R^1$, the spatiotemporal covariance and variogram functions are given by Eqns. (2.12) and (2.13), respectively. Here, R^d indicates d random fields defining spatial axes and R^1 indicates 1 random field defining time axis:

$$C_{s,t}(\mathbf{h_s}, \mathbf{h_t}) = k_1 C_s(\mathbf{h_s}) C_t(\mathbf{h_t}) + k_2 C_s(\mathbf{h_s}) + k_3 C_t(\mathbf{h_t}) \tag{2.12}$$

$$\gamma_{s,t}(\mathbf{h_s}, \mathbf{h_t}) = \left(k_2 + k_1 C_t(0)\right)\gamma_s(\mathbf{h_s}) + \left(k_3 + k_1 C_s(0)\right)\gamma_t(\mathbf{h_t}) - k_1 \gamma_s(\mathbf{h_s})\gamma_t(\mathbf{h_t}) \tag{2.13}$$

where,

γ_s = Spatial variogram model

γ_t = Temporal variogram model

$C_s(0)$ = Sill value for the spatial variogram model

$C_t(0)$ = Sill value for the temporal variogram model

$k_1 > 0,\ k_2 \geq 0$ and $k_3 \geq 0$

Using, $\gamma(0) = 0$ we get

$$\gamma_{s,t}(\mathbf{h_s}, 0) = (k_2 + k_1 C_t(0))\gamma_s(\mathbf{h_s}) = k_s \gamma_s(\mathbf{h_s}), \tag{2.14}$$

$$\text{and, } \gamma_{s,t}(0, \mathbf{h_t}) = (k_3 + k_1 C_s(0))\gamma_t(\mathbf{h_t}) = k_t \gamma_t(\mathbf{h_t}) \tag{2.15}$$

where,

k_s = Coefficient of proportionality between the space-time variograms $\gamma_{s,t}(\mathbf{h_s}, 0)$ and $\gamma_{s,t}(0, \mathbf{h_t})$

k_t = Coefficient of proportionality between the spatial and temporal variogram models $\gamma_s(\mathbf{h_s})$ and $\gamma_t(\mathbf{h_t})$

k_s and k_t are both assumed to be 1 in De Cesare et al. (2001). From Eqns. (2.14) and (2.15), we get

$$\begin{aligned} \left(k_2 + k_1 C_t(0)\right) &= k_s, \\ \left(k_3 + k_1 C_s(0)\right) &= k_t \end{aligned} \tag{2.16}$$

Combining Eqn. (2.16) with Eqn. (2.12), coefficients k_1, k_2 and k_3 can be solved as:

$$k_1 = \frac{k_s C_s(0) + k_t C_t(0) - C_{s,t}(0,0)}{C_s(0) C_t(0)} = \frac{k_s . sill_s + k_t . sill_t - sill_g}{sill_s sill_t} \tag{2.17}$$

$$k_2 = \frac{C_{s,t}(0,0) - k_t C_t(0)}{C_s(0)} = \frac{sill_g - k_t . sill_t}{sill_s} \tag{2.18}$$

$$k_3 = \frac{C_{s,t}(0,0) - k_s C_s(0)}{C_t(0)} = \frac{sill_g - k_s . sill_s}{sill_t} \tag{2.19}$$

For positive definiteness, sufficient condition is $k_1 > 0,\ k_2 \geq 0$ and $k_3 \geq 0$

Generally, it is difficult to check if a function is positive definite and, therefore, this observation causes major difficulties in the formation of parametric spatiotemporal covariance models. Geostatistical spatiotemporal models generally rely on the separability of the covariance functions. If two functions are positive definite then their products, their sums, convex combinations and limits also yield a positive definite function.

Using k_1, k_2 and k_3, we get: $k = \dfrac{k_1}{k_s k_t} = \dfrac{k_s C_s(0) + k_t C_t(0) - C_{s,t}(0,0)}{k_s C_s(0) k_t C_t(0)}$

$$0 < k \leq \frac{1}{\max\left\{\text{sill}\left(\gamma_{s,t}(\mathbf{h_s}, 0)\right); \text{sill}\left(\gamma_{s,t}(0, \mathbf{h_t})\right)\right\}} \tag{2.20}$$

These coefficients are used in two corollaries developed by De Iaco et al. (2001) to model the spatiotemporal variogram, which say that if either $\gamma_{s,t}(\mathbf{h_s}, 0)$ or $\gamma_{s,t}(0, \mathbf{h_t})$ is non-stationary, i.e. they do not have a bound, *k* will not satisfy the inequality given by Eqn. (2.20), however, the product-sum spatiotemporal variogram model would still be valid.

2.5.1.1.1 A wider class of models

For some constraints on coefficients k_2 *and* k_3 such that if $k_2 \neq 0$ or $k_3 \neq 0$ then the spatiotemporal variogram or covariance model cannot be derived from the integral representation proposed by Cressie and Huang (1999); however, the product-sum model of De Iaco et al. (2001) is applicable in that case. These constraints were used for two reasons – i) To ensure achieving the property of positive definiteness, and ii) to simplify the estimation of coefficients, or in other words to simplify the process of fitting the model to the data.

De Iaco et al. (2001) proposed the following product-sum model which does not require following the above two constraints, and nor does it require the spatial or temporal variograms to be stationary. Therefore, this makes the product-sum model of De Iaco et al. (2001) as shown in Eqn. (2.21) more general:

$$\begin{aligned}\gamma_{s,t}(\mathbf{h_s}, \mathbf{h_t}) = &\left(k_2 + k_1 C_t(0)\right)\gamma_s(\mathbf{h_s}) + \left(k_3 + k_1 C_s(0)\right)\gamma_t(\mathbf{h_t}) \\ &- k_1 \gamma_s(\mathbf{h_s})\gamma_t(\mathbf{h_t}) + k_4 \gamma 1_s(\mathbf{h_s}) + k_5 \gamma 2_t(\mathbf{h_t})\end{aligned} \tag{2.21}$$

where,

γ_s = Spatial variogram model (bounded)

γ_t = Temporal variogram model (bounded)

$\gamma 1_s$ = Spatial variogram model (not necessarily bounded)

$\gamma 2_t$ = Temporal variogram model (not necessarily bounded)

k_4 and k_5 = non-negative constants.

In a number of flow and transport scenarios, the spatial variability of the variable of interest, for example concentration, may exhibit a spatial trend (for example high concentration near the injector progressively becoming smaller closer to the boundaries of the reservoir), By adding a spatial and temporal variogram term in Equation 2.21 that may not necessarily be bounded, we can model the non-stationarity introduced by such spatial and/or temporal trends.

2.6 LESSONS LEARNT AND EXTENSION OF PREVIOUS LITERATURE

The existing literature on scale-up focus on variation of reservoir parameters or flow/transport processes with spatial scale. The existing scale-up methods consider only spatial scale-up at a particular instant in time. However, some processes that alter reservoir properties require investigation of scale-up jointly in space and time. Additionally, understanding the effect of heterogeneities on scale-up of reservoir properties in both space and time setting is crucial when going from laboratory experiments to pilot (or field) scale implementation. This research aims to scale-up reservoir properties and flow/transport parameters for a heterogeneous porous media in both space and time.

The concept of REV and the research associated with its estimation in the literature has focused only on spatial scales or temporal scales individually. Computation of the REV disregarding the joint variability in space and time may not be possible because some phenomena may be non-stationary when observed purely spatially or temporally. Defining the REV scale in such a case would be impossible; however, the same phenomena when investigated in a spatiotemporal context may exhibit stationarity, thus facilitating REV analysis in the combined spatial and temporal scales. Such a method can prove useful for analyzing the changes that might be introduced in the pore structure due to some reservoir altering processes such as chemical EOR, thermal recovery processes and CO_2 sequestration and to scale-up such processes to field scale.

Although dimensionless groups have been used for scaling up reservoir performance in heterogeneous media, there are two important drawbacks:

1. Existing dimensionless groups accounting for heterogeneity typically assume that heterogeneity exists in form of different permeability layers with contrasting properties. They do not consider heterogeneous permeability fields described by an underlying covariance (or variogram) model.
2. Reservoir heterogeneity affects flow dynamics such as dispersion or mixing zone length (MZL) not just in spatial setting but also temporally.

This research aims to alleviate these shortcomings by scaling the evolution of MZL in space and time due to different levels of heterogeneity defined by their correlation lengths. We will attempt to define a dimensionless group for scaling MZL accounting for the correlation lengths of the porous media.

The PT approach to scale-up reactive processes is relatively new with only couple of papers available in the literature that were published in past couple of years (Edery et al. 2010; Edery et al. 2011; Edery et al. 2011; Berkowitz et al. 2013). The major objective in those papers has been to simulate the physics of flow and transport due to reactions; however, the application of PT in those existing literature lacks two important objectives:

1. Representation of heterogeneity consistently at multiple scales in particle tracking models.
2. Investigating how heterogeneity affects the scale-up characteristics of these processes.

This research aims to fill that gap by proposing an algorithm that represents reservoir heterogeneity consistently at all scales employing dispersion variance conditions and parameter matching scheme. This algorithm when used in conjunction with a PT framework at multiple scales addresses some of these drawbacks.

Chapter 3: An Investigation of Scaling of Advection-Dispersion-Reaction Processes in Heterogeneous Media

3.1 OVERVIEW

Tertiary recovery processes such as chemical EOR, CO_2 flooding and thermal processes (Lashgari 2014) such as steam flooding are typically studied at the lab scale. Physical constants obtained from such experiments are inserted into simulation models based on numerical solution of relevant partial differential equations (PDE) to predict field scale performance. However, there are three major problems with this approach, which lead to inaccurate prediction of field scale EOR performance. These are:

1. There are multiple transport processes occurring in EOR and their characteristic behavior is different at different spatial scale i.e. the physical constants exhibit different variability between the laboratory and field scales. For example, dispersion/diffusion are usually neglected at lab scale, however, depending upon the heterogeneous characteristics of the field, dispersion might pose a challenge to maintain good volumetric sweep efficiency in the reservoir.
2. Heterogeneity typically occurs at multiple scales in a reservoir. It has been demonstrated that heterogeneity is the most important parameter that affects the scale dependence of different transport parameters (Dai et al. 2004; Dai et al. 2005; Dai et al. 2007; Dai et al. 2009). However, EOR lab studies are typically done using a small core that only samples a small range of the variability encountered in the reservoir.

3. We typically investigate either purely spatial or purely temporal behavior of transport processes or parameters studied at laboratory scale; however, we never study the combined coupled behavior of spatial and temporal variation in transport parameters at lab scale. The interaction due to coupling of spatial and time scale for the underlying parameters usually results in an emergent phenomenon that is not directly apparent from pure spatial or temporal investigation of the relevant flow and transport equations.

One of the major problems in tertiary recovery processes such as CO_2 flooding is the instability of the displacement process introduced due to reservoir heterogeneity which results in reduced sweep efficiency. Two mechanisms which affect reduced sweep efficiency are *viscous instability* and *channeling*, which are caused due to reduced viscosity of the injected fluid and heterogeneous permeability of the reservoir rock, respectively. The displacement instability causes the injected fluid to extend in the form of fingers that results in poor sweep efficiency. The focus of this chapter is on understanding the growth of Mixing Zone Length (MZL)/dispersion due to heterogeneity and to provide framework to scale-up MZL as a functional characteristic of heterogeneity and spatiotemporal scale.

3.2 OBJECTIVE

Performance predictions of reactive processes such as those that occur when injected fluids interact with subsurface rocks require accurate models for the processes. Frequently, these processes are studied at laboratory scale and modeling them at the field

scale entails scaling-up laboratory observations taking into account the spatial variability of parameters. The current practice is to perform spatial averaging of attributes measured at fine scale and account for residual variability by calibration and history matching. This results in poor predictions of future reservoir performance. In this paper we scale-up such reactive transport processes using a numerical procedure that accounts for both the spatial and temporal characteristics of these processes.

The first part of this chapter (referred to as Case Study 1) investigates spatiotemporal scale-up of MZL accounting for field heterogeneity and reactivity of CO_2. We use conventional flow scaling groups to assess their applicability in scaling of recovery (CO_2 concentration) and Mixing Zone Length (MZL) in presence of chemical reactivity and permeability heterogeneity through numerical simulations of CO_2 injection. We investigate scale-up by performing numerical simulations at three different spatial scales. The variation in MZL with spatiotemporal scale is plotted and various conclusions are deduced regarding the impact of permeability heterogeneity and conservative/reactive transport on the scale-up characteristics of MZL and dispersivity.

The second part of the chapter (referred to as Case Study 2) investigates the impact of multi-scale permeability heterogeneity on the spatiotemporal characteristics of MZL. A multi-scale heterogeneous model is sampled at three different spatial scales and we scale the MZL versus pore volumes injected profile as a function of reservoir heterogeneity. Finally, we compute the spatiotemporal REV of the MZL using both the spatial and temporal characteristics of the MZL.

3.3 INTRODUCTION

Advective-diffusive-reactive (ADR) transport in heterogeneous porous media occurs at several different scales starting from pore-scale to the field-scale. CO_2 when injected into the subsurface will first be dispersed by the pore-scale process and then as the CO_2 plume expands it will contact more of the porous medium structure. As the plume evolves it also reacts with the minerals of the rock wherever the reaction conditions (pH, temperature) are met. This combined diffusive-reactive process evolves according to the volume of the porous medium occupied by the plume, however, eventually converging to an asymptotic value (Frind et al. 1987). Generalized expressions for the evolving dispersion coefficient in an infinite media have been developed (Gelhar and Axness 1983; Dagan et al. 2003).

However, the macroscopic dispersivities developed based on the statistical theories assume the porous medium to be statistically homogeneous and large enough to develop asymptotic conditions. To our knowledge there are no existing theories that describe the scale dependence of reactive transport in a heterogeneous medium described by an arbitrary covariance structure.

The present work uses numerical models to investigate spatiotemporal evolution of reactive transport processes in a heterogeneous porous media at disparate scales. In order to study the spatiotemporal characteristics of MZL, the simulation package CMG-GEM^{TM} (Generalized Equation of State Model) a finite difference, generalized equation of state based compositional reservoir simulator is used. CMG-GEM is a reservoir flow simulator which also includes reactive transport model and it is specifically tailored to model geological CO_2 storage problems by coupling geochemical model with Equation

of State (EOS) model. The main components of the simulator include material balance equation, chemical equilibrium equations, and the reaction rate law for the dissolution and precipitation of minerals.

3.4 Case Study 1: Investigation Of Mixing Zone Length And Its Scale-up In Both Space and Time

Dispersion plays an important role during miscible displacement in heterogeneous permeable media as it could decrease the displacement efficiency (Arya et al. 1988). Dispersion accompanied by reactive transport and its variation in both space and time has not yet been understood thoroughly.

3.4.1 Description of Case Study 1

Numerical compositional simulations are performed for the following two types of flow mechanisms in order to investigate spatiotemporal scale-up of dispersivity. In both these cases, the process simulated is that of CO_2 storage in a saline aquifer with a vertical injector and a producer located at the ends of a two-dimensional (2-D) cross-section. The two cases are:

1. Two Phase Flow (CO_2 as injectant, and brine as in-situ fluid)
2. Two Phase Flow With Reactions (CO_2 as injectant, and brine as in-situ fluid, mineral composition of rock specified)

For each of the above two cases, simulations are run for the following three scales:

SCALE 1: 100 m X 20 m (100 X 1 X 100 grid blocks)

SCALE 2: 50 m X 10 m (100 X 1 X 100 grid blocks)

SCALE 3: 25 m X 5 m (100 X 1 X 100 grid blocks)

In order to maintain consistency across three scales of models, four scaling groups (Li and Lake 1996) are kept constant across the three scales:

1. Effective aspect ratio: $R_L = \frac{L}{H}\sqrt{\frac{\bar{k}_z}{\bar{k}_x}}$ (3.1)

2. Dip angle group: $N_\alpha = \frac{L}{H}\tan(\alpha_{\text{dip}})$ (3.2)

3. End-point mobility ratio: $M^o = \frac{\lambda^o_{r1}}{\lambda^o_{r2}} = \frac{k^o_{r1}\mu_2}{k^o_{r2}\mu_1}$ (3.3)

4. Buoyancy number: $N_g = \frac{\bar{k}_x \lambda^o_{r2} \Delta\rho g \cos(\alpha_{\text{dip}})}{u_T}\frac{H}{L}$ (3.4)

CO_2 is injected in a saline aquifer with constraints of constant injection rate and constant bottom-hole pressure for the injector and producer well, respectively. The dimensions of the three reservoir models with the corresponding CO_2 injection rates obtained by keeping the scaling groups constant are shown in Figure 3-1. The perforation locations of injector well and producer well for each spatial scale of model are indicated by dashed lines on left side and right side of cross sections, respectively, in Figure 3-1.

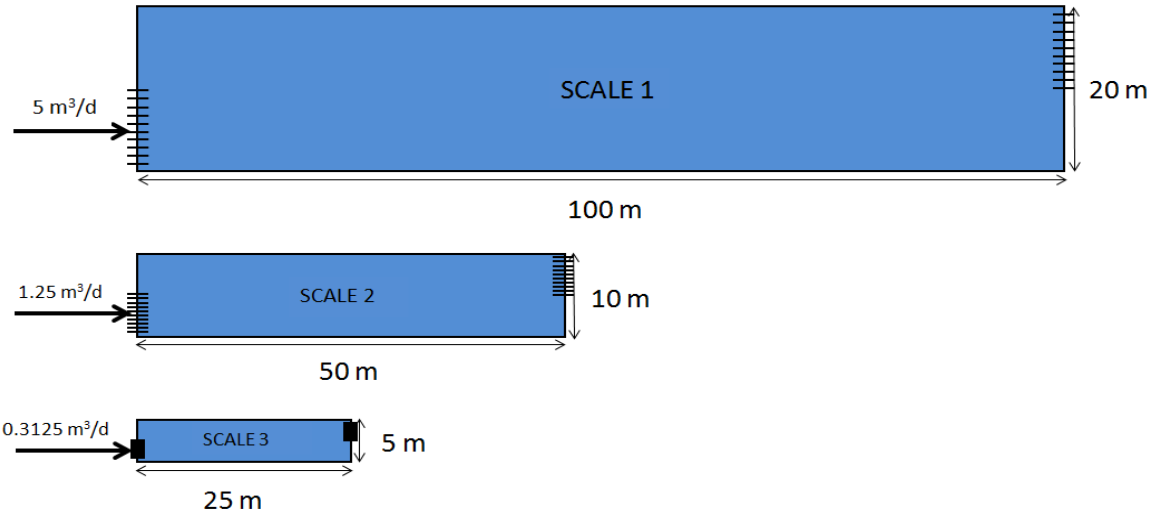

Figure 3-1: Cross-sectional reservoir models corresponding to three different length scales

CO_2 is injected until it breaks through at the producer on the opposite side. Long-term entrapment of CO_2 is achieved by the impermeable top seal. The schematic representation of the reservoir model as discussed here is shown in Figure 3-2. The reservoir fluid is considered to be brine of 1.90 molal (100,000 ppm) salinity which is a typical value (Burton 2008; Singh et al. 2012; Shafeen et al. 2004). CO_2 is injected until 100% CO_2 starts to breakthrough from the producer located at the other end of the cross-section.

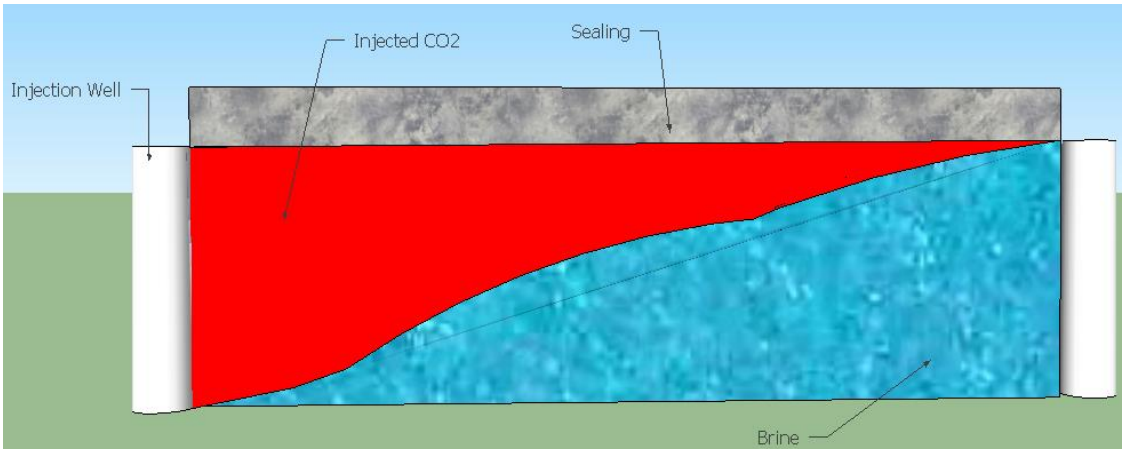

Figure 3-2: Schematic representation of a CO_2 plume on the field scale

3.4.1.1 Geological Characteristics

As mentioned previously, simulations were performed for two geological modeling scenarios: 1) homogeneous and 2) heterogeneous permeability field, respectively. The reservoir is assumed to have a constant porosity of 23%. Scenario 1 is modeled corresponding to following two cases:

i. homogeneous and isotropic permeability of 1 md
ii. homogeneous and isotropic permeability of 150 md

Scenario 2 is modeled with spatially heterogeneous but isotropic (kx = ky = kz) permeability. Several geostatistical realizations of permeability were generated using the object-based algorithm *ellipsim*. The permeability field is assumed to be binary with high permeability lenses of 150 md interspersed in a background matrix of 1 md. Figure 3-3 shows heterogeneous permeability realizations and also the ensemble mean for scenario 2.

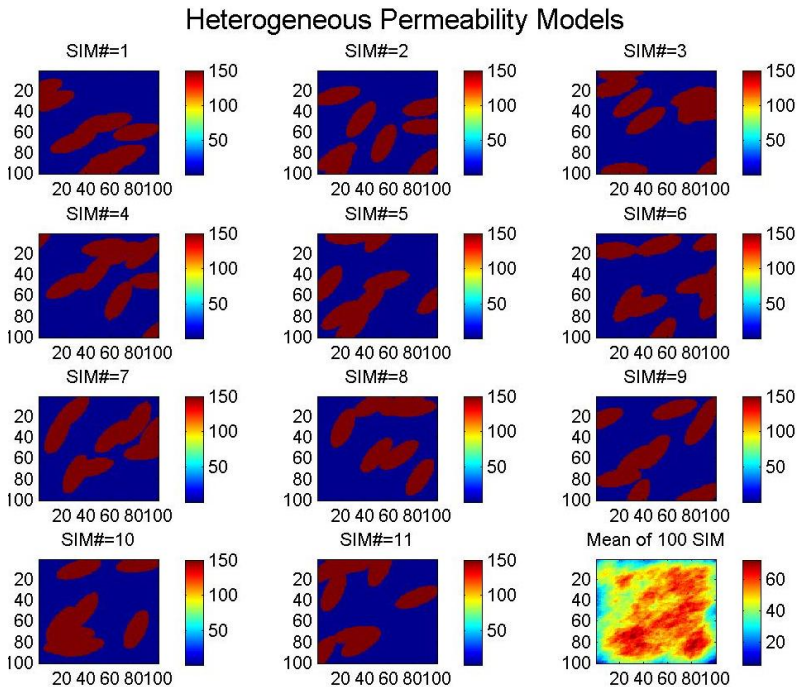

Figure 3-3: Several realizations of spatial heterogeneity in permeability and its mean used for scenario 2

3.4.1.2 Relative Permeability Curve

The relative permeability for fluids in a saline aquifer has significant impact on the injectivity of CO_2 (Burton et al. 2008). The plot of typical gas-liquid (brine-CO_2) relative permeability curve (Singh et al. 2012) used in simulations is shown in Figure 3-4.

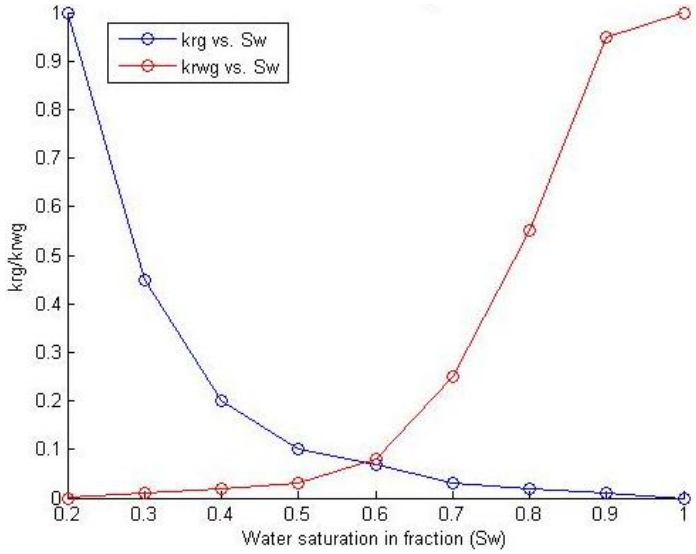

Figure 3-4: Typical Gas-liquid (CO_2-brine) relative permeability curve used in simulations

3.4.1.3 Fluid, Mineralogy and Reactions

The geochemical fluid and reactions are chosen to mimic typical reactions of CO_2-brine mixture with mineralogy such as that found at the Crystal Geyser site in Utah, and discussed in the following sections:

3.4.1.3.1 Mineralogy Reported at Crystal Geyser Site

CO_2-rich fluids leaking up along normal faults at the Crystal Geyser field site encounter and alter a wide range of lithologies similar to those likely to be encountered in the subsurface at other CO_2 sequestration sites. These fluid-rock interactions have occurred over geologic time scales (10^2 to 10^4 yrs) and the resultant rock types likely

represent end-products of CO_2-related alteration. At Crystal Geyser, calcite is the dominant mineral that is subject to alteration by CO_2-rich fluids, and its precipitation is largely driven by depressurization and degassing of these fluids in the near subsurface. Elevated calcite proportions can be found many tens of meters away from fossil and active seeps, indicating the lateral extent of CO_2-related alteration. To a lesser degree, clay minerals also appear slightly abundant near fossil CO_2 seeps, along with iron oxides. Most other minerals (such as dolomite, siderite, dawsonite etc.) predicted to precipitate by geochemical models of CO_2 sequestration are not found at the Crystal Geyser site or show no significant trends in abundance (Major et al. 2013).

3.4.1.3.2 Fluid and Reaction Parameters

Two components, CO_2 and C_1 (for methane), are included in the geochemical model where C_1 is used as a trace component to prevent gas or oil phase from completely disappearing in the model because of gas solubility in water. The PVT properties for CO_2 and C_1 components (Table 3-1) are obtained from Nghiem et al. (2004). The values associated with the chemical reactions are borrowed from the literature. There remains significant uncertainty related to initial mineral compositions and aqueous component concentrations.

Table 3-1: PVT properties of CO_2 and C_1 (Nghiem et al. 2004)

PVT Properties	**CO_2**	**C_1**
Molecular Wt. (g/gmole)	44.01	16.04
Critical Pressure (atm)	72.8	45.4
Critical Temperature (K)	304.2	109.6
Accentric factor	0.225	0.008
Critical Volume (m^3/kgmole)	0.094	0.099
Parachor	78	77
Specific Gravity	0.818	0.3
Boiling Point (^{0}C)	-78.45	-161.45
EOS omega A	0.457	0.457
EOS omega B	0.0778	0.0778
Binary interaction Coefficient	0.103	

There are three geochemical reactions and three mineral dissolution/precipitation reactions listed in Table 3-2(a). These selected geochemical and mineral reaction equations are consistent with the observations at the surface of the travertine mounds in Crystal Geyser site (Kim 2012). The travertine mounds observed in the Crystal Geyser site suggest carbonate mineralization that are formed by the process of calcium carbonate precipitation. The three mineral reactions in Table 3-2(a) are chosen to depict the carbonate mineralization process at Crystal Geyser. Additionally, seven aqueous components are chosen (other than gaseous solutes) in the geochemical model and their initial aqueous phase concentrations are listed in Table 3-2(b). The corresponding

reaction parameters for aqueous chemical equilibrium and minerals at 25 ^{o}C are shown in Tables 3-2(c) and (d), respectively (Nghiem et al. 2004; Nghiemw et al. 2004). These parameters are not directly measured through field sampling, but they have been obtained from the literature and several assumptions have been made on some uncertain parameters such as initial mineral compositions and aqueous component concentrations (Kim 2012).

Table 3-2: (a) Typical reactions of CO_2-brine mixture with rock minerals such as at the Crystal Geyser site in Utah, (b) Initial aqueous species concentration at 25 ^{o}C, (c) Reaction parameters for aqueous chemical equilibrium, (d) Reaction parameters for minerals

(a)

$$H_2O = H^+ + OH^-$$
$$CO_2(aq) + H_2O = H^+ + HCO_3^-$$
$$CO_3^{2-} + H^+ = HCO_3^-$$
$$CaCO_3 + H^+ = Ca^{2+} + HCO_3^-$$
$$Al_2Si_2O_5(OH)_4 + 6H^+ = 5H_2O + 2SiO_2 + 2Al^{3+}$$
$$CaAl_2Si_2O_8 + 8H^+ = Ca^{2+} + 2Al^{3+} + 2SiO_2(aq) + 4H_2O$$

(b)

Aqueous species	Molality
H^+	1.0000E-07
Ca^{++}	9.1185E-05
SiO_2 (aq)	2.3454E-08
Al^{+++}	2.3178E-11
OH^-	5.4563E-07
HCO_3^-	2.4893E-02
CO_3^{--}	1.1703E-05

(c)

Reactions	log K^a_{eq}
$H_2O = H^+ + OH^-$	-13.2631
$CO_2(aq) + H_2O = H^+ + HCO_3^-$	-6.3221
$CO_3^{--} + H^+ = HCO_3^-$	-10.2342

(d)

Mineral	log K^m_{eq}	log K_β	$\hat{A}_\beta$	$E_{a\beta}$	Initial volume fraction
Calcite	1.356	-8.79588	88	41870	0.0088
Anorthite	23.0603	-12	88	67830	0.0088
Kaolinite	5.4706	-13	17600	62760	0.0176

3.4.1.4 Models for Reaction Kinetics and Porosity Evolution

3.4.1.4.1 Rate of Reactions

CMG-GEM uses the formulation of Transition State Theory (TST) to estimate the reaction rate for mineral dissolution and precipitation reactions. The equation for the reaction rate is:

$$r = \mathrm{sgn}\left[1-\left(\frac{Q_{act}}{K_{eq}}\right)\right]\hat{A}S_w\left(\alpha_0+\sum_{i=1}^{nct}\alpha_i a_i^{\omega_i}\right)\left|1-\left(\frac{Q_{act}}{K_{eq}}\right)^{\xi}\right|^{\zeta} \tag{3.5}$$

where, $\hat{A} = \hat{A}_0.\frac{N_m}{N_m^0}$

The rate constant at temperature T_2 (K) can be calculated if rate constant is known at some other temperature T_1 (K) using Arrhenius equation as shown:

$$\alpha_i(T_2) = \alpha_i(T_1).\exp\left[-\frac{E_a}{R}\left(\frac{1}{T_2}-\frac{1}{T_1}\right)\right] \tag{3.6}$$

3.4.1.4.2 Porosity Change Due to Dissolution/Mineralization

Mineral dissolution and precipitation result in changing in the pore volume of the porous medium. The dissolution of minerals or the precipitation of solutes is determined internally by the simulator using a *super saturation index* (Lake, Bryant, and Araque-Martinez 2002) which is a function of pH of the reservoir fluids. For example, carbonate minerals tend to precipitate when pH >7 (basic) due to availability of carbonate ions at basic pH condition (Lake et al. 2002).

The porosity value after dissolution or precipitation is estimated using the following expressions:

$$\hat{\phi}^* \equiv \phi^* - \sum_{i=1}^{n_m} \left(\frac{N_i - N_i^0}{\rho_i} \right)$$
$$\phi = \hat{\phi}^* \left[1 + c_\phi \left(p - p^* \right) \right] \tag{3.7}$$

As a result of change in porosity due to dissolution or precipitation, the reservoir permeability also changes and the corresponding estimate of new absolute reservoir permeability is given by Carman-Kozeny equation as shown here:

$$\frac{k}{k^0} = \left(\frac{\phi}{\phi^0} \right)^3 \cdot \left(\frac{1-\phi^0}{1-\phi} \right)^2 \tag{3.8}$$

where,

a_i = chemical equilibrium coefficients

$\hat{A}$ = reactive surface area at the current time

$\hat{A}_0$ = reactive surface area at the initial (zero) time

c_ϕ = rock compressibility

E_a = activation energy

k^0 = initial permeability

K_{eq} = chemical equilibrium constant

N_i = total moles of mineral i per bulk volume at current time

N_i^0 = total moles of mineral i per bulk volume at initial (zero) time

p^* = reference pressure

Q_{act} = activity product

S_w = aqueous phase saturation

α_i = TST rate constant

ρ_i = molar density of mineral i

ξ, ζ = TST parameters (default values for both = 1)

ϕ^* = reference porosity without mineral precipitation/dissolution

$\hat{\phi}^*$ = reference porosity including mineral precipitation/dissolution

ϕ^0 = initial porosity

3.4.2 Mixing Zone Length and Dispersion Coefficient

The mixing zone length (MZL) at the interface between two chemical species is usually considered as the distance separating the concentration $\bar{c}$ = 0.84 and $\bar{c}$ = 0.16 (Bear 1972). The mixing zone length is determined by averaging the values of concentration across the transverse direction of flow.

$$\bar{c}(x,t) = \frac{1}{L_y}\int_0^{L_y} c(x,y,t)dy \tag{3.9}$$

The MZL can be determined numerically by taking the difference between the distance at which $\bar{c}$ = 0.84 and $\bar{c}$ = 0.16 are attained.

$$\text{MZL} = (x)_{\bar{c}=0.16} - (x)_{\bar{c}=0.84} \tag{3.10}$$

It can be shown that the MZL between $\bar{c}$ = 0.84 and $\bar{c}$ = 0.16 is related to the longitudinal dispersion through the expression (Menand and Woods 2005):

$$\text{MZL(t)} = 2\sqrt{2D_L t} \tag{3.11}$$

$$D_L = \frac{uL}{8}\left[\left(\frac{1-t_D}{\sqrt{t_D}}\right)_{\bar{c}=0.84} - \left(\frac{1-t_D}{\sqrt{t_D}}\right)_{\bar{c}=0.16}\right]^2 \tag{3.12}$$

where,

$$t_D = \frac{uAt}{\phi AL} = \frac{Qt}{V_p}$$

D_L = Longitudinal coefficient of mechanical dispersion
u = Darcy or superficial velocity
ϕ = Porosity
V_p = Pore volume
A = Cross sectional area
L = Lateral length of porous media
t = Time
Q = Volumetric flow rate
t_D = Dimensionless time (or pore volumes injected)

Once the MZL is numerically computed using Eqn. (3.10), dispersion coefficients can be computed using Eqn. (3.11). Since the concentration profiles evolve with time, therefore the MZL, and hence, dispersion coefficient could potentially evolve with time.

The numerical dispersion artifact in the simulation results is controlled by discretizing the reservoir model with adequate number of grid blocks. The number of grid blocks chosen for each reservoir model is well above the minimum typical value (20 grid blocks) needed to keep numerical dispersion under control. The numerical dispersion is quantitatively estimated using the following definition:

$$D_{num} = \begin{cases} \dfrac{\Delta x_D - \Delta t_D}{2}, & \text{Explicit (IMPES)} \\ \dfrac{\Delta x_D + \Delta t_D}{2}, & \text{Implicit} \end{cases}$$

The typical values of numerical dispersion for the two schemes (explicit and implicit) are 0.0125 and 0.0375, respectively. CMG's reservoir simulator uses fully implicit scheme for which the typical numerical dispersion value is less than or equal to 0.0375. For all the spatial scales of reservoir models used in this study, the numerical dispersion for those models lies in the range of 0.013 to 0.019.

3.4.3 Results and Discussions

3.4.3.1 Breakthrough Curves and Concentration Profiles of CO_2

Figure 3-5 shows the breakthrough curves for the models at the smallest and largest scales when the reaction of CO_2-brine with rocks is not modeled. At each scale there are three CO_2 breakthrough curves for three different permeability models. Out of the three permeability models considered two are homogeneous models, with 150 md and 1 md, and the third is a single realization of the heterogeneous models shown above. Figure 3-6 shows the breakthrough curves for the models at the smallest and largest scales obtained by considering reactive flow.

Figure 3-7 shows 2-D concentration profiles for the CO_2 at all the three spatial scales, both with and without reaction of CO_2-brine with rocks, in a heterogeneous media at the same pore volumes injected. At each spatial scale there are two 2-D concentration profiles, one on left without reactions and the one on right with reactions.

3.4.3.1.1 Impact of Reactivity

Chemical reactions are highly local as the reactions occur at the interface of reactive and reactant species and Figure 3-7 shows how the reactions effects are more pronounced as we go finer in scale. Castro-Alcalá et al. (2012) showed through visualization experiments that peak reaction rates will most likely occur at interfaces with high permeability contrast. It can be seen that as we refine the scale of the model, the

difference becomes more prominent between the reactive and nonreactive concentration profiles. The heterogeneous permeability model used in this study has high permeability contrast (combination of 1md and 150md), so it is likely that reactions occurring at those interfaces vary the expected growth of concentration profile. The reason why we see CO_2 concentration increase, and not decrease, at 50 days could be due to the fact that reactions first initiate dissolution (followed by precipitation of calcium carbonate) which will increase the porosity, and hence, increase the volume of injected CO_2 (Edery et al. 2011). It has been known that reactive transport in porous media may result in formation of fingers due to advancing reaction front (Aharonov et al. 1995; Lake et al. 2002). Diffusive processes tend to stabilize the reaction front. Depending on the relative strength of diffusive and reactive transport, mechanism, there will be stabilization of the reactive front (Aharonov et al. 1995).

The breakthrough curves and concentration profiles of CO_2 provide some insights into the main differences between the evolution of concentration due to reactive and nonreactive process. Steefel and Lasaga (1990) reported that the growth rate and characteristic wavelength of the reaction front depends on three parameters - chemical reaction rate, transport rate, and diffusion rate. Depending on the magnitude of these parameters it may be possible that reactivity could alter MZL even at large scales.

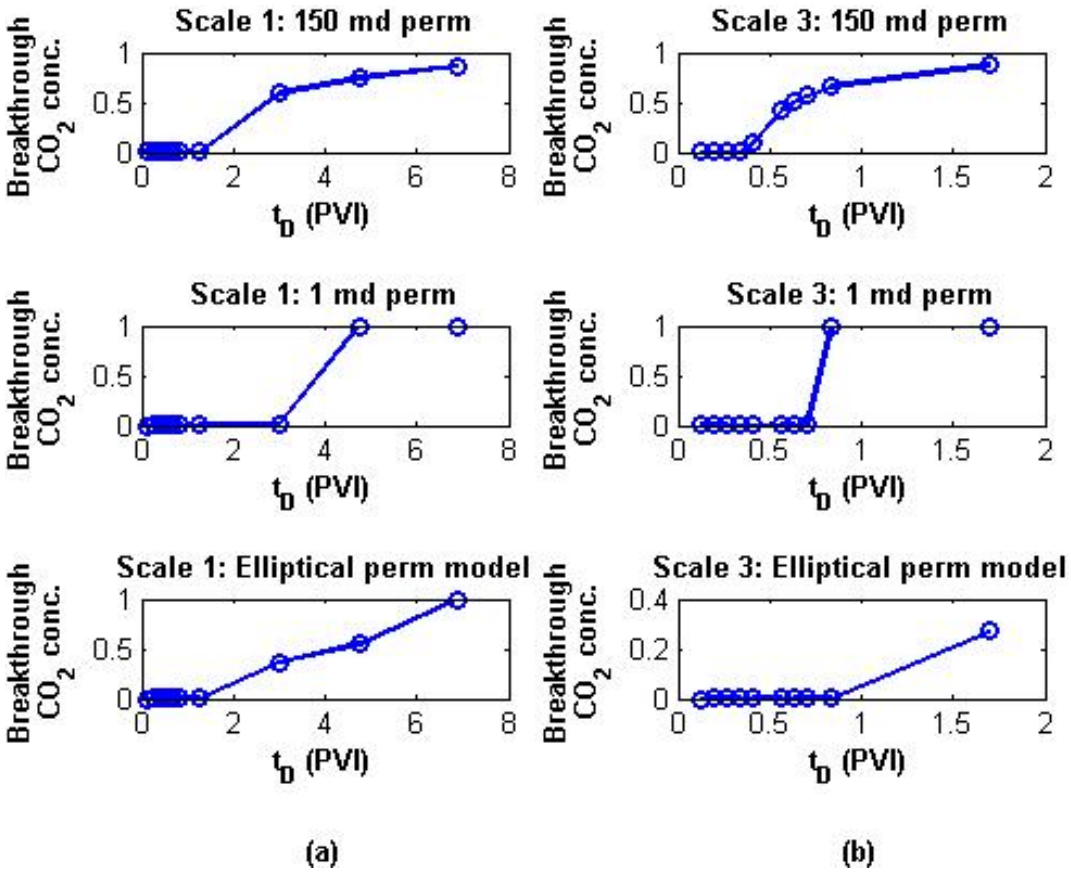

Figure 3-5: History of breakthrough CO_2 (global mole fraction) for 3 different permeability models of 150 md (top row), 1 md (middle row) and heterogeneous field (bottom row) at (a) Scale 1 (all subplots on left column), (b) Scale 3 (all subplots on right column)

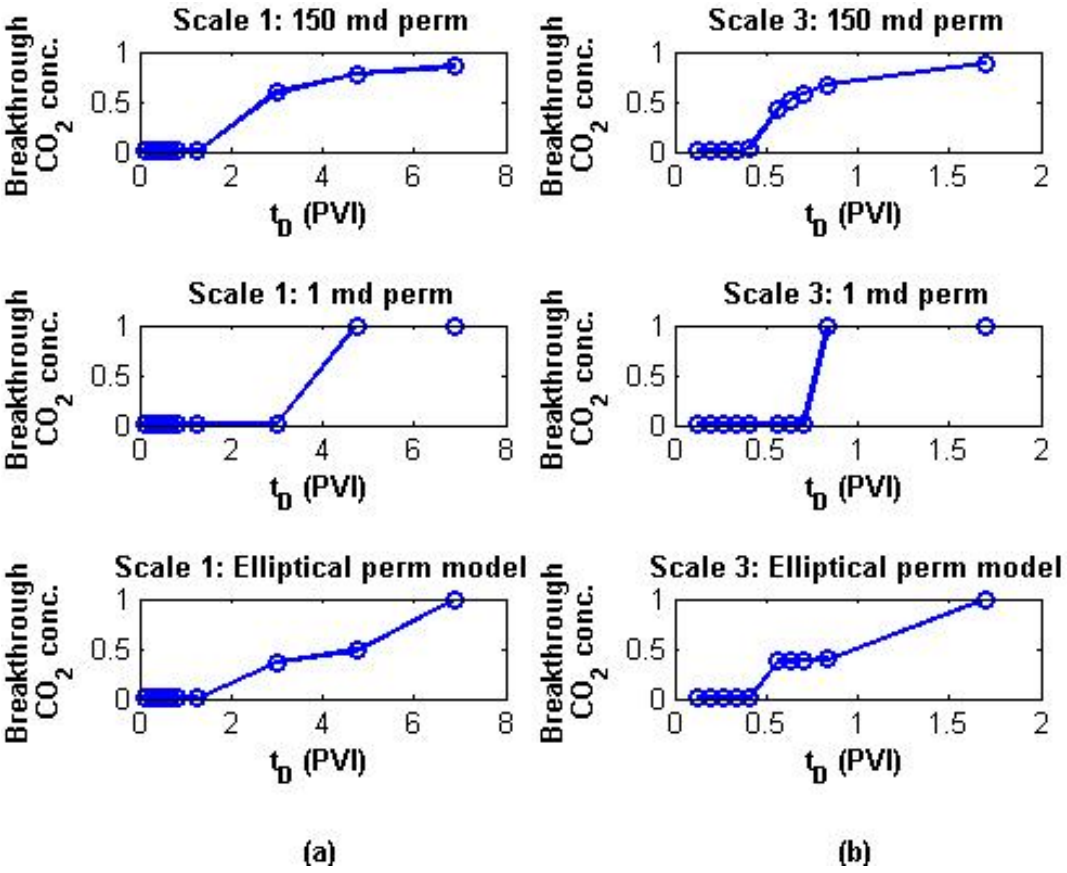

Figure 3-6: History of breakthrough CO_2 (global mole fraction) when reactions are modeled for 3 different permeability models of 150 md (top row), 1 md (middle row) and heterogeneous field (bottom row) at (a) Scale 1 (all subplots on left column), (b) Scale 3 (all subplots on right column)

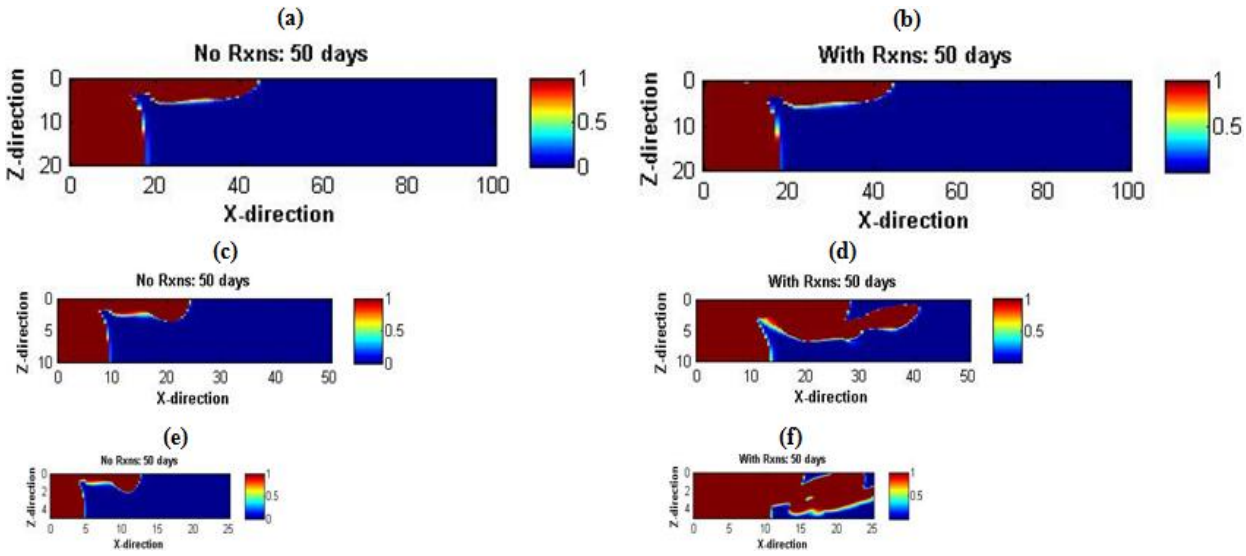

Figure 3-7: Maps of global CO_2 mole fraction at similar pore volumes injected for three different spatial scales in a heterogeneous permeability model (a) Scale 1 without reactions, (b) Scale 1 with reactions, (c) Scale 2 without reactions, (d) Scale 2 with reactions, (e) Scale 3 without reactions, (f) Scale 3 with reactions

3.4.3.2 Spatiotemporal Evolution of MZL/Dispersion Coefficient

MZL and dispersion coefficient can be determined using Eqns. (3.6) and (3.7), respectively, at various spatial scales and times. Figure 3-8 shows the spatiotemporal MZL and dispersion coefficient for two phase flow with and without reactive flow in the two homogeneous models as well as the heterogeneous model. The results of MZL and dispersion coefficient have been normalized at each spatial scale by the lateral length of each spatial scale and by the area normal to the longitudinal flow direction, respectively. Since the MZL and dispersion coefficient have a directly proportional relationship, therefore, the trend of results for MZL will be similar to those for dispersion coefficient.

3.4.3.2.1 Impact of Permeability

For the homogeneous 150 md permeable medium, it can be seen that MZL increases sharply with time (number of pore volumes injected) and then plateaus or increases much more gradually after some time. The time at which this change in profile of the MZL occurs is a function of the spatial scale of the reservoir and in general this time is longer for larger spatial scales. Similar behavior is observed for the cases with or without reactions in homogeneous media.

However, for the low permeability 1 md permeable medium, MZL decreases sharply with time and then the profile flattens out after some time. The time at which the MZL flattens out is a function of spatial scale of the reservoir and in general this time duration is longer for smaller spatial scales. The tight permeable media (1 md) allows for little spreading of fluid compared to the high permeability media (150 md) because it's difficult for the fluid to move through tight permeability pathways. As a result of the slow movement of the fluid, the streamlines of fluid converge spatially and move sharply as a front. An additional observation based on flow simulation results is that even though the velocity field in a homogeneous medium is uniform at late times, at intermediate times the velocity field exhibits heterogeneity due to the imposed boundary conditions. In low permeability medium the nature of the velocity heterogeneity is different because of the slower propagation of the boundary conditions. This causes the MZL to appear different in low and high permeability medium. The increasing and decreasing nature of MZL with

time in a high permeability and low permeability media, respectively, suggests that growth of MZL is primarily governed by the flow within the high permeability zones.

For a heterogeneous permeable media there is no clear trend with which the MZL varies in space and time. Heterogeneous media exhibit scaling characteristics observed for both high and low permeability media i.e. the MZL increases initially and then decreases at later time. This transition occurs mainly because the CO_2 plume samples higher permeability zones in the vicinity of the injector and later moves into the low permeability areas of the heterogeneous media.

The MZL and dispersion coefficient show a decreasing behavior corresponding to small permeability values with time due to solute hold up in the grains and this denotes that their travel time tends to infinity (Dagan et al. 2003). The solute hold up results in small variations in velocity (Fiori and Dagan 2003), and hence, it directly affects the dispersion coefficient (and hence, MZL) because it is well known that dispersion is caused by local variations in the velocity (Arya et al. 1988). Mathematically, this nonlinear decreasing behavior of dispersion is not captured by the first-order solution of the macrodispersivity transport equation through the Lagrangian and Eulerian approaches of Dagan (1990) and Gelhar and Axness (1983) which are symmetrical in logarithmic of conductivity. Dagan et al. (2003) argue that the solution from numerical approaches do not carry the simplification of an analytical solution for the Eulerian velocity field. Dagan et al. (2003) derive statistical moments of trajectories of solute particles which offer rational explanation to the confounding results of numerical simulations carried out by them and us in Figure 3-8 for permeability media of 1 md.

3.4.3.2.2 Impact of Reactivity

The spatial heterogeneity in Figure 3-3 reflects spatial variability in permeability field, however, mineralogy is assumed to be uniform across the space, and therefore, there are similar constituents of minerals inside and outside the ellipses. The results in Figure 3-8 suggest that there is no significant difference in MZL characteristics between conservative and reactive transport if the permeability of the reservoir is homogeneous. Similar result is also reported by Ovaysi and Piri (2013), where they performed reactive transport simulations on high resolution pore-scale data. However, for a reservoir with heterogeneous permeability, reactions affect scaling characteristics of MZL at small and intermediate length scales. This could be because of the fact that peak reaction rates are most likely to occur at interfaces with high permeability contrast (Castro-Alcalá et al. 2012). The heterogeneous permeability model used in this study has high permeability contrast (combination of 1md and 150md), so it is likely that reactions occurring at those interfaces vary the expected growth of MZL.

Deng et al. (2010) present two conclusions that support the results that we present in Figure 3-8: 1) the effect of reacting species on reservoir and flow properties decreases as we move from laboratory to field scale, 2) the change in reactivity with spatial scale is a function of spatial distribution of permeability in a rock.

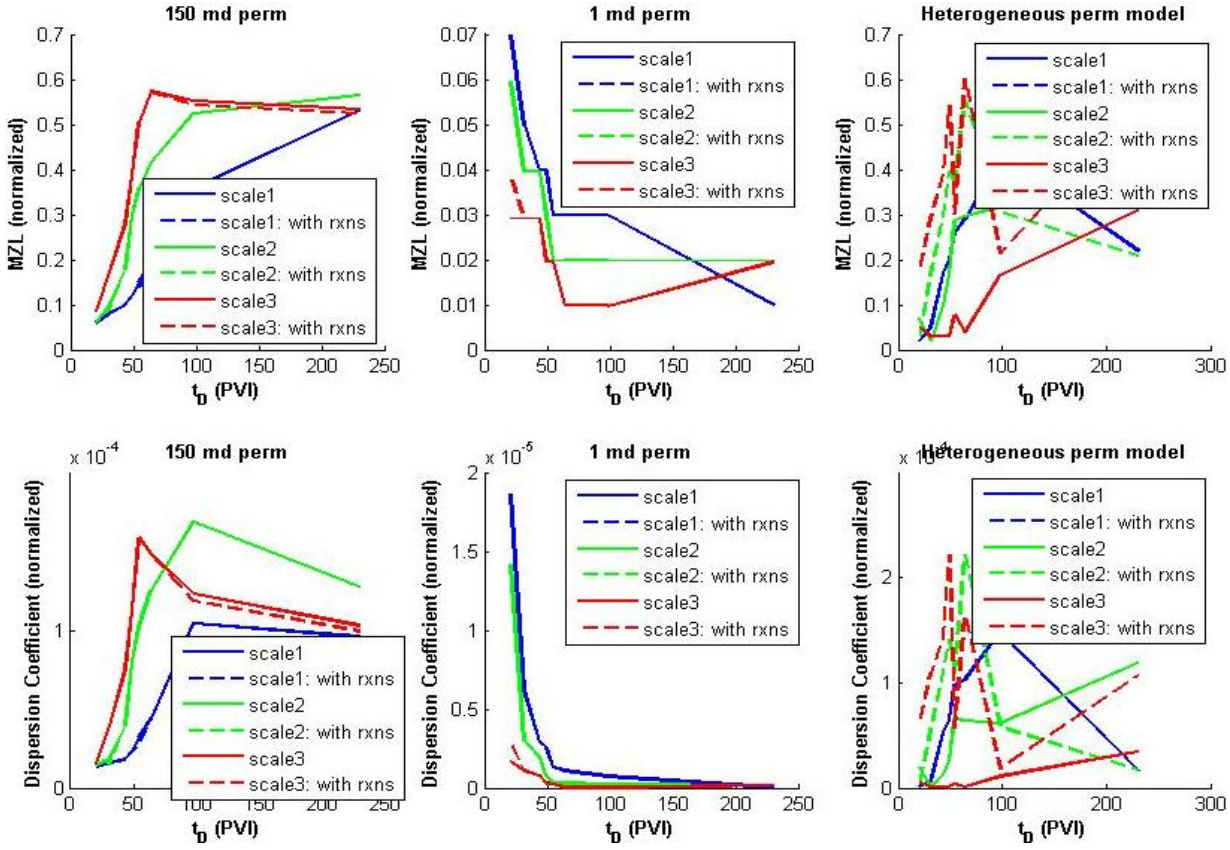

Figure 3-8: Spatiotemporal variation of normalized MZL (top row) and normalized dispersion coefficient (bottom row) for different permeability models of 150 md (1st column), 1 md (2nd column) and heterogeneous medium (3rd column). Six different legends represent 3 spatial scale models, where each model is populated with or without reactions.

The results of CO_2 concentration (Figure 3-7) and MZL (Figure 3-8) in the combined presence of chemical reactivity and physical heterogeneity suggest that the conventional flow scaling groups used in this illustrative study are not adequate enough to capture the scaling of recovery (CO_2 concentration) and transport parameters (MZL) when chemical reactivity and physical heterogeneity are coupled together.

3.5 CASE STUDY 2: EFFECT OF MULTI-SCALE HETEROGENEITY ON SCALING OF MIXING ZONE LENGTH

The objective in the following part of the chapter is to look at the effect of multi-scale heterogeneity at multi-scale on scale dependence of MZL. A dimensionless scaling group to scale-up MZL in heterogeneous media is proposed. The example also serves to illustrate the concept of a spatiotemporal REV.

3.5.1 Description of Case Study 2

This case study serves to demonstrate how MZL scales with the volume of investigation and time, where the covariance structure of the model is adjusted appropriately to reflect the heterogeneity within a volume of investigation. Consider a two dimensional grid with 200 x 100 blocks in the x and z directions, respectively. The dimension of each grid cell is 1m x 0.01m x 0.33m. Five fine scale permeability realizations were generated via unconditional sequential indicator simulation (SISIM) using anisotropic spherical variogram structure with horizontal (azimuth = 90 degrees) correlation length of 50m (major range) and vertical correlation length of 0.33m (minor range) which is equivalent to 50 grid blocks in x direction and 1 grid block in z direction, respectively. Permeability is assumed to be isotropic, hence, ratio of vertical to horizontal permeability is assumed to be 1. These simulated realizations are shown in Figure 3-9. Porosity is assumed to be constant at 23%.

From each realization of 200 x 100 grid blocks model we sub-sample 5 models each of size 100 x 60 grid blocks (aspect ratio of 5:3) by systematically scanning through the 200 x 100 grid blocks model to take various sections of the model. Since we generated 5 realizations of the 200 x 100 grid blocks model, therefore, we will have total

25 sub models each of size 100 x 60 grid blocks. These sub models are equivalent to scale 1 in Figure 3-1. Following a similar procedure, we sub-sample 25 models each of size 50 x 30 grid blocks and designate those as scale 2 and 25 models each of size 25 x 15 grid blocks designated as scale 3 in Figure 3-1. Models at all three scales of models have a similar aspect ratio (5:3). This procedure of sub-sampling models from the largest (200 x 100 grid blocks) model is schematically illustrated in Figure 3-10. This procedure also reflects the practice of quantifying recovery at various scales (core, pilot and field scales) using sub-samples from the field or basin scale.

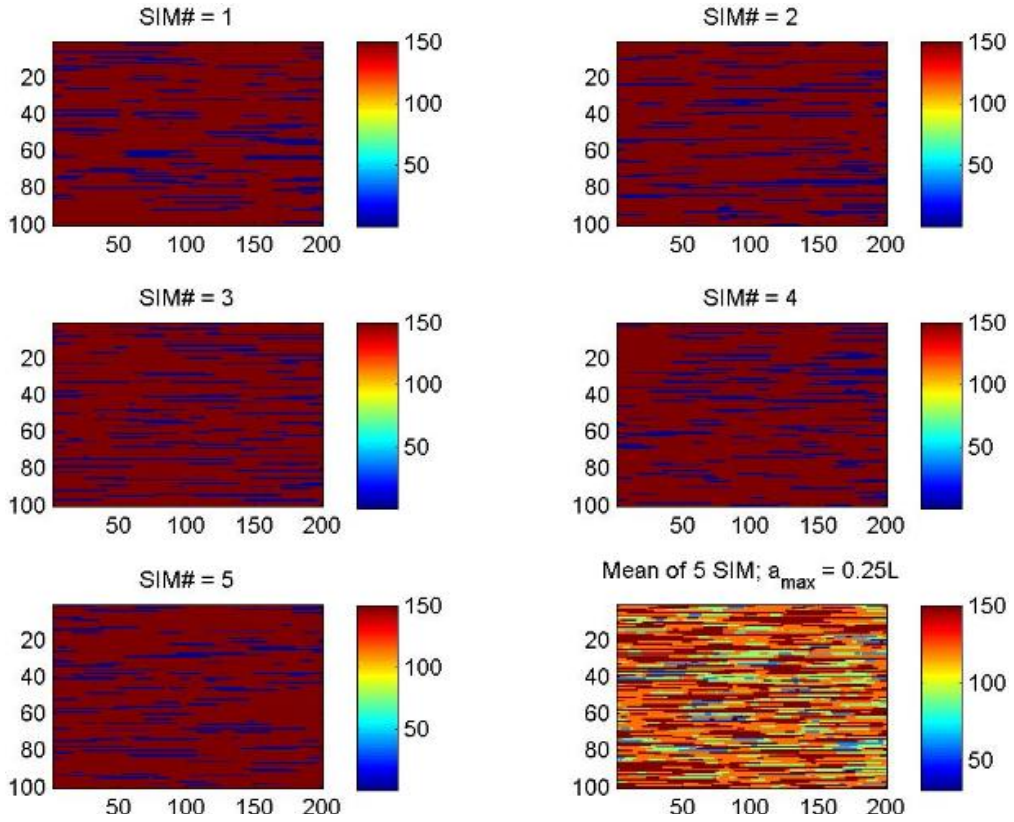

Figure 3-9: Five permeability models representative of the coarsest scale and sharing the same covariance model.

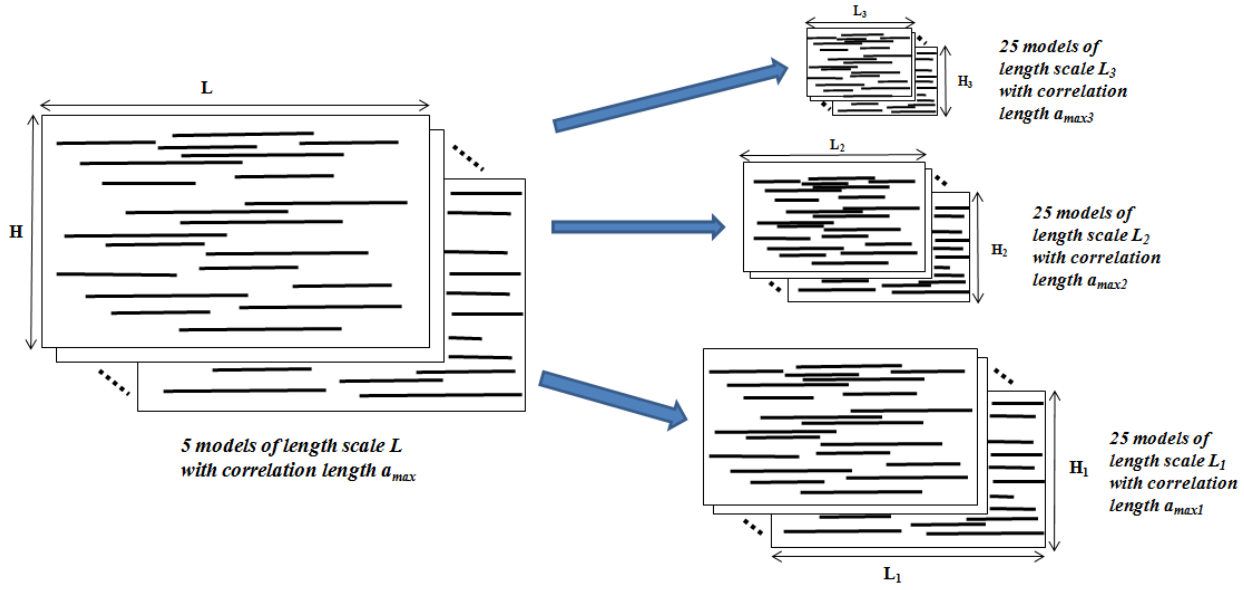

Figure 3-10: Schematic illustration of the models with different scales of heterogeneity extracted from the largest scale

3.5.1.1 Numerical modeling of flow and transport

We perform full physics CO_2 flow and transport modeling using all these 75 models with fluid parameters similar to the earlier case study. Similar time step sizes are used for all models. Similar to Case Study 1 earlier in this chapter, CO_2 is injected in a saline aquifer with constraints of constant injection rate and constant bottom-hole pressure for the injector and producer well, respectively. In order to maintain consistency across three spatial scales of models, four scaling groups (Li and Lake 1996) are kept constant in all models. The concentration profile of CO_2 (global mole fraction) is used to compute MZL corresponding to different spatial scales and at different times.

3.5.2 Scaling of MZL

Concentrations at different time scales from all models are used and averaged as per Eqn. (3.5). The averaged concentrations are subsequently used in Eqn. (3.6) to compute MZL corresponding to different spatial scales at different times. We then plot dimensional and dimensionless MZL curves against dimensionless time (pore volumes injected) as shown in Figure 3-12(a) and (b), respectively. The normalized results in Figure 3-12(b) show that increasing the correlation length in the flow direction increases the normalized MZL as the solute travels along continuous layers. The results also reflect the behavior observed for the heterogeneous model earlier in Figure 3-8; that is the MZL initially increases with time and then starts decreasing at later times.

3.5.2.1 Dimensionless Scaling Group

Qualitative similarity in the MZL curves depicted in Figure 3-12(a) and (b) for different heterogeneity indicates that it might be possible to obtain a single curve that can describe the evolution of MZL for any type of heterogeneity. To investigate this idea it is important to know that the growth of MZL is primarily governed by the flow within the high permeability zones (Sajjadi and Azaiez, 2013; Singh and Srinivasan, 2014). This suggests that MZL should be characterized by the length scale of high permeability layers. The effect of permeability on MZL is proportionate to the maximum normalized correlation length of the permeability field, $a_{\max}$. The MZL curves in Figure 3-12(a) show an exponential trend before they start to plateau after injection of certain pore volumes. Also, it is known that appropriate hydrodynamic scaling for miscible flow is proportional

to square of the characteristic length and time (Sajjadi and Azaiez 2013), which suggests that the scaling of MZL should also be proportionate to the square term. Using these two observations, it is postulated that the scaling of MZL to account for the effects of heterogeneous permeability field can be achieved by dividing both the normalized (also called dimensionless) MZL and the pore volumes injected by $exp(2a_{max})$. The normalized MZL (MZL_D) is the MZL calculated by differencing the concentration, divided by the lateral length (in the direction of flow) of the porous media. Therefore, we can write the scaled MZL (MZL_{Ds}) as shown in Eqn. (3.13):

$$\mathrm{MZL}_{Ds} = \frac{\mathrm{MZL}_D}{e^{2a_{\max}}} = \left(\frac{\mathrm{MZL}}{L}\right).\frac{1}{e^{2a_{\max}}} \tag{3.13}$$

The correlation length for the biggest model made up of 200 X 100 (= L X H) grid blocks is 50 blocks in the direction of reservoir lateral length (at azimuth angle of 90 degrees). The dimensionless form of the correlation length is equivalent to 0.25 (=50/200). If we decrease the model length by 50% from 200 grid blocks to 100 grid blocks then the correlation length increases by a factor of 0.25 to 0.5, which can be seen visually in the mean model of size 100 x 60 grid blocks (scale 1) in Figure 3-11. If we further decrease the model length by 50% two times consecutively to 50 and 25 grid blocks, respectively, then the correlation length increases by factor of 0.25 to 0.75 and 1.0, respectively, which can be seen qualitatively in the mean model of sizes 50 X 30 and 25 X 15, respectively, in Figure 3-11. Another rigorous way of estimating the correlation length for these models at various scales would be to compute the variograms of these models which would give us the correlation lengths of each model. These computed correlation lengths can then be normalized by the spatial length of each model.

Using the respective correlation lengths of different spatial scales of models as depicted in Figure 3-11, we use Eqn. (3.13) to scale the MZL curves, which eventually combines various curves of Figure 3-12(b) by merging them into a single MZL curve as shown in Figure 3-12(c). The variation in MZL as a function of heterogeneity (length of correlation) is now implicitly accounted for.

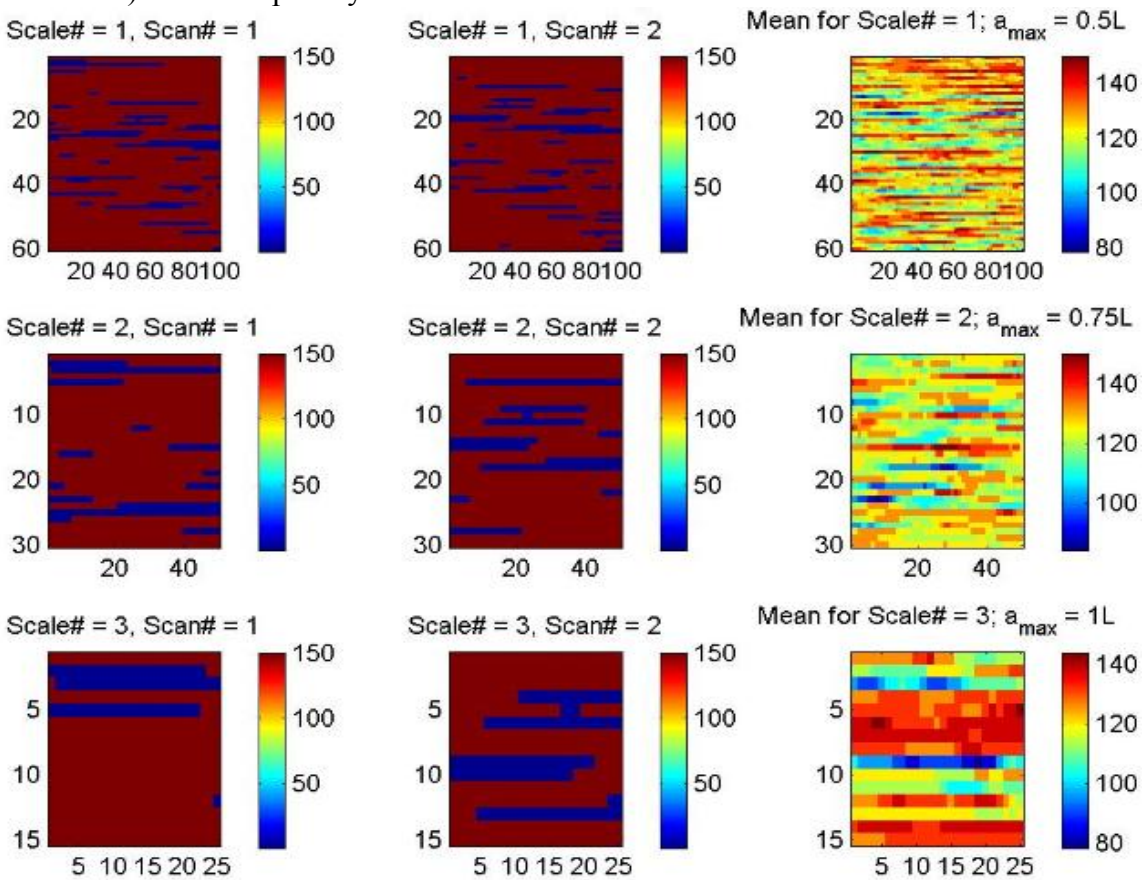

Figure 3-11: Sub-samples of permeability at different scales extracted from large scale realizations of dimension 200 X 100, and the mean of the subsamples

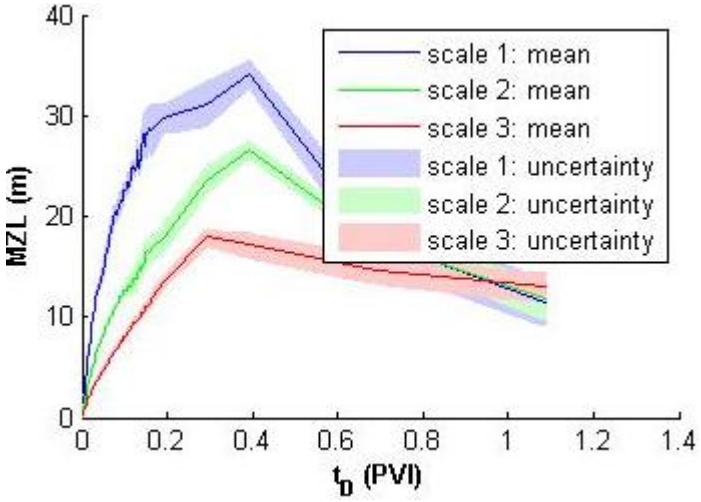

(a)

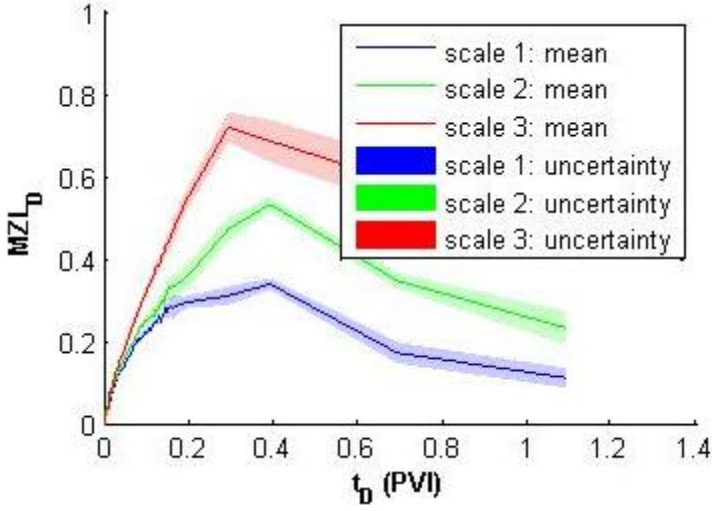

(b)

Figure 3-12

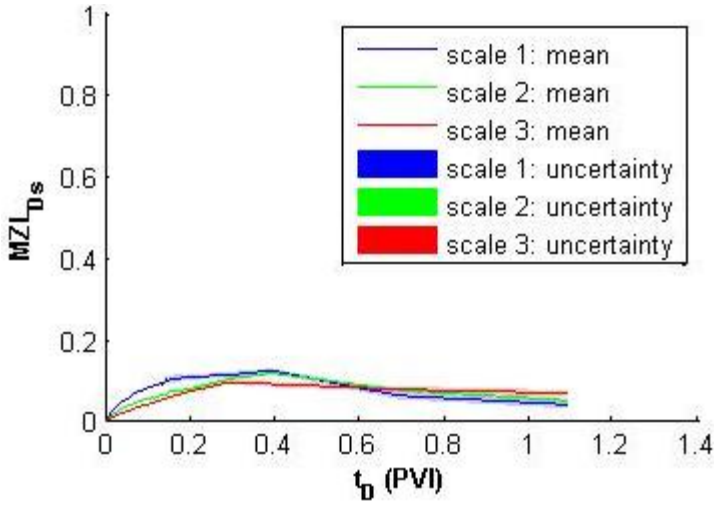

(c)

Figure 3-12: For three different spatial scales a) MZL in absolute value versus pore volumes injected, b) MZL normalized by lateral length versus pore volumes injected, c) MZL and pore volumes injected after rescaling to account for the correlation length of heterogeneity

3.5.2.2 REV

Statistics such as spatiotemporal variance of the mean of MZL can be calculated using the simulation results. The variance of the mean can in turn be used to compute the REV corresponding to the reactive transport process. The mean of MZL is computed using the simulation results for the five models at each individual spatial scale sub-sampled from each realization, and the variance is computed using the mean values for the 5 realizations. We are then left with the variance of the mean of MZL as a function of spatial scale and time. Figure 3-13 shows the spatiotemporal variance of mean MZL in the form of a surface plot with spatial scale (in m) and temporal scale (in pore volumes injected). Scale-up at increasing spatial scales introduces a smoothing effect, however,

scale-up in time introduces more variability with increasing time which plateaus after some time scale.

The spatial variance of MZL at different snapshots in time can be seen in Figure 3-13(a), which shows that spatial variance generally decreasing with increasing spatial scale at any snapshot of time. Figure 3-13(b) shows the diagonal plot with three different oblique cuts along the MZL surface plot of Figure 3-13(a) plotted against the product of spatial and temporal scales. This plot shows that variance of mean MZL decreases with the increasing product of spatial and temporal scale. The variance of mean MZL over spatial scale is computed by averaging over all times and is shown in Figure 3-14. This plot shows a decreasing trend with increasing spatial scale and depicts a diagnostic signature of negative unit slope at scales larger than the REV scale (Lake and Srinivasan 2004). The scale at which the slope of the variance of mean plot reaches -1 provides us the spatial REV scale i.e. the length scale over which variations in MZL from one spatial realization to the next dies out. In this case, the spatial REV scale is 50 m, which means that the REV of the MZL is comparable to the correlation length of the model 50 m. This suggests that the estimate of MZL averaged over all time steps will fluctuate in any permeable medium with lateral length smaller than 50 m, if the maximum correlation length of the geological formation is 50m. However, to prove the generality of this result flow simulations should be performed on permeability models with a range of correlation lengths followed by estimation of variance of mean plots similar to Figures 3-13 and 3-14 for all the models. The practical implication of this result is that the MZL (and consequently predictions of oil recovery) may fluctuate significantly, if the experiments

are performed using samples that are significantly smaller than the correlation length of the geologic formation.

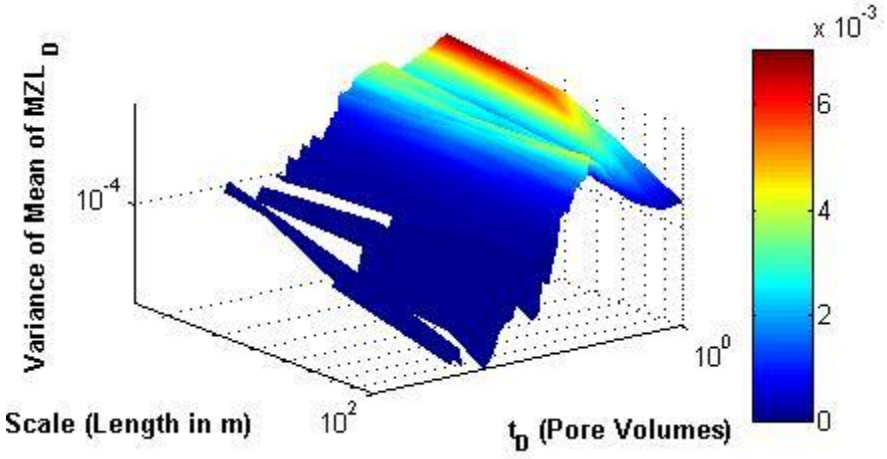

(a)

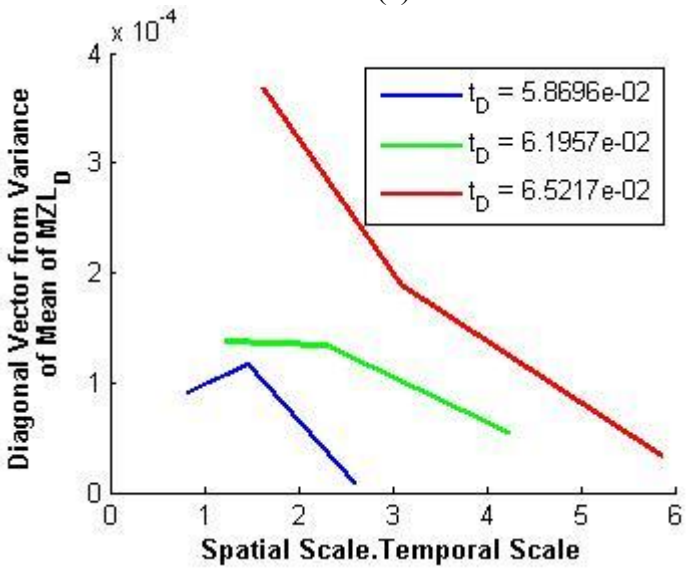

(b)

Figure 3-13: Spatiotemporal variance of mean MZL a) in form of a surface plot, b) in form of a diagonal plot with three different oblique cuts along the MZL surface plot

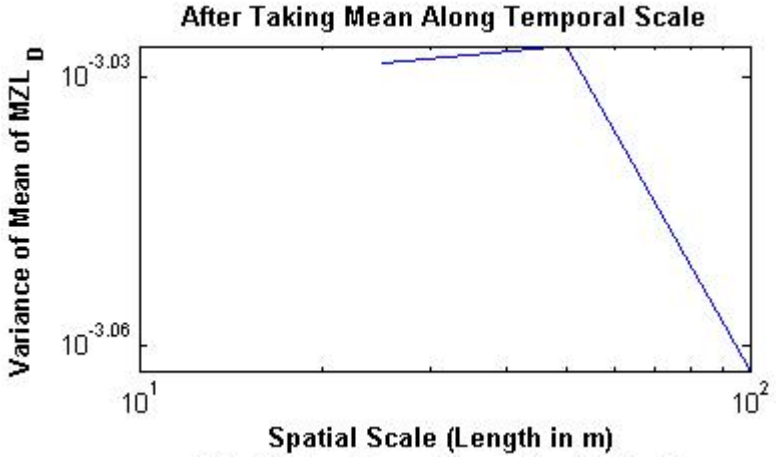

Figure 3-14: Spatial variance of mean MZL obtained by averaging over all times.

3.5.3 Time-dependence of MZL

The injection of CO_2 in the numerical model is continued until a steady state MZL is achieved. This is also the time at which the effluent concentration of injected fluid CO_2 becomes constant at the producer, which is about 212 days or 0.7 pore volumes injected. This is shown in Figure 3-12(a). Statistically, this can be seen in Figure 3-15 where variance of mean MZL plateaus after injection of 0.7 pore volumes. For a typical saline aquifers with average reservoir temperature > 35 ^{o}C and reservoir pressure > 3000 psi, the CO_2 formation volume factor is about 0.003 [reservoir volume/standard volume] (Shafeen et al. 2004), in which case 0.7 pore volumes at reservoir conditions would be equivalent to ~230 pore volumes (=0.7/ x 0.003) at standard conditions. This implies that the amount of CO_2 injected for the variability of the mean MZL to plateau would be 0.7 pore volumes at reservoir conditions or ~230 pore volumes at standard conditions.

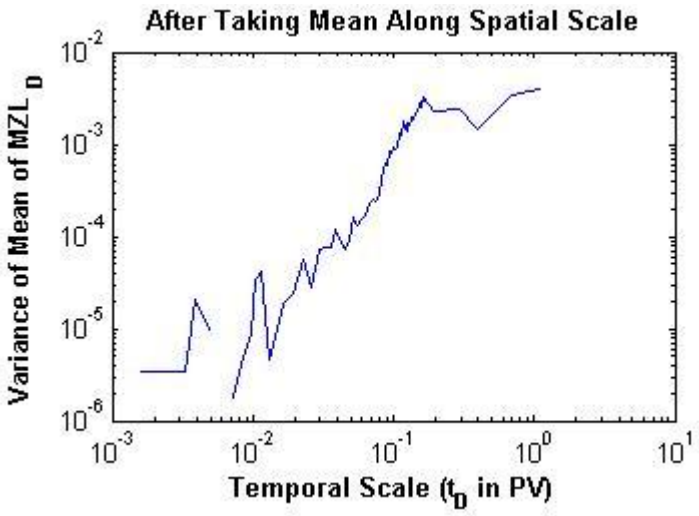

Figure 3-15: Variance of mean MZL in time after taking mean along all spatial scales.

3.6 SUMMARY AND CONCLUSIONS

The first part (Case Study 1) of this chapter investigates variation of MZL with length scale, time scale, flow field heterogeneity, and chemical reactivity through numerical simulations of CO_2 storage in a saline aquifer with a vertical injector and a producer located at the ends of two-dimensional reservoir cross-section. Three reservoir models with different length scales but similar aspect ratio are chosen. The models at each spatial scale were populated with homogeneous permeability of 1 md and 150 md as well as heterogeneous permeability. Both conservative and reactive transport of CO_2 is simulated on each model.

For a homogeneous model with high permeability (150 md) there is significant velocity variation at the CO_2-brine interface which causes the longitudinal dispersion to

increase with time, and the time at which the longitudinal dispersion plateaus increases with spatial scale. On the other hand homogeneous model with low permeability (1 md) exhibits variation sharpening of the injected CO_2 front which causes the longitudinal dispersion to decrease with time. Recently, Ovaysi and Piri (2013) showed that low velocities of the fluid particles first lead to decrease in dispersivity and then it becomes constant after steady-state concentration profile is established between the two boundaries. The results also suggest that there is no significant difference in MZL/dispersivity for conservative and reactive transport if the permeability of the reservoir is homogeneous.

However, there is significant deviation in values of MZL between conservative and reactive transport in a heterogeneous porous medium. This deviation between conservative and reactive transport in a heterogeneous medium is a reflection of the fact that larger-scale local variations in velocity occur because of mineral alteration due to precipitation/dissolution. The results obtained in the combined presence of chemical reactivity and physical heterogeneity suggest that the conventional flow scaling groups used in this illustrative study are not adequate enough to capture the scaling of recovery and transport parameters when chemical reactivity and physical heterogeneity are coupled together.

The second part (Case Study 2) of the chapter investigates the impact of multi-scale permeability heterogeneity on the spatiotemporal characteristics of MZL. Once again the numerical experiment was performed using models of three different spatial scales sub-sampled from 5 realizations generated at a larger scale. The results indicate that there is uncertainty in the profile of MZL versus time and that uncertainty is more at

the smaller scales. The MZL versus injected pore volumes curves is scaled using a function of the maximum correlation length of heterogeneity and this rescaling result in merging various MZL curves into a single MZL curve irrespective of the heterogeneity. Finally, spatiotemporal REV of the MZL is estimated using both the spatial and temporal characteristics of the MZL.

Key results from this chapter are that 1) the scaling characteristics of MZL distinctly differ for low permeability and high permeability media, 2) heterogeneous media with spatial arrangements of both high and low permeability regions exhibit scaling characteristics of both high and low permeability media, 3) reactions affect scaling characteristics of MZL in heterogeneous media, 4) a simple rescaling can combine various MZL curves by merging them into a single MZL curve irrespective of the correlation length of heterogeneity, and 5) estimates of MZL will fluctuate corresponding to displacements in a permeable medium whose lateral length is smaller than the correlation length of geological formation.

These results carry important implication on how laboratory experiments have to be designed and later scaled-up to predict field response. Additionally, results also suggest that the space and time discretization of recovery processes in numerical flow simulations should be done appropriately based on the combined spatiotemporal REV scale of the process.

Chapter 4: A Statistical Analysis of Scaling of Advection-Dispersion-Reaction Processes in Heterogeneous Media

4.1 OVERVIEW

For accurate predictions of reservoir recovery it is important to properly scale-up reservoir attributes such as petrophysical properties, which are heterogeneously distributed in space. In the case of transport properties such as species concentrations, dispersion coefficients etc. spatial variations are induced by variations in rock properties, but in addition there are also changes with time introduced by reactive processes such as those accompanying CO_2 injection in geological formations or during in-situ combustion. The governing equation for transport of fluids and chemical species in porous media is described by advection-dispersion-reaction (ADR) equation, also commonly known as the transport equation. The scaling of transport parameters in the presence of such reactive processes is challenging because of the wide variation in temporal and spatial scales of the important sub-processes. For example, advection and diffusion happen over length scales that are much larger than the scale of chemical reactions. This chapter attempts to use the conceptual knowledge about the spatiotemporal evolution of the transport processes and perform spatiotemporal scale-up considering both the spatial and temporal characteristics of these processes. Our attempt is to come up with a rigorous approach to assign appropriate values for transport parameters (such as longitudinal dispersion coefficient) at different length scales given a observed value at a particular scale. Our goal is also to quantify the uncertainty associated with the estimate for the transport parameter.

4.2 OBJECTIVE

The overall objective is to demonstrate a statistical approach to scale-up reservoir attributes in space and time whose spatiotemporal evolution can be described using a space-time equation. Subsequently, a semi-analytical approach to derive the spatiotemporal REV scale is presented.

In the first case study a simple stochastic function is used to describe the evolution of concentration with time inside a reservoir. Scale-up of the CO_2 concentration considering the spatiotemporal uncertainties associated with the CO_2 concentration is performed. In the second case study spatiotemporal scale-up of CO_2 concentration associated with a diffusive-reactive process in geological formations whose spatiotemporal evolution is described by a stochastic PDE is performed. In both these case studies a spatiotemporal correlation function of concentration is used to compute the variance of mean concentration and an REV is defined as the space-time scale over which the stabilization of this variance is achieved. The spatiotemporal covariance function summarizes the uncertainty associated with the evolution of CO_2 concentration in both space and time. Beyond the spatiotemporal REV scale, major fluctuations in mean CO_2 concentration over space and time are dampened.

The semi-analytical models for scale-up of the processes considered in these two case studies indicate that purely spatial or temporal investigation of scale-up does not produce accurate estimate of REV. In some cases, it may not even be possible to define an REV because of spatial trends in concentration (due to boundary conditions).

However, when scaling is investigated in a spatiotemporal setting, then the REV can be defined fairly accurately.

4.3 REVIEW OF STATISTICAL CONCEPTS

4.3.1 Variance of the Mean: REV

The variance of the mean of an attribute plotted against the length (or time) scale is a good tool to evaluate REV of an attribute (or a representative time step of a dynamic process). The REV of an attribute, the volume at which the averaging becomes stable (Bear 1972), can be determined from a log-log plot of the variance of the attribute's mean vs. length/time scale (Lake and Srinivasan 2004; Leung 2009). This plot depicts a diagnostic signature of negative unit slope at scales larger than REV. The slope value signifies independence between the block means at that scale. The variances of the linear average of an attribute f over a purely spatial volume V is given by the following equation:

$$Var(\overline{f}) = \frac{2\sigma^2}{V^2}\left(\int_V \int_{\eta_i} \rho_{corr}(\eta) d\eta d\xi\right)$$

If instead of purely spatial volume we have a spatiotemporal volume composed of spatial and temporal axes, then the variances of the attribute f over a spatiotemporal volume in 2-D or 3-D, respectively, is given by the following equations:

$$Var(\overline{f}) = \frac{2\sigma^2}{(V)^2}\left(\int_{\zeta_2=0}^{\zeta_2=T} \int_{\eta_2}^{\eta_2=\zeta_2} \int_{\zeta_1=0}^{\zeta_1=L} \int_{\eta_1}^{\eta_1=\zeta_1} \rho_{corr}\left\{\eta_1(L), \eta_2(T)\right\} d\eta d\xi \right) \tag{4.1}$$

$$Var(\overline{f}) = \frac{2\sigma^2}{(V)^2}\left(\int_{\zeta_3=0}^{\zeta_3=T} \int_{\eta_3}^{\eta_3=\zeta_3} \int_{\zeta_2=0}^{\zeta_2=B} \int_{\eta_2}^{\eta_2=\zeta_2} \int_{\zeta_1=0}^{\zeta_1=L} \int_{\eta_1}^{\eta_1=\zeta_1} \rho_{corr}\left\{\eta_1(L), \eta_2(B), \eta_3(T)\right\} d\eta d\xi \right) \tag{4.2}$$

where,

σ^2 = variance of attribute f

ρ_{corr} = spatial autocorrelation function

η_i = all possible lags within the spatiotemporal region,

where subscript i = 1, 2, 3 denote different axes

V = Volume over which scale-up is investigated

(for 2D or 3D spatiotemporal regions, V is $L \times T$ and

$L \times B \times T$, respectively)

L = lateral length of the reservoir

B = breadth of the reservoir

T = total time of spatiotemporal region

This variance of the mean represented by Eqns. (4.1) and (4.2) is used to investigate the scaling characteristics of the two processes described above. The important extension to the variance of mean concept is to compute the REV scale in combined space and time scales. This is achieved by implementing Eqn. (4.1) and (4.2) using the spatiotemporal correlation function describing the process and numerically integrating it over the spatial and temporal lags and scales.

An alternate procedure to compute the variance of the mean is to compute the concentration profile numerically using the solutions to the governing equations for the two cases described above and then estimate the variance of the mean numerically by averaging the concentration directly over a range of spatial and time scales. We use that

result to verify the results obtained by performing the convolution integral of the spatiotemporal covariance through right hand side (RHS) of Eqns. (4.1) and (4.2).

4.3.2 Semivariogram

A semivariogram summarizes the pattern of spatial or temporal variation of an observed phenomenon. Specifically, semivariogram is a measure of the *dissimilarity* between data pairs as the distance between them increases and is defined as:

$$\hat{\gamma}_h = \frac{1}{2N(\mathbf{h})} \sum_{i=1}^{N(h)} \left[f(\mathbf{u_i}) - f(\mathbf{u_i} + \mathbf{h}) \right]^2$$

where,

$\mathbf{h}$ = lag distance (in space or time)

$N(\mathbf{h})$ = number of data points at separated by lag $\mathbf{h}$

In the case of a second-order stationary phenomenon, the semivariogram is essentially complimentary to the auto-covariance of the data (Deutsch and Journel 1997).

4.3.2.1 Principal Features of a Stable Semivariogram

If the mean and variance of the observed phenomenon is constant for any sub-region of the domain (random field/data set) then the semivariogram is a legitimate complimentary representation of the autocorrelation function, and in that case the difference between any pair of data points at any separation is purely a function of their separation distance and this property is described as *stationarity*. For a stationary process, an increase in semivariance with increasing lag distance is generally observed, up to some threshold separation which is known as *range*. Semivariance plateaus at a value

known as *sill* at lag distances larger than the range, where sill is a non-spatial variance of all data pairs used to compute the variogram function.

4.3.2.2 Spatiotemporal Variogram/Covariance

The variogram and covariance function are two of the most fundamental and necessary measures in geostatistical predictions and both measure the extent of statistical correlation as a function of spatial or temporal distance. We can also measure the statistical correlation as a function of coupled spatial and temporal distances, in which case we call that correlation function as spatiotemporal covariance (or variogram).

Spatiotemporal variogram (or covariance) can be empirically estimated using the computational procedure detailed in Appendix A, and the empirically estimated spatiotemporal variogram/covariance can be modeled using product-sum model of De Iaco et al. (2001), a simple and most commonly used form of the spatiotemporal covariance/variogram.

4.3.3 Spatiotemporal Variogram Model: Product-Sum Model (De Iaco et al. 2001)

The product-sum model is based on the Cressie-Huang theorem of covariance functions (Cressie and Huang 1999). For a second-order stationary spatiotemporal random field, where space is represented by $s \in R^d$ and time by $t \in R^1$, the spatiotemporal covariance and variogram functions are given by Eqns. (4.3) and (4.4), respectively. Here, R^d indicates a d dimensional domain and R^1 indicates a one dimensional domain:

$$C_{s,t}(\mathbf{h_s}, \mathbf{h_t}) = k_1 C_s(\mathbf{h_s}) C_t(\mathbf{h_t}) + k_2 C_s(\mathbf{h_s}) + k_3 C_t(\mathbf{h_t}) \tag{4.3}$$

$$\gamma_{s,t}(\mathbf{h_s}, \mathbf{h_t}) = \left(k_2 + k_1 C_t(0)\right)\gamma_s(\mathbf{h_s}) + \left(k_3 + k_1 C_s(0)\right)\gamma_t(\mathbf{h_t}) - k_1 \gamma_s(\mathbf{h_s})\gamma_t(\mathbf{h_t}) \tag{4.4}$$

where,

γ_s = Spatial variogram model

γ_t = Temporal variogram model

$C_s(0)$ = Sill value for the spatial variogram model

$C_t(0)$ = Sill value for the temporal variogram model

$k_1 > 0,\ k_2 \geq 0$ and $k_3 \geq 0$

Using $\gamma(0) = 0$, we get

$$\gamma_{s,t}(\mathbf{h_s}, 0) = (k_2 + k_1 C_t(0))\gamma_s(\mathbf{h_s}) = k_s \gamma_s(\mathbf{h_s}), \tag{4.5}$$

$$\text{and, } \gamma_{s,t}(0, \mathbf{h_t}) = (k_3 + k_1 C_s(0))\gamma_t(\mathbf{h_t}) = k_t \gamma_t(\mathbf{h_t}) \tag{4.6}$$

where,

k_s = Coefficient of proportionality between the space-time variograms $\gamma_{s,t}(\mathbf{h_s}, 0)$ and $\gamma_{s,t}(0, \mathbf{h_t})$

k_t = Coefficient of proportionality between the spatial and temporal variogram models $\gamma_s(\mathbf{h_s})$ and $\gamma_t(\mathbf{h_t})$

k_s and k_t are both assumed to be 1 in De Cesare et al. (2001). From Eqns. (4.5) and (4.6), we get

$$\begin{aligned} \left(k_2 + k_1 C_t(0)\right) &= k_s, \\ \left(k_3 + k_1 C_s(0)\right) &= k_t \end{aligned} \tag{4.7}$$

Combining Eqn. (4.7) with Eqn. (4.3), coefficients k_1, k_2 and k_3 can be solved as:

$$k_1 = \frac{k_s C_s(0) + k_t C_t(0) - C_{s,t}(0,0)}{C_s(0) C_t(0)} = \frac{k_s . sill_s + k_t . sill_t - sill_g}{sill_s sill_t} \tag{4.8}$$

$$k_2 = \frac{C_{s,t}(0,0) - k_t C_t(0)}{C_s(0)} = \frac{sill_g - k_t . sill_t}{sill_s} \tag{4.9}$$

$$k_3 = \frac{C_{s,t}(0,0) - k_s C_s(0)}{C_t(0)} = \frac{sill_g - k_s . sill_s}{sill_t} \tag{4.10}$$

If two functions are positive definite then their products, their sums, convex combinations and limits also yield a positive definite function. In the case of the

spatiotemporal covariance model described above, for positive definiteness the sufficient condition is $k_1 > 0,\ k_2 \geq 0$ and $k_3 \geq 0$.

Using k_1, k_2 and k_3, we get: $k = \dfrac{k_1}{k_s k_t} = \dfrac{k_s C_s(0) + k_t C_t(0) - C_{s,t}(0,0)}{k_s C_s(0) k_t C_t(0)}$

$$0 < k \leq \frac{1}{\max\left\{\text{sill}\left(\gamma_{s,t}(\mathbf{h_s}, 0)\right); \text{sill}\left(\gamma_{s,t}(0, \mathbf{h_t})\right)\right\}} \tag{4.11}$$

These coefficients are used in two corollaries presented in De Iaco et al. (2001) that extend the model for the spatiotemporal covariance to the case where either $\gamma_{s,t}(\mathbf{h_s}, 0)$ or $\gamma_{s,t}(0, \mathbf{h_t})$ is non-stationary, i.e. they do not have a bound.

4.4 Illustration of Key Concepts Using Synthetic Case Studies

4.4.1 Space-Time Evolution of Processes Associated With CO_2 Migration

Even though we understand the physics of CO_2 migration in porous media, sometimes using the complex physics to derive simple statistical correlations may be too daunting and may not provide us insight into the scaling characteristics of the complex spatiotemporal phenomenon. In lieu of the more physically representative transport model, we can use a simplistic model that mimics the spatiotemporal evolution of the transport process. Eqn. (4.12) represents a very general components-of-variation model (Cressie and Wikle 2011) which is similar to the mixed-effects model proposed by Wikle (2003):

$$Y(s;t) = \mu_m(s;t) + \beta_m(s) + \gamma_m(t) + \kappa_m(s;t) + \delta_m(s;t); \qquad s \in R^d,\ t = R^1 \tag{4.12}$$

where,

$\mu_m(s;t)$ = deterministic mean

$\beta_m(s)$ = mean-zero random effect representing location-specific variability common to all times

$\gamma_m(t)$ = mean-zero random effect representing time-specific variability common to all locations

$\kappa_m(s;t)$ = mean-zero random effect capturing the spatiotemporal interaction not found in the larger-scale deterministic trend $\mu_m(s;t)$

$\delta_m(s;t)$ = mean-zero random effect representing the micro-scale spatiotemporal variability that is modeled by white noise in $R^d \times R^1$

All random effects are assumed independent of each other.

Components-of-variation model described by Equation (4.12) provides sufficient flexibility to generate non-stationary/stationary spatiotemporal processes because the structure of this function could vary with space and time.

4.4.2 Description of Case Study

Simple analytical functions can be associated with CO_2 concentration evolving with time inside the reservoir. Consider, for example, the analytical expression shown in Eqn. (4.13) which is constructed using the components-of-variation model presented in Eqn. (4.12), except for a little variation that the mean-zero Gaussian random effect is transformed to a uniform score so as to avoid the problem of having negative concentrations. The analytical expression for the concentration profile is:

$$c(\mathrm{x,t}) = \text{constant} \times \left(\frac{t}{x^{0.1}} \right) + \mathrm{U(t)} \tag{4.13}$$

where,

t = time

x = lateral distance in x-direction

U(t) = uniform transform of unconditional Gaussian noise at time 't'

The stochastic part of this analytical expression is meant to introduce randomness or diffusive flux. Concentration profiles at different snapshots in time are shown in Figure 4-1 and they indicate that concentration values decrease continuously towards increasing X-axis whereas they increase continuously with time at a fixed spatial coordinate. It is apparent that spatial variogram of concentration profile at any snapshot of time will be non-stationary because the concentration increases continuously in a particular direction. The spatiotemporal variogram calculated using the concentration values at one location at a certain time instant and the concentration value at another location at a different time instant will exhibit a nugget effect because of difference in concentration values in two different images at zero spatial lag.

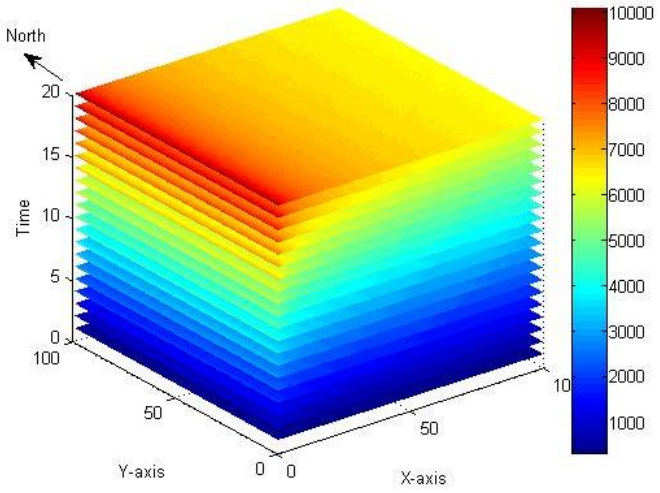

Figure 4-1: Concentration profiles in space and time corresponding to a simplified components-of-variation model for concentration.

4.4.3 Empirical Variograms

4.4.3.1 Purely Spatial and Purely Temporal Variograms

Figure 4-2 shows purely spatial and purely temporal variograms that are computed by keeping $\tau = 0$ (i.e. spatial lags computed on the same time slice) and $h_i = 0$ (i.e. zero spatial lag i.e. the variogram is computed over time lags keeping the location fixed), respectively. Purely spatial variograms are computed along rows (N-S), columns (E-W) and NW-SE directions. The spatial variogram along rows (N-S) is flat corresponding to a very small variogram value indicating very little variability. This is evident in the concentration maps shown in Figure 4-1 as there is no concentration variation along N-S direction within the same image. The constant value in spatial variogram along N-S direction is slightly greater than zero because of small variations in concentration due to presence of stochastic noise. The spatial variogram in the E-W direction exhibits an increasing nature because of the consistent concentration gradient in the E-W direction. However, the variogram value has not reached its sill (=1, after normalizing) even after considering approximately the largest lag distance (~99). The variogram along NW-SE direction has exactly the same shape as in the E-W direction, and that is because at any snapshot of time the concentration is constant along the Y-axis for any value along the X-axis. Purely temporal variograms at zero lags along N-S, E-W and NW-SE directions are exactly similar as the concentration variations at all locations changes similarly. The sharply increasing nature of the purely temporal variogram indicates that variation of concentration with unit time is more pronounced compared to its variation in the spatial directions. This is due to the weak dependence of concentration on the spatial location and the strong dependence on time as prescribed in Eq. (4.13).

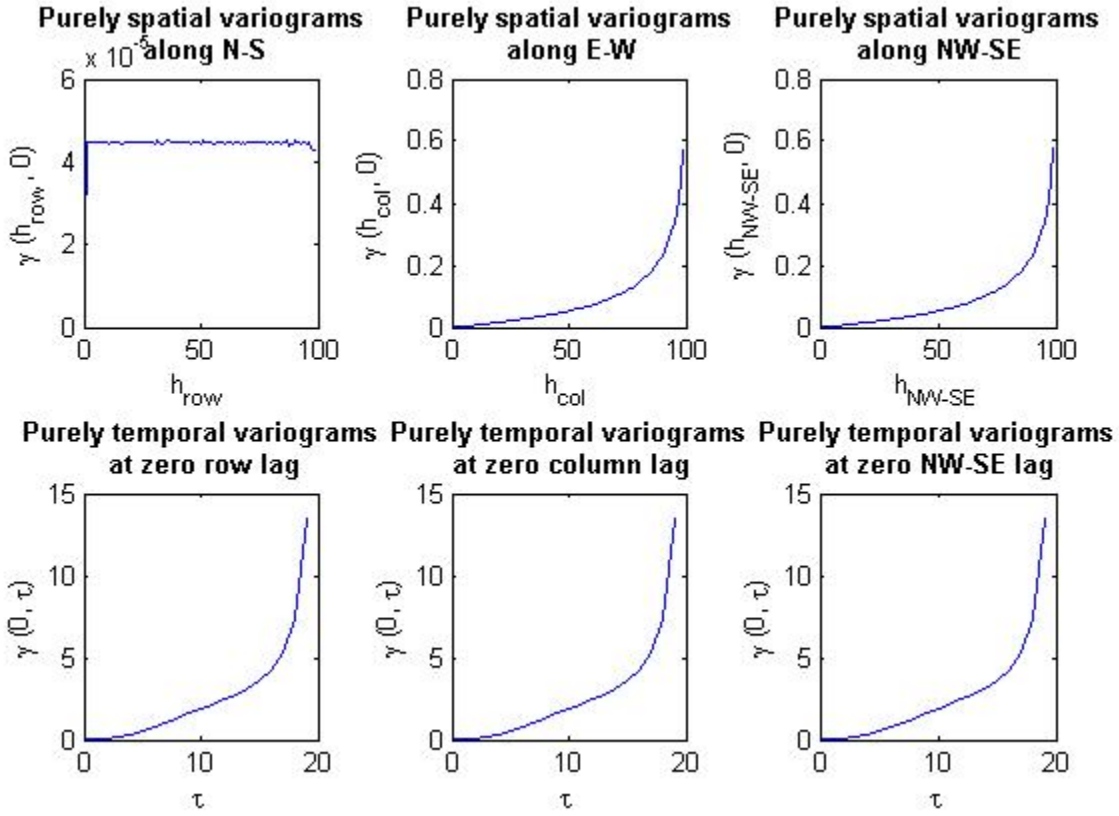

Figure 4-2: Purely spatial and purely temporal variograms (normalized) by the variance of the lag-pairs.

The purely spatial variograms along E-W and NW-SE directions in Figure 4-2 suggest that change in concentration with spatial lag is very gradual and less in magnitude. It can be seen in the concentration profilea in Fig. 4-1 that there is very little spatial variability in concentration at early times but the variability increases as time progresses. This contributes to the rise of the purely spatial variograms along E-W and NW-SE directions. Spatial concentration is a combination of the value dictated by the deterministic trend and that arising because of stochastic perturbation about that trend.

This results in the concentration in any direction to exhibit uncertainty. Depending on whether the deterministic trend or the stochastic residual is more dominant, the resultant variogram either exhibits non-stationarity (if trend is dominant) or stationarity (if the stationary stochastic perturbation is dominant). After normalizing the variogram, the sill is still well below 1 until the maximum allowed spatial lag is reached, therefore, indicating that the sill stabilization may be achieved at some higher spatial lag. The limited spatial extent of the model and strong spatial trend component makes it difficult for the spatial variogram to stabilize within the maximum allowed spatial lag. The reason for temporal non-stationarity is that the concentration values at a particular location exhibit a consistent increasing trend with time.

4.4.3.2 Spatiotemporal Variograms With Discrete Time Lags

Using the computational procedure detailed in Appendix A, spatiotemporal variograms for concentration data along N-S, E-W and NW-SE directions in Figure 4-1 can be obtained for various temporal lags ($\tau \geq 0$) as shown in Figure 4-3. Because the injection is along the entire left edge of the model, there is almost no variability in the N-S direction even though the mean concentration of each time slice is higher as more and more of the chemical species is injected. This results in the spatiotemporal variogram along the N-S directions for $\tau > 0$ to be flat (exhibiting no systematic spatial variability) albeit with higher and higher variance values because of the continuous increase in mean concentration. The spatiotemporal variogram along the E-W for $\tau > 0$ goes from a decreasing characteristic for small τ's to a constant variogram value for intermediate τ's to an increasing characteristic for higher τ's. The increasing or decreasing nature of the

spatiotemporal variogram is because of the disparate influence of time (t) and spatial position (x) on the concentration value as indicated by Eqn. (4.13).

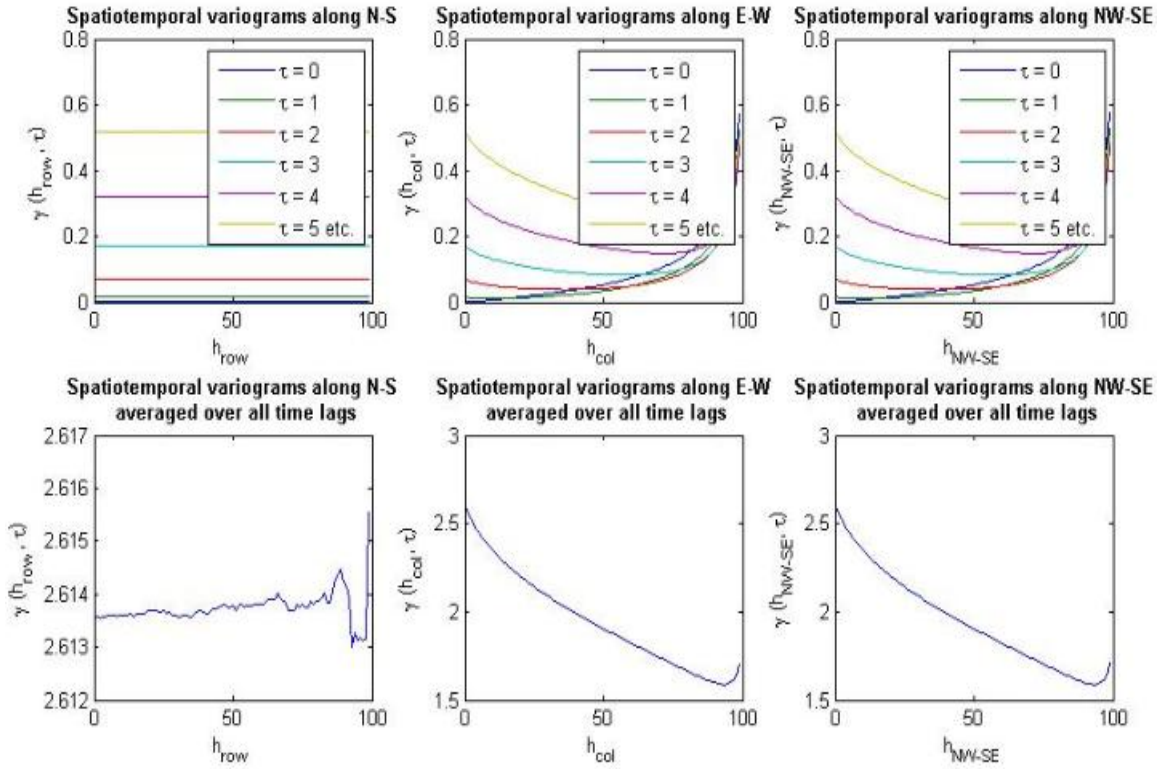

Figure 4-3: Top row: Spatiotemporal variograms (normalized) for various time lags along N-W, E-W and NW-SE, and Bottom row: Spatiotemporal variograms averaged over all time lags along N-W, E-W and NW-SE

The spatiotemporal framework is a combination of variability of concentration considering spatial as well as temporal lags. Specifically, spatiotemporal variogram can be assumed as some function of spatial and temporal variograms. In this case, because the temporal variogram is non-stationary and sharply increasing (as shown earlier), its magnitude can potentially overwhelm the magnitude of the spatial variogram in order to

yield a spatiotemporal variogram whose magnitude is greater than 1, thus, making it non-stationary as shown in Figure 4-4.

The non-stationarity of the spatiotemporal variogram is somewhat subdued if the concentration evolution function of Eqn. (4.13) is altered such that the degree of increase in concentration with time is not as steep. Physically this implies some property in the reservoir which changes very gradually with time such as mineralization due to CO_2 storage that takes place over hundreds to thousands of years.

4.4.3.3 Spatiotemporal Variograms with Continuous Time Lags

Data from Figure 4-3 can also be used to develop spatiotemporal variograms along N-W, E-W and NW-SE with continuous temporal lags. Figure 4-4 shows spatiotemporal variograms in the form of surface plots and diagonal cross sections through such plots. In summary, variograms along the N-S direction are flat for all temporal lags while variogram along the E-W direction transition from a decreasing characteristic at small τ's to an increasing characteristic at large τ's. This is because of the same reason as discussed above.

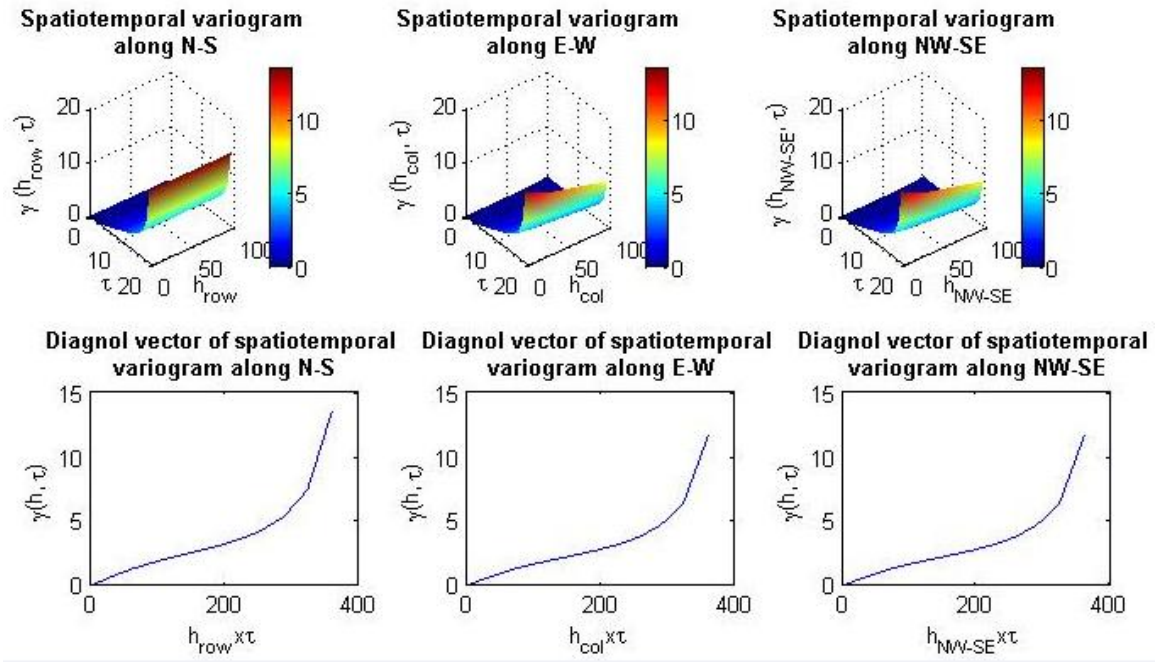

Figure 4-4: Top row: Spatiotemporal variogram (normalized) 3-D surface plots, and Bottom row: Diagonal sections through surface plots in the N-W, E-W and NW-SE directions, where the x-axis on diagonal sections represent the product of spatial and temporal lags.

4.4.3 Modeled Spatiotemporal Variograms

As mentioned earlier, the product-sum spatiotemporal variogram model would be legitimate (De Iaco et al. , 2001) if either $\gamma_{s,t}(\mathbf{h_s},0)$ or $\gamma_{s,t}(0,\mathbf{h_t})$ is non-stationary i.e. they do not have a bound. As observed above, the empirical $\gamma_{s,t}(\mathbf{h_s},0)$ variogram is stationary while empirical $\gamma_{s,t}(0,\mathbf{h_t})$ variogram is non-stationary. Purely spatial variograms along all directions were modeled as a single spherical structure. The purely temporal variogram was difficult to match with a standard model, so its empirical values were used in the De Iaco et al. (2001) spatiotemporal variogram model. The fitted

spatiotemporal variograms using De Iaco et al. (2001) model are shown in Figure 4-5. It can be seen that the fit is pretty good even with simplifying assumptions regarding the purely spatial variogram models. The values of k_s and k_t for which this match was obtained are 1 and 1.01, respectively.

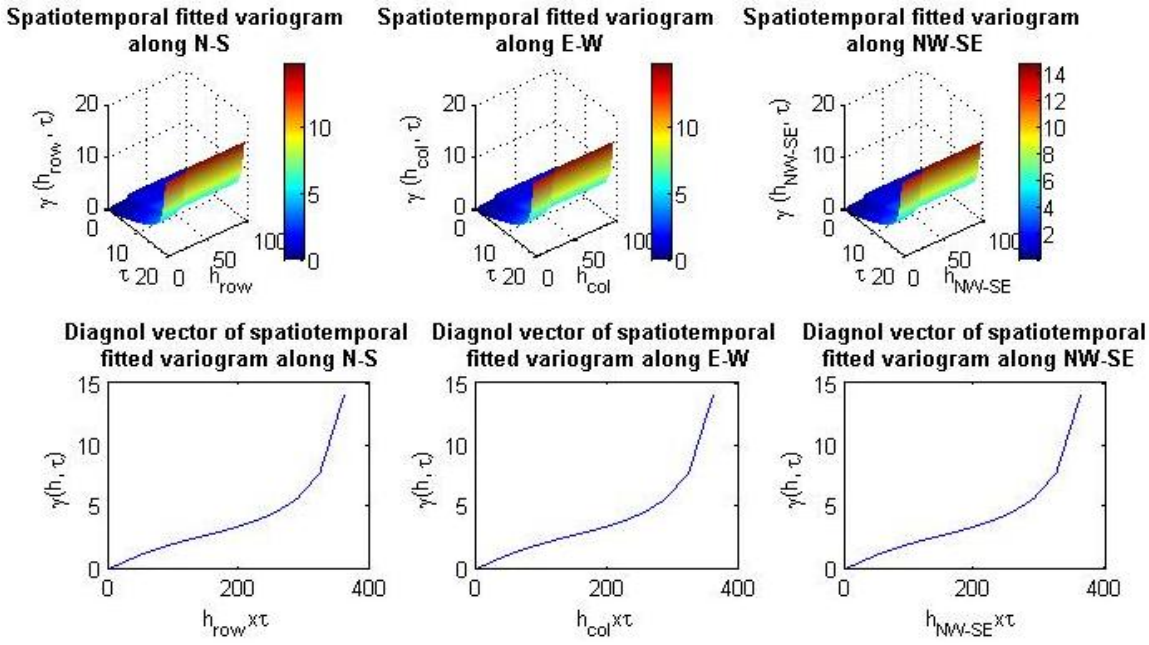

Figure 4-5: Top row: Spatiotemporal fitted variogram (normalized) 3-D surface plots, and Bottom row: Diagonal sections through surface plots in the N-W, E-W and NW-SE directions, where the x-axis on diagonal sections represent the product of spatial and temporal lags. Note the x-axis is the product of the spatial and temporal lags.

4.4.4 Variance of Mean: REV

Variance of the mean is estimated by directly averaging the concentration values as well as by using the spatiotemporal variogram within the equation:

$$Var(\bar{f}) = \frac{2\sigma^2}{(L \times B \times T)^2} \left(\int_{\zeta_3=0}^{\zeta_3=T} \int_{\eta_3}^{\eta_3=\zeta_3} \int_{\zeta_2=0}^{\zeta_2=B} \int_{\eta_2}^{\eta_2=\zeta_2} \int_{\zeta_1=0}^{\zeta_1=L} \int_{\eta_1}^{\eta_1=\zeta_1} \rho_{corr} \{\eta_1(L), \eta_2(B), \eta_3(T)\} d\eta d\xi \right) \quad (4.14)$$

Figures 4-6 shows variance of mean concentration at discrete time lags computed using both the approaches mentioned above. It shows that the variance of mean concentration at small time lags is comparatively flat compared to the variance of mean profile at large time lags ($\tau \sim 19$). The results in Figure 4-6 indicate that at short time lags, the concentration profile represented using the Eq. 4-11 does not exhibit much variability and so the variance of the mean remains mostly invariant. Whereas at larger temporal lags, the concentration profile exhibits substantial variability and consequently the variance plot at higher temporal lags eventually exhibit the characteristic transition to -1 slope.

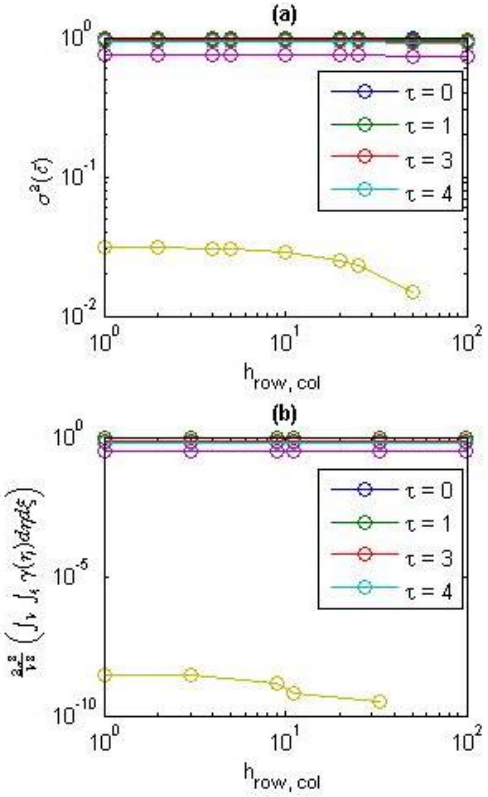

Figure 4-6: Variance of mean concentration computed using a) numerical values of concentration, and b) variogram, from Eqn. (4.2)

This spatiotemporal variance of mean data can also be presented in the form of 3-D surface plots and sections through the 3-D plot as shown in Figure 4-7. The surface plots show that the variance of mean concentration computed using both approaches decrease with increasing temporal scale. A diagnostic signature of -1 slope can be seen in both the variance of mean plots computed using both ways. Spatiotemporal REV scale (~ 10) estimated from both methods matches well. The difference in curvatures of the two plots before REV is reached could be because of two reasons - 1) estimated variograms

are approximate and are not representative of the correlation in all directions, 2) there is a small error in performing the quadrature procedure for integration.

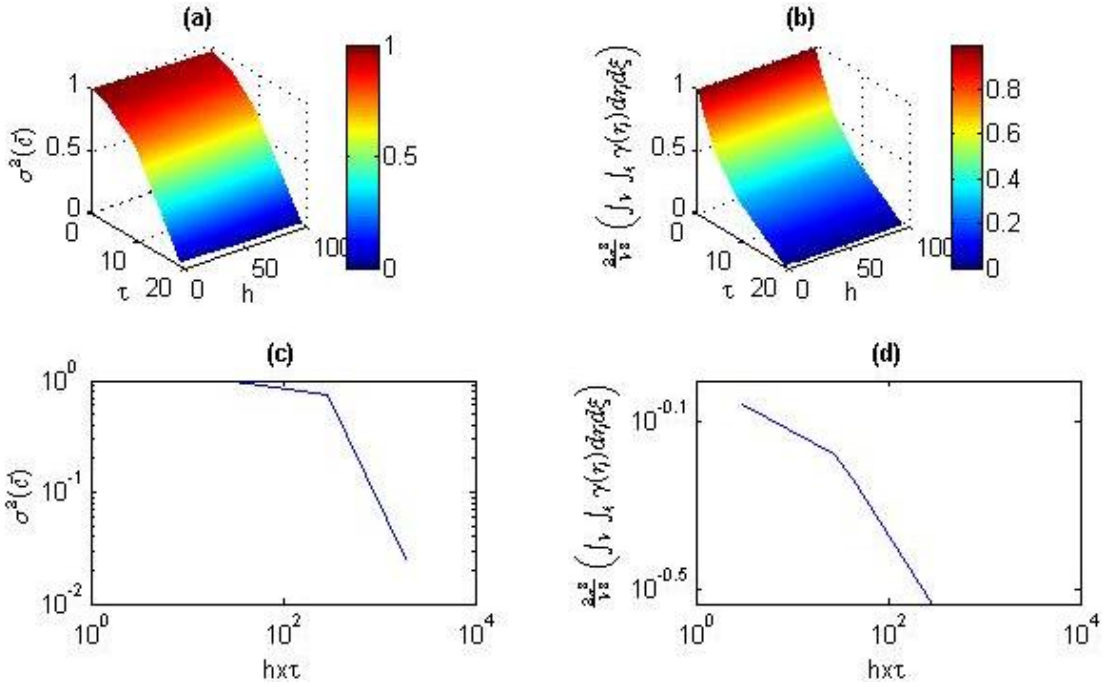

Figure 4-7: Variance of mean concentration computed a) by averaging the concentration values, and b) by evaluating the space-time integrals of the spatiotemporal covariance, c) along the diagonal cut through the surface in (a), d) along the diagonal cut through the surface in (b).

4.4.5 Conclusions

The results from the synthetic case study suggest that the effect of temporal scale on REV can be significant for certain processes and in that case it is important to determine a spatiotemporal REV scale. The temporal effect on REV scale could have

direct application in CO_2 sequestration where the reservoir attributes such as petrophysical properties could change substantially (Izgec et al. 2007) with time.

4.5 SCALE-UP ANALYSIS OF DIFFUSION-REACTION PROCESSES

4.5.1 Theoretical Basis

This approach is most useful when prior knowledge of the process is available. Heine (1955) investigated two dimensional, second order, linear and non-stochastic PDEs such that the concentration *c* can be described using a partial differential equation (PDE).

A deterministic PDE can be converted into a stochastic PDE by exchanging 0 on the right hand side of deterministic PDE with a stochastic term that has a zero mean. The two dimensional PDE could either be purely spatial or it could be spatiotemporal. As we are interested in a process with changes with both space and time, therefore, we will consider the PDE in terms of space *s* and time *t*. Consider a spatiotemporal process *c(s; t)* such that *s* denotes a location in space that has a domain *D* (usually two dimensional Euclidean space) and *t* is any time along the time dimension. The stochastic term in the two dimensional stochastic PDE is written as $\delta(s;t)$ and this term is a mean-zero, two dimensional stochastic process that represents the uncertainty in the relationship depicted by the PDE.

4.5.2 Description of Case Study

The spatiotemporal process involving diffusion and reaction processes associated with the migration of CO_2 in geological formations can be represented using the following stochastic partial differential equation (PDE) (Heine 1955):

$$\frac{\partial c(s;t)}{\partial t} - D\frac{\partial^2 c(s;t)}{\partial s^2} + \alpha c(s;t) = \delta(s;t) \tag{4.15}$$

where,

α = reaction constant

D = Diffusion constant

$\delta(.;.)$ = mean-zero stochastic term i.e. $\{E[\delta(.;.)] = 0\}$

This equation shows that the rate of change in $c(s; t)$ is equal to the spreading or smoothening of $c(s; t)$ in space (through diffusion), and a mechanism opposing the "spread" by the "loss" of a certain multiple of $c(s; t)$ (through reaction). The process $c(s; t)$ is represented stochastically, and therefore, we would therefore be interested in its moments. The PDE in deterministic form for the above stochastic PDE can be written as:

$$\frac{\partial c}{\partial t} = D\frac{\partial^2 c}{\partial s^2} - \alpha c \tag{4.16}$$

This deterministic form of the PDE represents a homogeneous diffusion-reaction (DR) process. The purpose of introducing a stochastic term to form a stochastic PDE is to bring a statistical balance between the randomness caused by $\delta(.;.)$, and the smoothing effect of the diffusion component and the loss (reaction) component. Furthermore, the stochastic PDE represents a spatiotemporal process that is stationary in both space and time.

4.5.3 Covariance of Diffusion-Reaction Equation

Heine (1955) showed that the concentration $c(s;t)$ obtained by solving the PDE has a stationary spatiotemporal covariance function $C_c(.;.)$ and he derived an analytical expression for it. The DR process is discretized in a 1-D space with s varying from 0 till 40 m and the time scale t varying from 0 till 0.8 years. The DR process entails simulating the dissipation of an initial injection of concentration 1, where the initial and boundary conditions used to obtain the covariance model are:

$$\text{I.C.}: \left\{ \begin{array}{l} c(s;0) = 1 \text{ for } 15 \le s \le 24 \\ c(s;0) = 0, \text{ otherwise} \end{array} \right\}$$

$$\text{B.C.}: \left\{ \begin{array}{l} c(1;\, t) = 0 \;\forall\; t \\ c(40;\, t) = 0 \;\forall\; t \end{array} \right\}$$

If, $\mathbf{h}$ (spatial lag) $\in R$ and τ (temporal lag) $\in R$, then the corresponding spatiotemporal correlation function, $\rho_c(\mathbf{h};\tau)$, for $c(s;t)$ as derived by Heine (1955) is:

$$\frac{C_c(\mathbf{h};\tau)}{C_c(0;0)} \equiv \rho_c(\mathbf{h};\tau)$$

$$= \frac{1}{2} \left\{ \begin{array}{l} e^{-\mathbf{h}(\alpha/D)^{1/2}} Erfc\left(\dfrac{2\tau(\alpha/D)^{1/2} - \mathbf{h}/D}{2(\tau/D)^{1/2}} \right) + \\ e^{\mathbf{h}(\alpha/D)^{1/2}} Erfc\left(\dfrac{2\tau(\alpha/D)^{1/2} + \mathbf{h}/D}{2(\tau/D)^{1/2}} \right) \end{array} \right\} \qquad (4.17)$$

where,

$Erfc$ = complementary error function

The limit cases of purely spatial and purely temporal correlation function can be written as:

$$\rho_c(\mathbf{h};0) = e^{-\mathbf{h}(\alpha/D)^{1/2}}, \qquad \mathbf{h} > 0$$

$$\rho_c(0;\tau) = Erfc\left(\tau^{1/2}\alpha^{1/2}\right), \qquad \tau > 0$$

These correlation functions in pure spatial and temporal setting are plotted for 4 different scenarios in Figure 4-8, representing varying degree of magnitude of diffusion or reaction in the combined DR transport process. These plots clearly show that when reaction component is present the variation of concentration is significant with time (parts a and c), however, in absence of reactions the variation of concentration with time is relatively negligible (parts b and d). Also, transport just by reactions themselves (part c) tend to vary the concentration more significantly in space when compared to transport just by diffusion (part d) or transport by combined diffusion and reaction (part a).

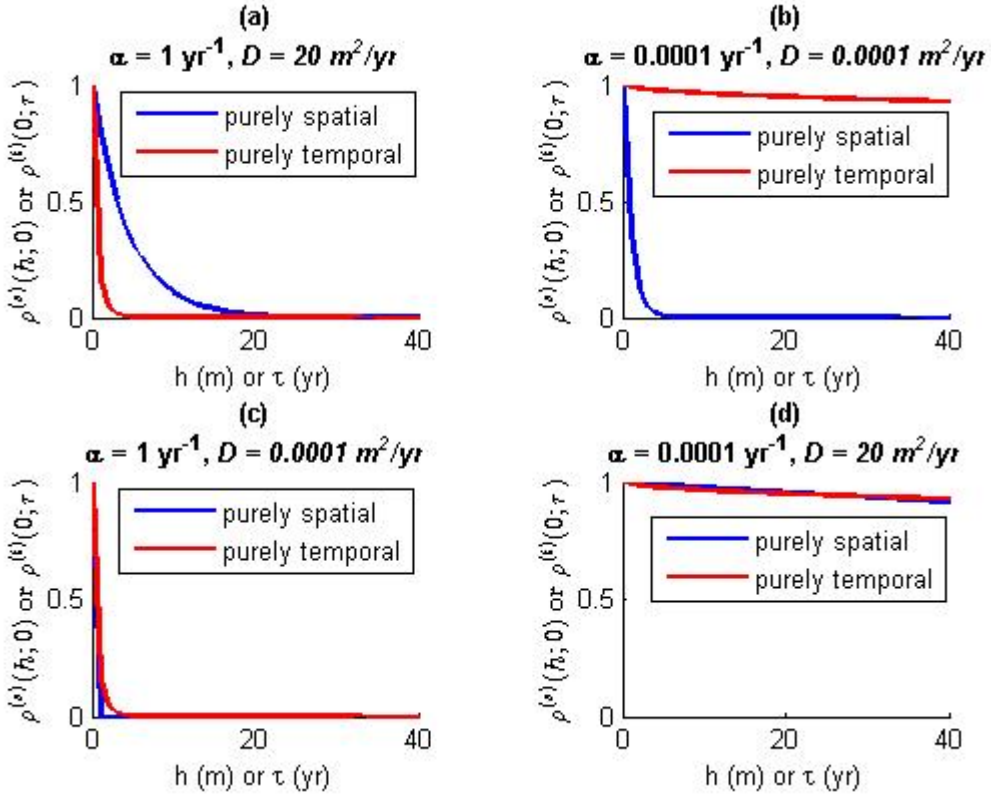

Figure 4-8: Spatial and temporal correlation function of concentration in presence of (a) diffusion and reaction, (b) no diffusion and no reaction, (c) reactions but no diffusion, and (d) diffusion but no reactions

4.5.4 Variance of the Mean: REV

Variance of the mean can again be calculated using the concentration values computed by solving the DR equation as well as using the spatiotemporal covariance function derived for the concentrations.

4.5.4.1 Scale-up Using Correlation Function of DR Equation

We calculate the variance of the mean by integrating the correlation function in Eqn. (4.17) over all time and spatial lag scales. The parameters used to calculate correlation function in Eqn. (4.17) are $\alpha = 1\ \mathrm{yr}^{-1}$, $D = 20\ \mathrm{m}^2/yr$, $h = 1\ \mathrm{m}$, $\tau = 0.01\ \mathrm{yr}$. Figure 4-9 shows the spatiotemporal variance of $\bar{c}(s;t)$ in the form of a 3D surface plot with spatial lag $\boldsymbol{h}$ and temporal lag τ as the coordinate axes. The results in Figure 4-9 show that the curvature of the variance of mean surface at longer temporal lags is different from that at small temporal lags. This implies that the REV scale (scale at which slope of curvature reaches -1) changes rather significantly with time. The results also indicate that the spatial scale of the REV also varies significantly at early times. This suggests that it is important to consider both spatial and temporal scales when considering determining a spatiotemporal REV scale.

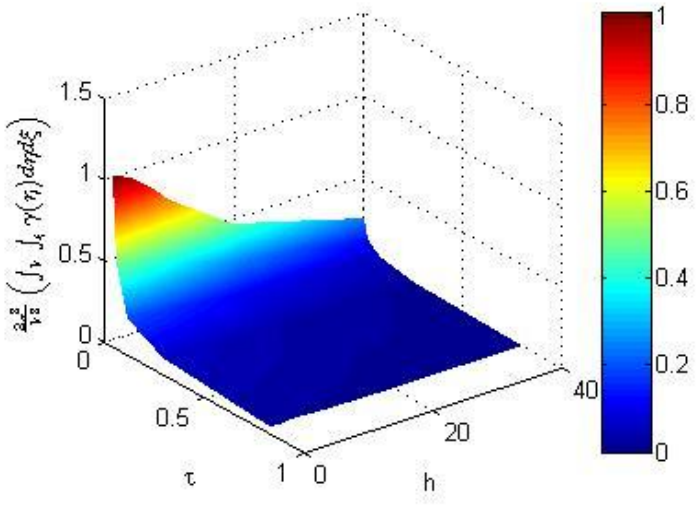

Figure 4-9: Spatiotemporal variance of mean concentration computed by integrating the spatiotemporal covariance over spatial and temporal lags.

The spatiotemporal variance of mean along a diagonal section through the 3D surface plot is shown in Figure 4-10. The x-axis of this plot is the product of the spatial and temporal lags. This plot depicts a diagnostic signature of negative unit slope at scales larger than and equal to REV scale in space and time. The scale at which the variance of mean concentration along this diagnostic plot reaches -1 provides us the combined spatiotemporal REV scale beyond which the major fluctuations in concentrations of CO_2 due to the combined effects of diffusion and reaction dies out.

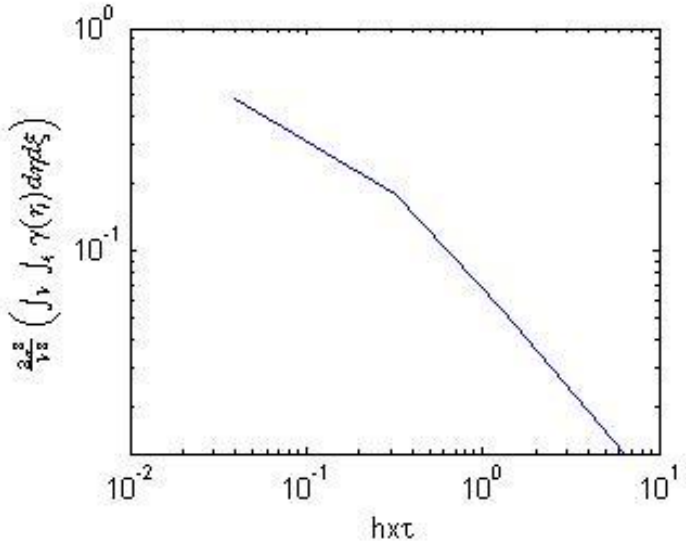

Figure 4-10: Spatiotemporal variance along a diagonal through the 3-D surface plot of the variance of the mean computed using the spatiotemporal covariance.

4.5.4.2 Scale-up Using Spatiotemporal Concentration Profile

4.5.4.2.1 Spatiotemporal Process Described by the diffusion-reaction PDE

The spatiotemporal concentration profile is numerically computed for a simple DR process described by Eqn. (4.16), where the reaction rate term is assumed to be a simple first order reaction ($r = \alpha[c]$). As noted in Chapter 2 on literature review, reaction rate can take many complex empirical forms, and specifically for CO_2 sequestration many reaction rates have been proposed because of the complexity of the subsurface systems.

The DR process is solved in a 1-D space with *s* varying from 0 till 40 m and the time scale *t* varying from 0 till 0.8 years. The values of reaction rate constant, diffusion constant, spatial discretization and time step used for solving the problem are $\alpha = 1\ \text{yr}^{-1},\ D = 20\ \text{m}^2 / yr,\ \Delta x = 1\ \text{m},\ \Delta t = 0.01\ \text{yr}$, respectively. These parameter values are similar to the values used in the previous section.

4. 5.4.2.2 Numerical Solution of the Spatiotemporal Process

To numerically solve for $c(s;t)$ from Eqn. (4.16) we replace the first-order partial derivative in time with a forward difference and the second-order partial derivative in space with a centered difference (Cressie and Wikle 2011) as shown below:

$$\frac{c(s;t+\tau)-c(s;t)}{\tau} = D\left\{\frac{c(s;t+\tau)-2c(s;t)+c(s-h;t)}{h^2}\right\} - \alpha c(s;t) \tag{4.18}$$

Eqn. (4.18) can be rewritten as following:

$$c(s;t+\tau) = \theta_1 c(s;t) + \theta_2 c(s+h;t) + \theta_2 c(s-h;t) \tag{4.19}$$

where,
$\theta_1 \equiv \left(1-\alpha\tau-2D\tau/h^2\right),\ \theta_2 \equiv D\tau/h^2,\ \alpha\tau<1$ and $2D\tau/h^2<1$.

Eqn. (4.19) can be written in vectorial difference form as:

$$c_{t+\tau} = Mc_t + M^{(b)}c_t^{(b)} \tag{4.20}$$

where, *M* is an *n* x *n* tri-diagonal propagator matrix and $M^{(b)}$ is an *n* x *2* boundary propagator matrix, as shown below:

$$M \equiv \begin{bmatrix} \theta_1 & \theta_2 & 0 & \cdots & \cdots & 0 \\ \theta_2 & \theta_1 & \theta_2 & \cdots & \cdots & 0 \\ 0 & \theta_2 & \theta_1 & \ddots & & \vdots \\ \vdots & \vdots & \ddots & \ddots & \ddots & \vdots \\ \vdots & \vdots & & \ddots & \theta_1 & \theta_2 \\ 0 & 0 & 0 & \cdots & \theta_2 & \theta_1 \end{bmatrix}, \quad M^{(b)} \equiv \begin{bmatrix} \theta_2 & 0 \\ 0 & 0 \\ \vdots & \vdots \\ 0 & \theta_2 \end{bmatrix} \tag{4.21}$$

For a given initial and boundary conditions the vector difference form of the PDE shown in Eqn. (4.20) can be solved. As mentioned earlier, the DR process entails simulating the dissipation of an initial injection of concentration 1 for which the following set of initial and boundary conditions are used to obtain the numerical solution of $c(s;t)$:

$$\text{I.C.}: \begin{Bmatrix} c(s;0) = 1 \text{ for } 15 \le s \le 24 \\ c(s;0) = 0, \text{ otherwise} \end{Bmatrix}$$

$$\text{B.C.}: \begin{Bmatrix} c(1;\, t) = 0 \ \forall \ t \\ c(40;\, t) = 0 \ \forall \ t \end{Bmatrix}$$

These initial and boundary conditions are consistent with those used to derive the spatiotemporal covariance model. The solution to the stochastic DR equation given by Eqn. (4.15) can also be found in a similar fashion using the above equations and constraints, except that an additional term of random error is included in Eqn. (4.20) as shown here:

$$c_{t+\tau} = Mc_t + M^{(b)}c_t^{(b)} + \delta_{t+1}, \qquad t = 0,1,..., \tag{4.22}$$

Where,

δ_t is an independent and identically distributed (*iid*) random variable.

Using the above method we solve the stochastic DR equation given by Eqn. (4.15) to find the numerical solution of $c(s;t)$ with similar set of values as used to obtain the spatiotemporal covariance: $\alpha = 1\ \text{yr}^{-1}$, $D = 20\ \text{m}^2/yr$, $h = 1\ \text{m}$, $\tau = 0.01\ \text{yr}$. The spatiotemporal profile of $c(s;t)$ using these parameters is shown below:

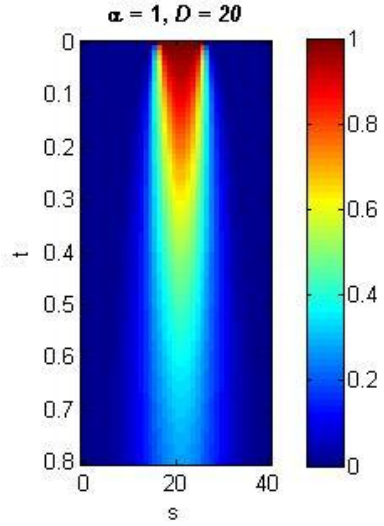

Figure 4-11: Simulated numerical solution of $c(s;t)$. Each 1D slice through the above figure represents the concentration distribution at a particular snapshot in time.

Figure 4-12 shows three different scenarios of concentration profile in presence of: a) no diffusion and no reaction, b) reactions but no diffusion, and c) diffusion but no reactions. As stated earlier in Chapter 3, transport due to reactions result in a sharp advancing reactive front (Aharonov et al. 1995; Lake et al. 2002), and diffusion process tends to stabilize the reaction front which can be seen clearly in the Figure 4-12. However, if the transport is due to diffusion process only with no reactions (part c) then the smoothing effect of diffusion tends to spread faster as compared to when both transport is by both diffusion and reactions (Figure 4-11).

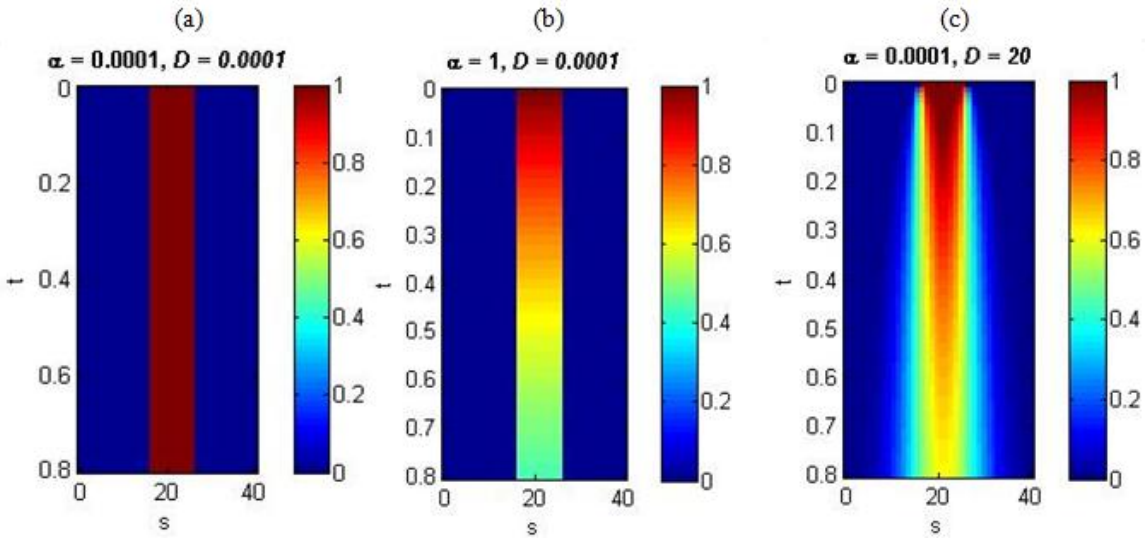

Figure 4-12: Numerical solutions of concentration in presence of (a) no diffusion and no reaction, (b) reactions but no diffusion, and (c) diffusion but no reactions

We solve for REV from variance of the mean plot by numerically averaging the concentrations of Figure 4-11. This is represented mathematically as $\mathrm{var}\{\bar{c}(s;t)\}$, and plotted against the length and time scale to assess the spatiotemporal REV scale of the physical property. Figure 4-13 shows the spatiotemporal variance of $\bar{c}(s;t)$ on a 3-D surface plot similar to Figure 4-9.

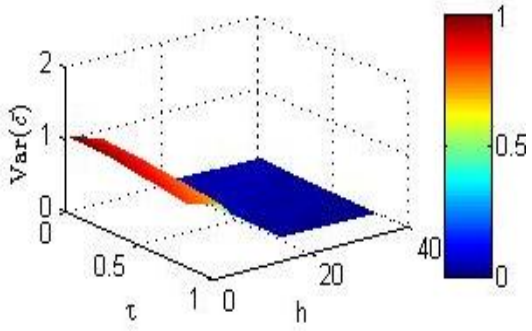

Figure 4-13: Spatiotemporal variance of mean concentration computed by numerically solving the DR equation and averaging the concentration values.

The spatiotemporal variance along a diagonal section through the 3D surface plot is shown in Figure 4-14. This plot also depicts a diagnostic signature of negative unit slope at scales larger than and equal to REV scale in space and time. Once again, the x-axis of the plot has units of the product of spatial and temporal scales.

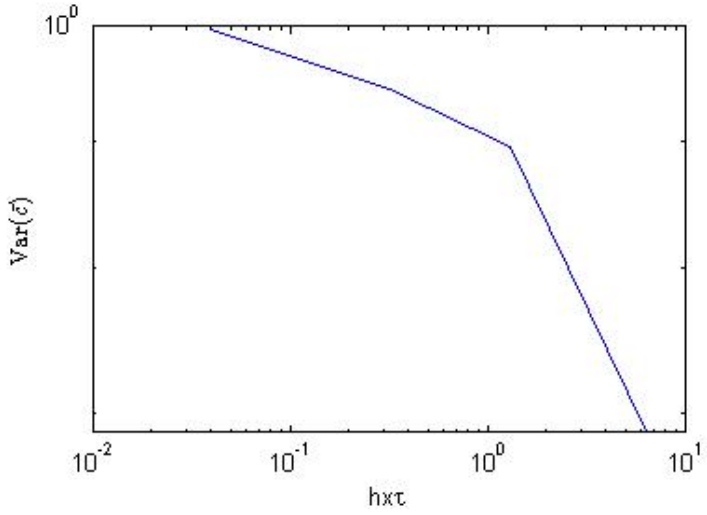

Figure 4-14: Spatiotemporal variance, using $\mathrm{var}\{\bar{c}(s;t)\}$, along the diagonal of surf plot shown in Figure 4-

If we compare the spatiotemporal REV along the diagonal sections through the surface plots i.e. Figure 4-10 and Figure 4-14, we observe that there is some difference in the two results because of error in performing the numerical integration and also because the numerical solution of the stochastic DR equation introduces some numerical dispersion. The overall profile for the variation in $\mathrm{var}\{\bar{c}(s;t)\}$ from Figure 4-14 compared to the profile in Figure 4-10 is quite similar. These profiles indicate that the stable REV scale for this process occurs for a product value of 6.4 ($=\tau \times h$). This implies that when performing numerical simulation of the process, the spatial discretization scale and the

time stepping has to be specified such that the combination of spatial and temporal scale exceeds 6.4 ($=\tau \times h$) in order to have an REV representation of the process.

4.5.5 Conclusions

The combined spatial and temporal REV scaling of the processes associated with CO_2 sequestration is analyzed in this chapter. The spatiotemporal REV computed in the two case studies presented in this chapter show significant sensitivity of REV on the temporal scale. Conventionally, REV has always been estimated on spatial scale without considering the effect of reservoir properties changing with time. The results presented in the above two case studies show that for reactive processes an accurate assessment of REV is possible only when the spatial and temporal scales are coupled together.

The spatial scales of the sub-processes in reactive systems are intrinsically coupled nonlinearly with their temporal scales. Due to this nonlinear coupling of spatial and temporal scales the numerical solutions are sensitive to the selection of the spatial and temporal discretization. The proposed semi-analytical technique to scale-up in both space and time provides guidance for selection of spatial and temporal discretizations that take into account the uncertainties introduced by sub-scale processes.

Chapter 5: Application to Scale-up Analysis of Pore-Scale Spatiotemporal CO_2 Dissolution Data

5.1 Overview

One of the potential risks associated with subsurface storage of CO_2 is the seepage of CO_2 through existing faults and fractures. There have been a number of studies devoted to this topic (Shipton et al. 2004; Kim 2012). Some of these studies show that geochemistry, especially mineralization, plays an important role in rendering the faults as conduits for CO_2 movement while others (Kim 2012) show that mineralization due to CO_2 injection can result in seep migration and flow diversion. Therefore, understanding the changes in reservoir flow dynamics with time due to geochemistry and its effective impact at different scales is important in order to engineer CO_2 storage strategies and ensure long term storage in the subsurface.

We apply a statistical scale-up approach using high-resolution pore-scale data for conservative flow as well as for reactive flow measured under laboratory conditions (Ovaysi and Piri 2010; Ovaysi and Piri 2011; Ovaysi and Piri 2013; Ovaysi and Piri 2014). The available pore-scale reactive attribute information is used to obtain a tangible parameter such as reaction rate constant which has relevance in modeling reactive transport. Reaction rate constant is estimated using the pore-scale reactive attribute and an equation derived from first order reaction rate law, which is then scaled-up to a spatiotemporal REV scale through statistical approach.

The results for scale-up of pore-scale data indicate that the REV in reservoir with reactive flow changes with time and is greater when compared to REV for conservative

flow. The change in REV with time for reservoirs with reactive flow is due to changes in pore structure because of dissolution. This change in pore structure will also be affected by heterogeneity that occurs over a wide range of length scales in porous media. As a result of this, it is possible these noticeable changes at pore-scale may be further amplified in magnitude when analyzed at the reservoir scale. The results for scale-up of pore-scale data presented in this chapter support the conclusions drawn by other authors regarding flow channeling and seep migration due to changes in pore structure. Finally, the reaction rate constant averaged in space and time over its spatiotemporal REV scale yields a single value which is devoid of uncertainties arising due to evolution of fine scale reaction constant in space and time. This scaled-up reaction constant can serve as an effective quantity which can be used as an input in reactive flow transport simulations.

5.2 OBJECTIVE

After CO_2 is injected in a subsurface saline aquifer, causes the CO_2 to mix with the with aqueous species (e.g., Fe(III), Mn(IV), Ca(II) etc.) present in in-situ brine. Reactions with rock minerals lead to dissolution and/or precipitation which alters the pore structure (Gharbi et al. 2013) by changing the porosity, and hence, permeability (Johnson et al. 2004; Gunter et al. 1997; Izgec et al. 2005). A schematic representation of changes occurring in the reservoir due to CO_2 injection is shown in Figure 5-1. CO_2 migration in time accounting for geochemistry changes the reservoir properties (Gharbi et al. 2013; Izgec et al. 2007), and hence requires a scaled-up procedure that accounts for changes in reservoir with time.

Spatial scale-up of reservoir properties and flow response at a single snapshot of time has been described by other authors (Leung 2009; Lake and Srinivasan 2004), however, scale-up of dynamic quantities such as reaction parameters cannot be correctly described just in a single snapshot of time The aim of this chapter is to apply the scale-up analysis procedure discussed in previous chapters to high-resolution pore-scale spatial and spatiotemporal data for conservative and reactive processes. The REV for conservative process is modeled using the 3-D pressure data and the REV for reactive process is modeled using three different types of data – fluid/matrix pore geometry alteration data, dissolution (due to porosity change) data, and volume-based dimensionless CO_2 concentration data – all in 2-D spatial snapshots at various time instants. Results of scale-up estimated using attributes of conservative process and reactive process are presented and compared with discussions. Finally, the importance of this research work is highlighted.

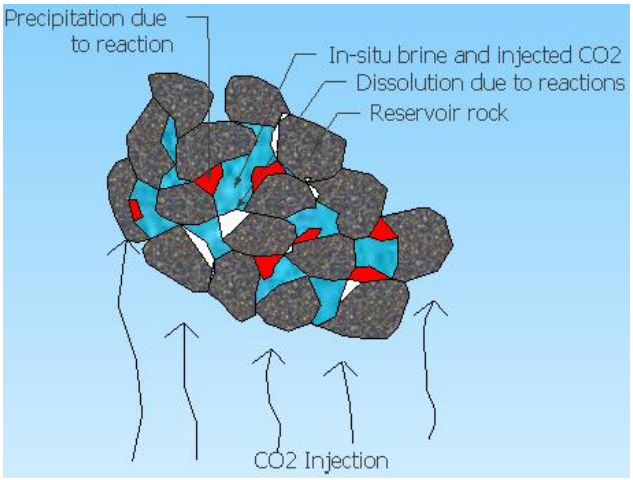

Figure 5-1: Schematic representation of the changes introduced in reservoir due to reactive flow because of CO_2 injection.

5.3 METHOD

5.3.1 Representation of Pore Scale Porous Media

The high resolution images at 3.398 μm resolution of fluid flow in a sandstone acquired using computed microtomography by Ovaysi and Piri (2010) are used. The microtomography image provides the coordinates of the matrix and the pore space in three dimensions, and a particle is assigned to each coordinate of pore space. To simplify the computational expense, a 1.02 mm x 1.02 mm x 1.02 mm sample with scattered data points is chosen. Figure 5-2 illustrates the original X-ray image of the reconstructed porous media (sandstone) used in this chapter (Ovaysi and Piri 2010).

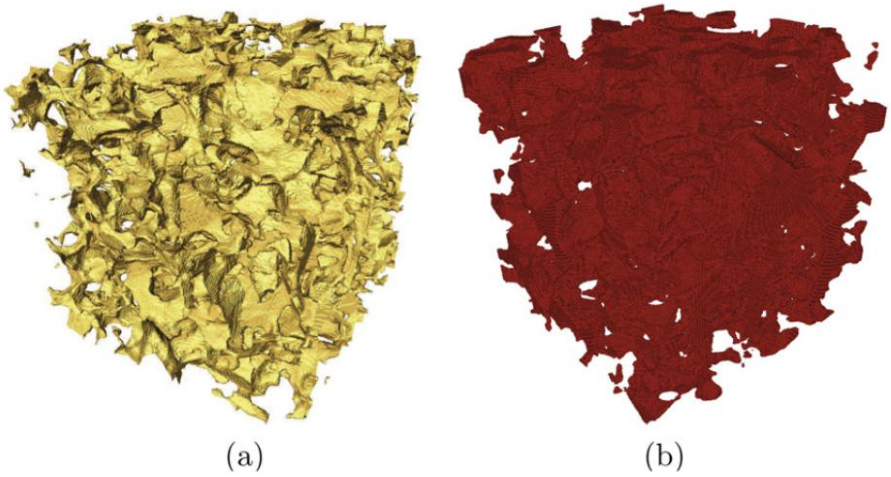

Figure 5-2: Reconstruction of the porous media using X-ray microtomography for (a) matrix (b) pore space

5.3.2 Simulated Concentration Data: Model Description/Mathematical Formulation

The data used in this work is simulated within the pore scale representation using a modified moving particle semi-implicit (MMPS) technique, a Lagrangian particle-based

technique, which can model the flow of incompressible and compressible fluids inside the pore space (Ovaysi and Piri 2010) represented by high resolution images as shown in Figure 5-2. MMPS has been validated against analytical, numerical, and experimental data available in the literature, with particular emphasis on assessing the accuracy of the velocity field and longitudinal dispersion coefficient over a wide range of Peclet numbers including those for flow regimes dominated by inertia and turbulence (Ovaysi and Piri 2013).

Experimental data is simulated in 3-D by solving Navier-Stokes (N-S) equations for conservative process (advective-diffusive) and reactive process (advective-diffusive-reactive), respectively, using MMPS technique. Additionally, for reactive processes such as dissolution of rock material by CO_2 dissolved in brine, we need to solve for the transport of chemical species due to molecular diffusion, electrical coupling and chemical reactions. Since we are interested in the effect of temporal changes in reservoir pore structure due to reactive process and its effect on scaled-up response, therefore, reactive process data is simulated for discrete time periods from $t = 0$ till $t = 20$ sec in intervals of 2 sec.

5.3.2.1 Mathematical Formulation for Conservative Process

The mathematical formulations for conservative process with flow of incompressible fluid and uniform density is given by N-S equations, Eqn. (5.1), and the convection-diffusion equation. N-S equations consist of time-dependent conservation of momentum, a continuity equation for conservation of mass, and a time-dependent conservation of energy equation. In the time-dependent conservation of momentum

equation, the term on the left represents unsteady acceleration, the first term on right hand side represents pressure gradient and the second term represents viscosity which operates as a diffusion of momentum. For an incompressible fluid the density of fluid is constant and in that case the continuity equation simplifies to a specific case which is equivalent to conservation of volume.

$$\left.\begin{aligned} &\frac{\partial \mathbf{v}}{\partial t} = -\frac{1}{\rho}\nabla P + \frac{\mu}{\rho}\nabla^2 \mathbf{v} + \mathbf{g} \\ &\nabla . \mathbf{v} = 0 \\ &\frac{\partial c}{\partial t} = D\nabla^2 c \end{aligned}\right\} \qquad (5.1)$$

Where,

$\mathbf{v}$ = average velocity with which the quantity is moving

ρ = density

μ = viscosity of a nonreactive solute

$\mathbf{g}$ = gravity vector

P = pressure

c = concentration of nonreactive solute

D = diffusion coefficient

The independent variables in the problem are spatial coordinates of the domain, and time. The dependent variables in the problem are the pressure, density and concentration.

5.3.2.2 Mathematical Formulation for Reactive Process

Apart from N-S equations for flow of incompressible fluid and uniform density, the presence of chemical species such as CO_2 causes chemical reactions and the accompanying transport of charged species governed by molecular diffusion, electrical

coupling forces and chemical reactions. The transport by molecular diffusion in a non-ideal system with reactive species is accounted for by adding a non-ideal term with activity coefficient. The activity coefficients for nonreactive species are assumed to be one. The mathematical formulation describing transport of reactive species is given by Eqn. (5.2).

$$\left.\begin{aligned}
&\frac{\partial \mathbf{v}}{\partial t} = -\frac{1}{\rho}\nabla P + \frac{\mu}{\rho}\nabla^2 \mathbf{v} + \mathbf{g} \\
&\nabla.\mathbf{v} = 0 \\
&\frac{\partial c_i}{\partial t} = \left(\frac{\partial c_i}{\partial t}\right)_{\text{diffusion}} + \left(\frac{\partial c_i}{\partial t}\right)_{\text{electrical coupling}} + \left(\frac{\partial c_i}{\partial t}\right)_{\text{chemical reactions}} \\
&\left(\frac{\partial c_i}{\partial t}\right)_{\text{diffusion}} = D_i\left(\nabla^2 c_i + \nabla.\left(c_i \nabla \ln \gamma_i\right)\right) \\
&\left(\frac{\partial c_i}{\partial t}\right)_{\text{electrical coupling}} = -\lambda z_i c_i \\
&\lambda = \frac{\sum_i^N z_i c_i + \Delta t \sum_i^N z_i \left(\frac{\partial c_i}{\partial t}\right)_{\text{diffusion}}}{\Delta t z_i^2 c_i}
\end{aligned}\right\} \qquad (5.2)$$

where,

c_i = concentration of species *i*

D_i = diffusion coefficient of species *i*

γ_i = activity coefficient of species *i*

z_i = charge of species *i*

5.3.2.3 Modified Moving Particle Semi-Implicit (MMPS) Formulation

MMPS is a Lagrangian particle-based technique, that can model the flow of incompressible and compressible fluids inside high resolution images of the pore space

(Ovaysi and Piri 2010) as shown in Figure 5-2. Before performing the MMPS simulation, the reconstructed porous media needs to be discretized into particles as described earlier and a particle search in the neighborhood of all individual particles is performed. Then the pressure projection is used on the Lagrangian version of the governing equations (i.e. N-S equations) to estimate the velocity and pressure fields in the system. This is done by splitting the velocity into the explicit and implicit parts ($\mathbf{v_E}$ and $\mathbf{v_I}$, respectively), whereas the pressure field is splitted into static and dynamic pressures (P_s and P_d, respectively) as shown:

$\mathbf{v} = \mathbf{v_E} + \mathbf{v_I}$, and

$P = P_s + P_d$

Employing the explicit and implicit velocities in the governing equations lead to:

$$\frac{\partial \mathbf{v_E}}{\partial t} = -\frac{1}{\rho}\nabla P_s + \frac{\mu}{\rho}\nabla^2 \mathbf{v} + \mathbf{g}$$

$$\frac{\partial \mathbf{v_I}}{\partial t} = -\frac{1}{\rho}\nabla P_d$$

The term static pressure is used for the pressure caused solely due to external pressures such as upstream and downstream pressures, whereas the term dynamic pressure is used for the pressure caused by the dynamic movement of fluid. The solutions to the dynamic and static pressures are obtained using the following equations:

$$\nabla^2 P_d = \frac{\rho}{\Delta t}\nabla . \mathbf{v_E}$$

$$\nabla^2 P_s = 0$$

This information about velocity and pressure fields is then used subsequently to move the fluid particles at each time step following which a new neighborhood particle

search is carried out depending on how fast the particles move. In the context of computational expense, the speed of MMPS simulations is comparable to the speed of traditional CFD methods such as finite volume method.

For further discussion on the MMPS method and values of the parameters used in above mathematical formulations the reader can refer to Ovaysi and Piri (2010; 2011; 2013).

5.3.3 Scale-up Analysis

The variance of the mean of different attributes from conservative and reactive processes was computed assuming linear averaging. As mentioned earlier in this dissertation, the variance of the mean of any attribute can be computed on a 3-D space-time basis by evaluating the space-time integrals of the spatiotemporal covariance function:

$$Var(\overline{f}) = \frac{2\sigma^2}{(V)^2}\left(\int_{\zeta_3=0}^{\zeta_3=H} \int_{\eta_3}^{\eta_3=\zeta_3} \int_{\zeta_2=0}^{\zeta_2=B} \int_{\eta_2}^{\eta_2=\zeta_2} \int_{\zeta_1=0}^{\zeta_1=L} \int_{\eta_1}^{\eta_1=\zeta_1} \rho_{corr}\left\{\eta_1(L),\eta_2(B),\eta_3(H)\right\} d\eta d\xi \right) \quad (5.3)$$

$$Var(\overline{f}) = \frac{2\sigma^2}{(V)^2}\left(\int_{\zeta_3=0}^{\zeta_3=T} \int_{\eta_3}^{\eta_3=\zeta_3} \int_{\zeta_2=0}^{\zeta_2=B} \int_{\eta_2}^{\eta_2=\zeta_2} \int_{\zeta_1=0}^{\zeta_1=L} \int_{\eta_1}^{\eta_1=\zeta_1} \rho_{corr}\left\{\eta_1(L),\eta_2(B),\eta_3(T)\right\} d\eta d\xi \right) \quad (5.4)$$

where,

σ^2 = variance of attribute f

ρ_{corr} = spatial autocorrelation function

η = all possible lags within the spatiotemporal region

V = Volume over which scale-up is investigated

(for 3D spatial volume and spatiotemporal volume, V is $L \times B \times H$ and $L \times B \times T$, respectively)

L = length

B = breadth

H = height

T = total time of spatiotemporal region

This variance of the mean concept represented by Eqn. (5.3) and (5.4) is used to analyze the scaling characteristics of the conservative and reactive processes using the pore scale experimental data. Variance of the mean of concentration is computed numerically by averaging the experimental data directly over the spatial (or temporal) domain. We also compute the variance of the mean concentration by performing the convolution integral of the variogram obtained using the experimental data. Theoretically, the variance of the mean plot computed using either LHS or RHS of the variance formulation should be similar; however, there is usually some difference in the two results because of error in performing the numerical integration and also in approximating the empirical variograms using simplified positive definite variogram models.

5.4 DATA

Concentration data for both the conservative process and reactive process is available in the form of point estimate values and we interpolate the scatter data using Delaunay triangulation technique from Matlab® function directory ("TriScatteredInterp" R2013b) to obtain gridded data. Gridded data renders the task of variogram inference and modeling easier. Delaunay triangulation for a set of points is a technique by which only one circle can be circumscribed about each triangle and it is ensured that no point is contained inside the circumcirle associated with each triangle. Delaunay triangulation avoids narrow angled triangles and it maximizes minimum limit of all the angles of the triangles in the triangulation. This technique can be used to perform interpolation of a set of point data to a 2-D or 3-D grid.

5.4.1 Conservative Process (Advection-Diffusion)

The scatter of pressure in 3-D space for a conservative process is shown in Figure 5-3. We interpolate this scatter data as explained above to obtain the corresponding gridded which is shown in Figure 5-4.

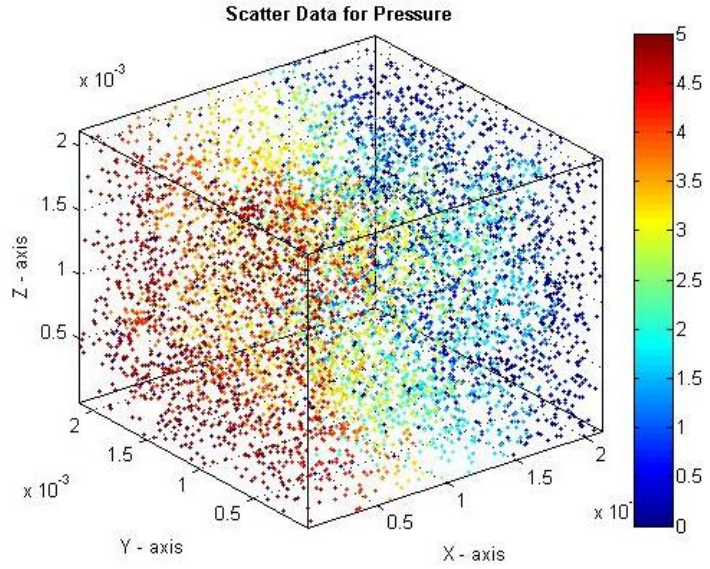

Figure 5-3: Scatter dataset of pressure (in MPa) in 3-D space

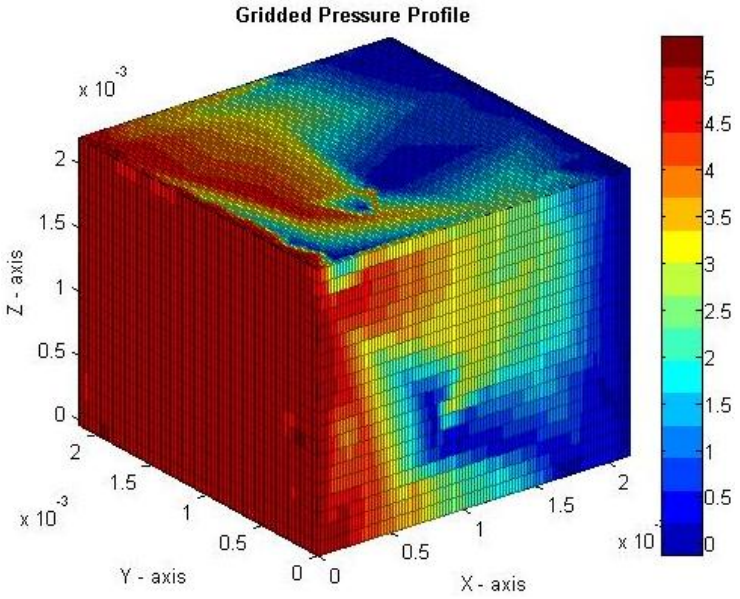

Figure 5-4: Gridded dataset of pressure (in MPa) in 3-D space

5.4.2 Reactive Process

Scatter data of three attributes, which are: 1) pore geometry alteration data (legend = 0, 1 for matrix and fluid, respectively) - this attribute is hereby denoted as PGA, and 2) dissolution due to change in porosity i.e. $1-\Delta\phi/\phi$ - this attribute is hereby denoted as CIP, and 3) volume-based dimensionless CO_2 concentration - this attribute is hereby denoted as CO2CONC, is shown in Figure 5-5. These are corresponding to the reactive process for time t = 20 sec in 3-D porous medium space. Since attribute PGA is just a spatial representation of fluid or matrix, it does not have any physical unit. The dissolution data denoted by CIP is a fraction of change in porosity, therefore, it does not have any physical unit. For example, CIP = 1 denotes no change in matrix mass compared to its initial mass, and CIP = 0 denotes that there is no remaining mass of matrix as the entire matrix has dissolved into fluid. We interpolate this scatter data using the Delaunay triangulation technique as explained earlier to obtain the corresponding gridded data of PGA, CIP and CO2CONC as shown in Figure 5-6. The grid sizes of the gridded data in X, Y and Z directions are 100, 100 and 20, respectively.

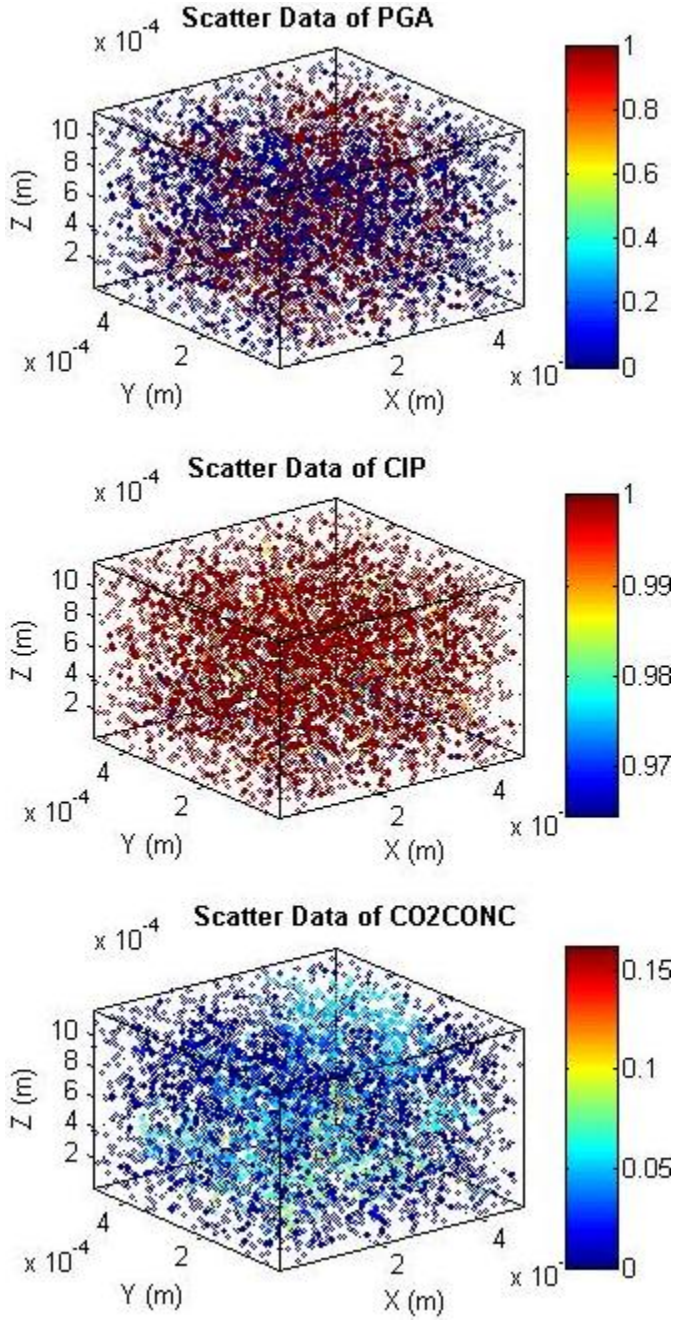

Figure 5-5: Scatter dataset of pore geometry alteration PGA (top), change in porosity CIP (middle) and concentration of CO2 - CO2CONC (bottom) in 3-D space.

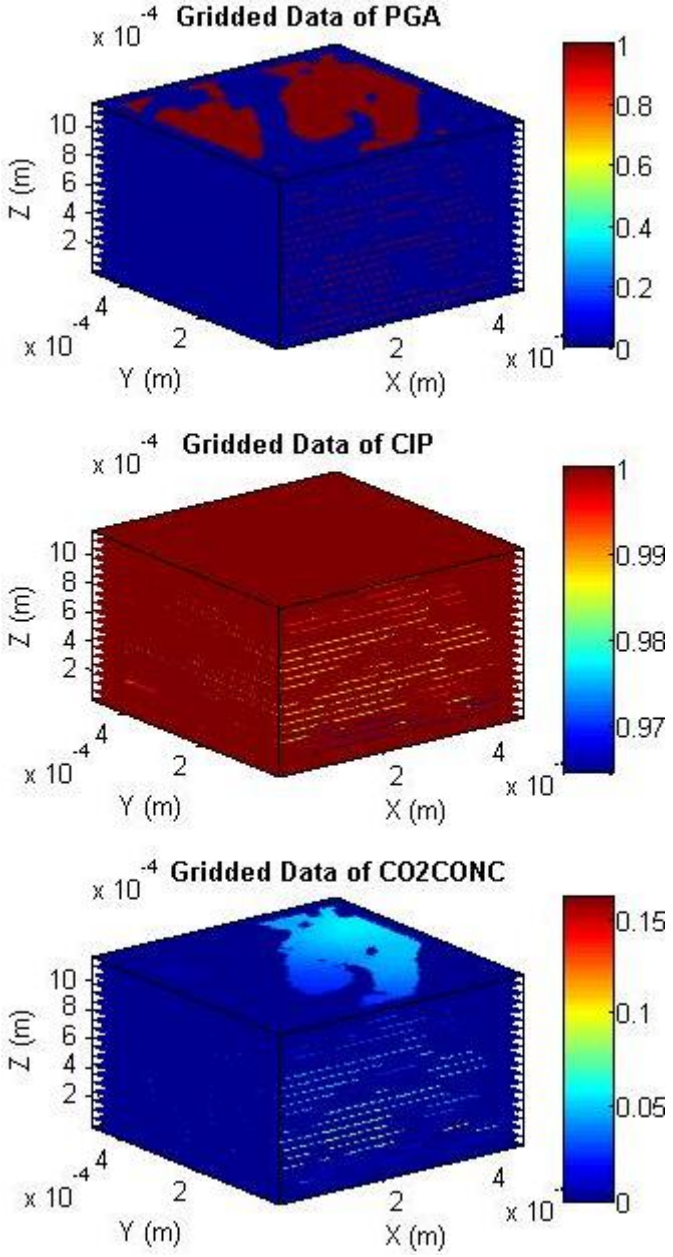

Figure 5-6: Gridded dataset of PGA (top), CIP (middle) and CO2CONC (bottom) computed in 3-D space

Since we are interested in temporal changes due to reactive process, therefore, we interpolate the 3-D spatial binary datasets for all times from t = 0 sec till t = 20 sec. Interpolation is done on scatter datasets of all three attributes which are fluid/matrix pore geometry alteration (denoted as PGA), dissolution due to change in porosity i.e. $1-\Delta\phi/\phi$ (denoted as CIP), and volume-based dimensionless CO_2 concentration (denoted as CO2CONC), corresponding to the reactive process for all times from t = 0 sec till t = 20 sec. Figure 5-7, Figure 5-8 and Figure 5-9 show gridded 3-D spatial data at various times for PGA, CIP and CO2CONC, respectively. The grid sizes of the gridded data in X, Y and Z directions are 100, 100 and 20, respectively.

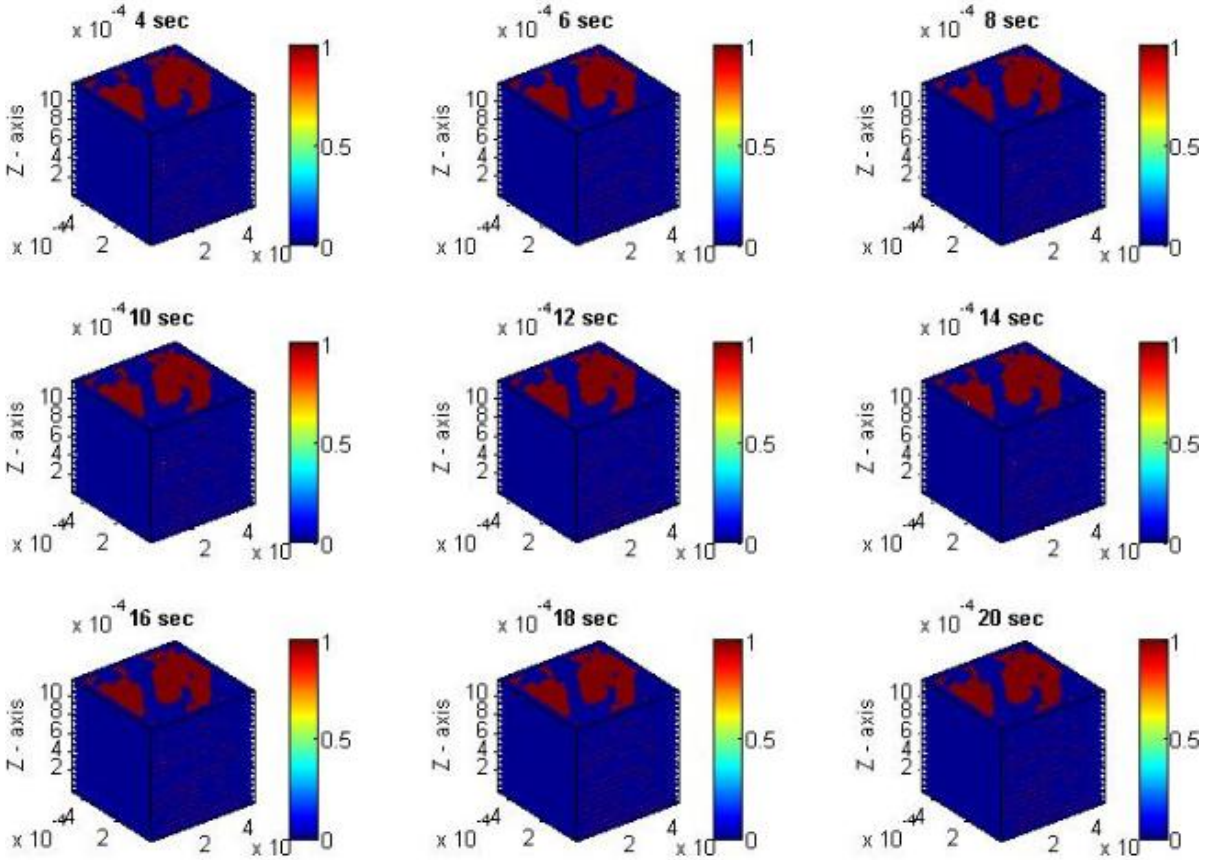

Figure 5-7: Gridded 3-D spatial data for pore geometry (legend = 0, 1 for matrix and fluid, respectively) alteration (denoted as PGA) at all times

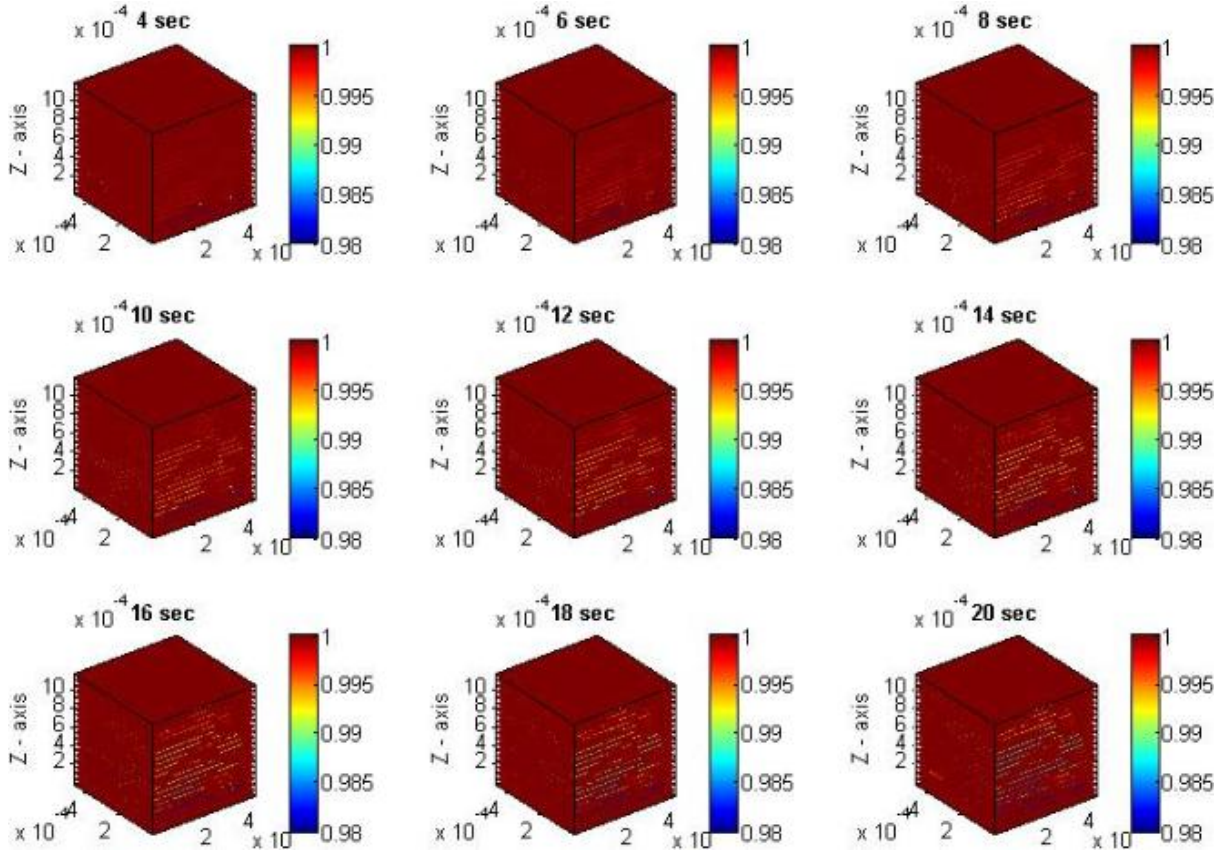

Figure 5-8: Gridded 3-D spatial data for dissolution due to change in porosity (denoted by CIP) at all times

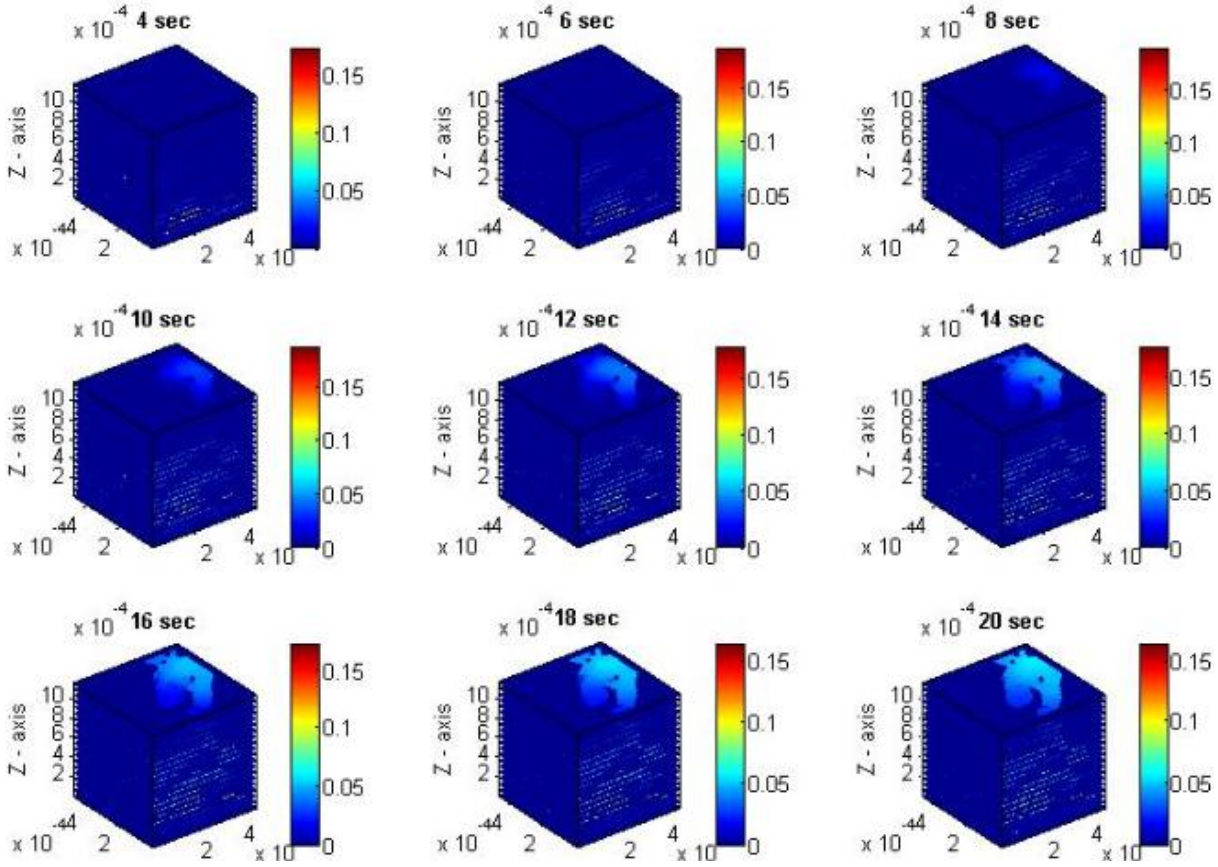

Figure 5-9: Gridded 3-D spatial data for volume-based dimensionless CO_2 concentration (denoted by CO2CONC) at all times.

To analyze the above 3-D spatial data at various times, we choose three XY planes from the 3-D spatial data corresponding to the reactive process. These slices exhibit the maximum spatial variation in values. For each 2-D slice, we consider the variation over all time periods. We thus get a 3-D spatiotemporal dataset, where the 3rd dimension now represents time. Figure 5-9 shows the spatiotemporal data for the three different quantities (fluid/matrix denoted by PGA, $1-\Delta\phi/\phi$ denoted by CIP and volume-based dimensionless CO_2 concentration denoted by CO2CONC, respectively)

corresponding to the reactive process. Each column in Figure 5-10 shows the spatial distribution of a particular parameter (PGA, CIP or CO2CONC) along different slices through the 3D model and its evolution with time. The concentration variations along slices Z = 2, 3 and 4, respectively are shown.

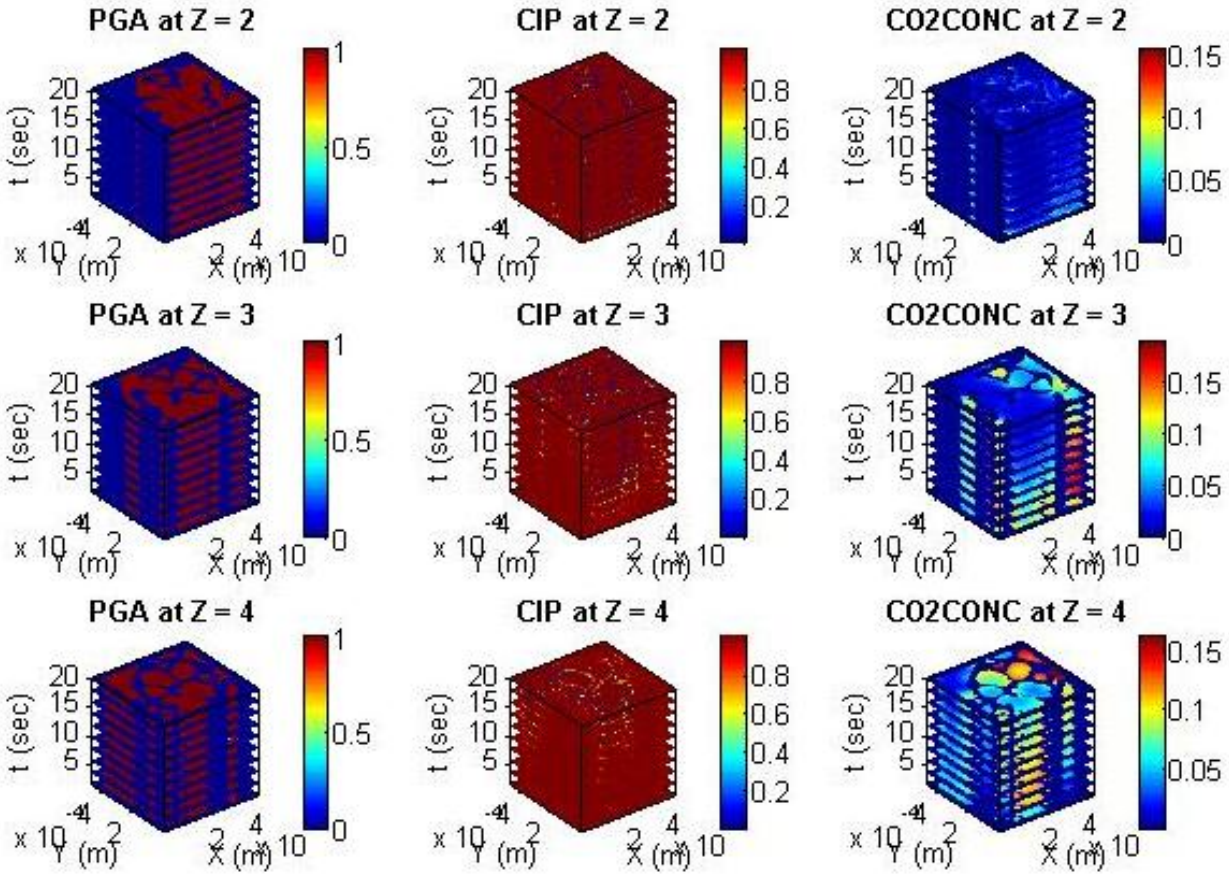

Figure 5-10: Gridded spatiotemporal variation of pore geometry alteration (PGA), change in porosity (CIP) and CO2CONC corresponding to a reactive transport process is shown.

5.5 RESULTS AND DISCUSSION

We compute the scaling characteristics of conservative flow as well as reactive flow due to injection of CO_2 for the exactly same porous medium. The REV for conservative process is computed using the 3-D pressure data while the REV for reactive process is computed using three different types of data - fluid/matrix pore geometry alteration (PGA), dissolution data (CIP) and volume-based dimensionless CO_2 concentration – all for the 3-D spatiotemporal volumes previously described. We first compute the variograms of these variables and subsequently model them using the geostatistical software library GSLIB (Deutsch and Journel 1997).

Results of the scale-up computations are presented and compared with discussions. Finally, the importance of this research work is highlighted.

5.5.1 Conservative (Advection-Diffusion) Process

5.5.1.1 Scale-up Using Variogram

We compute empirical variograms along various directions using the 3-D spatial gridded data of pressure from Figure 5-4. Empirical variograms for regularly spaced gridded data were computed using *gam* program of GSLIB library (Deutsch and Journel 1997). The empirical variograms along various azimuth (θ) and dip (ϕ) angles are shown in Figure 5-11 and a 2-D variogram slice through the 3-D modeled variogram is shown in Figure 5-12. It is apparent from Figure 5-11 that empirical variograms of the pressure attribute in the case of a conservative/nonreactive flow are nonstationary, and therefore, empirical variograms are fitted using a nested structure of *spherical* and *power* models.

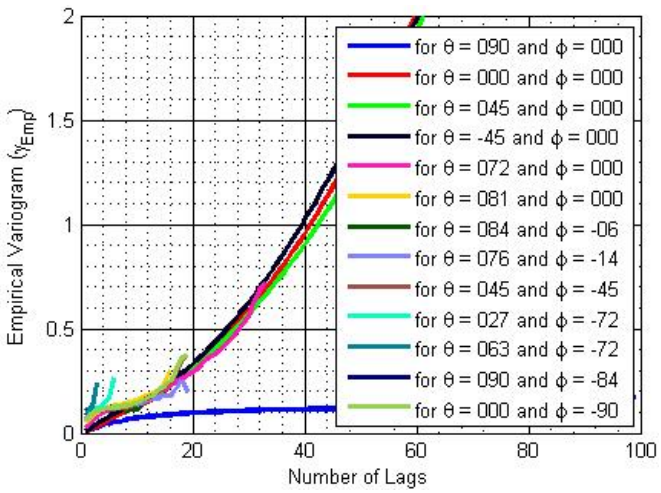

Figure 5-11: Empirical variograms for 3D spatial data for pressure

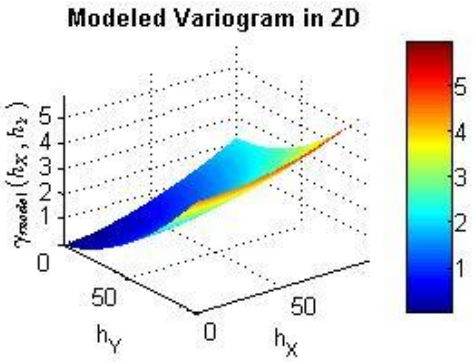

Figure 5-12: A projection through the 3-D variogram model computed using the spatiotemporal data for pressure

Figure 5-13 shows the variance of the mean computed by evaluating the convolution integral of the spatiotemporal variogram function for pressure data over all spatial lag scales. Figure 5-13 shows a surface plot of spatial variance plotted purely as a function of spatial lags.

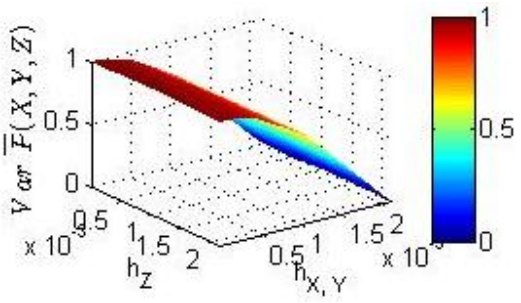

Figure 5-13: Variance of mean pressure computed by evaluating the spatiotemporal integral of the model covariance

The variance of the mean pressure along the diagonal of the surface plot is shown in Figure 5-14. This plot depicts a diagnostic signature of negative unit slope at scales larger than and equal to REV scale. The scale at which the slope along this diagnostic plot reaches -1 provides us the volumetric REV scale and for this case it is achieved for a volume of ~10^{-10} m^3 or 0.1 mm^3 (=h_X X h_Y X h_Z).

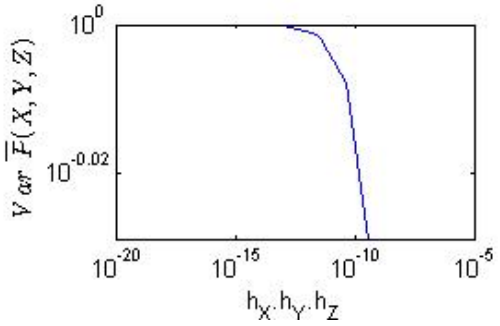

Figure 5-14: Variance of the mean along the diagonal of the plot shown in Figure 5-13

5.5.1.2 Scale-up Using Averaging

5.5.1.2.1 Linear Averaging

For comparison, we compute the REV by directly computing the variance of the average of the pressure data (without computing the covariance or variogram). For this

we first estimate the upscaled pressure using linear (arithmetic) averaging. The upscaled pressure using linear averaging is obtained for various spatial lags; for example, Figure 5-15 shows upscaled 3-D pressure for two different grid sizes:

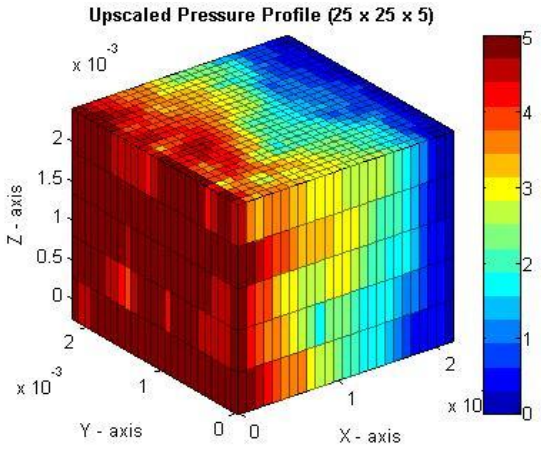

(a)

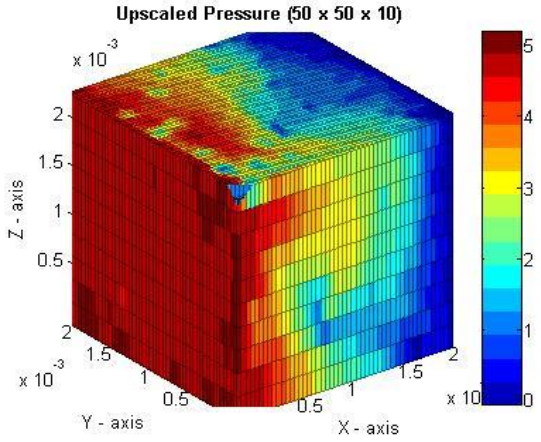

(b)

Figure 5-15: Upscaled pressure using linear averaging for grid sizes of a) 25 X 25 X 5, b) 50 X 50 X 10

The variance of mean computed using linear averaging of pressure data can be plotted against the spatial lags. Figure 5-16 shows the purely spatial variance in the form of a surface plot similar to Figure 5-13.

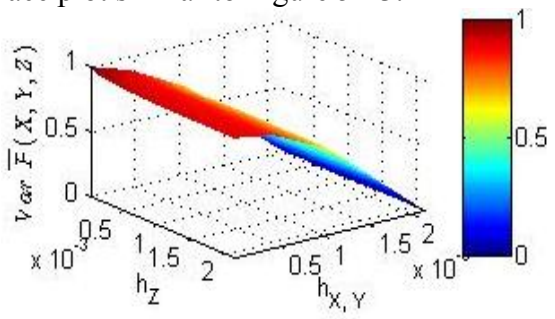

Figure 5-16: Variance of mean pressure computed directly using the pressure values available at the pore scale.

The variance along the diagonal of the surface plot of Figure 5-16 is shown in Figure 5-17.

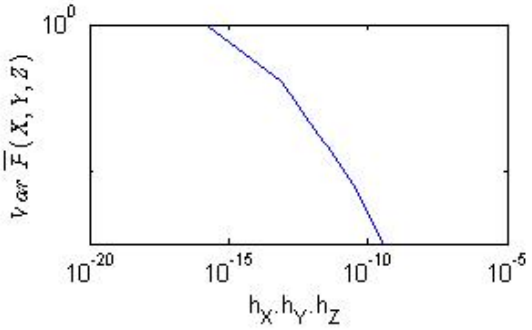

Figure 5-17: Variance of mean pressure extracted along the diagonal of the surface plot shown in Figure 5-16

We compare the REV scale obtained using both the spatial integration of the variogram as well as the direct averaging of pressure values. While there is some difference in the two results because of the error in performing numerical integration and also in approximating empirical variograms using standard models, the overall profiles

are quite similar. These profiles indicate that the stable REV scale for this process occurs for a volume of ~10^{-10} m^3 or 0.1 mm^3 (=h_X X h_Y X h_Z).

5.5.1.2.2 Nonlinear Averaging

In order to see the effect of nonlinear averaging on the REV, we compute the REV using the nonlinear averaging of the pressure data (without computing the covariance or variogram) and compare it with the REV computed using linear averaging and shown in Figure 5-17. The upscaled pressure is computed using the averaging formulation depicted in Eqn. (5.5) where the value of averaging exponent for nonlinear averaging is assumed as 0.5:

$$\bar{P} = \left[\frac{1}{V_b} \int_{V_b} (P)^{\omega} \, dV \right]^{1/\omega} = \left[\frac{1}{V_b} \sum_Z \sum_Y \sum_X \{P(X,Y,Z)\}^{\omega} \right]^{1/\omega} \tag{5.5}$$

where,

$P(X,Y,Z)$ = Fine scale gridded pressure data

$\bar{P}$ = Upscaled pressure

V_b = Coarse block bulk volume

ω = Averaging exponent (assumed 0.5 for nonlinear averaging)

The upscaled pressure using nonlinear averaging are obtained for various spatial lags; for example, Figure 5-18 shows upscaled 3-D pressure for two different grid sizes. These upscaled pressures computed using nonlinear averaging are very similar in profiles to the upscaled pressure computed using linear averaging and shown in Figure 5-15. The upscaled pressures obtained from linear and nonlinear averaging as shown in Figure 5-15 and 5-18, respectively, are very similar even on fine scale where grid size is 50 x 50 x 10.

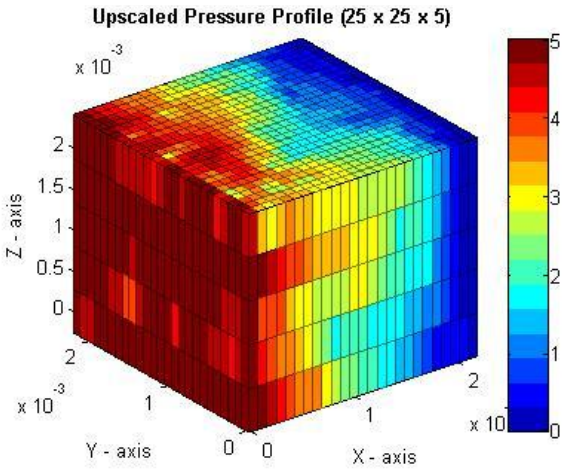

(a)

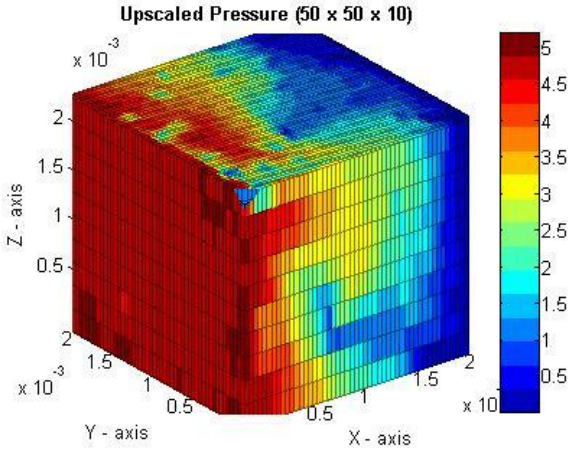

(b)

Figure 5-18: Upscaled pressure using nonlinear averaging for grid sizes of a) 25 X 25 X 5, b) 50 X 50 X 10

The purely spatial variance of mean computed using nonlinear averaging is shown in Figure 5-19 in the form of a surface plot similar to Figure 5-16.

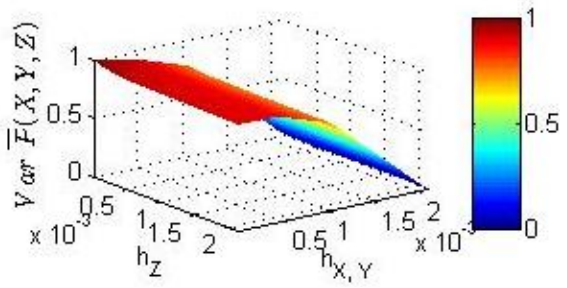

Figure 5-19: Variance of mean pressure computed directly using the pressure values available at the pore scale.

The variance along the diagonal of the surface plot of Figure 5-19 is shown in Figure 5-20.

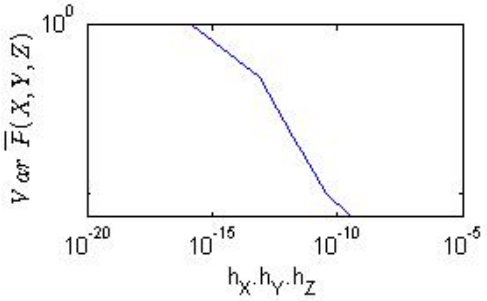

Figure 5-20: Variance of mean pressure extracted along the diagonal of the surface plot shown in Figure 5-19.

We compare the REV scale obtained using linear averaging and nonlinear averaging of pressure values. While there is a very slight different difference in the two upscaled results because of the averaging exponent, the overall profiles and REV scales are quite similar. The stable REV scale obtained from both linear averaging and nonlinear averaging occurs for a volume of ~10^{-10} m^3 or 0.1 mm^3 (=h_X x h_Y x h_Z).

Since we have established that the direct averaging (linear or nonlinear) as well as the integration of variogram (or covariance) gives similar results, therefore, in the

remaining part of the chapter we only show the results obtained by integrating the variogram, except where the variogram cannot be modeled accurately to represent the variance of the mean.

5.5.2 Reactive (Advection-Diffusion-Reaction) Process

5.5.2.1 Scale-up Using Variogram

We compute empirical variograms along several spatial and temporal lags using the 3-D spatiotemporal data of Figure 5-10. The empirical variograms of pore geometry alteration (PGA), dissolution due to change in porosity (CIP), and volume-based dimensionless CO_2 concentration (CO2CONC) from Figure 5-10 are shown in Figure 5-21 only along a few select directions. It is apparent from Figure 5-21 that empirical variograms of all three attributes for reactive flow are stationary, and therefore, empirical variograms for all three attributes are fitted using a *spherical* model. The corresponding spatiotemporal variogram models for all three attributes are shown in Figure 5-22.

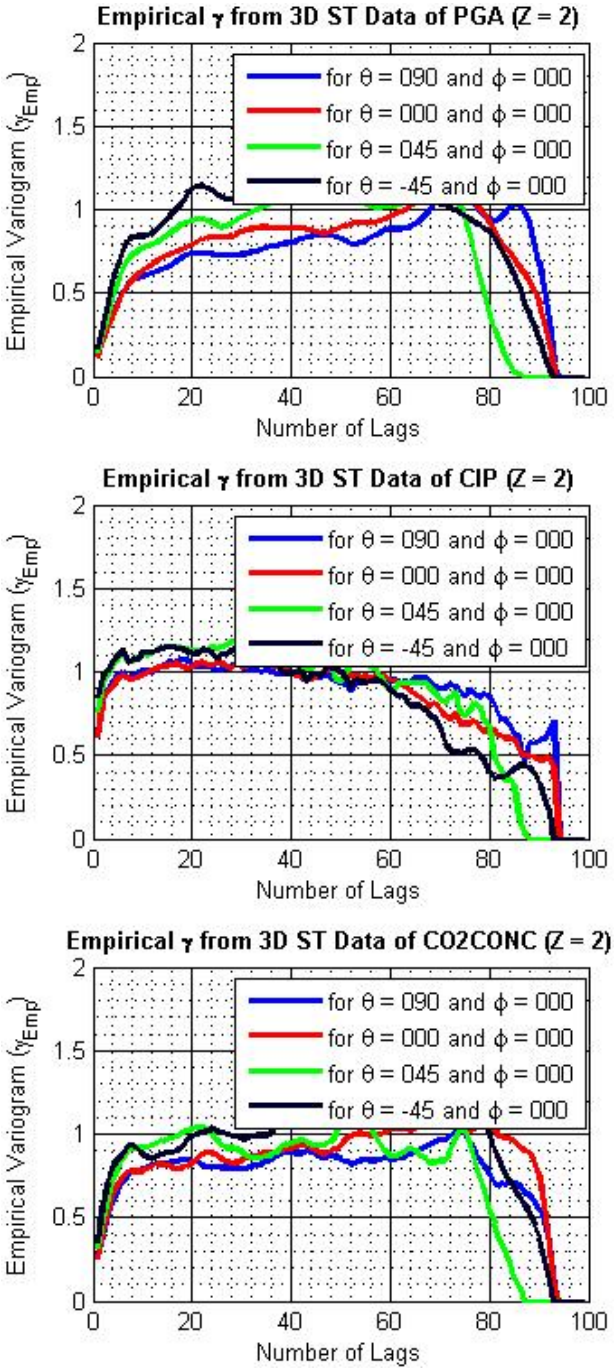

Figure 5-21: Empirical variograms of PGA (top), CIP (middle) and CO2CONC (bottom) computed using spatiotemporal data for the reactive process along a few select directions.

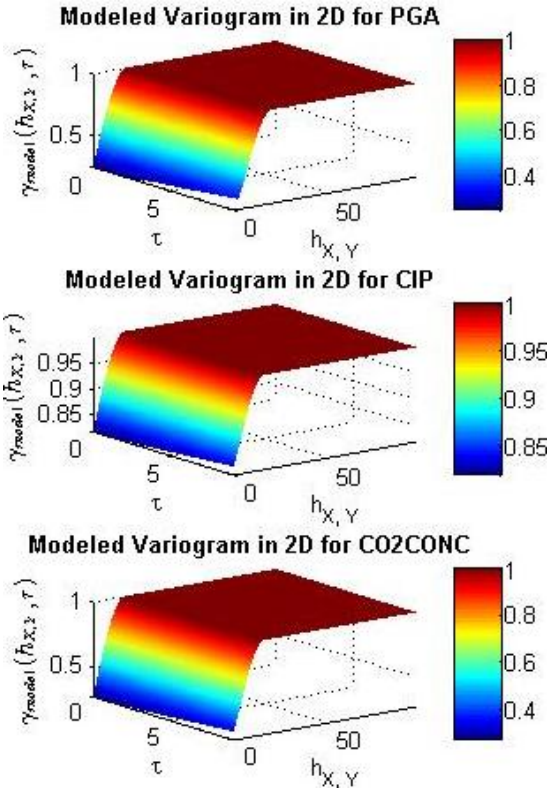

Figure 5-22: Spatiotemporal variogram models for PGA (top), CIP (middle) and CO2CONC (bottom)

Figure 5-23 through Figure 5-25 show the spatiotemporal variance of the mean plots computed by performing the integration of the spatiotemporal variogram function over all spatial and temporal lags. Results for Figure 5-24 are divided into two figures - Figure 5-24(a) obtained by the integration of the spatiotemporal variogram function over all spatial and temporal lags, and Figure 5-24(b) obtained by directly using the CIP data available at the pore scale. This exception of showing variance of mean by two methods in Figure 5-24 is made because the spatiotemporal variogram could not be modeled accurately for the CIP data to represent the variance of the mean.

The spatiotemporal variance of mean plots from Figure 5-23 through Figure 5-25 are for the three attributes – fluid/matrix pore geometry alteration (PGA), dissolution due to change in porosity (CIP) and volume-based dimensionless CO_2 concentration, respectively. Each of these three figures also shows a section along the diagonal of the surface plot. The results in Figure 5-23 through Figure 5-25 show that the curvature of the variance of mean profile at higher temporal lags differs significantly from the curvature at small temporal lags, which indicates that the REV scale (scale at which slope of curvature reaches -1) changes with time. This temporal change in REV is possibly due to the alteration in pore structure by the reactive processes, such as those associated with CO_2 storage in geological formations. This suggests that it's important to consider both spatial and temporal scales when considering determining an accurate REV scale.

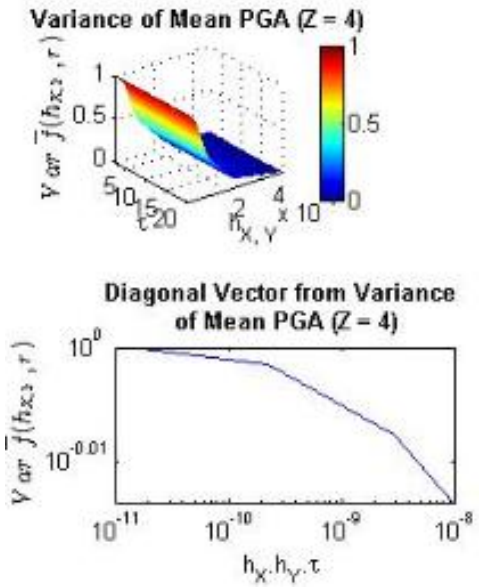

Figure 5-23: Spatiotemporal variance of mean PGA by performing space-time integration of the spatiotemporal variogram model over spatial and temporal lags.

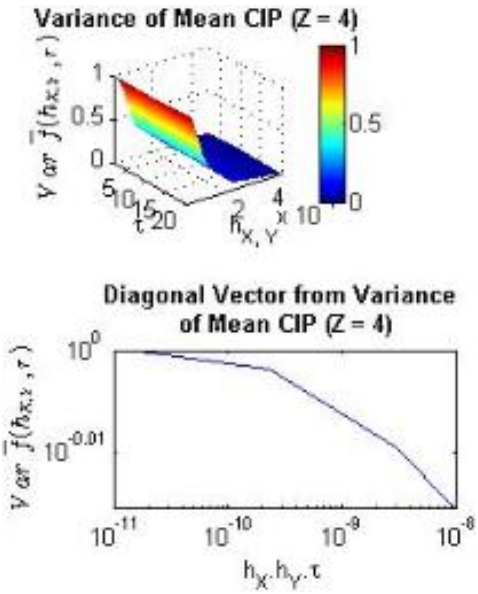

Figure 5-24(a): Spatiotemporal variance of mean CIP by performing integration of the spatiotemporal variogram model over spatial and temporal lags.

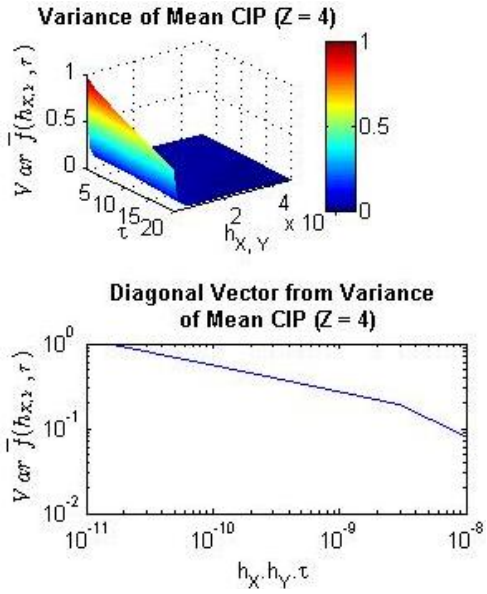

Figure 5-24(b): Spatiotemporal variance of mean CIP by directly using the CIP data available at the pore scale.

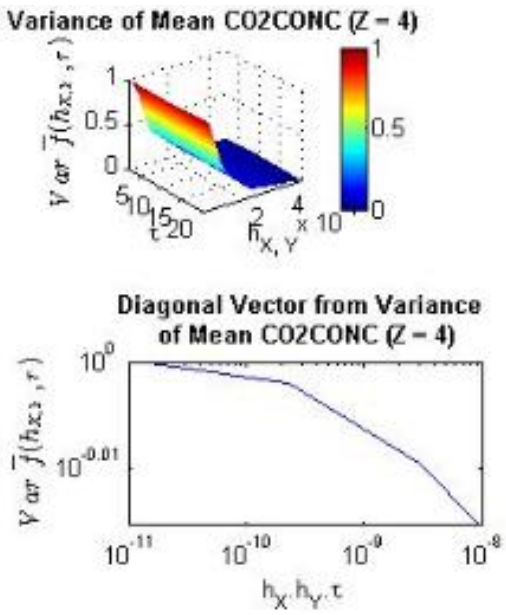

Figure 5-25: Spatiotemporal variance of mean CO2CONC by performing integration of the spatiotemporal variogram model over spatial and temporal lags.

The REV profiles indicate that the stable REV scale for two attributes PGA (Figure 5-23) and CO2CONC (Figure 5-25) occur for a spatiotemporal volume of ~3 X 10^{-9} m^2-sec or 3 X 10^{-3} mm^2-sec (=h_X X h_Y X τ), whereas, the stable REV scale for the attribute CIP (Figure 5-24(b)) occurs for a spatiotemporal volume of ~10^{-8} m^2-sec or 10 mm^2-sec (=h_X X h_Y X τ). The reason why the two attributes of PGA and CO2CONC show similar scaling behavior is because CO2CONC is a fluid which occupies pore space, and hence, it probably acts as a proxy for pore space, whereas the actual pore space data is also available and represented by attribute PGA in this work. However, attribute CIP scales differently than the other two attributes because dissolution is a

complex function of fluid composition, rock mineralogy and reservoir conditions. Also, the REV scale of attribute CIP is greater than the REV scale of other two attributes (PGA and CO2CONC) because dissolution alters the pore structure, therefore, introducing more heterogeneity into the porous medium which translates into higher REV scale.

5.5.3 Reaction Rate Constant

The available pore-scale reactive attribute data is used to obtain a tangible parameter such as reaction rate constant which has relevance in modeling reactive transport. Reaction rate constant is then scaled-up to a spatiotemporal REV scale through statistical approach. The reaction rate constant averaged in space and time over this spatiotemporal REV scale has the minimum uncertainty (variance) when specified to the numerical simulation model for a reactive transport process. This scaled-up reaction constant can serve as an effective quantity which can be employed in reactive flow transport simulations.

5.5.3.1 Derivation of Fine-Scale Reaction Rate Constant

For a chemically and physically heterogeneous subsurface system, the reaction rate term can be highly empirical and a function of many parameters. Reaction rate equation shows the effect of concentrations (of reactants), temperature, pressure, pH etc on the rate of the reaction. For example, for typical CO_2 mineral trapping reactions, the reaction rate could be a function of reactive surface area, activation energy, temperature, pH etc. to name the few. Liu and Maroto-Valer (2011) have discussed the effect of a few parameters on reaction rate that could help shorten the time of initiation of mineral

trapping mechanism. For example high pH, high reservoir temperature and high pressure favor the precipitation of mineral carbonates. However, for sake of simplicity in demonstrating the scale-up of reaction rate constant let us assume a first order reaction that depends only on the concentration of one reactant, for example CO_2, such that the reaction rate (or rate law) for that reaction with respect to CO_2 concentration is:

$$r = \alpha[c] \tag{5.6}$$

Using the first order rate law shown in Eqn. (5.6) we can derive an expression for reaction rate constant in terms of concentration and time (Lake et al. 2002) as following:

$$\because\ r = -\frac{dc}{dt}$$

$$\Rightarrow -\frac{dc}{dt} = \alpha c \Rightarrow -\int_{c=c_{ic}}^{c=c} \frac{dc}{c} = \alpha \int_{t=0}^{t=t} dt \Rightarrow -[\ln(c) - \ln(c_{ic})] = \alpha[t-0] \Rightarrow -\ln\left[\frac{c}{c_{ic}}\right] = \alpha t$$

$$\therefore \Rightarrow \alpha = -\frac{\ln\left[\frac{c}{c_{ic}}\right]}{t} \tag{5.7}$$

where,

r = reaction rate

α = reaction rate constant

c = volume-based dimensionless concentration of CO_2 at time t

c_{ic} = volume-based dimensionless initial concentration of CO_2 at time t = 0

The pore scale CO_2 concentration data presented earlier in the chapter varies in space and time, and therefore, the derived reaction rate constant which is a function of concentration will also vary two dimensionally in space and time. However, for reactive transport simulations we typically require only a single value of reaction rate constant

which is representative of the field scale conditions and that has minimum uncertainty due to subscale processes both in space and time.

Using the derived expression of reaction rate constant, Eqn. (5.7), and the pore scale CO_2 concentration data we can scale-up the reaction rate constant as demonstrated in the following section.

5.5.3.2 Scale-up of Reaction Rate Constant Using Averaging

We compute the REV of reaction rate constant by using the variance of the mean concept described earlier for which we require upscaled reaction rate constant on spatial and temporal scales. We can upscale reaction rate constant in space and time using the following two methods:

i. Method-1: First upscale the concentration data by taking linear averages for a particular coarse block size of spatial and temporal grids. Let's say the resultant upscaled concentration value obtained is $\bar{c}(s;t)$. Now substitute $\bar{c}(s;t)$ in Eqn. (5.8) to compute the upscaled reaction rate constant, $\bar{\alpha}(s;t)$. Repeat this procedure by increasing the coarse block size of spatial and temporal grids to obtain upscaled reaction rate constant for various coarse block sizes of spatial and temporal grids.

$$\bar{\alpha}(s;t) = -\frac{\ln\left[\dfrac{\bar{c}(s;t)}{c_{ic}}\right]}{t} \tag{5.8}$$

ii. Method-2: Compute the fine scale reaction rate constant, $\alpha(s;t)$, by substituting the fine scale concentration data, $c(s;t)$, in Eqn. (5.7). Now

upscale the fine scale reaction rate constant through linear averaging for various coarse block sizes of spatial and temporal grids.

Method-2 is not preferred in estimating the upscaled reaction rate constant because it assumes that the reaction constant averages linearly with space and time, which is not the case. Using the variance of mean concept we plot the reaction constant against the spatiotemporal lags as shown in the form of a surface plot in Figure 5-26. Each surface plot in Figure 5-26 corresponds to the CO_2 concentration data (CO2CONC) at three different Z from Figure 5-10.

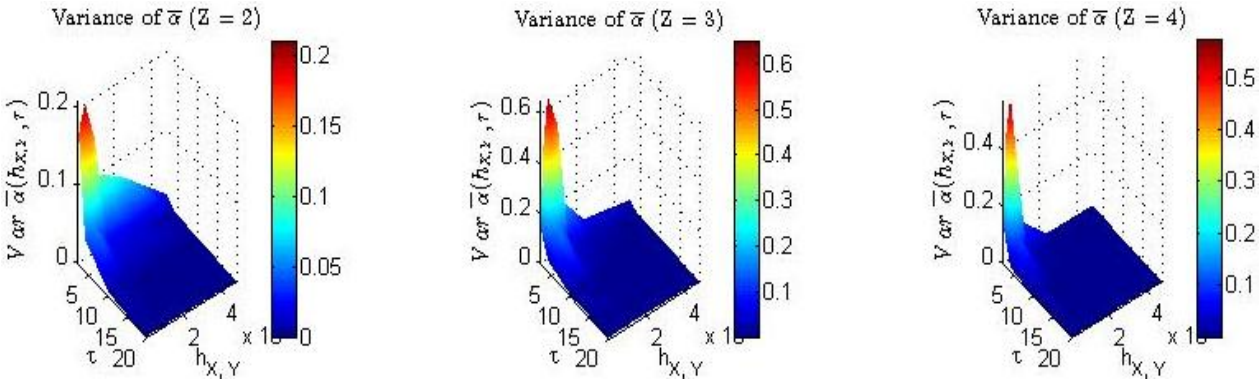

Figure 5-26: Variance of mean reaction rate constant computed using averaged concentrations corresponding to different spatial scales.

The spatiotemporal variance of the mean reaction rate constant along the diagonal of the surface plots are shown in Figure 5-27. The scale at which the variance of mean along these diagnostic plots reaches -1 provides us the spatiotemporal REV scale. The REV profiles indicate that the stable REV scale occur for a spatiotemporal volume of ~$4x10^{-9}$ m^2-sec or $4x10^{-3}$ mm^2-sec (=h_X x h_Y x τ).

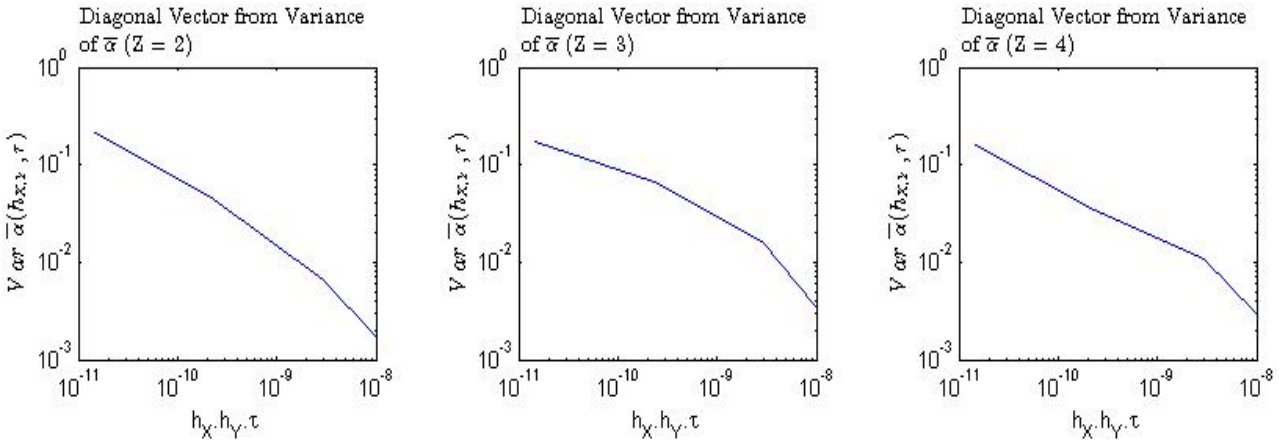

Figure 5-27: Variance of mean reaction rate constant computed using averaging Method-1.

The REV spatiotemporal volume of ~4X10^{-9} m^2-sec for reaction rate constant (Figure 5-27) and the REV spatiotemporal volume of ~3X10^{-9} m^2-sec for CO_2 concentration (Figure 5-25) are almost similar. This similarity in REVs of reaction rate constant and CO_2 concentration could be due to the fact that reaction rate constant in Eqn. (5.7) is a function of only one dependent variable which is concentration. If a reaction constant is a complex function of more than one dependent variable such as reactive surface area, temperature, pressure, pH etc, then it is possible that the REV scale of reaction constant may have a complex dependence on the REV scale of each dependent variable which forms the expression of reaction rate constant.

The purpose of computing REV scale of reaction constant is to obtain a single scaled-up value of reaction constant that can be used as input in reactive transport simulations. This scaled-up value of reaction constant will minimize the uncertainties arising due to sub-processes associated with reaction constant. We can minimize those uncertainties in two ways:

i. By utilizing the single scaled-up value of reactions constant at REV scale. For this, we simply take the combined space-time REV scale of reaction constant and split that combined spatiotemporal scale into individual spatial and temporal scales. Once we have the individual spatial and temporal scales which form the combined spatiotemporal REV scale of reaction constant, we use Method-1 described above to estimate the scaled-up single value of reaction constant.

ii. By selecting the magnitude of spatial and temporal discretizations for numerical simulations of reactive processes in a way that their product is equal to or greater than the REV scale of reaction constant.

5.6 CONCLUSIONS

The scaling characteristics of the conservative and reactive processes were investigated using high-resolution pore-scale data. The reactive transport process due to CO_2 migration in the subsurface was simulated on the actual pore scale representation of the rock and the simulated values were taken as the experimental information available. The results indicate that the scaling characteristic of reactive processes which alter pore structure is significantly different than the scaling characteristics of conservative processes. Due to this the REV scale for attributes associated with reactive process is higher than the REV scale for conservative process. Two attributes associated with reactive process (PGA and CO2CONC) show similar scaling behavior whereas the attribute CIP show a different scaling behavior than the other two attributes. Even though the spatiotemporal REV scale computed through the two attributes of PGA and

CO2CONC indicate structural changes in pores with time when compared to the REV scale computed from CIP attribute, they do not reveal complete information of structural changes in pore. This is because the additional increase in REV scale is revealed when computed using the attribute CIP, as compared to the REV scale computed using PGA or CO2CONC, and that could be because dissolution (denoted as CIP) is a complex function of fluid composition, rock mineralogy and reservoir conditions, which cannot be captured by two attributes of PGA and/or CO2CONC alone.

Two major implications resulting from the scale-up analysis using the available pore-scale experimental information of both conservative and reactive processes are that: 1) Only some selected attributes associated with reactive process (such as CIP here) can reveal the complete information about pore structural changes while other attributes (such as PGA and CO2CONC here) may reveal only partial information about pore structural changes, and 2) Scaling characteristic of reactive processes which alter pore structure with time is significantly different than the scaling characteristics of conservative processes and a robust assessment of REV should involve coupling of temporal scale with spatial scale.

The available pore-scale CO_2 concentration data was used in an equation derived from first order reaction rate law to obtain a tangible parameter such as reaction rate constant which has relevance in modeling reactive transport. The REV scale of reaction constant may have a complex dependence on the REV scale of each dependent variable which forms the expression of reaction rate constant. The scaled-up reaction rate constant averaged in space and time over its spatiotemporal REV scale provides one single value of reaction constant which has minimum uncertainty due to subscale spatial and temporal

processes. This scaled-up single value of reaction constant can be used as an input in reactive flow transport simulations.

Chapter 6: A Particle Tracking Approach for Analyzing Scale-up of Reactive-Diffusive Process in Heterogeneous Media

6.1 OVERVIEW

The flow of reactive fluids in porous media such as during CO_2 sequestration, chemical EOR etc. is inherently multi-physics and the processes occur over multiple temporal and length scales. In most cases, advection and diffusion are much slower temporal processes (years) than chemical reactions (minutes or hours), and spatially, advection and diffusion take place over the entire reservoir while chemical reactions in porous media occur locally around the reaction front (Lake et al. 2002). Reactions originate at nanoscale at which scale they are far from equilibrium, however, they are defined as complex emergent phenomena at field-scale (Deyoreo and Depaolo 2009). This has tremendous implication for scaling experiments performed at the laboratory bench-top characterized by a Damkohler number (Da) of the order of 10^3, to the field-scale where the time scale for the fluid flow to that of chemical reactions (Da) is about 10^7.

We need a method to scale-up such behavior across relevant scales of interest i.e. from laboratory scale to field-scale to accurately predict the behavior of reactive processes in porous media. Our objective is to understand, quantify and scale-up the behavior of reactive-diffusive processes in geologic media from continuum to field-scale. This study can also help answer several questions such as - 1) what is the most appropriate scale for an accurate description of reactive dynamics? 2) what is the impact

of heterogeneity and its uncertainties on reactive dynamics at field-scale? 3) which parameter plays an important role at different scales?

In practice the detailed behavior of reactive transport in porous media is studied using full-physics reactive transport simulations. Additionally, if we want to answer the questions described above then it will be computationally cumbersome to run full-physics reactive flow simulations to answer each question. Instead, a simplified scheme for multi-scale modeling can be used that includes the relevant physics and allows us to better understand the role of finer scales on the behavior of subsurface flow.

A probabilistic framework of particle tracking across multiple scales is used to answer some of these questions and to consistently evaluate the behavior of reaction dynamics across scales. This multi-scale modeling uses a hierarchical approach that is based on consistently modeling subsurface heterogeneity from the macro-scale down to the finer scales and then computing reactive flow parameters by executing a particle tracking algorithm on these representations of heterogeneity.

6.2 OBJECTIVE

In order to accurately characterize reactive processes there are two challenges that must be addressed: 1) incorporating consistent reservoir heterogeneity at all levels of scales, 2) accurate scale-up accounting for the multi-scale and multi-physics nature of diffusion-reaction system in heterogeneous medium. It has been difficult to address these two challenges using traditional volume-averaging or ensemble-averaging approaches based on partial differential equations (PDEs) with effective reaction and mass transfer parameters due to difficulty in treating heterogeneity at multiple scales. Also, large-scale

simulations in order to obtain fine grid information required for those approaches are computationally expensive to perform. A key contribution of this work is to address these two challenges using a particle tracking (PT) method and an algorithm which accounts for consistent reservoir heterogeneity at all scales through dispersion variance conditions and parameter matching scheme.

In particle tracking, particles are introduced numerically at an injection location into the media and the movement of these particles from one grid block to another grid block is ascertained using transition probabilities that are a function of space and time. Transition probabilities are calculated using an equation analogous to the solution of the diffusion-reaction equation and in addition the heterogeneity of the media is accounted for. In our approach, permeability of the reservoir is generated geostatistically using conditional sequential Gaussian simulations (Remy et al. 2009). Reservoir heterogeneity structure is consistently preserved at all scales by estimating downscaled covariance parameters (sill, min. range, and max. range) such that the dispersion variance (Journel and Huijbregts 2003) conditions are honored. A parameter matching scheme is also implemented to preserve the computed variances. We determine permeability models at ten increasing resolutions of scale by appropriately downscaling the covariance and thereby accomplish consistent heterogeneity across all scales.

To address the two challenges described above, several realizations of permeability at each scale are run through the particle tracking algorithm. The distribution of particles at the end of travel time is compared for all models and several statistical properties, including reaction surface area and mixing zone length (MZL), are derived to characterize the scaling of reactive-diffusive processes.

6.3 PARTICLE TRACKING

6.3.1 General Description

Particle tracking is used to model the impact of process parameters and heterogeneity characteristics on process performance and is alternative fast approximation to running full-physics reactive transport simulations. Particle tracking uses transition probability to move particles. Particles are introduced at an injection point into the reservoir and the movement of those particles from one grid block to another grid block is controlled by transition probabilities that are specified so as to mimic the physics of the transport process. The movement of particle from one grid block to the other is controlled by Monte-Carlo sampling of the transition probability distribution that is in turn governed by the flow characteristics (porosity, permeability) of the particular grid block. Transition probabilities are calculated using Eqn. (6.1) that mimics the solution of Fick's second law of diffusion, which describes the concentration at a certain distance from the injection point over time, in addition to accounting for non-Fickian transport by including the effect of disorder of heterogeneous permeable media.

$$\text{Prob}(\text{grid}_\text{A} \text{ to } \text{grid}_\text{B}) = \exp\left(-\bar{k}_{AB}\right) + \exp\left(-\frac{r_{AB}^2}{4Dt}\right) \tag{6.1}$$

where,

$\bar{k}_{AB}$ = harmonic mean permeability between grids A and B

r_{AB}^2 = product of distance from injection point to grids A and B

D = diffusion coefficient

t = time

For each grid block movement in space, the probability for particle remaining in the same block and for particle transitioning to all the neighboring grid blocks is calculated. In the case of a 2-D grid, there will be 4 neighboring blocks (as shown in

Figure 6-1) or 6 neighboring blocks in the case of a 3-D grid. The grid block location to which the particle is moved is then determined by Monte-Carlo sampling of this transition probability distribution. Each injected particle proceeds ahead under constraints specified by the transition probability until it arrives at a location where further transition to a neighboring block is not possible. This process of particle transitioning from one grid block to another grid block is repeated for all the injected particles at any time step. At the end of final time step, the particles are counted in every grid block which serves as an analogue for concentration. We run PT for a long time over which the reaction front stabilizes and irregularities in the fluid displacement front depend only on fluctuations of fluid velocities due to heterogeneities.

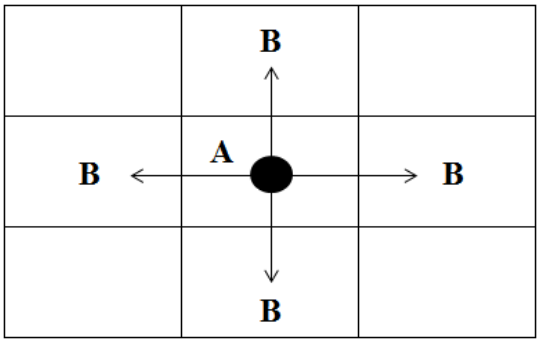

Figure 6-1: Schematic of the possible particle movements from grid A to grid B

6.3.2 Reactive Flow Proxy

Reactive transport (precipitation and dissolution) inside a porous media involves both irreversible and reversible phases (Edery et al. 2011). Typically reactions occur over a small section of an initially uniform reaction front (Hoefner and Fogler 1988). As time

progresses, changes in the uniform reaction front result due to preferential flow of reactant species through random permeable media (Lai et al. 2014).

We run PT for a long time over which the reaction front stabilizes and irregularities in the fluid displacement front depend only on fluctuations of fluid velocities due to heterogeneities. At the end of the final time step, the particles are counted in every grid block which serves as an analogue for concentration. At the end of this time we can estimate the scaling characteristics of the region indicated by non-zero particle count (or particle count above certain critical limit) along the boundary where particles cease to move further as illustrated schematically by a thick red line in Figure 6-2. Additionally, the length of this boundary as illustrated in Figure 6-2 is a proxy for the reaction surface area, which directly contributes to recovery of the displaced fluid. Therefore, length of the boundary can be a proxy for the recovery factor (RF) and can be used to estimate scaling characteristics of RF across multiple scales.

6.3.2.1 Automated Procedure to Determine the Location of Reaction Front Boundary

The location of the reaction front in any single model as illustrated in Figure 6-2 is determined automatically as described in the following steps:

i. Normalize the matrix $\mathbf{M}$ containing the number of particles to form a concentration matrix as: $\mathbf{M}_c = \frac{\mathbf{M} - \min(\mathbf{M})}{\max(\mathbf{M}) - \min(\mathbf{M})}$

ii. Provide a minimum threshold of concentration (value lying between 0 and 1) for which the reaction front is be determined.

iii. Identify the locations (rows and columns) in $\mathbf{M}_c$ where the concentration values are equal to the threshold provided in step (ii).

iv. From the locations identified in step (iii), trace the boundary line from that area and determine its coordinates.

v. After determining the coordinates of the boundary line (i.e. the reaction front), create a binary/indicator representation of the boundary line by assigning 'true' (or 1) to the coordinates forming the boundary and assigning 'false' (or 0) to the remaining coordinates in $\mathbf{M}_c$.

vi. Using the binary/indicator representation of the boundary line we can then find the indices and the concentration along the boundary of the reaction front.

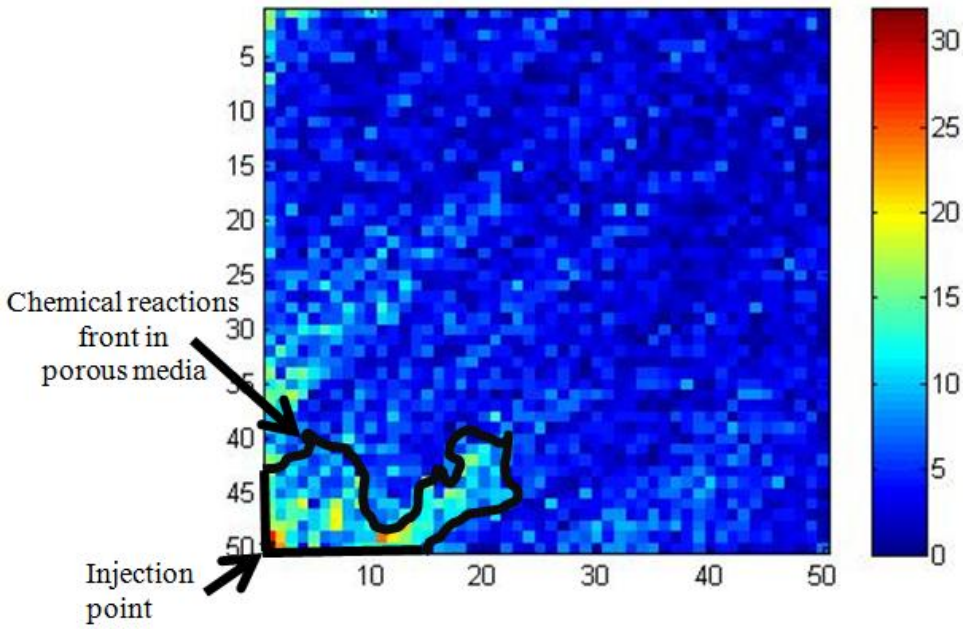

Figure 6-2: Schematic of the volume used for performing scaling calculations.

Using the proxy of reaction front and boundary length as described above for each scale of model, we can determine the scaling characteristics of reaction dynamics and RF, respectively. The uncertainty in the scaling characteristics can be determined by running all available models (realizations) of reservoir heterogeneity at multiple scales.

6.4 DEVELOPMENT OF NESTED HETEROGENEOUS MODELS

We look at the effect of grid-scale heterogeneity on reactive dynamics at various scales. To do this multiple realizations with consistent representation of heterogeneity that occur at multiple scales need to be generated. The correlation model at the largest scale is specified in the form of a 2-D anisotropy described by a spherical covariance model:

$$Cov(h) = \begin{cases} Cov(0) - \left[1.5\left(\frac{h''}{a_{\min}} \right) - 0.5\left(\frac{h''}{a_{\min}} \right)^3 \right], & \text{if } h'' \le a_{\min} \\ 0 \quad , & \text{otherwise} \end{cases} \tag{6.2}$$

For further details on how to perform anisotropic modeling and estimate the transformed lag vector h'' on a isotropic bases, the reader can refer to Journel and Huijbregts (2003). To generate heterogeneous permeability realizations geostatistical algorithm of conditional sequential Gaussian simulation was used, for which one of the input is the covariance model. In order to model heterogeneity across scales smaller than the largest scale, appropriate covariance parameters across these scales must be known. This can be achieved by downscaling the covariance from coarse scale to any scale of interest and establishing the parameters of the covariance model through a nonlinear inverse problem as described in the following section.

6.5 CONSISTENT COVARIANCE MODELING ACROSS SCALES

Data in subsurface engineering applications is usually acquired at different spatial scales, from fine (or small) scale such as well-log data or core data to coarse (or large) scale such as seismic data or well-test data. The information provided by fine scale data is at higher resolution than the information provided by coarse scale data. Fine scale data is often referred to as point support data whereas coarse scale data is referred to as block support data. Additionally, reservoir geology or spatial structure heterogeneity information may be available which can be described in form of a variogram or covariance model. Because the fine scale geologic structures are embedded within the large scale (reservoir scale) structures, it is necessary that the covariance model at the fine scale be consistent with the model at the larger scale.

While solving for any reservoir attribute at finer scale, it is a common practice to use correlation model defined at a coarse scale than the fine scale at which reservoir attribute is to be estimated. Even though the practice of using coarse scale covariance to estimate a property at finer scale produces a solution, the resultant property lacks the correct sub-grid variability and the computed attribute does not exhibit the correct spatial variability. To determine the reservoir attribute at a fine scale grid we first need to have a correct estimate of sub-grid covariance which is achieved by downscaling the covariance from coarse scale to fine scale. For this, each coarse scale grid should be discretized to fine scale grids as illustrated schematically in following figure:

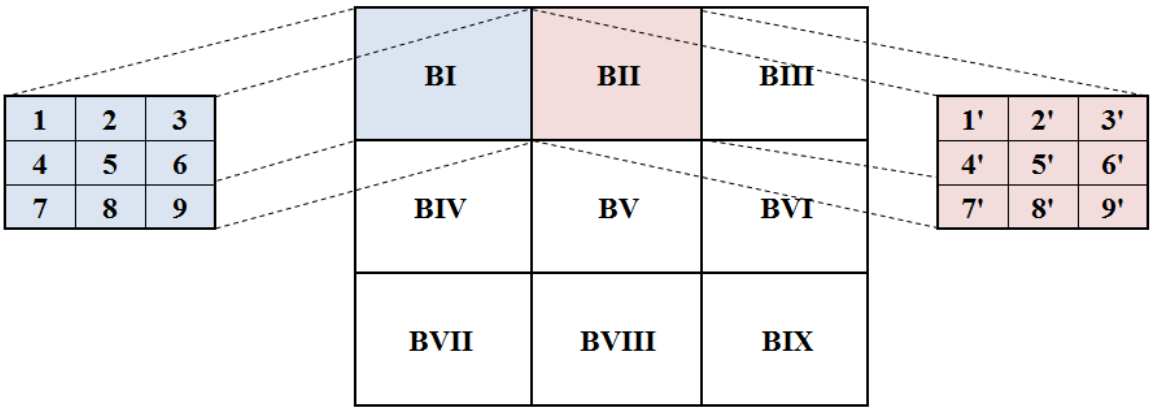

Figure 6-3: Graphical representation of a property at two scales

The average covariance between every fine grid block in one coarse block to the fine grid blocks in the second coarse block can be computed as shown in Eqn. (6.3):

$$\overline{Cov}(i,j) = \left[\frac{1}{\left(n_{BI} \times n_{BJ}\right)} \sum_{i=1}^{n_{BI}} \sum_{j=1'}^{n_{BJ}} \left[Cov(i,j) \right]^{\omega} \right]^{1/\omega} \tag{6.3}$$

where,

n_{BI}, n_{BJ} = number of fine scale blocks in coarse blocks BI and BJ, respectively,

where BI, BJ = BI, BII,...BIX

This average covariance shown in Eqn. (6.3) assumes a non-linear averaging relationship (defined by the parameter ω) between the attribute value at fine scale and that at the coarse scale. The power exponent ω generally ranges from -1 (corresponding to harmonic mean) to +1 (indicating arithmetic average). If the parameters of the fine scale covariance model $Cov(i,j)$ have been selected correctly, the block covariance $\overline{Cov}(i,j)$ should identify the covariance model given by Eqn. (6.2). In other words, the downscaled covariance parameters (sill, min. range, and max. range) can be established by matching the block average of fine scale covariance (defined as $\overline{Cov}(i,j)$) to the

coarse scale covariance model (defined as $Cov(BI, BJ)$) specified. This is achieved by minimizing the squared difference of fine scale covariance and block average covariance as shown by Eqn. (6.4).

$$obj = \min\left[Cov(BI, BJ) - \overline{Cov}(i, j) \right]^2, \text{ where } BI, BJ = \text{BI, BII,...BIX} \qquad (6.4)$$

Typically, the parameters that define a covariance are *sill* (or variance), *max range* (maximum distance after which a property is no longer correlated), *min range* (minimum distance after which a property is no longer correlated, usually at a direction perpendicular to *max range*), and *azimuth angle* (direction of maximum range/continuity) as shown here mathematically:

$$Cov(i, j) = f\left(sill, a_{\min}, a_{\max}, \theta\right) \qquad (6.5)$$

The matching procedure proceeds in two steps as follows:

i. Fix both the ranges and the azimuth angle while varying sill
ii. After we obtain the optimized sill we fix the sill and azimuth while varying the minimum and maximum ranges.

Note that in the above, the azimuth angle is fixed throughout the downscaling process and assumed to be the same as for the coarse scale variability. In the case of complex geologic structures, this assumption can be relaxed but at the expense of adding another loop to the optimization procedure. The objective function in Eqn. (6.4) is minimized using Nelder-Mead method (Nelder and Mead 1965), which is a well-defined nonlinear unconstrained optimization method. It is used for minimizing the objective

function in a multi-dimensional space and does not require any derivative information. It belongs to a class of direct search methods and is a simplex-based method.

After obtaining the parameters for the downscaled covariance, conditional sequential Gaussian simulation is used to generate different realizations of 2-D heterogeneous permeability maps as shown in the following section.

6.6 Results And Discussion

6.6.1 Covariance Modeling Across Scales

Using the method described above in section 6.5, we can derive several models of heterogeneous permeability (md) at different resolution starting from a coarse scale model of size 5X5. Figure 6-4 shows various realizations, their mean, and variance of the coarse scale (5X5) permeability field. Figure 6-5 through Figure 6-8 show similar results for fine scale permeability at different resolutions. These models are generated using conditional sequential Gaussian simulation. The black circles on each image show the location of conditioning (or "hard") data such as well-log data or core data. It can be noticed in Figure 6-5 through Figure 6-8 that the mean gets smoother and the variance gets more banded because of the regularly spaced conditioning data. Even though we generate the models at ten different spatial scales starting from 5X5 to 50X50, the five scales we choose to demonstrate our results cover the entire range of scales.

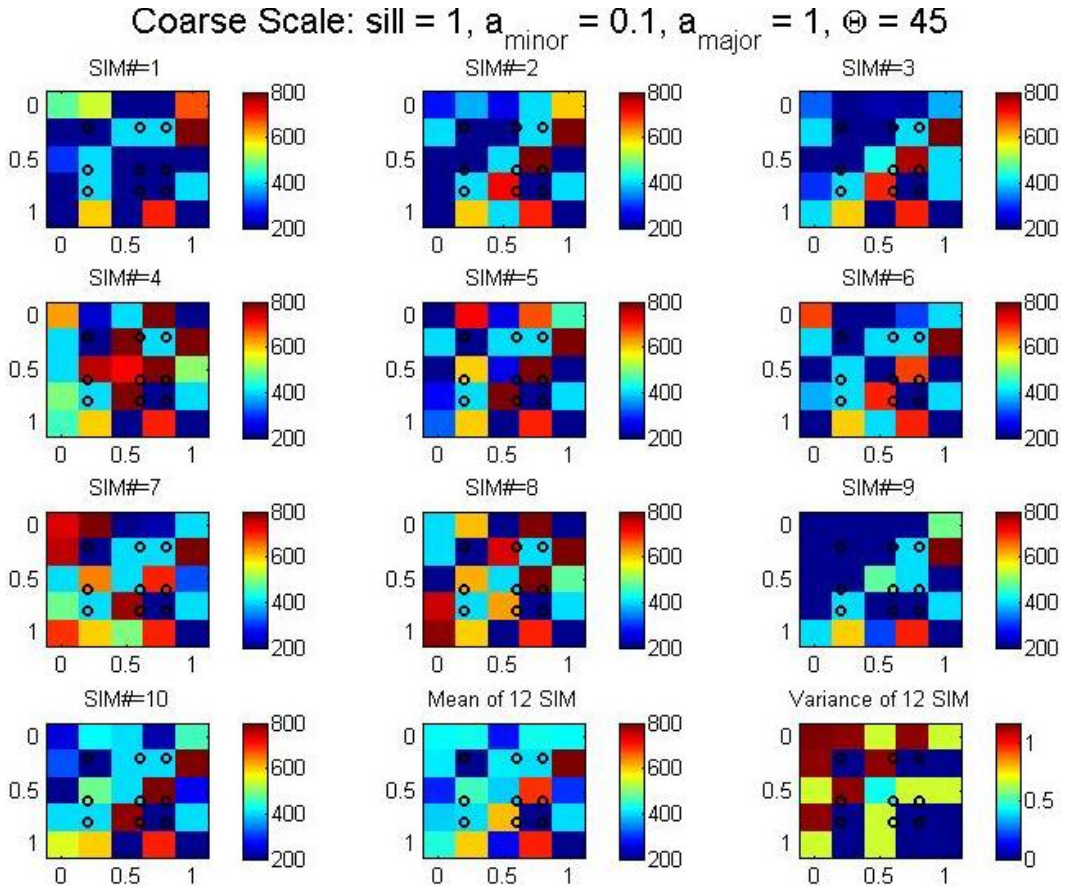

Figure 6-4: Different realizations, their mean, and variance of the coarse scale (5X5) permeability

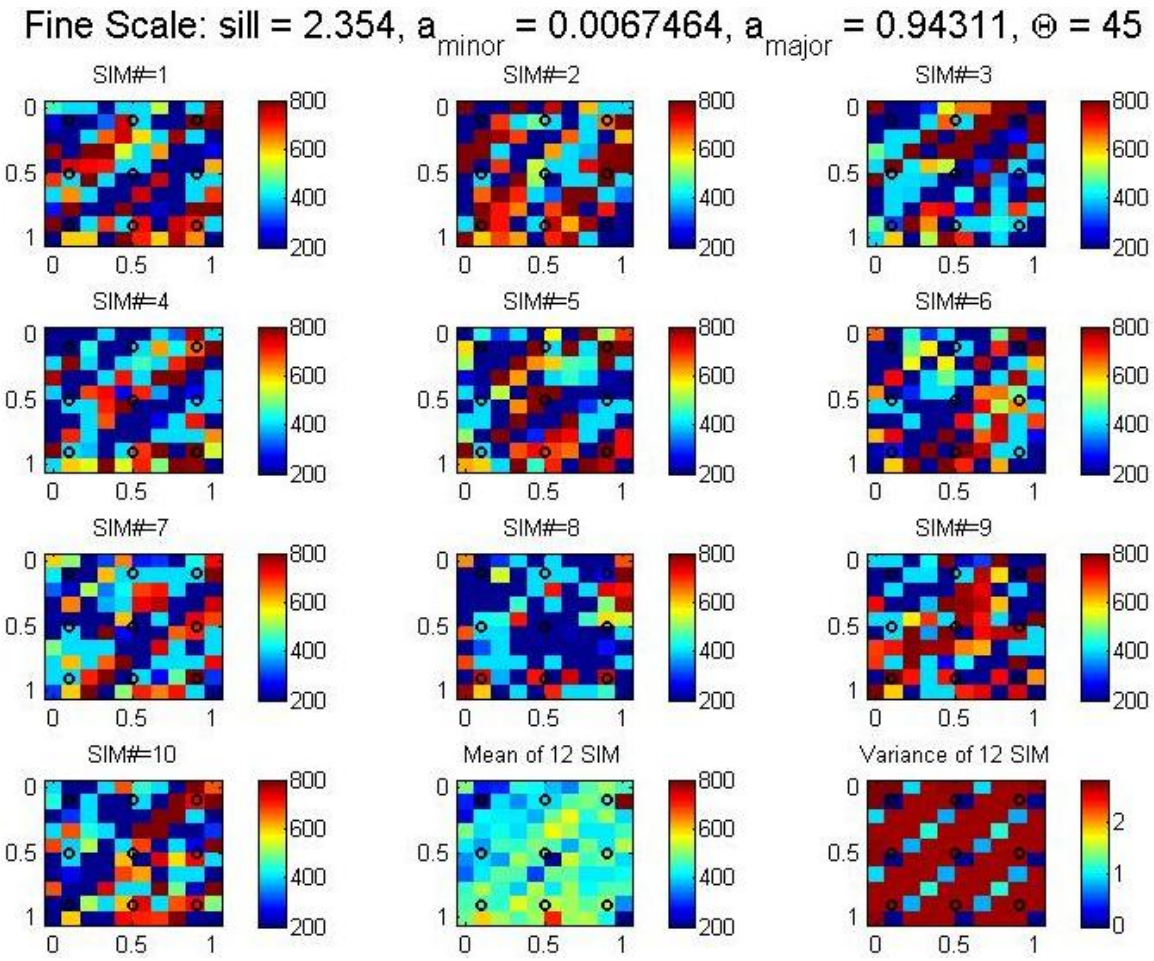

Figure 6-5: Different realizations, their mean, and variance at a finer scale (10X10) permeability. These realizations reflect a covariance model consistent with the coarse scale model.

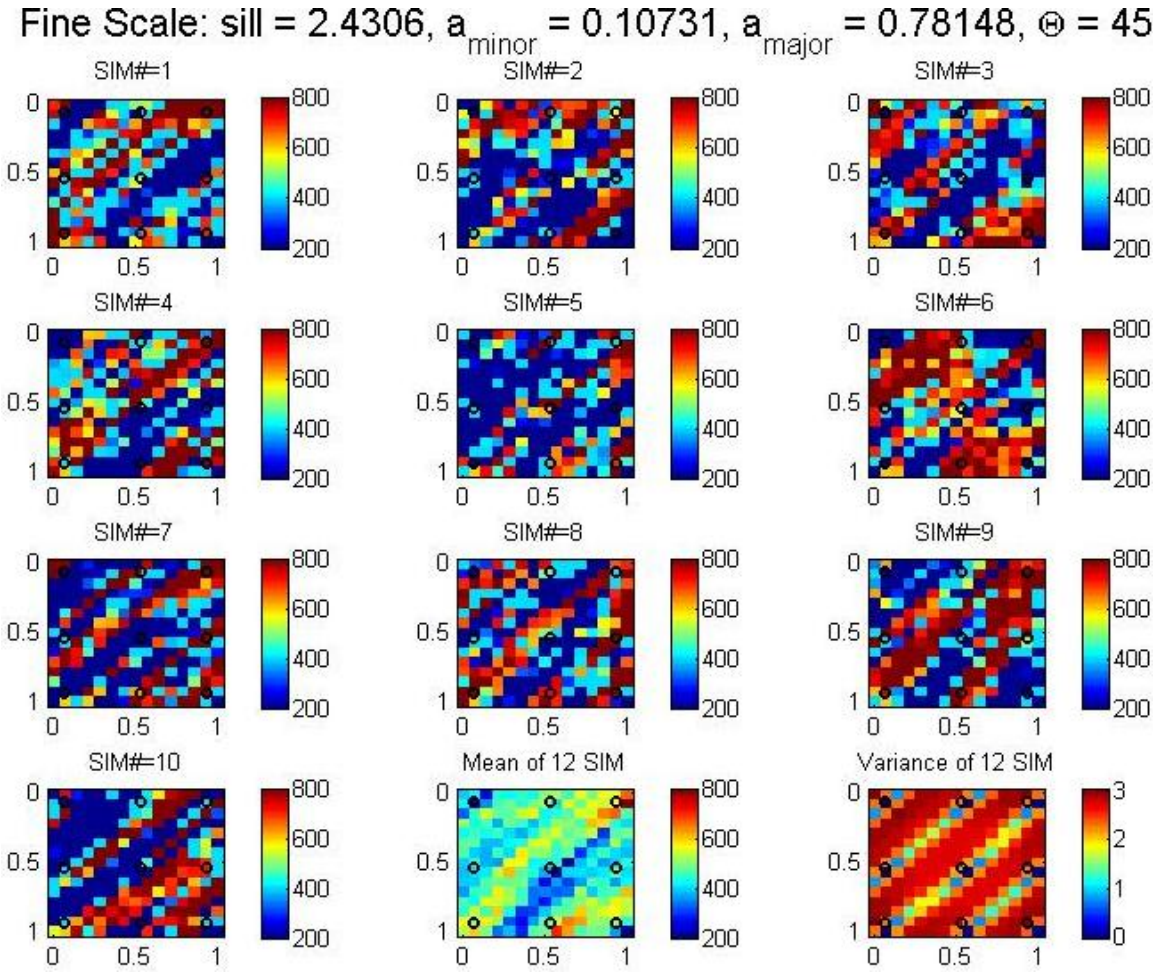

Figure 6-6: Different realizations, their mean, and variance of fine scale (15X15) permeability. These realizations reflect a covariance model consistent with the coarse scale model.

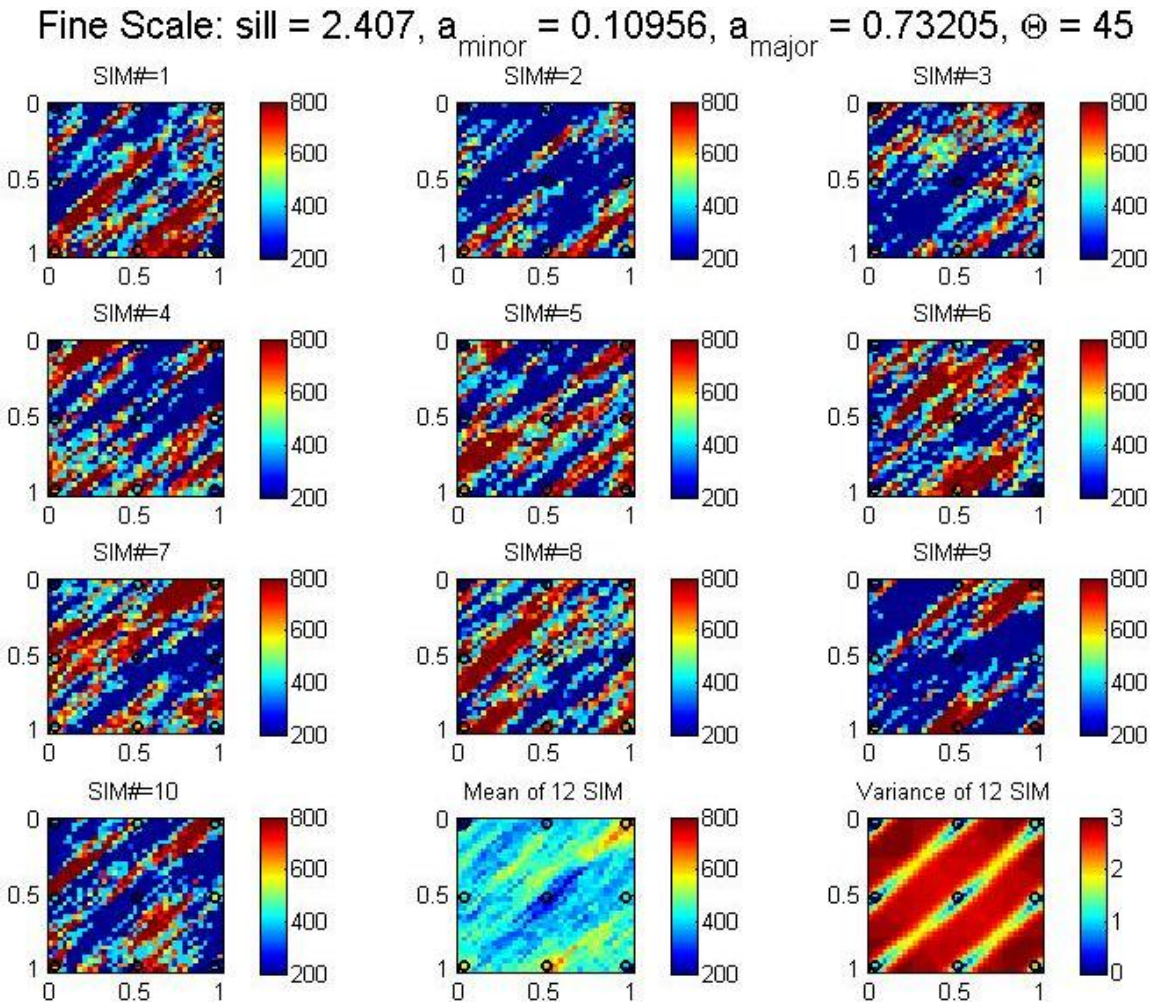

Figure 6-7: Different realizations, their mean, and variance of fine scale (35X35) permeability. These realizations reflect a covariance model consistent with the coarse scale model.

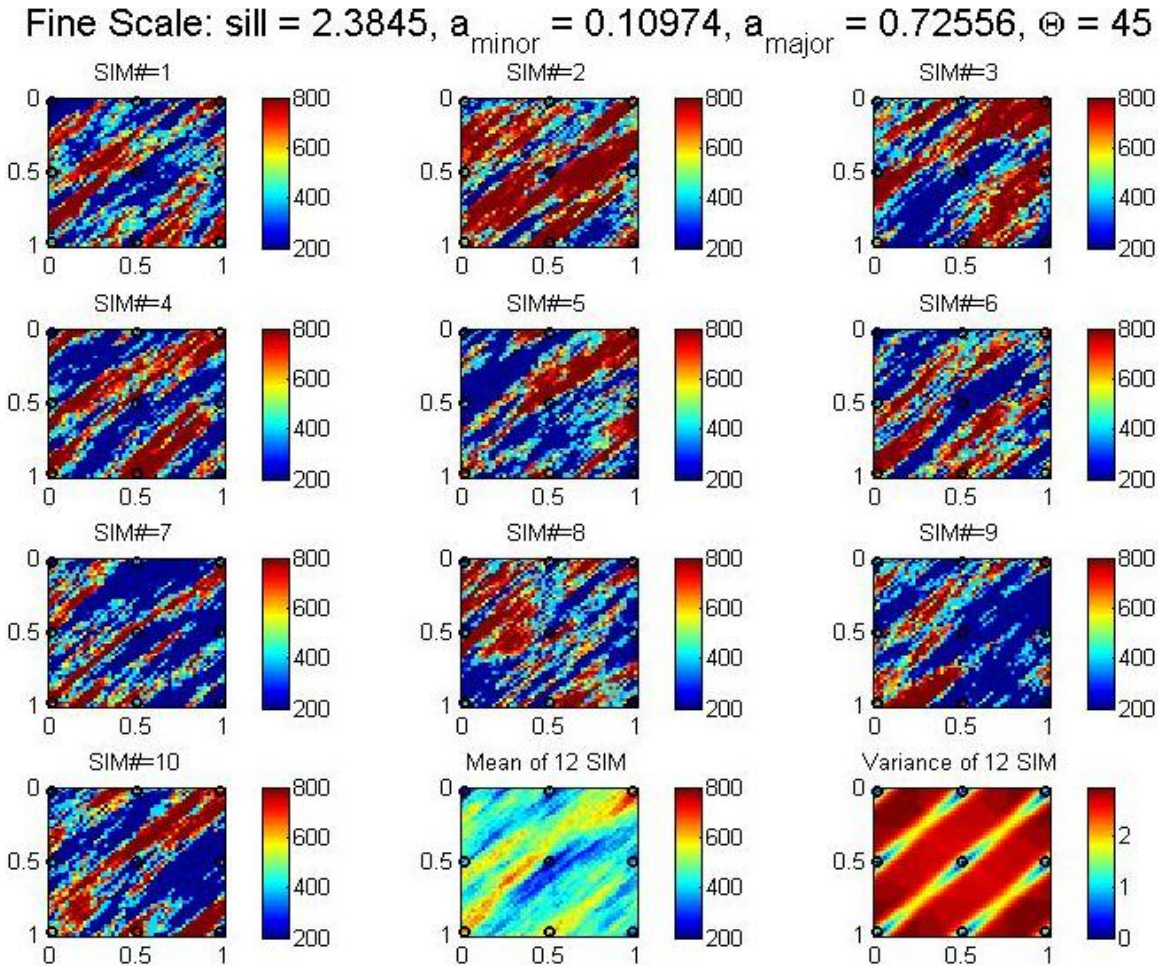

Figure 6-8: Different realizations, their mean, and variance of fine scale (50X50) permeability. These realizations reflect a covariance model consistent with the coarse scale model.

The covariance model parameters estimated using the downscaling scheme for the above permeability realizations at various spatial scales are presented in Table 6-1. These covariance parameters (sill, min. range and max. range) at each fine scale form a covariance model which is consistent with the coarse scale covariance model. Each of

these parameters is plotted against the spatial scale in Figure 6-9. Figure 6-9 shows that with the increasing spatial scale:

- the sill first increases and then plateaus to a stable value
- the a_{min} decreases before increasing and plateauing to a stable value
- the a_{maj} increases and then plateaus to a stable value

The strange behavior of a_{min} at small scales could be attributed to ergodic fluctuations due to the small size of the domain that results in some fluctuations that are comparable to the size of he domain. The same is not true for *sill* or a_{maj} because the larger magnitude of these two parameters and any fluctuation is small compared to the magnitude of the parameter.

Table 6-1: Parameters of the covariance models at various spatial scales

Grid Discretization	Covariance Model Type	Sill (Normalized)	Correlation Length	
			Minor	Major
5 x 5	Spherical	1	0.1	1
10 x 10	Spherical	2.354	0.0067464	0.94311
15 x 15	Spherical	2.4306	0.10731	0.78148
20 x 20	Spherical	2.4414	0.10777	0.75773
25 x 25	Spherical	2.435	0.1078	0.74865
30 x 30	Spherical	2.4194	0.10871	0.73997
35 x 35	Spherical	2.407	0.10956	0.73205
40 x 40	Spherical	2.399	0.10969	0.72824
45 x 45	Spherical	2.3913	0.10958	0.72743
50 x 50	Spherical	2.3845	0.10974	0.72556

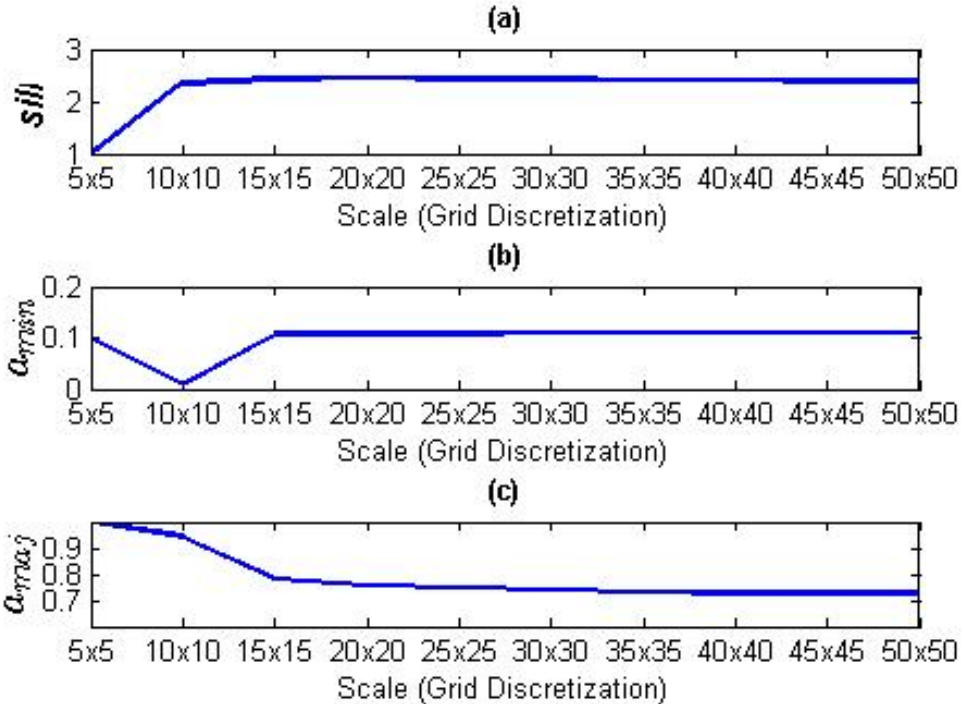

Figure 6-9: a) sill, b) minor correlation length, and c) major correlation length – all at various scales.

6.6.2 Flow Modeling Across Scales

The permeability models at different scales depicted in Figure 6-4 through Figure 6-8 are run through the PT code and the corresponding distributions of random walk of particles in the 2-D space after sufficient duration are shown in Figure 6-10 through Figure 6-14. The particle density results for four realizations are shown in Figure 6-10 through Figure 6-14. The mean of 12 realizations and the normalized variance of particle density over 12 realizations are also shown. These figures are shown at different scales, starting from the coarse scale (5X5) to fine scale (50X50). The black inverted triangle on the bottom left corner of each image shows the location of particle injection.

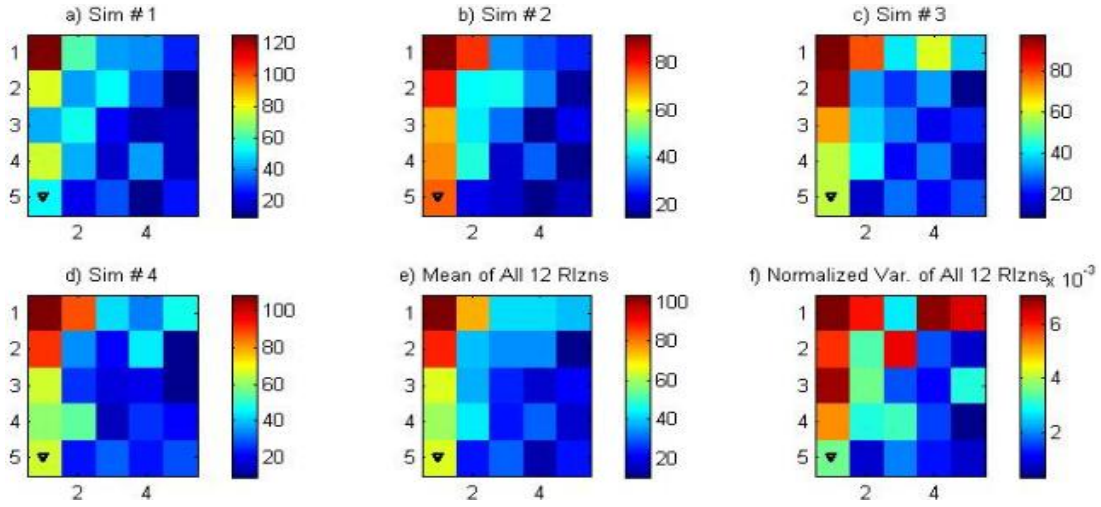

Figure 6-10: Particle density corresponding to four permeability realizations at the coarse scale (5X5) a) Realization 1, b) Realization 2, c) Realization 3 d) Realization 4 e) Mean particle density over 12 realizations and f) normalized variance of particle density over 12 realizations.

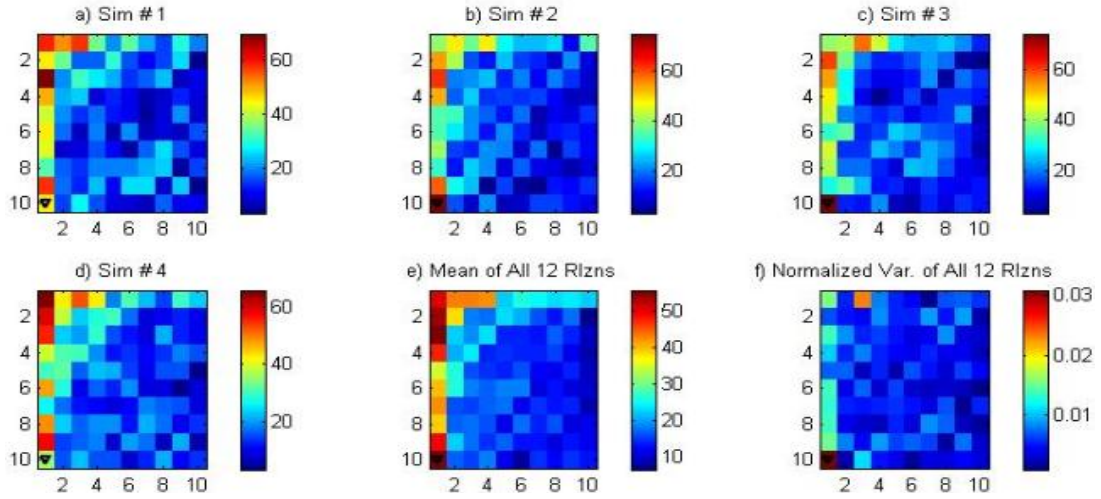

Figure 6-11: Particle density corresponding to four permeability realizations at the 10X10 scale a) Realization 1, b) Realization 2, c) Realization 3 d) Realization 4 e) Mean particle density over 12 realizations and f) normalized variance of particle density over 12 realizations.

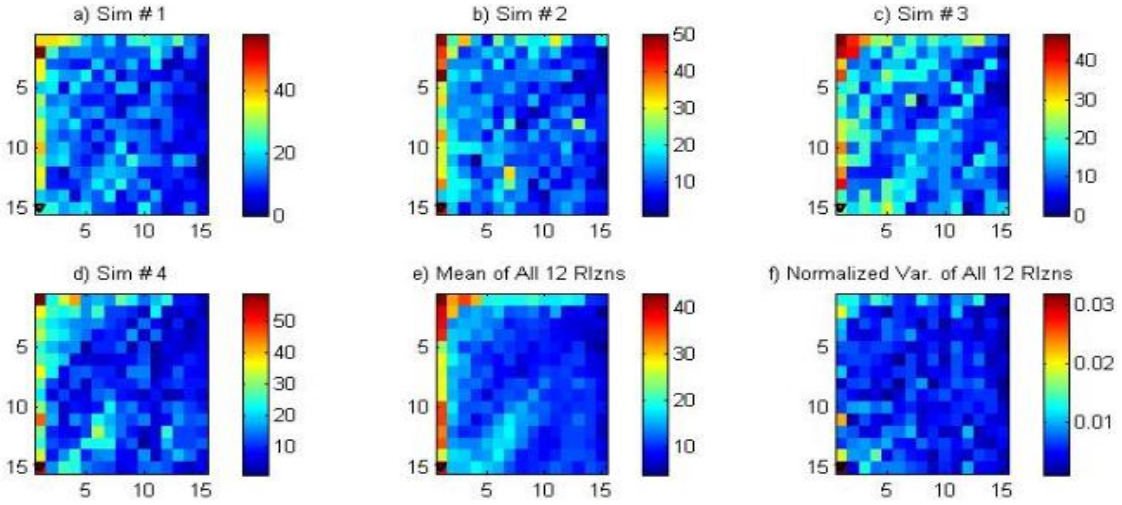

Figure 6-12: Particle density corresponding to four permeability realizations at the 15X15 scale a) Realization 1, b) Realization 2, c) Realization 3 d) Realization 4 e) Mean particle density over 12 realizations and f) normalized variance of particle density over 12 realizations.

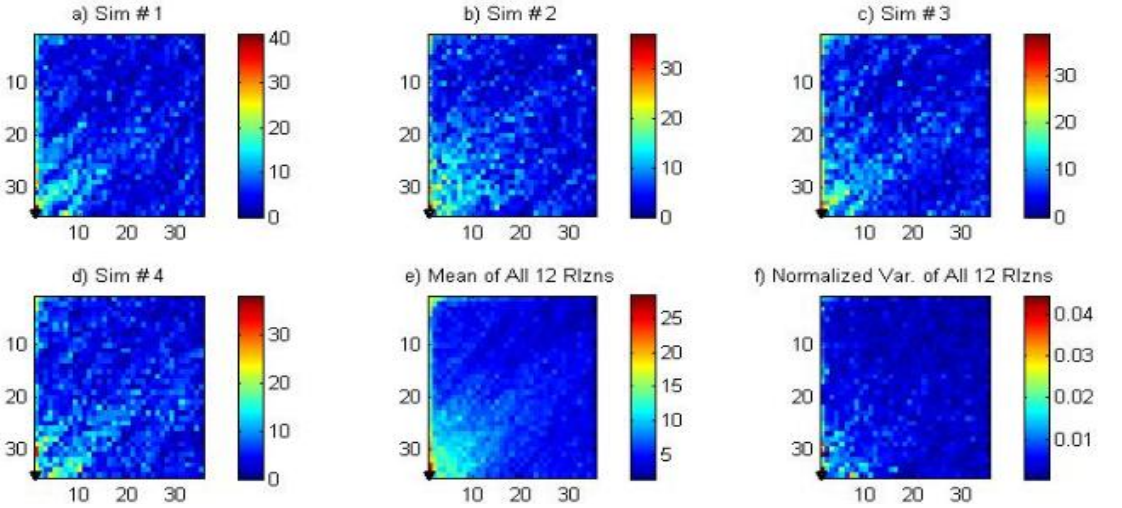

Figure 6-13: Particle density corresponding to four permeability realizations at the 35X35 scale a) Realization 1, b) Realization 2, c) Realization 3 d) Realization 4 e) Mean particle density over 12 realizations and f) normalized variance of particle density over 12 realizations.

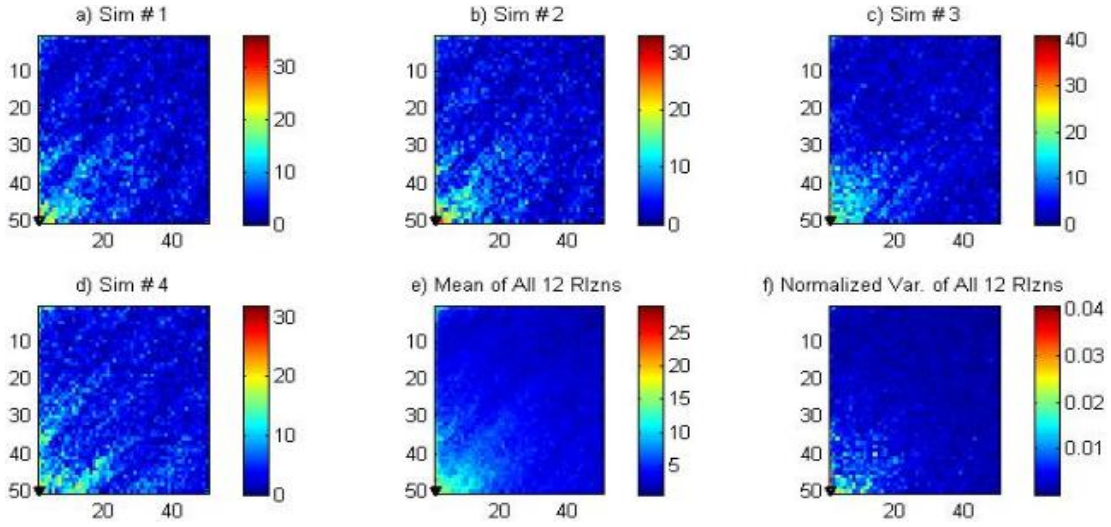

Figure 6-14: Particle density corresponding to four permeability realizations at the 50X50 scale a) Realization 1, b) Realization 2, c) Realization 3 d) Realization 4 e) Mean particle density over 12 realizations and f) normalized variance of particle density over 12 realizations.

The length of the boundary of the region with non-zero particle density at the end of run time should serve as a good proxy for the extent of the chemical reactions front as explained earlier. The particle distribution along this boundary at increasing scales can be used to deduce some statistics and infer scale-up behavior as discussed in following sections.

6.6.3 Scale-up of Reaction Surface Area

The total number of non-zero particles forming the boundary is a proxy for the concentration of the fluid at the reaction front, and this directly implies effective mass transfer. Therefore, the total number of non-zero particles forming the boundary can be a

proxy for the effective mass transfer. Figure 6-15 shows the total number of non-zero particles along the boundary (normalized) with its uncertainty (estimated using various realizations) versus the spatial scale. It can be clearly seen that the total number of non-zero particles along the boundary decrease with increasing spatial scale. This result is consistent with the findings of other authors (Chen et al. 2013; Deng et al. 2010; Zhu 2011) where they show that the parameters related to reactivity in a reservoir such as effective mass transfer coefficient (Deng et al. 2010 show that effective mass transfer coefficient is proportional to the square root of reaction constant in Eqn. 9) and temperature decrease with the reservoir domain size. Figure 6-16 shows variance of all non-zero particles forming the boundary from any single model (with its uncertainty estimated using various realizations) versus the spatial scale. It can be seen clearly that the variance of these non-zero particles forming the boundary decreases with increasing spatial scale. This implies that the spatial uncertainty in magnitude of prevailing reactivity decreases with increasing spatial scale of porous media.

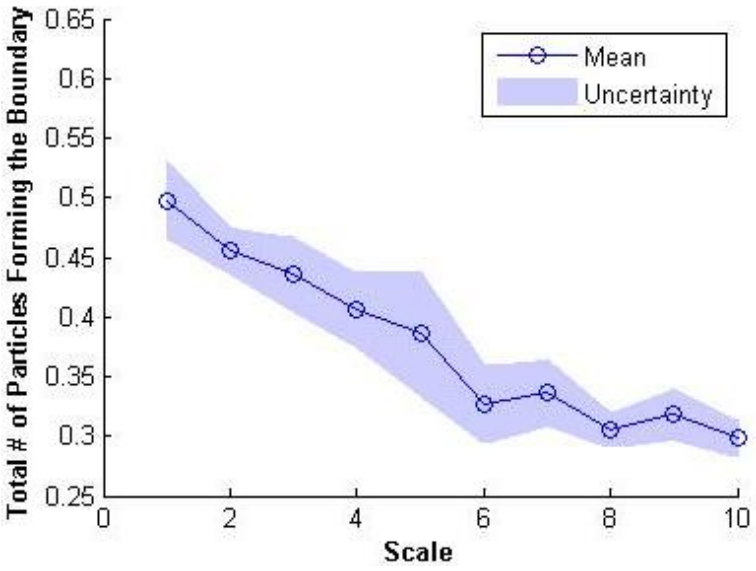

Figure 6-15: Total number of particles (normalized) along the boundary as a function of model size.

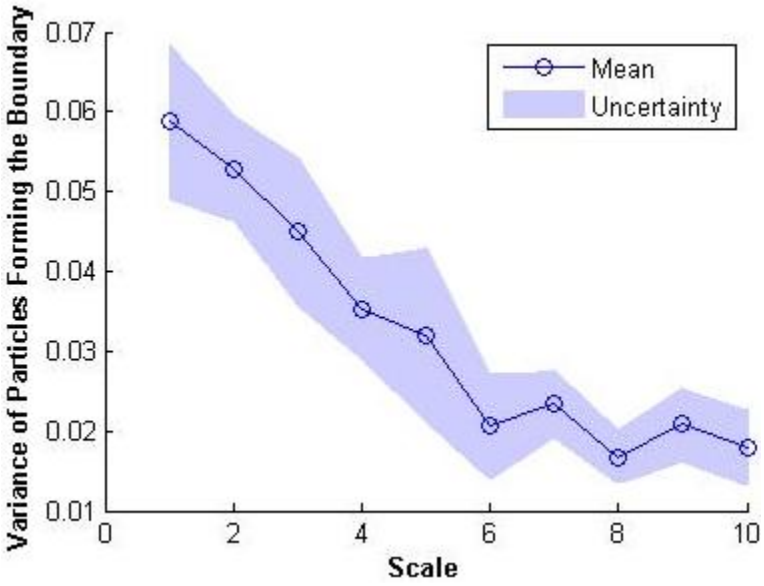

Figure 6-16: Variance of all particles from any single model (normalized) along the boundary as a function of model size.

As discussed in section on Particle Tracking Proxy, the length of the boundary (formed by non-zero particles) is a proxy for reactive surface area. Figure 6-17 shows length of the boundary formed by non-zero particles as a function of the spatial scale. It can be observed that the length of the boundary (formed by non-zero particles) shows a slight increase at small scales after which it decreases gradually for larger scales. This initial increase is the result of model boundary effects when scale is too small as seen in Figures 6-10 through Figure 6-14. It can be clearly seen in those plots that at small scales more number of particles tend to move towards model's boundary, resulting in the longer length of the non-zero particles' boundary. This result is consistent with the findings of other authors (Leung 2009; Leung and Srinivasan 2011) where they show that the recovery factor (RF) exhibits a slight increase at small scales and decreases gradually at large scales. Even though their postulation about the boundary effects was true, they did not present any proof to substantiate it. However, we support our conjecture of boundary effects by the 2-D particles distribution plots in Figure 6-10 through Figure 6-14 which clearly show the particles drifting along the boundary at small spatial scales because of which reaction surface area exhibits a slight increase at small scales. Deng et al. (2010) show that effective mass transfer coefficient (or the recovery) is proportional to the square root of reaction constant. It makes sense that the scaling of reaction surface area would be analogous to scaling of RF because RF is a function of displacement sweep efficiency which depends on how much length of the porous media has been contacted by the injected fluid, or in context of PT how far have the particles moved inside the porous media. The overall decreasing trend in Figure 6-17 is thus consistent with the common observation of decreasing RF when going from laboratory scale study to pilot scale.

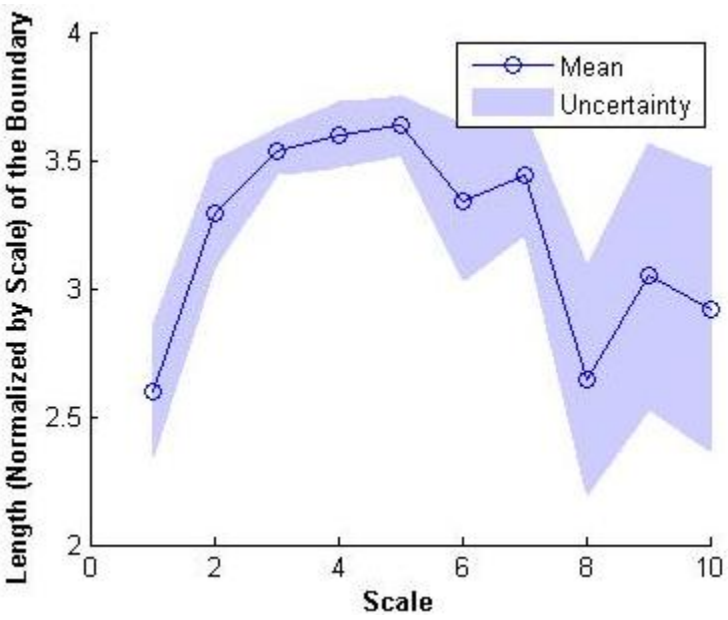

Figure 6-17: Length of boundary (formed by non-zero particles) as a function of model size based on results of PT

6.6.4 Scale-up of Mixing Zone Length

The mixing zone length (MZL) at the interface between two chemical species is usually considered as the distance separating the concentration c = 0.84 and c = 0.16 (Bear 1972) as depicted by Eqn. (6.6). The number of particles in a grid cell is a proxy for the concentration of the fluid, and using the number of particles as concentration the MZL can be determined numerically by taking the difference between the distance at which c = 0.84 and c = 0.16 are attained.

$$\mathrm{MZL} = (x)_{c=0.16} - (x)_{c=0.84} \tag{6.6}$$

The concentrations and their corresponding distances required to estimate MZL from the 2-D PT simulations are shown schematically in Figure 6-18. The two boundaries constituting the concentrations of c = 0.84 and c = 0.16 at the end of simulation run time are shown schematically in Figure 6-18 by thick black line and red line, respectively. The boundary lines formed by the concentration of c = 0.84 and c = 0.16 can be determined using the procedure described in section 6.3.2.1 and by assigning the threshold values of 0.84 and 0.16 in step (ii) for boundary lines forming the concentration of c = 0.84 and c = 0.16, respectively. All possible perpendicular distances between the points on two irregular concentration boundaries provide a vector comprising of all possible MZL values for this type of 2-D model. These perpendicular distances between the two boundaries are estimated using a script 'distance2curve' from Matlab File Exchange. As an illustration, few examples of these mixing zone lengths for a single model are shown visually by dotted white arrow lines in Figure 6-18. To obtain a single MZL value for any particular model we simply take a linear average of all possible MZL values estimated for that model as depicted in Eqn. (6.7).

$$\overline{\mathrm{MZL}} = \frac{\sum_{i=1}^{n} \mathrm{MZL}_i}{n} \tag{6.7}$$

It is assumed that linear averaging of MZL is appropriate because MZL is linearly related to the concentration difference as depicted by Eqn. (6.6).

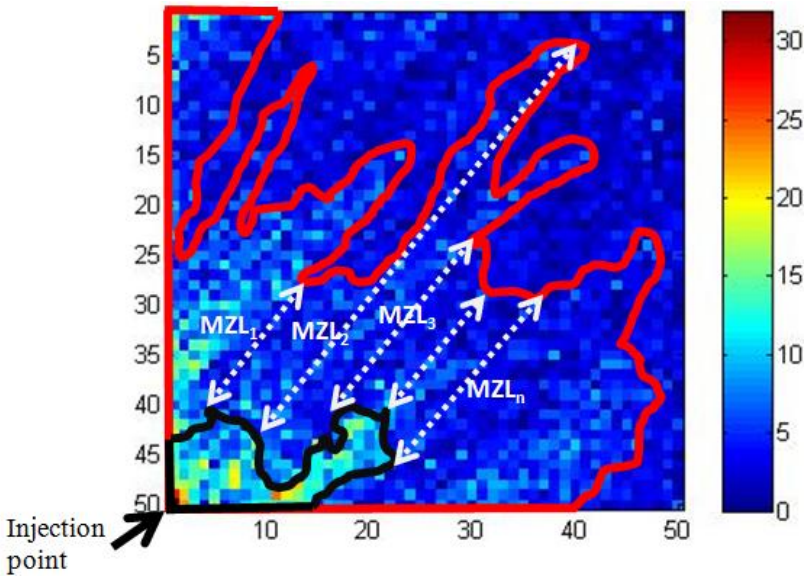

Figure 6-18: Schematic of the concentration boundaries for c = 0.84 (black line) and c = 0.16 (red line), plus the perpendicular distances between the points on these two boundaries used for performing MZL calculations.

The process described above to estimate MZL, and illustrated schematically in Figure 6-18, is repeated for models at all scales. The MZL estimated at each scale is then normalized by the length of that scale. Figure 6-19 shows the MZL (normalized) with its uncertainty (estimated using various realizations) versus the spatial scale. It can be clearly seen that the MZL initially increases with increasing spatial scales and then plateaus at intermediate to large scales. The permeability values of the porous media used in deriving this MZL result lie in the range of 200 md to 800 md as depicted in Figure 6-5 through Figure 6-8. In context of those high permeability values, this result is similar to the ones seen earlier in sections 3.4.3.2 and 3.5.2.1 of Chapter 3. In those earlier sections, we used full physics numerical simulations to conclude that the growth of MZL is primarily governed by the flow within the high permeability zones.

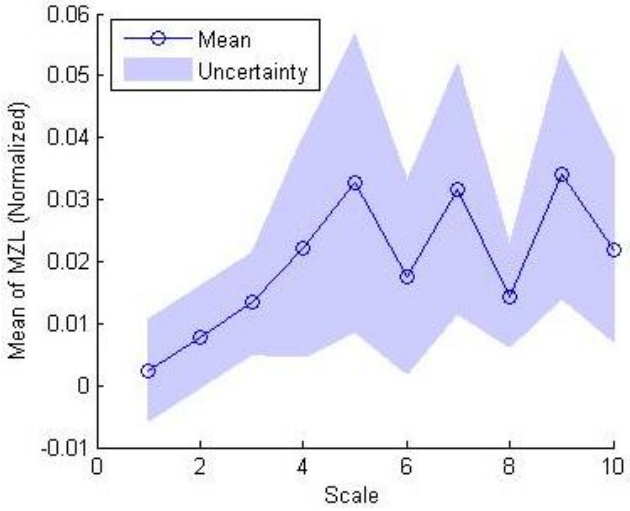

Figure 6-19: MZL as a function of model size based on results of PT

The variance of MZL and mean MZL are shown in Figure 6-20(a) and 6-20(b), respectively. These plots show that variance of MZL (and mean MZL) exhibits a slight increase at small scales and decreases gradually at large scales. This initial increase is the result of model boundary effects when scale is too small as seen in Figure 6-10. It can be clearly seen in those plots that at small scales more number of particles tend to move towards model's boundary, resulting in the longer length of the non-zero particles' boundary.

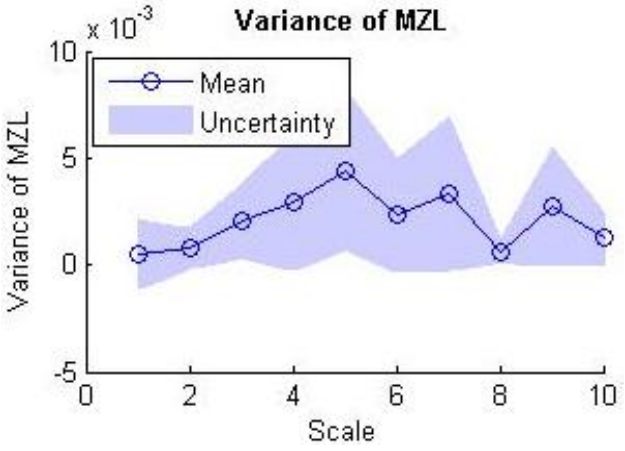

(a)

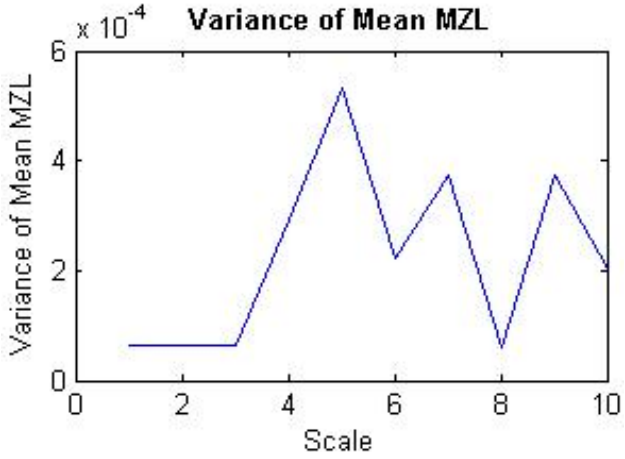

(b)

Figure 6-20: Variance of a) MZL, and b) mean MZL as a function of model size

6.7 CONCLUSIONS

Particle tracking performed on heterogeneous permeability models consistent across a hierarchy of scales are used to study the scaling of reactive-transport processes.

The movement of particle from one grid block to the other is controlled by the transition probability that is calculated using an equation that mimics the behavior of diffusion and non-Fickian transport through heterogeneous permeable media.

Scale-up result for reaction surface area in a porous media, shown by Figure 6-17, indicates that the effective reactivity exemplified by coefficients such as mass transfer coefficient, temperature, or sorption coefficient, decreases with increasing porous media size, except for a slight increase at small scales due to the boundary effects of the model. This result is consistent with results reported by other authors (Chen et al. 2013; Deng et al. 2010; Zhu 2011; Leung 2009; Leung and Srinivasan 2011). Also, spatial uncertainty in magnitude of reaction surface area (Figure 6-17) decreases with increasing porous media size.

Scale-up result for MZL, shown by Figure 6-19, indicates that the MZL increases with increasing scale of high permeability models. Similar result was seen earlier in sections 3.4.3.2 and 3.5.2.1 of Chapter 3 where it was shown using full physics numerical simulations that the growth of MZL is primarily governed by the flow within the high permeability zones.

These results are important towards understanding the scale-appropriate behavior of physical and chemical heterogeneities in porous media and can be used for designing laboratory experiments in addition to predict scaled-up field response. The particle tracking approach is significantly less expensive in terms of computational time.

Chapter 7: Conclusions and Recommendations for Future Work

7.1 CONCLUSIONS

Complex interdependencies between the chemical and physical processes in reservoir properties result in scale and support relationships that cannot be explained purely in spatial or temporal terms. Accurate assessment of reservoir properties and transport processes in reservoirs associated with chemical reactions is a function of combined spatial and temporal scales in addition to geological heterogeneity.

The objectives of this research were to:

1. Analyze spatiotemporal scale-up of the Mixing Zone Length (MZL) of a chemical species in the presence of:
    a. chemical reactions and heterogeneity
    b. multi-scale heterogeneities
2. Analyze scale-up of flow and transport related reservoir in combined spatial and temporal scales.
3. Scale-up of Diffusion-Reactive (DR) processes from continuum to field-scale accounting for multi-scale and multi-physics phenomena in heterogeneous porous media

The first objective is studied using two case studies in Chapter 3. In the first case study we use full-physics numerical simulations to investigate spatiotemporal scale-up of MZL in the presence of heterogeneity and chemical reactivity of CO_2. We first apply conventional flow scaling groups to scale recovery (CO_2 concentration) and MZL in presence of chemical reactivity and permeability heterogeneity and demonstrate that these

conventional practices are inadequate for representing the complex interplay between reaction and heterogeneity. In the second case study we use full-physics numerical simulations to investigate the impact of multi-scale nature of permeability heterogeneity on the spatiotemporal characteristics of MZL. Simulations were performed at three different spatial scales and for three types of permeability models. For a homogeneous model with high permeability (150 md), the MZL is controlled by the dispersion tensor and increases with time, and the time at which the MZL plateaus increases with increase in reservoir spatial scale. On the other hand in homogeneous model with low permeability (1 md) MZL is again controlled by the dispersion tensor but this time, it decreases with time. This decrease in MZL with time can be attributed to the lower fluid velocity in low permeability media. These observations indicated that accurate scaling of MZL is possible only when the time scale is also considered in addition to length scale of the reservoir. There is no significant difference in MZL for conservative and reactive transport if the permeability of the reservoir is homogeneous. However, there is significant deviation in values of MZL between conservative and reactive transport in a heterogeneous porous medium, which is a reflection of the fact that larger-scale local variations in velocity occur because of mineral alteration due to precipitation/dissolution.

In light of the second case study, a scaling scheme was proposed that can normalize the MZL curves corresponding to different correlation lengths of heterogeneity into a single MZL curve. This scaling scheme utilizes the correlation length of the media and the dimensions of the model. The results of the case study also point to the fact that when transport is modeled using discrete grid blocks that are smaller than the correlation length of the geologic heterogeneity, substantial variation in the effective properties of

the grid block result. This variation is described by the variance of the mean at the sub-REV scales. Thus for accurate numerical simulations of recovery processes, the spatiotemporal numerical discretization should be done appropriately based on the combined spatiotemporal REV scale of the process.

The second objective is explored in two chapters, Chapters 4 and 5, through synthetic case studies and experimental pore-scale CO_2 injection data, respectively. In Chapter 4, the computation of spatiotemporal REV is demonstrated for two case studies involving a theoretical solution to the Dispersion-Reaction Equation. The results show significant sensitivity of REV on the temporal scale. Chapter 5 addressed the impact of reactive processes on scale-up of reservoir properties. The scaling characteristics of the conservative and reactive processes were investigated using the variance-based statistical approach using high-resolution pore-scale data for CO_2 injection. The results indicated that the scaling characteristic of reactive processes, which alter pore structure with time, is significantly different than the scaling characteristics of conservative processes and a robust assessment of REV should involve coupling of temporal scale with spatial scale.

In order to accomplish the third objective, a particle tracking (PT) framework across multiple scales is used to consistently evaluate the behavior of reaction dynamics across scales. Particle tracking acts as a fast approximation to the full physics simulation. The ensemble statistics computed using the PT algorithm also prove useful in cases that are difficult to address using more rigorous volume-averaging or ensemble-averaging approaches due to difficulty in treating heterogeneity at multiple scales. This PT method was combined with an algorithm that accounts for consistent scaling of reservoir heterogeneity at all scales through dispersion variance conditions and a parameter

matching scheme. Scale-up results indicate that the effective mass transfer and the spatial uncertainty in its magnitude decrease with increasing domain size of the reservoir. Scale-up results for reaction surface area indicate that it decreases with increasing porous media scales. Scale-up result for the MZL indicated that the MZL increases with increasing length scale of high permeability models. All these results derived from PT are consistent with the results reported by other authors (Chen et al. 2013; Deng et al. 2010; Zhu 2011; Leung 2009; Leung and Srinivasan 2011; Sajjadi and Azaiez, 2013; Singh and Srinivasan, 2014).

7.2 CONTRIBUTIONS

An original contribution of this work is to investigate and scale-up flow response and transport parameters for reactive processes in heterogeneous media. The conventional scaling laws are inadequate to scale-up the recovery response and transport parameters when the effect of reactions and heterogeneity are coupled together. This work looks at reactive transport processes at a combination of temporal and spatial scales in order to arrive at the REV scale of parameters such as the Mixing Zone Length (MZL) and effective reaction constant. In addition, the research has resulted in the development of a simple scaling group to scale the MZL in presence of multi-scale reservoir heterogeneity. This scaling group explicitly takes into account the correlation length of the underlying reservoir heterogeneity.

This research illustrates and extends the use of the variance of mean concept to analyze the scale-up of phenomena exhibiting spatiotemporal variability. The current practice is to perform spatial averaging of attributes and account for residual variability

by calibration and history matching. This results in poor predictions of future reservoir performance. The proposed semi-analytical technique to scale-up in both space and time provides guidance for selection of spatial and temporal discretizations that takes into account the uncertainties due to sub-processes (which are typically difficult to describe) at multiple temporal scales.

Additionally, this research provides a method using particle tracking to scale-up flow and transport while addressing the multi-scale and multi-physics nature of Dispersive-Reactive processes. In order to demonstrate the application of particle tracking we developed a consistent procedure for scaling up heterogeneity across scales using the dispersion-variance relationship and a parameter identification scheme. We demonstrate that the PT method can quantify statistical properties such as reaction surface area and MZL in a heterogeneous medium at various scales.

7.3 IMPLICATIONS OF THIS RESEARCH

The research procedures and results carry the following important implications:

i. Designing of experiments and their scale-up: We investigated evolution of transport parameters such as MZL (longitudinal dispersivity) as a function of several parameters such as reactivity and permeability heterogeneity at various spatial and temporal scales. The ensemble of results at varying spatiotemporal scales provides guidance on how to assign variance to laboratory experiment results when they are used to predict recovery at field scales.

ii. Characterizing scale-appropriate behavior of reactivity in context of CO_2 sequestration processes: The changes observed in REV scale between conservative process and reactive process estimated using the pore scale data suggests that the alteration of pore structure of the porous media plays an important role in determining the scaling characteristics of transport parameters. Quantifying the REV in a spatiotemporal context is therefore an important implication of the research.

iii. Quantifying the uncertainty due to sub-processes: Semi-analytical scale-up of any reservoir or flow parameter to its spatiotemporal REV scale can minimize the uncertainty due to sub-processes associated with that parameter. It provides a criterion to select spatial and temporal discretizations which could minimize the uncertainty and complements the more conventional Courant–Friedrichs–Lewy (CFL) condition used to evaluate the stability and accuracy of numerical simulation results.

7.4 Recommendations For Future Work

This dissertation presented procedures to scale-up reservoir attributes and processes in the combined presence of geological heterogeneity and chemical reactions. Based on the results discussed in previous chapters and the subsequent conclusions, the following recommendations can be made for future work:

i. It is apparent that chemical heterogeneity, in addition to geological heterogeneity, affects the scale-up of transport processes. Chemical heterogeneity could be in form of spatially varying reactive surface area,

mineral compositions, compositions of reactive species etc. Usually the reactive surface area, an important parameter in context of mineral trapping for CO_2 sequestration, is measured at laboratory scale and assumed as a constant at the field scale, however, in reality the reactive surface area would not only be heterogeneous spatially but also vary with the scale at which the phenomenon is studied.

ii. It would be useful to assess the effect of different types of averaging schemes other than arithmetic averaging. As described previously, determination of REV involves averaging which could be either linear or non-linear. However, for flow of non-Newtonian fluids the permeability, pressure, velocity, and viscosity are all related non-linearly to each other and arithmetic averaging of these may not be appropriate.

iii. The complete workflow for scale-up analysis comprises of identifying the main physical mechanisms impacting the flow and transport of fluids at the smaller scales, performing parameter estimations (history matching) at the smaller scales and then deriving the scale-up characteristics at the larger (field) scales. The results obtained using these scaled up quantities in reservoir scale simulations can then be compared against the actual field observations in order to validate the scale-up procedure. The complete implementation of this workflow for a field case would be a very worthwhile focus for future efforts.

Appendix A: Illustration for Computing Spatiotemporal Variogram

Empirical variogram along various directions for the simple process developed in Eqn. (A.1), and shown in Figure (A-1), can be inferred numerically as illustrated in Figure A-2. This simple spatiotemporal stochastic model was used in Chapter 3. Figure A-2 illustrates computation of spatiotemporal variograms along the rows (N-S direction), columns (E-W direction), and at a 45^0 angle for the data shown in Figure A-1.

The analytical expression for the concentration profile shown in Figure A-1 is:

$$C(x,t) = \text{constant} \times \left(\frac{t}{x^{0.1}} \right) + U(t) \qquad (A.1)$$

where,

t = time

x = lateral distance in x-direction

U(t) = uniform transform of unconditional Gaussian noise at time 't'

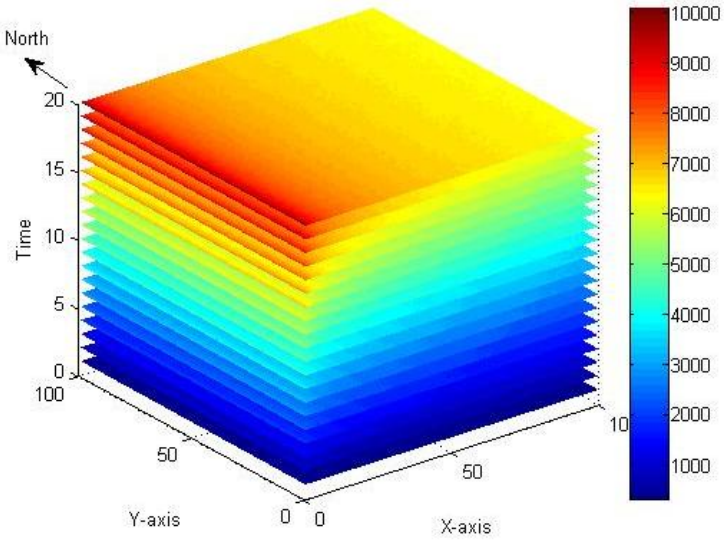

Figure A-1: Concentration profiles in space and time

Matrix at t=1		
c_1	c_2	c_3
c_4	c_5	c_6
c_7	c_8	c_9

Matrix at t=2		
c'_1	c'_2	c'_3
c'_4	c'_5	c'_6
c'_7	c'_8	c'_9

Matrix at t=3		
c''_1	c''_2	c''_3
c''_4	c''_5	c''_6
c''_7	c''_8	c''_9

$$\gamma(h_x=1,h_y=0,\tau=0)=\frac{\left[\begin{array}{l}\{(c_1-c_2)^2+(c_2-c_3)^2+(c_4-c_5)^2+(c_5-c_6)^2+(c_7-c_8)^2+(c_8-c_9)^2\}+\\ \{(c'_1-c'_2)^2+(c'_2-c'_3)^2+(c'_4-c'_5)^2+(c'_5-c'_6)^2+(c'_7-c'_8)^2+(c'_8-c'_9)^2\}+\\ \{(c''_1-c''_2)^2+(c''_2-c''_3)^2+(c''_4-c''_5)^2+(c''_5-c''_6)^2+(c''_7-c''_8)^2+(c''_8-c''_9)^2\}\end{array}\right]}{[2\times 18]}$$

$$\gamma(h_x=0,h_y=1,\tau=0)=\frac{\left[\begin{array}{l}\{(c_1-c_4)^2+(c_4-c_7)^2+(c_2-c_5)^2+(c_5-c_8)^2+(c_3-c_6)^2+(c_6-c_9)^2\}+\\ \{(c'_1-c'_4)^2+(c'_4-c'_7)^2+(c'_2-c'_5)^2+(c'_5-c'_8)^2+(c'_3-c'_6)^2+(c'_6-c'_9)^2\}+\\ \{(c''_1-c''_4)^2+(c''_4-c''_7)^2+(c''_2-c''_5)^2+(c''_5-c''_8)^2+(c''_3-c''_6)^2+(c''_6-c''_9)^2\}\end{array}\right]}{[2\times 18]}$$

$$\gamma(h_x=1,h_y=1,\tau=0)=\frac{\left[\begin{array}{l}\{(c_1-c_5)^2+(c_2-c_6)^2+(c_4-c_8)^2+(c_5-c_9)^2\}+\\ \{(c'_1-c'_5)^2+(c'_2-c'_6)^2+(c'_4-c'_8)^2+(c'_5-c'_9)^2\}+\\ \{(c''_1-c''_5)^2+(c''_2-c''_6)^2+(c''_4-c''_8)^2+(c''_5-c''_9)^2\}\end{array}\right]}{[2\times 12]}$$

$$\gamma(h_x=1,h_y=0,\tau=1)=\frac{\left[\begin{array}{l}\{(c_1-c'_2)^2+(c_2-c'_3)^2+(c_4-c'_5)^2+(c_5-c'_6)^2+(c_7-c'_8)^2+(c_8-c'_9)^2\}+\\ \{(c'_1-c''_2)^2+(c'_2-c''_3)^2+(c'_4-c''_5)^2+(c'_5-c''_6)^2+(c'_7-c''_8)^2+(c'_8-c''_9)^2\}\end{array}\right]}{[2\times 12]}$$

$$\gamma(h_x=0,h_y=1,\tau=1)=\frac{\left[\begin{array}{l}\{(c_1-c'_4)^2+(c_4-c'_7)^2+(c_2-c'_5)^2+(c_5-c'_8)^2+(c_3-c'_6)^2+(c_6-c'_9)^2\}+\\ \{(c'_1-c''_4)^2+(c'_4-c''_7)^2+(c'_2-c''_5)^2+(c'_5-c''_8)^2+(c'_3-c''_6)^2+(c'_6-c''_9)^2\}\end{array}\right]}{[2\times 12]}$$

Figure A-2: Illustration of spatiotemporal variogram calculation along various directions

Appendix B: Code for Covariance Downscaling and Particle Tracking

B.1 Code For Covariance Downscaling

```
%% -------------------------PARAMETERS-------------------------

%# ---------Editable Parameters----------
omega = 1; % Arithematic averaging
n = 5;
ithScaleLevel = 10; %# Downscaling level
nRlzn = 12;
mod_type = 'Sph';
theta = 45; % degrees

%# ---------Fixed Variables----------
VarioStruct = struct('Sph', 1, 'Exp', 2, 'Gauss', 3);
VarioType = VarioStruct.(mod_type);

cScale = 'Scale1'; % coarse scale
fScale = strcat('Scale', num2str(ithScaleLevel)); % fine scale

nRow.Scale1 = n;
nCol.Scale1 = n;
nRow.(fScale) = ithScaleLevel*nRow.Scale1;
nCol.(fScale) = ithScaleLevel*nCol.Scale1;

%# -----------Final parameters of coarse scaled covariance----------
a_Min.cScale = 0.1; % x(1) range along minor direction
a_Maj.cScale = 1; % x(2) range along major direction

%# --------Initial guess of parameters for fine scaled covariance------
sill0.fScale = 1;
a0_Min.fScale = 0.3; % nCol.(fScale)./2 range along minor direction
a0_Maj.fScale = 0.9; % nCol.(fScale) range along major direction
theta0.fScale = 45; % degrees

%# ----------Lower limit parameters of covariance----------
sillL.fScale = 0;
aL_Min.fScale = 0;
aL_Maj.fScale = 0;
thetaL.fScale = 0;

%# -------Upper limit parameters of covariance----------
sillU.fScale = 100;
aU_Min.fScale = 100; % nCol.(fScale);
```

```
aU_Maj.fScale = 100; % nCol.(fScale);
thetaU.fScale = 180;

nCell.Scale1 = nRow.Scale1*nCol.Scale1;
nCell.(fScale) = nRow.(fScale)*nCol.(fScale);

sill.cScale = 1;

%% -----------CHECK TO SEE IF COVARIANCE FILE ALREADY EXISTS-----------

%# -----------------cScale File Name------------------
covarFileName.cScale  =  strcat('covar_',  num2str(n),  'x',  num2str(n),
'Grid',...
    cScale, '_fromS1.mat');

%# -----------------fScale File Name------------------
covarFileName.fScale  =  strcat('covar_',  num2str(n),  'x',  num2str(n),
'Grid',...
    fScale, '_fromS1.mat');

%% ----------COARSE SCALE COVARIANCE USING 'general_CovModel.m'--------

if ~exist(covarFileName.cScale, 'file')
    %# -----------------Compute Covariance------------------
    [covar.cScale]   =   general_pointCov(nRow.(cScale),   nCol.(cScale),
a_Min.cScale,...
        a_Maj.cScale, theta, sill.cScale, mod_type);

    %# -----------------Save the Covariance------------------
    save(covarFileName.cScale, 'covar')
else
    load(covarFileName.cScale);
end

%% -----------OPTIMIZATION TO OBTAIN DOWNSCALED COVARIANCE PARAMETERS--

if ~exist(covarFileName.fScale, 'file')
    %# -----------------Sill Optimization------------------
    opts = optimset('display', 'iter');
    [w,  fval,  exitflag]  =  fminsearchbnd(@(w)  general_minimizeCov(w(1),
a_Min.cScale,...
        a_Maj.cScale, theta, covar, nCol, nRow, cScale, fScale, omega,
mod_type),...
        [sill0.fScale]);

    %# -----------------Range Optimization------------------
    sill.fScale = w;
```

```
    opts = optimset('display', 'iter');
    [x,        fval,        exitflag]        =        fminsearchbnd(@(x)
general_minimizeCov(sill.fScale, x(1),...
        x(2),   theta,   covar,   nCol,   nRow,   cScale,   fScale,   omega,
mod_type),...
        [a0_Min.fScale,         a0_Maj.fScale],         [aL_Min.fScale,
aL_Maj.fScale],...
        [aU_Min.fScale, aU_Maj.fScale], opts);
    a_Min.fScale = x(1);
    a_Maj.fScale = x(2);

    %# -----------------Save the Covariance------------------
    save(covarFileName.fScale, 'sill', 'a_Min', 'a_Maj')
else
    load(covarFileName.fScale)
end

%% ----------------DEFINE HARD DATA----------------

%# ----------------Magnitude of Hard Data----------------
HD = [2, 4, 6, 4, 2, 7, 8, 4, 2]*1e+02;

%% ----------------RUN SGSIM.EXE, POSTSIM.EXE AND KB2D.EXE-------------

%# ----------------cScale----------------
[k.cScale, ~, KB2DVariance.cScale, S.cScale] =...
    general_run_SGSIMexePOSTSIMexeKB2Dexe(nRlzn,            nRow.Scale1,
nCol.Scale1,...
    1,  a_Maj.cScale,  a_Min.cScale,  sill.cScale,  theta,  VarioType,  HD,
cScale);

%# ----------------fScale----------------
[k.fScale, ~, KB2DVariance.fScale, S.fScale] =...
    general_run_SGSIMexePOSTSIMexeKB2Dexe(nRlzn, nRow.(fScale),...
    nCol.(fScale),    1,    a_Maj.fScale,    a_Min.fScale,    sill.fScale,
theta,...
    VarioType, HD, fScale);

%% ---------MAKE GSLIB FILES FOR SIMULATED DATA-----------

%# ----------------File Names----------------
GSLIBFileName_to_make.cScale    =    strcat('k_',    num2str(n),    'x',
num2str(n), 'Grid', cScale, '_fromS1_sgsim_gslib_format.dat');
GSLIBFileName_to_make.fScale    =    strcat('k_',    num2str(n),    'x',
num2str(n), 'Grid', fScale, '_fromS1_sgsim_gslib_format.dat');

%# ----------------Header Names----------------
header_property_name_want = 'k_Realizations';
```

```
%# ----------------Create GSLIB Files----------------
write_property_to_gslib_file_general(nRlzn,
GSLIBFileName_to_make.cScale,...
    header_property_name_want,                          reshape(k.cScale,
nRow.(cScale)*nCol.(cScale), nRlzn))
write_property_to_gslib_file_general(nRlzn,
GSLIBFileName_to_make.fScale,...
    header_property_name_want,                          reshape(k.fScale,
nRow.(fScale)*nCol.(fScale), nRlzn))

%% ----------------RUN TRANS.EXE TO GENERATE REALIZATIONS--------------

%# ----------------cScale----------------
[kTransformed.cScale]    =    general_run_TRANSexe(nRlzn,    nRow.Scale1,
nCol.Scale1, 1,...
    HD, GSLIBFileName_to_make.cScale, cScale);

%# ----------------fScale----------------
[kTransformed.fScale]   =   general_run_TRANSexe(nRlzn,   nRow.(fScale),
nCol.(fScale),...
    1, HD, GSLIBFileName_to_make.fScale, fScale);
```

B.2 CODE FOR PARTICLE TRACKING

```
%% --------------MAKE FILES TO BE USED IN RANDOM WALKER----------------

%# ------------Make Permeability TXT File For Random Walker------------
PermModels_TXTFileName = [PropName, '_', num2str(n), 'x', num2str(n),
'Grid', fScale, '_fromS1.txt'];
PermModelsTemp = fopen(PermModels_TXTFileName, 'wt');
fprintf(PermModelsTemp, '%d\n', nRlzn_want);
fclose(PermModelsTemp);
dlmwrite(PermModels_TXTFileName, Prop_ColumnData_nModels(:,...
    randi(nRlzn, nRlzn_want, 1)), '-append', 'newline', 'pc');

%# --------------Make Random Walker Parameter File----------------
RandWalkerParam_FileName = ['RandomWalk_', PropName, '_', num2str(n),
'x',...
    num2str(n), 'Grid', fScale, '_fromS1.par'];
nT = n*ithScaleLevel*10; % # of time steps

general_makeRandomWalker_ParamFile(nxyzDownscaled,
PermModels_TXTFileName,...
    nT, RandWalkerParam_FileName)
```

```
%% ---------------READ RANDOM WALKER PARAMETER FILE-------------------

[WalkerParamFile, ~] = fopen(RandWalkerParam_FileName);

%# --------------Read Grid Dimensions----------------
GridDim = textscan(WalkerParamFile, '%d%d%d%s', 1);
nXDownscaled = GridDim{1}; nYDownscaled = GridDim{2}; nZDownscaled =
GridDim{3};
%# --------------Read # of Injectors----------------
Injector = textscan(WalkerParamFile, '%d%s', 1);
nInj = Injector{1};
%# --------------Read Coordinates of Injectors----------------
InjCoord = textscan(WalkerParamFile, '%d%d%d', nInj);
InjX = InjCoord{1};
InjY = InjCoord{2};
InjZ = InjCoord{3};
%# --------------Read # of Monitoring Locations----------------
Monitor = textscan(WalkerParamFile, '%d%s', 1);
nMonitors = Monitor{1};
%# --------------Read Coordinates of Monitoring Locations--------------
MonitCoord = textscan(WalkerParamFile, '%d%d%d', nMonitors);

clear GridDim Injector InjCoord Monitor MonitCoord WalkerParamFileName;
%# --------------Read Permeability File Name----------------
temp = textscan(WalkerParamFile, '%s', 1);
PermFileName = char(temp{1});
%# --------------Open, Read and Close Permeability File----------------
PermFile = fopen(PermFileName);
temp = textscan(PermFile, '%d', 1);
nPermModels = temp{1};
fclose(PermFile);
perm_temp = csvread(PermFileName, 1, 0);
perms = zeros(nXDownscaled, nYDownscaled, nZDownscaled, nPermModels);
perms(:, :, :, 1:nPermModels) = reshape(perm_temp, nXDownscaled,
nYDownscaled,...
    nZDownscaled, nPermModels);
perms = double(perms);

% Top and bottom boundary is closed, lateral boundaries are const
pressure
max_perm(1:nPermModels, 1) = max(max(max(perms)));

clear counter i j k perm_temp PermFileName

%# --------------Read Pressure File Name----------------
temp = textscan(WalkerParamFile, '%s', 1);
pr_file = char(temp{1});
pr_fid = fopen(pr_file);
```

```
counter = 0;
pressures = ones(nXDownscaled, nYDownscaled, nZDownscaled);
for k = 1:nZDownscaled
    for j = 1:nYDownscaled
        for i = 1:nXDownscaled
            counter = counter + 1;
            temp = textscan(pr_fid, '%d', 1);
            pressures(i,j,k) = temp{1};
        end
    end
end

max_pr = max(max(max(pressures)));
min_pr = min(min(min(pressures)));
clear counter i j k pr_temp pr_file
temp = textscan(WalkerParamFile, '%d', 1);
total_steps = temp{1};
fclose(WalkerParamFile);
clear temp;

%% ------------INITIALIZE ARRAYS FOR SATURATION AND PRESSURE ANALOG----
---------

final_particle_count = zeros(nXDownscaled, nYDownscaled, nZDownscaled,
nPermModels);

%% Hayek et al.: Input parameters

D = 1e-09; % m^2/s

%% --------------START THE PARTICLE TRACKING----------------

for current_model = 1:nPermModels
    start_time = cputime;
    particle_count = zeros(nXDownscaled, nYDownscaled, nZDownscaled);

    for curr_step = 1:total_steps
        tSec = curr_step*365*24*3600; % year to sec

        for iInj = 1:nInj
            particle_count(InjX(iInj),   InjY(iInj),   InjZ(iInj))   =
particle_count(InjX(iInj), InjY(iInj), InjZ(iInj)) + 20;
        end

        [X, Y] = find(particle_count);
        num_nonzero = length(X);
        particle_locations = zeros(num_nonzero, 3);
        particle_locations(1:num_nonzero, 1) = X;
```

```
        particle_locations(1:num_nonzero, 2) = Y;
        particle_locations(1:num_nonzero, 3) = 1;
        clear X Y

        for locs = 1:num_nonzero
            nodeX = particle_locations(locs, 1);
            nodeY = particle_locations(locs, 2);
            nodeZ = particle_locations(locs, 3);

            movements = particle_count(nodeX, nodeY, nodeZ);

            for num_particles = 1:movements
                will_move = 1;
                i = nodeX; j = nodeY; k = nodeZ;
                while (will_move == 1)
    %# ----------------Calculate Transition Probability----------------
                    transition_prob = zeros(7, 1);
                    if (i == 1)
                        transition_prob(2) = 0;
                    else
                        transition_prob(2) = (exp(-(perms(i - 1, j, k,
current_model)*perms(i, j, k, current_model))/((perms(i - 1, j, k,
current_model) +...
                            perms(i,                j,                k,
current_model))*max_perm(current_model))) +...
                            exp(-double((i*(i - 1))/(4*D*tSec))));
                    end

                    if (i == nXDownscaled)
                        transition_prob(1) = 0;
                    else
                        transition_prob(1) = (exp(-(perms(i + 1, j, k,
current_model)*perms(i, j, k, current_model))/((perms(i + 1, j, k,
current_model) +...
                            perms(i,                j,                k,
current_model))*max_perm(current_model))) +...
                            exp(-double((i*(i + 1))/(4*D*tSec))));
                    end

                    if (j == 1)
                        transition_prob(4) = 0;
                    else
                        transition_prob(4) = (exp(-(perms(i, j - 1, k,
current_model)*perms(i, j, k, current_model))/((perms(i, j - 1, k,
current_model) +...
                            perms(i,                j,                k,
current_model))*max_perm(current_model))) +...
                            exp(-double((j*(j - 1))/(4*D*tSec))));
                    end
```

```
                    if (j == nYDownscaled)
                        transition_prob(3) = 0;
                    else
                        transition_prob(3) = (exp(-(perms(i, j + 1, k,
current_model)*perms(i, j, k, current_model))/((perms(i, j + 1, k,
current_model) +...
                            perms(i,                j,                k,
current_model))*max_perm(current_model))) +...
                            exp(-double((j*(j + 1))/(4*D*tSec))));
                    end

                    if k == nZDownscaled
                        transition_prob(5) = 0;
                    else
                        transition_prob(5) = (exp(-(perms(i, j, k + 1,
current_model)*perms(i, j, k, current_model))/((perms(i, j, k + 1,
current_model) +...
                            perms(i,                j,                k,
current_model))*max_perm(current_model))) +...
                            exp(-double((k*(k + 1))/(4*D*tSec))));
                    end

                    if k == 1
                        transition_prob(6) = 0;
                    else
                        transition_prob(6) = (exp(-(perms(i, j, k - 1,
current_model)*perms(i, j, k, current_model))/((perms(i, j, k - 1,
current_model) +...
                            perms(i,                j,                k,
current_model))*max_perm(current_model))) +...
                            exp(-double((k*(k - 1))/(4*D*tSec))));
                    end
%#  ----------------Sample from transition probabiltiy and count
particles----------------
                    transition_prob(7)    =    (exp(-perms(i,    j,    k,
current_model)/max_perm(current_model)) +...
                            exp(-double((i*j)/(4*D*tSec))));
                    for num = 1:7
                        if transition_prob(num) < 0
                            transition_prob(num) = 0;
                        end
                    end

                    total_move = sum(transition_prob);
                    transition_prob = transition_prob/total_move;

                    if total_move == 0
                        break
```

```
                    end

                    num = discretesample(transition_prob, 1);

                    switch num
                        case 1
                            particle_count(i    +    1,    j,    k)    =
particle_count(i + 1, j, k) + 1;
                            particle_count(i, j, k) = particle_count(i,
j, k) - 1;
                            i = i + 1;
                        case 2
                            particle_count(i    -    1,    j,    k)    =
particle_count(i - 1, j, k) + 1;
                            particle_count(i, j, k) = particle_count(i,
j, k) - 1;
                            i = i - 1;
                        case 3
                            particle_count(i,    j    +    1,    k)    =
particle_count(i, j + 1, k) + 1;
                            particle_count(i, j, k) = particle_count(i,
j, k) - 1;
                            j = j + 1;
                        case 4
                            particle_count(i,    j    -    1,    k)    =
particle_count(i, j - 1, k) + 1;
                            particle_count(i, j, k) = particle_count(i,
j, k) - 1;
                            j = j - 1;
                        case 5
                            particle_count(i,    j,    k    +    1)    =
particle_count(i, j, k + 1) + 1;
                            particle_count(i, j, k) = particle_count(i,
j, k) - 1;
                            k = k + 1;
                        case 6
                            particle_count(i,    j,    k    -    1)    =
particle_count(i, j, k - 1) + 1;
                            particle_count(i, j, k) = particle_count(i,
j, k) - 1;
                            k = k - 1;
                        case 7
                            will_move = 0;
                    end
                end
            end
        end
    end
```

```
    disp(['Completed model # ', num2str(current_model), ' in ',
num2str(cputime - start_time), ' secs.']);
    final_particle_count(:, :, :, current_model) = particle_count;
    clear i j k u v w distance dist_temp counter parti_count
dist_matrix dist_temp
    clear particle_count;
end
final_particle_count = squeeze(final_particle_count);
```

Glossary

SYMBOLS:

a = stoichiometric coefficient

a_i = chemical equilibrium coefficients

$a_{\max}$ = maximum correlation length of a heterogeneous field

$\mathbf{a_1}$ = drift vector in RWPT (related to advection)

$\mathbf{a_2}$ = displacement matrix in RWPT (related to dispersion)

A = Cross sectional area

$\widehat{A}$ = reactive surface area at the current time

$\widehat{A}_0$ = reactive surface area at the initial (zero) time

b_1 and b_2 = diffusion behavior parameters in non-Fickian formulation

c = concentration

c_i = concentration of species i

c_ϕ = rock compressibility

C_c = covariance of concentration for diffusive-reactive processes

C_o = variance at a lower cutoff

D = Diffusion constant

D_L = Longitudinal coefficient of mechanical dispersion

D_i = diffusion coefficient of species i

Da = Damkohler number

E_a = activation energy

f = Fine scale attribute

$\overline{f}$ = Mean of attribute

$\mathbf{h}$ = spatial lag

H = Global window width

I = unit matrix

$j(S_{1D})$ = Leverett j - function

k^0 = initial permeability

$\bar{k}_{AB}$ = harmonic mean permeability between grids A and B

$\bar{k}_x$ = Average permeability in x-direction

k_{rj}^o = endpoint relative permeability of phase j

K_{eq} = chemical equilibrium constant

L = Lateral length of porous media

L_D = lower triangular matrix of the Cholesky decomposition of the dimensionless co variance matrix

$n_1,\ n_2,\ n_{Pc}$ = petrophysical relations

$N(\mathbf{h})$ = number of data points at separated by lag **h**

N_i = total moles of mineral i per bulk volume at current time

N_i^0 = total moles of mineral i per bulk volume at initial (zero) time

p^* = reference pressure

$p_\kappa(\alpha; x, t)$ = pdf of reaction rate in combined space and time

Q = Volumetric flow rate

Q_{act} = activity product

r = reaction rate law

r_{AB}^2 = product of distance from injection point to grids A and B

s = spatial distance along x, y or z direction

S_{jD} = dimensionless (or normalized) saturation of phase j

S_w = aqueous phase saturation

t = time

t_D = Dimensionless time (or pore volumes injected)

u_i = Darcy or superficial velocity of phase i

U(t) = uniform transform of unconditional Gaussian noise at time 't'

$\mathbf{v}$ = average fluid flow velocity

V_b = coarse block bulk volume

V_{DP} = Dykstra-Parsons coefficient

V_p = Pore volume

w = vector of N uncorrelated random variables from a standard normal distribution

z = direction perpendicular to the external surface

z_i = charge of species i

GREEK SYMBOLS:

α = reaction rate constant

α_i = TST rate constant

α_{dip} = reservoir dip angle

$\beta_m(s)$ = mean-zero random effect representing location-specific variability common to all times

$\delta_m(s;t)$ = mean-zero random effect representing the micro-scale spatiotemporal variability that is modeled by white noise in $R^d \times R^1$

γ_i = activity coefficient of species i

γ_s = Spatial variogram model (bounded)

γ_t = Temporal variogram model (bounded)

$\gamma 1_s$ = Spatial variogram model (not necessarily bounded)

$\gamma 2_t$ = Temporal variogram model (not necessarily bounded)

$\gamma_m(t)$ = mean-zero random effect representing time-specific variability common to all locations

η_{Dx}, η_{Dz} = sizes of a dimensionless pixel

η_i = all possible spatial lags within L or $V\left(= L \times B \times H\right)$

λ_{rj}^{o} = endpoint relative mobility of phase j

λ_{Di}^{*} = dimensionless effective correlation length in i direction (i = x or z)

$\lambda_{Dx}(=\lambda_x / L), \lambda_{Dz}(=\lambda_z / H)$ = dimensionless power-law upper cutoffs defined on a normally distributed field

μ_j = viscosity of phase j

$\mu_m(s;t)$ = deterministic mean of the components-of-variation model

θ = contact angle

θ_s = spatial anisotropy parameter

θ_t = temporal anisotropy parameter

$\kappa_m(s;t)$ = mean-zero random effect capturing the spatiotemporal interaction not found in the larger-scale deterministic $\mu_m(s;t)$

ξ, ζ = TST parameters (default values for both = 1)

ρ_{corr} = autocorrelation function

ρ_i = molar density of mineral i

$\Delta\rho$ = density difference between two phases

σ = oil/water interfacial tension

σ^2 = variance of fine scale attribute *f*

τ = temporal lag

ϕ = porosity

ϕ^* = reference porosity without mineral precipitation/dissolution

$\hat{\phi}^*$ = reference porosity including mineral precipitation/dissolution

ϕ^0 = initial porosity

ω = averaging exponent

SUBSCRIPTS:

D = dimensionless

i = chemical species index

j = phase index

max = maximum quantity

x, *y*, *z* = refers to coordinate directions x, y, z (z also represents elevation)

ACRONYMS:

B.C. = boundary conditions

BT = breakthrough

CIP = change in porosity $(1-\Delta\phi/\phi)$

CO2CONC = volume based dimensionless CO_2 concentration

I.C. = initial conditions

LHS = left hand side

MZL = mixing zone length

PDE = partial differential equation

PGA = pore geometry alteration

PV = pore volume

PVI = pore volumes injected

REV = representative elementary volume

RHS = right hand side

SDE = stochastic differential equation

SGSIM = sequential Gaussian simulation

SISIM = sequential indicator simulation

NOTES:

1. **bolded** quantities refer to vector or matrix

Bibliography

Aarão Reis, F. D. A., and Dung di Caprio. 2014. "Crossover from Anomalous to Normal Diffusion in Porous Media." *Physical Review E* 89 (6): 062126. doi:10.1103/PhysRevE.89.062126.

Aharonov, E., J. A. Whitehead, P. B. Kelemen, and M. Spiegelman. 1995. "Channeling Instability of Upwelling Melt in the Mantle." *Journal of Geophysical Research* 100 (B10): 20433–20,450. doi:10.1029/95JB01307.

Arya, Atul, Tom Hewett, Ronald Larson, and Larry W. Lake. 1988. "Dispersion and Reservoir Heterogeneity." *SPE Reservoir Engineering* 3 (1). doi:10.2118/14364-PA.

Battiato, I., and D.M. Tartakovsky. 2011. "Applicability Regimes for Macroscopic Models of Reactive Transport in Porous Media." *Journal of Contaminant Hydrology* 120-121 (March): 18–26. doi:10.1016/j.jconhyd.2010.05.005.

Bear, Jacob. 1972. *Dynamics of Fluids in Porous Media*. American Elsevier Pub. Co.

Berkowitz, Brian, Andrea Cortis, Marco Dentz, and Harvey Scher. 2006. "Modeling Non-Fickian Transport in Geological Formations as a Continuous Time Random Walk." *Reviews of Geophysics* 44 (2): RG2003. doi:10.1029/2005RG000178.

Berkowitz, Yotam, Yaniv Edery, Harvey Scher, and Brian Berkowitz. 2013. "Fickian and Non-Fickian Diffusion with Bimolecular Reactions." *Physical Review E* 87 (3): 032812. doi:10.1103/PhysRevE.87.032812.

Bijeljic, Branko, and Martin J. Blunt. 2006. "Pore-Scale Modeling and Continuous Time Random Walk Analysis of Dispersion in Porous Media." *Water Resources Research* 42 (1): W01202. doi:10.1029/2005WR004578.

Burton, McMillan. 2008. "Surface Dissolution: Addressing Technical Challenges of CO_2 Injection and Storage in Brine Aquifers." The University of Texas at Austin.

Burton, McMillan, Navanit Kumar, and Steven Bryant. 2008. "Time-Dependent Injectivity During CO_2 Storage in Aquifers." In . Society of Petroleum Engineers. doi:10.2118/113937-MS.

Castro-Alcalá, Eduardo, Daniel Fernàndez-Garcia, Jesus Carrera, and Diogo Bolster. 2012. "Visualization of Mixing Processes in a Heterogeneous Sand Box Aquifer." *Environmental Science & Technology* 46 (6): 3228–35. doi:10.1021/es201779p.

Chen, X., B. M. Ng, Y. Sun, and C. H. Tong. 2013. "A Computational Method for Simulating Subsurface Flow and Reactive Transport in Heterogeneous Porous Media Embedded with Flexible Uncertainty Quantification." *Water Resources Research* 49 (9): 5740–55. doi:10.1002/wrcr.20454.

Christie, M. A. 2001. "Flow in Porous Media -- Scale up of Multiphase Flow." *Current Opinion in Colloid & Interface Science* 6 (3): 236–41. doi:10.1016/S1359-0294(01)00087-5.

Costanza-Robinson, Molly S., Benjamin D. Estabrook, and David F. Fouhey. 2011. "Representative Elementary Volume Estimation for Porosity, Moisture

Saturation, and Air-Water Interfacial Areas in Unsaturated Porous Media: Data Quality Implications." *Water Resources Research* 47 (7): W07513. doi:10.1029/2010WR009655.

Cressie, Noel, and Hsin-Cheng Huang. 1999. "Classes of Nonseparable, Spatio-Temporal Stationary Covariance Functions." *Journal of the American Statistical Association* 94 (448): 1330–40. doi:10.2307/2669946.

Cressie, Noel, and Christopher K. Wikle. 2011. *Statistics for Spatio-Temporal Data*. John Wiley and Sons.

Cushman, John H. 1982. "Proofs of the Volume Averaging Theorems for Multiphase Flow." *Advances in Water Resources* 5 (4): 248–53. doi:10.1016/0309-1708(82)90009-4.

Dagan, G., A. Fiori, and I. Janković. 2003. "Flow and Transport in Highly Heterogeneous Formations: 1. Conceptual Framework and Validity of First-Order Approximations." *Water Resources Research* 39 (9): n/a – n/a. doi:10.1029/2002WR001717.

Dagan, Gideon. 1990. "Transport in Heterogeneous Porous Formations: Spatial Moments, Ergodicity, and Effective Dispersion." *Water Resources Research* 26 (6): 1281–90. doi:10.1029/WR026i006p01281.

Dai, Zhenxue, Robert W. Ritzi Jr., Chaocheng Huang, Yoram N. Rubin, and David F. Dominic. 2004. "Transport in Heterogeneous Sediments with Multimodal Conductivity and Hierarchical Organization across Scales." *Journal of Hydrology* 294 (1–3): 68–86. doi:10.1016/j.jhydrol.2003.10.024.

Dai, Zhenxue, Robert W. Ritzi, and David F. Dominic. 2005. "Improving Permeability Semivariograms with Transition Probability Models of Hierarchical Sedimentary Architecture Derived from Outcrop Analog Studies." *Water Resources Research* 41 (7): n/a – n/a. doi:10.1029/2004WR003515.

Dai, Zhenxue, Andrew Wolfsberg, Zhiming Lu, and Hailin Deng. 2009. "Scale Dependence of Sorption Coefficients for Contaminant Transport in Saturated Fractured Rock." *Geophysical Research Letters* 36 (1). doi:10.1029/2008GL036516.

Dai, Zhenxue, Andrew Wolfsberg, Zhiming Lu, and Paul Reimus. 2007. "Upscaling Matrix Diffusion Coefficients for Heterogeneous Fractured Rocks." *Geophysical Research Letters* 34 (7): n/a – n/a. doi:10.1029/2007GL029332.

Das, Amal K. 1991. "A non- Fickian Diffusion Equation." *Journal of Applied Physics* 70 (3): 1355–58. doi:10.1063/1.349592.

De Cesare, L, D.e Myers, and D Posa. 2001. "Product-Sum Covariance for Space-Time Modeling: An Environmental Application." *Environmetrics* 12 (1): 11–23. doi:10.1002/1099-095X(200102)12:1<11::AID-ENV426>3.0.CO;2-P.

De Iaco, S., D.E. Myers, and D. Posa. 2001. "Space–time Analysis Using a General Product–sum Model." *Statistics & Probability Letters* 52 (1): 21–28. doi:10.1016/S0167-7152(00)00200-5.

Deng, Hailin, Zhenxue Dai, Andrew Wolfsberg, Zhiming Lu, Ming Ye, and Paul Reimus. 2010. "Upscaling of Reactive Mass Transport in Fractured Rocks with Multimodal Reactive Mineral Facies." *Water Resources Research* 46 (6): n/a – n/a. doi:10.1029/2009WR008363.

Dentz, Marco, Andrea Cortis, Harvey Scher, and Brian Berkowitz. 2004. "Time Behavior of Solute Transport in Heterogeneous Media: Transition from Anomalous to Normal Transport." *Advances in Water Resources* 27 (2): 155–73. doi:10.1016/j.advwatres.2003.11.002.

Deutsch, Clayton V., and André G. Journel. 1997. *GSLIB: Geostatistical Software Library and User's Guide*. 2nd ed. Oxford University Press, USA.

Deyoreo, J., and D. J. Depaolo. 2009. "Nanoscale Controls on CO_2-Water-Rock Interactions in Saline Reservoirs." *AGU Fall Meeting Abstracts* 12 (December): 01.

Dongxiao, Zhang, and C.L. Winter. 1999. "Moment-Equation Approach to Single Phase Fluid Flow in Heterogeneous Reservoirs." *SPE Journal* 4 (June). doi:10.2118/56842-PA.

Durlofsky, LJ. 2003. *Upscaling of Geocellular Models for Reservoir Flow Simulation: A Review of Recent Progress*. 7th International Forum on Reservoir Simulation: Stanford University.

Edery, Yaniv, Alberto Guadagnini, Harvey Scher, and Brian Berkowitz. 2011. "Reactive Transport in Disordered Media: Role of Fluctuations in Interpretation of Laboratory Experiments." *Advances in Water Resources*. doi:10.1016/j.advwatres.2011.12.008.

Edery, Yaniv, Harvey Scher, and Brian Berkowitz. 2010. "Particle Tracking Model of Bimolecular Reactive Transport in Porous Media." *Water Resources Research* 46 (7): n/a – n/a. doi:10.1029/2009WR009017.

Edery, Yaniv, Harvey Scher, and Brian Berkowitz. 2011. "Dissolution and Precipitation Dynamics during Dedolomitization." *Water Resources Research* 47 (8): W08535. doi:10.1029/2011WR010551.

Emmanuel, Simon, and Brian Berkowitz. 2005. "Mixing-Induced Precipitation and Porosity Evolution in Porous Media." *Advances in Water Resources* 28 (4): 337–44. doi:10.1016/j.advwatres.2004.11.010.

Fiori, A., and G. Dagan. 2003. "Time-Dependent Transport in Heterogeneous Formations of Bimodal Structures: 2. Results." *Water Resources Research* 39 (5): n/a – n/a. doi:10.1029/2002WR001398.

Frind, E. O., E. A. Sudicky, and S. L. Schellenberg. 1987. "Micro-Scale Modelling in the Study of Plume Evolution in Heterogeneous Media." *Stochastic Hydrology and Hydraulics* 1 (4): 263–79. doi:10.1007/BF01543098.

Gardiner, Crispin. 2009. *Stochastic Methods: A Handbook for the Natural and Social Sciences*. Springer Berlin Heidelberg.

Gelhar, Lynn W., and Carl L. Axness. 1983. “Three-Dimensional Stochastic Analysis of Macrodispersion in Aquifers.” *Water Resources Research* 19 (1): 161–80. doi:10.1029/WR019i001p00161.

Genton, Marc G. 2007. “Separable Approximations of Space-Time Covariance Matrices.” *Environmetrics* 18 (7): 681–95. doi:10.1002/env.854.

Gharbi, Oussama, Branko Bijeljic, Edo Boek, and Martin J. Blunt. 2013. “Changes in Pore Structure and Connectivity Induced by CO_2 Injection in Carbonates: A Combined Pore-Scale Approach.” *Energy Procedia* 37: 5367–78. doi:10.1016/j.egypro.2013.06.455.

Gharbi, Ridha, Ekwere Peters, and Ali Elkamel. 1998. “Scaling Miscible Fluid Displacements in Porous Media.” *Energy Fuels* 12 (4): 801–11. doi:10.1021/ef980020a.

Gneiting, Tilmann. 2002. “Nonseparable, Stationary Covariance Functions for Space–Time Data.” *Journal of the American Statistical Association* 97 (458): 590–600. doi:10.1198/016214502760047113.

Grindrod, Peter. 1991. *Patterns and Waves: The Theory and Applications of Reaction-Diffusion Equations*. Oxford; New York: Oxford University Press.

Grzybowski, Bartosz A. 2009. *Chemistry in Motion: Reaction-Diffusion Systems for Micro- and Nanotechnology*. John Wiley & Sons.

Gunter, W. D., B. Wiwehar, and E. H. Perkins. 1997. “Aquifer Disposal of CO_2-Rich Greenhouse Gases: Extension of the Time Scale of Experiment for CO_2-Sequestering Reactions by Geochemical Modelling.” *Mineralogy and Petrology* 59 (1-2): 121–40. doi:10.1007/BF01163065.

Hassanizadeh, S. Majid, and Diganta Bhusan Das. 2005. *Upscaling Multiphase Flow in Porous Media: From Pore to Core and beyond*. Springer.

Heine, V. 1955. “Models for Two-Dimensional Stationary Stochastic Processes.” *Biometrika* 42 (1-2): 170–78. doi:10.1093/biomet/42.1-2.170.

Hoefner, M. L., and H. S. Fogler. 1988. “Pore Evolution and Channel Formation during Flow and Reaction in Porous Media.” *AIChE Journal* 34 (1): 45–54. doi:10.1002/aic.690340107.

Howes, Frederick A., and Stephen Whitaker. 1985. “The Spatial Averaging Theorem Revisited.” *Chemical Engineering Science* 40 (8): 1387–92. doi:10.1016/0009-2509(85)80078-6.

Izgec, Omer, Birol Demiral, Henri Bertin, and Serhat Akin. 2005. “CO_2 Injection in Carbonates.” In *Proceedings of SPE Western Regional Meeting*. doi:10.2118/93773-MS.

Izgec, Omer, Birol Demiral, Henri Bertin, and Serhat Akin. 2007. “CO_2 Injection into Saline Carbonate Aquifer Formations II: Comparison of Numerical Simulations to Experiments.” *Transport in Porous Media* 73 (1): 57–74. doi:10.1007/s11242-007-9160-1.

Johnson, James W., John J. Nitao, and Kevin G. Knauss. 2004. “Reactive Transport Modelling of CO_2 Storage in Saline Aquifers to Elucidate Fundamental Processes, Trapping Mechanisms and Sequestration Partitioning.” *Geological Society, London, Special Publications* 233 (1): 107–28. doi:10.1144/GSL.SP.2004.233.01.08.

Journel, André G., and Ch J. Huijbregts. 2003. *Mining Geostatistics*. BLACKBURN Press.

Kim, Eric. 2012. “Investigation of CO_2 Seeps at the Crystal Geyser Site Using Numerical Modeling with Geochemistry.” Thesis, Austin, Texas.: The University of Texas at Austin.

Lai, Keng-Hsin, Jui-Sheng Chen, Chen-Wuing Liu, and Suh-Yuh Yang. 2014. “Effect of Permeability–porosity Functions on Simulated Morphological Evolution of a Chemical Dissolution Front.” *Hydrological Processes* 28 (1): 16–24. doi:10.1002/hyp.9492.

Lake, Larry W., S. L. Bryant, and Aura N. Araque-Martinez. 2002. *Geochemistry and Fluid Flow*. Elsevier.

Lake, Larry W., and Sanjay Srinivasan. 2004. “Statistical Scale-up of Reservoir Properties: Concepts and Applications.” *Journal of Petroleum Science and Engineering* 44 (1–2): 27–39. doi:10.1016/j.petrol.2004.02.003.

Lake, Larry W., Sanjay Srinivasan, and Abraham John. 2005. “Statistical Scale-up: Concepts and Application to Reservoir Flow Simulation.” In *Geostatistics Banff 2004*, edited by Oy Leuangthong and Clayton V. Deutsch, 14:681–90. Dordrecht: Springer Netherlands.

Lamy-Chappuis, Benoit, Doug Angus, Quentin Fisher, Carlos Grattoni, and Bruce W. D. Yardley. 2014. “Rapid Porosity and Permeability Changes of Calcareous Sandstone due to CO_2-Enriched Brine Injection.” *Geophysical Research Letters* 41 (2): 2013GL058534. doi:10.1002/2013GL058534.

Lashgari, Hamid Reza. 2014. "Development of a Four-Phase Thermal-Chemical Reservoir Simulator for Heavy Oil." PhD Dissertation, Austin, Texas.: The University of Texas at Austin.

Leung, Juliana. 2009. “Reservoir Modeling Accounting for Scale-up of Heterogeneity and Transport Processes.” PhD Dissertation, Austin, Texas.: The University of Texas at Austin.

Leung, Juliana, and Sanjay Srinivasan. 2011. “Analysis of Uncertainty Introduced by Scaleup of Reservoir Attributes and Flow Response in Heterogeneous Reservoirs.” *SPE Journal*. doi:10.2118/145678-PA.

Li, Dachang, and Larry Lake. 1996. “Scaling Fluid Flow Through Heterogeneous Permeable Media.” *Society of Petroleum Engineers*.

Li, Li, Carl I. Steefel, and Li Yang. 2008. “Scale Dependence of Mineral Dissolution Rates within Single Pores and Fractures.” *Geochimica et Cosmochimica Acta* 72 (2): 360–77. doi:16/j.gca.2007.10.027.

Liu, Qi, and M. Mercedes Maroto-Valer. 2011. “Parameters Affecting Mineral Trapping of CO_2 Sequestration in Brines.” *Greenhouse Gases: Science and Technology* 1 (3): 211–22. doi:10.1002/ghg.29.

Li, Zhongwei. 2006. *Temporal Scaling and Complexity Analyses of Dynamic Groundwater Systems*. ProQuest.

Luquot, L., O. Rodriguez, and P. Gouze. 2014. “Experimental Characterization of Porosity Structure and Transport Property Changes in Limestone Undergoing Different Dissolution Regimes.” *Transport in Porous Media* 101 (3): 507–32. doi:10.1007/s11242-013-0257-4.

Ma, Chunsheng. 2003. “Families of Spatio-Temporal Stationary Covariance Models.” *Journal of Statistical Planning and Inference* 116 (2): 489–501. doi:10.1016/S0378-3758(02)00353-1.

Ma, Chunsheng. 2005. “Spatio-Temporal Variograms and Covariance Models.” *Advances in Applied Probability* 37 (3): 706–25. doi:10.1239/aap/1127483743.

Major, J. R., P. Eichhubl, and T. A. Dewers. 2013. “Extent and Effect of Fault-Controlled CO_2 Alteration on Reservoir and Seal Rocks and Implications for Geomechanical Failure at Crystal Geyser, Green River, Utah.” *AGU Fall Meeting Abstracts* 23 (December): 1242.

Menand, T., and A. W. Woods. 2005. “Dispersion, Scale, and Time Dependence of Mixing Zones under Gravitationally Stable and Unstable Displacements in Porous Media.” *Water Resources Research* 41 (May): 13 PP. doi:200510.1029/2004WR003701.

Montroll, Elliott W., and George H. Weiss. 1965. “Random Walks on Lattices. II.” *Journal of Mathematical Physics* 6 (2): 167–81. doi:10.1063/1.1704269.

Nelder, J. A., and R. Mead. 1965. “A Simplex Method for Function Minimization.” *The Computer Journal* 7 (4): 308–13. doi:10.1093/comjnl/7.4.308.

Nghiem, Long, Peter Sammon, Jim Grabenstetter, and Hiroshi Ohkuma. 2004. “Modeling CO_2 Storage in Aquifers with a Fully-Coupled Geochemical EOS Compositional Simulator.” In . Society of Petroleum Engineers. doi:10.2118/89474-MS.

Nghiemw, L., A. Shrivastavar, B. Kohse, and P. Sammon. 2004. “Simulation of CO_2 EOR and Sequestration Processes With a Geochemical EOS Compositional Simulator.” In . Petroleum Society of Canada. doi:10.2118/2004-051.

Nœtinger, B., and T. Estebenet. 2000. “Up-Scaling of Double Porosity Fractured Media Using Continuous-Time Random Walks Methods.” *Transport in Porous Media* 39 (3): 315–37. doi:10.1023/A:1006639025910.

Odén, Magnus, Auli Niemi, Chin-Fu Tsang, and Johan Öhman. 2008. “Regional Channelized Transport in Fractured Media with Matrix Diffusion and Linear Sorption.” *Water Resources Research* 44 (2): W02421. doi:10.1029/2006WR005632.

Ovaysi, Saeed, and Mohammad Piri. 2010. “Direct Pore-Level Modeling of Incompressible Fluid Flow in Porous Media.” *Journal of Computational Physics* 229 (19): 7456–76. doi:10.1016/j.jcp.2010.06.028.

Ovaysi, Saeed, and Mohammad Piri. 2011. “Pore-Scale Modeling of Dispersion in Disordered Porous Media.” *Journal of Contaminant Hydrology* 124 (1–4): 68–81. doi:10.1016/j.jconhyd.2011.02.004.

Ovaysi, Saeed, and Mohammad Piri. 2013. “Pore-Scale Dissolution of $CO_2 + SO_2$ in Deep Saline Aquifers.” *International Journal of Greenhouse Gas Control* 15 (July): 119–33. doi:10.1016/j.ijggc.2013.02.009.

Ovaysi, Saeed, and Mohammad Piri. 2014. “Pore-Space Alteration Induced by Brine Acidification in Subsurface Geologic Formations.” *Water Resources Research* 50 (1): 440–52. doi:10.1002/2013WR014289.

Palanichamy, Jegathambal, Torsten Becker, Martin Spiller, Jürgen Köngeter, and Sankaralingam Mohan. 2009. “Multicomponent Reaction Modelling Using a Stochastic Algorithm.” *Computing and Visualization in Science* 12 (2): 51–61. doi:10.1007/s00791-007-0080-y.

Peters, Ekwere J. 1983. “Scaling Unstable Immiscible Displacements,” January. https://www.onepetro.org/general/SPE-12331-MS.

Qi, Dasheng, and Tim Hesketh. 2005. “An Analysis of Upscaling Techniques for Reservoir Simulation.” *Petroleum Science and Technology* 23 (7-8): 827–42. doi:10.1081/LFT-200033132.

Quintard, Michel, and Stephen Whitaker. 1994. “Convection, Dispersion, and Interfacial Transport of Contaminants: Homogeneous Porous Media.” *Advances in Water Resources* 17 (4): 221–39. doi:10.1016/0309-1708(94)90002-7.

Remy, Nicolas, Alexandre Boucher, and Jianbing Wu. 2009. *Applied Geostatistics with SGeMS: A User’s Guide*. 1 Har/Cdr. Cambridge University Press.

Romushkevich, Raisa, Anton Parshin, Dmitry Miklashevskiy, Irina Bayuk, Stanislav Ursegov, Sergey Safonov, Igor Gerasimov, et al. 2013. “Experimental Investigations of Spatial and Temporal Variations in Rock Thermal Properties as Necessary Stage in Thermal EOR.” In . Society of Petroleum Engineers. doi:10.2118/165474-MS.

Russian, Anna. 2013. “Anomalous Dynamics of Darcy Flow and Diffusion through Heterogeneous Media.” PhD Dissertation, UNIVERSITAT POLIT`ECNICA DE CATALUNYA. http://www.tesisenred.net/handle/10803/116499.

Sagi, Yoav, Miri Brook, Ido Almog, and Nir Davidson. 2012. “Observation of Anomalous Diffusion and Fractional Self-Similarity in One Dimension.” *Physical Review Letters* 108 (9): 093002. doi:10.1103/PhysRevLett.108.093002.

Sajjadi, M., and J. Azaiez. 2013. “Scaling and Unified Characterization of Flow Instabilities in Layered Heterogeneous Porous Media.” *Physical Review E* 88 (3): 033017. doi:10.1103/PhysRevE.88.033017.

Schabenberger, Oliver, and Carol A. Gotway. 2004. *Statistical Methods for Spatial Data Analysis*. CRC Press.

Shafeen, A, E Croiset, P. L Douglas, and I Chatzis. 2004. "CO_2 Sequestration in Ontario, Canada. Part I: Storage Evaluation of Potential Reservoirs." *Energy Conversion and Management* 45 (17): 2645–59. doi:10.1016/j.enconman.2003.12.003.

Shipton, Z. K., J. P. Evans, D. Kirschner, P. T. Kolesar, A. P. Williams, and J. Heath. 2004. "Analysis of CO_2 Leakage Through 'low-Permeability' Faults from Natural Reservoirs in the Colorado Plateau, East-Central Utah." *Geological Society, London, Special Publications* 233 (1): 43–58. doi:10.1144/GSL.SP.2004.233.01.05.

Shook, M., D. Li, and L. W. Lake. 1992. *Scaling Immiscible Flow through Permeable Media by Inspectional Analysis*. Vol. 16, No. 4. In Situ.

Singh, Harpreet, Seyyed Abolfazl Hosseini, and Farzam Javadpour. 2012. "Enhanced CO_2 Storage In Deep Saline Aquifers By Nanoparticles: Numerical Simulation Results." In . Society of Petroleum Engineers. doi:10.2118/156983-MS.

Singh, Harpreet, and Sanjay Srinivasan. 2014. "Scale up of Reactive Processes in Heterogeneous Media - Numerical Experiments and Semi-Analytical Modeling." In . Tulsa, Oklahoma, USA: Society of Petroleum Engineers. doi:10.2118/169133-MS.

Steefel Carl I., and Lasaga Antonio C. 1990. "Evolution of Dissolution Patterns." In *Chemical Modeling of Aqueous Systems II*, 416:212–25. ACS Symposium Series 416. American Chemical Society. http://dx.doi.org/10.1021/bk-1990-0416.ch016.

Szymczak, P., and A. J. C. Ladd. 2013. "Interacting Length Scales in the Reactive-Infiltration Instability." *Geophysical Research Letters* 40 (12): 3036–41. doi:10.1002/grl.50564.

Tartakovsky, Daniel M., Marco Dentz, and Peter C. Lichtner. 2009. "Probability Density Functions for Advective-Reactive Transport with Uncertain Reaction Rates." *Water Resources Research* 45 (7): n/a – n/a. doi:10.1029/2008WR007383.

Tóth, J. 1962. "A Theory of Groundwater Motion in Small Drainage Basins in Central Alberta, Canada." *Journal of Geophysical Research* 67 (11): 4375–88. doi:10.1029/JZ067i011p04375.

Tóth, J. 1963. "A Theoretical Analysis of Groundwater Flow in Small Drainage Basins." *Journal of Geophysical Research* 68 (16): 4795–4812. doi:10.1029/JZ068i016p04795.

"TriScatteredInterp." R2013b. MathWorks. http://www.mathworks.com/help/matlab/ref/triscatteredinterp.html.

Tutolo, Benjamin M., Andrew J. Luhmann, Xiang-Zhao Kong, Martin O. Saar, and William E. Seyfried. 2014. "Experimental Observation of Permeability Changes In Dolomite at CO_2 Sequestration Conditions." *Environmental Science & Technology* 48 (4): 2445–52. doi:10.1021/es4036946.

Urquhart, Alexander Sebastian MacDonald. 2011. “Structural Controls on CO_2 Leakage and Diagenesis in a Natural Long-Term Carbon Sequestration Analogue : Little Grand Wash Fault, Utah.” http://repositories.lib.utexas.edu/handle/2152/20200.

Whitaker, Stephen. 1999. *The Method of Volume Averaging*. Springer.

Wikle, Christopher K. 2003. “Hierarchical Models in Environmental Science.” *International Statistical Review* 71 (2): 181–99. doi:10.1111/j.1751-5823.2003.tb00192.x.

Wood, Derek, Larry Lake, Russell Johns, and Vanessa Nunez. 2008. “A Screening Model for CO_2 Flooding and Storage in Gulf Coast Reservoirs Based on Dimensionless Groups.” *SPE Reservoir Evaluation & Engineering* 11 (3). doi:10.2118/100021-PA.

Yang, An-Ping. 1990. “Stochastic Heterogeneity and Dispersion.” PhD Dissertation, Austin, Texas.: The University of Texas at Austin.

Zhu, Zhouyuan. 2011. “Upscaling for Field-Scale In-Situ Combustion Simulation.” In . Society of Petroleum Engineers. doi:10.2118/152375-STU.

Zijl, Wouter. 1999. “Scale Aspects of Groundwater Flow and Transport Systems.” *Hydrogeology Journal* 7 (1): 139–50. doi:10.1007/s100400050185.